

MIXED HTPB/PARAFFIN FUELS AND METALLIC ADDITIVES FOR HYBRID
ROCKET APPLICATIONS

A Dissertation

by

JAMES C. THOMAS

Submitted to the Office of Graduate and Professional Studies of
Texas A&M University
in partial fulfillment of the requirements for the degree of

DOCTOR OF PHILOSOPHY

Chair of Committee,	Eric L. Petersen
Committee Members,	Waruna D. Kulatilaka
	Timothy J. Jacobs
	Adonios N. Karpetis
Head of Department,	Andreas A. Polycarpou

December 2018

Major Subject: Mechanical Engineering

Copyright 2018 James C. Thomas

ABSTRACT

Hybrid rockets have distinct advantages over their pure solid or liquid propellant counterparts, but their widespread application has been hindered by characteristically low regression rates and combustion efficiencies. A comprehensive review of hybrid rocket enhancement strategies is given within, with special emphasis on metallic additives and mixed-fuel (HTPB/paraffin) systems.

Several metallic additives (micro-aluminum, micro-magnesium, micro-titanium, micro-zirconium, nano-aluminum, nano-boron, and magnesium-coated nano-boron) were selected as potential candidates for hybrid rocket applications and characterized by applicable microscopy techniques. The regression rates and combustion efficiencies of plain HTPB and HTPB loaded with each additive at various concentrations (10%, 20% and 30% by mass) burning in GOX were evaluated at moderate oxidizer mass fluxes (10-150 kg/m²-s) and pressures (<125 psia).

In general, the inclusion of any of the metallic additives led to a reduction in the regression rate. The one exception to this trend was the formulation containing 10% micro-zirconium which yielded a moderate (10-20%) increase in regression rate. The observed trends were more prevalent at higher oxidizer mass fluxes and higher additive loadings. The reductions in regression rate were attributed to heat transfer blocking effects derived from accumulation of mass on the fuel surface layer. These phenomena were especially prevalent in highly loaded fuel formulations containing nano-aluminum or boron which exhibited unstable combustion and periodic surface layer shedding.

Zirconium appears to be the best metallic additive available since it can yield the highest theoretical density specific impulse under the lowest O/F operation ratio without resulting in substantial decreases in the fuel regression rate or mass flux. Combustion efficiency data of all fuel formulations were well correlated to the fuel residence time, and high combustion efficiencies (>95%) were achievable when a satisfactory residence time (~75 ms) was realized.

The inclusion of molten paraffin in HTPB at concentrations of 10-75% as a regression rate enhancement strategy was evaluated under similar conditions. The plain paraffin fuel exhibited a 300% increase in regression rate in comparison to plain HTPB, but none of the mixed-fuel systems showed signs of regression rate enhancement at the tested operating conditions.

DEDICATION

This work is dedicated to my family without whom I would not have been able to accomplish everything I have. My mother, Betty Thomas, and my father, Kelly Thomas, have guided me since I was a child and their various contributions to my life cannot be summarized in such a 'short' document. My sisters, Cassy and Cara Thomas, have supported me in all my undertakings and goals. My wife, Lauren Thomas, has sacrificed much to see me through to my goals, and her love and support is much appreciated. I love you all.

ACKNOWLEDGEMENTS

The research presented herein is the culmination of many years of hard work and would not have been successful without the contributions of many people. Numerous colleagues of mine at Texas A&M University's Propulsion Laboratory have contributed to various aspects of my research and deserve recognition. These colleagues include Felix Rodriguez, Andrew Tykol, Jacob Stahl, Gordon Morrow, Catherine Dillier, Thomas Sammet, Erica Petersen, Andrew Demko, Gabriel Homan-Cruz, Ray Matthews, and many others. In particular, Felix Rodriguez was instrumental in performing all of the ballistic experiments discussed herein, Andrew Tykol was heavily involved in performing the ballistic experiments on mixed fuel systems, and Jacob Stahl and Gordon Morrow were contributory in early developmental efforts.

Dr. Eric L. Petersen, of Texas A&M University, has served as my research advisor and mentor since I was accepted into the Propulsion Laboratory in 2011. Working under Dr. Petersen has been more than an opportunity, but a privilege in itself. His dedication to his research, work, teaching, and advising is unparalleled by any professor or industry member I have met to date. His efforts and guidance have been critical to my own professional development and success, and I look forward to continuing my research efforts under his guidance as a post-doctoral research associate.

Dr. Waruna Kulatilaka, Dr. Timothy Jacobs, and Dr. Adonios Karpelis, all of Texas A&M University, were selected as committee members for their dedication to their work, their past experience with similar combustion systems, and for their potential to

improve the quality of the research presented herein. I would like to express my sincere thanks to all of my committee members for their time and efforts.

CONTRIBUTORS AND FUNDING SOURCES

Contributors

This work was supervised by a dissertation committee consisting of Professors Eric L. Petersen, Waruna D. Kulatilaka, and Timothy J. Jacobs of the J. Mike Walker '66 Department of Mechanical Engineering, and Professor Adonios N. Karpetis of the Department of Aerospace Engineering.

All work for the dissertation was completed by the student, under the advisement of Dr. Eric L. Petersen of the J. Mike Walker '66 Department of Mechanical Engineering.

Funding Sources

Funding for this thesis work was provided, in part, by several sources. These included Helicon Chemical Company through an SBIR grant (Phases 1 and 2) from the U.S. Navy; the TEES Turbomachinery Laboratory; the Petersen Research Group; and the National Science Foundation under grant EEC-1560155.

TABLE OF CONTENTS

	Page
ABSTRACT	ii
DEDICATION	iv
ACKNOWLEDGEMENTS	v
CONTRIBUTORS AND FUNDING SOURCES	vii
TABLE OF CONTENTS	viii
LIST OF FIGURES	xiii
LIST OF TABLES	xxiii
1. INTRODUCTION.....	1
2. LITERATURE REVIEW: HYBRID ROCKET PERFORMANCE	
ENHANCEMENT STRATEGIES	9
2.1. Oxidizer and Fuel Selection	9
2.1.1. Oxidizers.....	10
2.1.2. Fuels	15
2.1.2.1. Mixed-fuel (HTPB/Paraffin) Systems	23
2.1.3. Summary.....	34
2.2. Oxidizer Flow Manipulation	35
2.3. Combustion Port Geometry Augmentation.....	40
2.3.1. Additive Manufacturing	41
2.4. Energetic Additives	45

2.4.1.	Oxidizer Inclusion	46
2.4.2.	Metal-Based Additives	49
2.4.2.1.	Pure Metals	53
2.4.2.2.	Metal Hydrides	66
2.4.2.3.	Metal Blends.....	75
2.4.2.4.	Boron Carbide	78
2.4.2.5.	Metal Borides	79
2.4.2.6.	Advanced Particle Synthesis Strategies.....	81
2.4.2.7.	Summary.....	89
2.5.	Unconventional Geometries	90
3.	THEORETICAL PERFORMANCE ANALYSES	96
3.1.	Stoichiometric Combustion.....	96
3.1.1.	Plain HTPB Reacting with Oxygen.....	97
3.1.2.	Plain Metals Reacting with Oxygen.....	98
3.1.3.	Metal-Loaded HTPB Reacting with Oxygen	102
3.2.	Chemical Equilibrium Analyses	105
3.2.1.	HTPB Loaded with Selected Metals	106
3.2.2.	HTPB Loaded with Aluminum or Boron	110
4.	HYBRID ROCKET PERFORMANCE MODEL.....	113
5.	BALLISTIC STAND DESIGN.....	125
5.1.	Fuel Grain and Chamber Sizing	126
5.2.	Combustion Chamber	127

5.3.	Chamber Stress Analysis	130
5.4.	Thrust Measurement System	134
5.5.	Oxidizer Delivery System	135
5.6.	Power and Data Acquisition System	136
5.7.	Failure Modes and Effects Analysis	137
5.8.	Summary	139
6.	EXPERIMENTAL METHODOLOGY: ADDITIVE CHARACTERIZATION.....	140
6.1.	Scanning Electron Microscopy.....	140
6.2.	Transmission Electron Microscopy.....	141
6.3.	Additive Characterization Results	141
6.3.1.	Micro-Aluminum Particles	141
6.3.2.	Nano-Aluminum Particles	142
6.3.3.	Nano-Boron Particles	143
6.3.4.	Micro-Magnesium Particles	145
6.3.5.	Micro-Titanium Particles.....	146
6.3.6.	Micro-Zirconium Particles	147
6.3.7.	Magnesium-Coated Nano-Boron Particles	148
7.	EXPERIMENTAL METHODOLOGY: FUEL GRAIN MANUFACTURING ...	152
7.1.	Curing Calculations	152
7.2.	Manufacturing Procedures.....	154
7.2.1.	Baseline (HTPB) Fuel Specimen.....	155
7.2.2.	Mixed (HTPB/Paraffin) Fuel Specimen.....	158

7.2.3. Metal-Loaded Fuel Specimen.....	160
7.3. Fuel Density Measurements	164
8. EXPERIMENTAL METHODOLOGY: BALLISTIC TESTING	166
8.1. Data Reduction.....	167
9. RESULTS AND DISCUSSION: METAL LOADED FUEL SYSTEMS	173
9.1. Micro-Aluminum Fuels	174
9.2. Micro-Magnesium Fuels	180
9.3. Micro-Titanium Fuels.....	184
9.4. Micro-Zirconium Fuels	188
9.5. Nano-Aluminum Fuels	192
9.6. Nano-Boron Fuels	197
9.7. Magnesium-Coated Nano-Boron Fuels.....	203
9.8. Bimetallic Fuels.....	205
9.9. Summary	215
10. RESULTS AND DISCUSSION: MIXED-FUEL SYSTEMS	225
11. SUMMARY AND CONCLUSIONS	229
REFERENCES	233
APPENDIX A – BURN SIMULATION PROGRAM.....	276
APPENDIX B – BURN SIMULATION PROGRAM OUTPUT	290
APPENDIX C – COMBUSTION CHAMBER DESIGN DRAWINGS	304
APPENDIX D – MEASUREMENT UNCERTAINTY ANALYSIS.....	307
APPENDIX E – THESIS PRESENTATION.....	313

APPENDIX F – CURRICULUM VITAE331

LIST OF FIGURES

	Page
Figure 1. Typical configurations of liquid, solid, and hybrid chemical propulsion concepts.	1
Figure 2. Classical hybrid rocket configuration depicting the separate oxidizer tank and fuel grain.....	2
Figure 3. Physical processes involved in the regression and combustion of hybrid rocket fuels.	4
Figure 4. Regression rate regimes and the corresponding effects of key parameters.	4
Figure 5. Theoretical specific impulse performance of various oxidizers reacting with (left) plain HTPB and (right) 20% aluminized HTPB at a chamber pressure of 300 psia and nozzle expansion ratio of 60:1.	10
Figure 6. The effects of oxidizer selection (GOX versus N ₂ O) on plain and aluminized HTPB regression rate.	13
Figure 7. Visualization of paraffin fuel entrainment during combustion in oxygen crossflow.....	19
Figure 8. Direct visualization of swirling oxidizer flow during the combustion of a PMMA/GOX hybrid fuel grain.	37
Figure 9. Effect of diaphragms on the regression rate of hybrid fuel grains.	39
Figure 10. Hybrid fuel grain size effects on regression rate and additive particle effectiveness.	41
Figure 11. Fuel grain geometries manufactured with internal flow injection structures.....	43

Figure 12. Post-combustion images of ABS fuel grain with helical fuel structures.	44
Figure 13. Comparison of heats of combustion with oxygen of several fuels.	50
Figure 14. Comparison of available energy per total propellant mass for metals combusting with oxygen.	51
Figure 15. Enhancement of regression rate seen with increased aluminum loading in HTPB fuels burning in FLOX.	55
Figure 16. Regression rate behavior of (left) plain HTPB and (right) aluminized HTPB with coal burning in gaseous oxygen in a single and double slab burner configuration.	56
Figure 17. The effects of nano-aluminum addition to HTPB fuels burning in gaseous oxygen.	58
Figure 18. The effects of various aluminum additives on HTPB regression rate.	60
Figure 19. The effects of various boron additives on HTPB regression rate.	60
Figure 20. (left) Gravimetric and (right) volumetric specific impulse performance variation with the inclusion of various metal hydrides in comparison to plain HTPB burning in oxygen.	67
Figure 21. Regression rate dependence on lithium hydride (LiH) loading in butyl rubber burning in oxygen.	68
Figure 22. Regression rate measurements of HTPB fuels with metallic additives burning in gaseous oxygen.	72
Figure 23. Regression rate comparisons of fuel formulations containing MgH_2 and AlH_3	72
Figure 24. Double tube hybrid motor with internal distributed injection pattern.	90

Figure 25. Schematic representation of the VH-20 vortex flow hybrid rocket engine.	91
Figure 26. External and cross-section representation of the lab-scale vortex flow pancake hybrid developed at SPLab.....	92
Figure 27. 3D-printed an ABS pancake type motor with vortex flow, N ₂ O regenerative cooling, a truncated aerospike nozzle, and secondary fluid injection.	93
Figure 28. End-burning, axial flow hybrid rocket motor configuration during combustion.	94
Figure 29. 3D-printed fuel grain with secondary liquid fuel storage compartments for passive thrust control.	95
Figure 30. Theoretical performance for HTPB and pure metals combusting with stoichiometric oxygen. Charts depict (top) gravimetric and volumetric heat of combustion and (bottom) melting and boiling temperature of pure metals and their respective oxides.	101
Figure 31. Theoretical heat of combustion and stoichiometric O/F ratios for (top) aluminum-loaded and (bottom) boron-loaded HTPB burning in pure oxygen.	104
Figure 32. Theoretical performance of HTPB R-45M fuel loaded with selected metals at a mass concentration of 50% burning in oxygen gas (O_2). Plots depict (top left) specific impulse, (top right) density impulse, (bottom left) characteristic velocity, and (bottom right) adiabatic flame temperature as calculated with NASA's CEA at 1,000 psia.	108
Figure 33. Theoretical performance of HTPB R-45M fuel loaded with selected metals at a mass concentration of 50% burning in nitrous oxide (N_2O). Plots depict (top left) specific impulse, (top right) density impulse, (bottom left) characteristic velocity, and (bottom right) adiabatic flame temperature as calculated with NASA's CEA at 1,000 psia.	109

Figure 34. Theoretical performance of HTPB R-45M fuel loaded with various concentrations of aluminum burning in oxygen gas (O_2). Plots depict (left) the maximum specific and density impulse, and (right) oxidizer-to-fuel ratios corresponding to the maximum performance condition for several merits of performance. Calculations were completed with NASA’s CEA at 1,000 psia. 111

Figure 35. Theoretical performance of HTPB R-45M fuel loaded with various concentrations of boron burning in oxygen gas (O_2). Plots depict (left) the maximum specific and density impulse, and (right) oxidizer-to-fuel ratios corresponding to the maximum performance condition for several merits of performance. Calculations were completed with NASA’s CEA at 1,000 psia. 112

Figure 36. Diagram of a hybrid rocket propulsion system with key features illustrated. 114

Figure 37. Characteristic velocity, c^* , specific impulse, I_{sp} , specific heat ratio, γ , and adiabatic flame temperature, T_c , calculated by CEA for each formulation over the operating (O/F) range and a pressure of 75 psia. 119

Figure 38. Calculation algorithm for hybrid rocket motor performance model. 120

Figure 39. Oxidizer mass flux for plain and aluminized motor formulations versus burn time. 122

Figure 40. Motor radial regression rate for plain and aluminized motor formulations versus burn time. 122

Figure 41. Propulsive thrust force for plain and aluminized motor formulations versus burn time. 124

Figure 42. Specific impulse for plain and aluminized motor formulations versus burn time. 124

Figure 43. Subsystems of the hybrid rocket ballistic test stand. 125

Figure 44. Hybrid rocket ballistic test stand. Key components are highlighted.....	126
Figure 45. Solid (left) and wireframe (right) Solidworks models of the combustion chamber assembly.	128
Figure 46. Components of the combustion chamber section.	129
Figure 47. Ignition bulkhead assembly and mounted solid propellant sample.	130
Figure 47. Stress distributions inside of the chamber walls with an internal pressure of 100 psi and atmospheric pressure outside of the vessel.	131
Figure 48. Factor of safety of chamber wall thickness versus chamber operating pressure.....	132
Figure 49. Schematic of the oxidizer delivery and DAQ subsystems.	136
Figure 50. SEM images of aluminum micro-particles at increasing magnification.	142
Figure 51. TEM images of aluminum nano-particles at increasing magnification.	143
Figure 52. TEM images of boron nano-particles at increasing magnification.	144
Figure 53. Atomic surface maps of a single boron nano-particle. (a) plain particle surface, (b) atomic boron [B] map, (c) atomic oxygen [O] map, (d) atomic magnesium [Mg] map, and (e) atomic iron [Fe] map.	145
Figure 54. SEM images of magnesium micro-particles at increasing magnification.....	146
Figure 55. SEM images of titanium micro-particles at increasing magnification.	147
Figure 56. SEM images of zirconium micro-particles at increasing magnification.	148
Figure 57. TEM images of magnesium-coated boron nano-particles at increasing magnification.	149

Figure 58. Atomic surface maps of a single boron nano-particle. (a) plain particle surface, (b) atomic boron [B] map, (c) atomic magnesium [Mg] map, and (d) atomic oxygen [O] map.	151
Figure 59. Representative mixed-fuel grains. (left to right) Plain HTPB, HTPB containing 0%, 10%, 25%, 50%, 75% paraffin, and plain paraffin.	154
Figure 60. Representative metal-loaded fuel grains. (left to right) Plain HTPB and HTPB containing 10% micro-Al, nano-Al, nano-B, micro-Mg, micro-Ti, and micro-Zr particles.	155
Figure 61. Unassembled mold components for baseline (plain HTPB) fuel specimen.	156
Figure 62. (left) Fuel mixture after mixing containing entrained air bubbles in atmosphere, (middle) fuel mixture containing entrained air bubbles under vacuum, and (right) fuel mixture containing no entrained air bubbles.	157
Figure 63. (top) Unassembled and (bottom) mold components for mixed-fuel (HTPB/paraffin) specimen.	161
Figure 64. Roller assembly utilized to mitigate additive particle settling effects during fuel curing. Fully processed motors are shown.	163
Figure 65. Representative set of transient data traces for plain HTPB burning in GOX. ..	168
Figure 66. Regression rates of plain HTPB and fuel samples loaded with 10%, 20%, and 30% micro-aluminum.	176
Figure 67. Combustion efficiencies of plain HTPB and fuel samples loaded with 10%, 20%, and 30% micro-aluminum.	178
Figure 68. SEM analysis of the combustion residue collected during the motor firing of HTPB loaded with 30% micro-aluminum burning in GOX.	179

Figure 69. EDS analysis of the combustion residue collected during the motor firing of HTPB loaded with 30% micro-aluminum burning in GOX. Atomic maps show the overlay of (red) aluminum, (green) oxygen, and (blue) carbon.	179
Figure 70. Regression rates of plain HTPB and fuel samples loaded with 10%, 20%, and 30% micro-magnesium.	181
Figure 71. Combustion efficiencies of plain HTPB and fuel samples loaded with 10%, 20%, and 30% micro-magnesium.	182
Figure 72. SEM analysis of the combustion residue collected during the motor firing of HTPB loaded with 30% micro-magnesium burning in GOX.	183
Figure 73. EDS analysis of the combustion residue collected during the motor firing of HTPB loaded with 30% micro-magnesium burning in GOX. Atomic maps show the overlay of (red) magnesium, (green) oxygen, and (blue) carbon.	184
Figure 74. Regression rates of plain HTPB and fuel samples loaded with 10%, 20%, and 30% micro-titanium.	185
Figure 75. Combustion efficiencies of plain HTPB and fuel samples loaded with 10%, 20%, and 30% micro-titanium.	186
Figure 76. SEM analysis of the combustion residue collected during the motor firing of HTPB loaded with 30% micro-titanium burning in GOX.	187
Figure 77. EDS analysis of the combustion residue collected during the motor firing of HTPB loaded with 30% micro-titanium burning in GOX. Atomic maps show the overlay of (red) titanium, (green) oxygen, and (blue) carbon.	187
Figure 78. Regression rates of plain HTPB and fuel samples loaded with 10%, 20%, and 30% micro-zirconium.	189
Figure 79. Combustion efficiencies of plain HTPB and fuel samples loaded with 10%, 20%, and 30% micro-zirconium.	190

Figure 80. SEM analysis of the combustion residue collected during the motor firing of HTPB loaded with 30% micro-zirconium burning in GOX.	191
Figure 81. EDS analysis of the combustion residue collected during the motor firing of HTPB loaded with 30% micro-zirconium burning in GOX. Atomic maps show the overlay of (red) zirconium, (green) oxygen, and (blue) carbon.	192
Figure 82. Regression rates of plain HTPB and fuel samples loaded with 10% and 20% nano-aluminum.	194
Figure 83. Transient pressure data trace for a 20% nano-aluminum fuel burning in GOX exhibiting large pressure excursions.	195
Figure 84. Fuel grains loaded with (left) 20% micro-aluminum and (right) 20% nano-aluminum. A layer of molten material accumulated on the combustion port surface of fuel containing 20% nano-aluminum.	196
Figure 85. Combustion efficiencies of plain HTPB and fuel samples loaded with 10% and 20% nano-aluminum.	197
Figure 86. Regression rates of plain HTPB and fuel samples loaded with 10%, 20%, and 30% nano-boron.	199
Figure 87. (top) Injector- and (bottom) nozzle-side views of fuel grains containing (left) 20% and (right) 30% nano-boron. A layer of molten material accumulated on the combustion port surfaces.	200
Figure 88. Combustion efficiencies of plain HTPB and fuel samples loaded with 10%, 20%, and 30% nano-boron.	201
Figure 89. SEM analysis of the combustion residue collected during the motor firing of HTPB loaded with 30% nano-boron burning in GOX.	202

Figure 90. EDS analysis of the combustion residue collected during the motor firing of HTPB loaded with 30% nano-boron burning in GOX. Atomic maps show the overlay of (red) boron, (green) oxygen, and (blue) carbon.	203
Figure 91. Regression rates of plain HTPB and fuel samples loaded with 10% and 20% magnesium-coated nano-boron.	204
Figure 92. Combustion efficiencies of plain HTPB and fuel samples loaded with 10% and 20% magnesium-coated nano-boron.	205
Figure 93. Regression rates of plain HTPB and fuel samples loaded with 10% micro-aluminum, nano-boron, and a 35:65 mixture of each.	206
Figure 94. Combustion efficiencies of plain HTPB and fuel samples loaded with 10% micro-aluminum, nano-boron, and a 35:65 mixture of each.	207
Figure 95. Regression rates of plain HTPB and fuel samples loaded with 10% micro-magnesium, nano-boron, a 35:65 mixture of each, and magnesium-coated nano-boron.	208
Figure 96. Combustion efficiencies of plain HTPB and fuel samples loaded with 10% micro-magnesium, nano-boron, a 35:65 mixture of each, and magnesium-coated nano-boron.	209
Figure 97. Regression rates of plain HTPB and fuel samples loaded with 10% micro-titanium, nano-boron, and a 35:65 mixture of each.	210
Figure 98. Combustion efficiencies of plain HTPB and fuel samples loaded with 10% micro-titanium, nano-boron, and a 35:65 mixture of each.	211
Figure 99. Regression rates of plain HTPB and fuel samples loaded with 10% micro-zirconium, nano-boron, and a 35:65 mixture of each.	212
Figure 100. Combustion efficiencies of plain HTPB and fuel samples loaded with 10% micro-zirconium, nano-boron, and a 35:65 mixture of each.	213

Figure 101. Regression rates of plain HTPB and fuel samples loaded with 10% nano-aluminum, nano-boron, and a 35:65 mixture of each.....	214
Figure 102. Combustion efficiencies of plain HTPB and fuel samples loaded with 10% nano-aluminum, nano-boron, and a 35:65 mixture of each.....	215
Figure 103. Relative effects of metallic additives at a loading of 10% on the regression rate of HTPB fuels burning in GOX.....	218
Figure 104. Relative effects of metallic additives at a loading of 10% on the combustion efficiency of HTPB fuels burning in GOX.....	219
Figure 105. Relative effects of metallic additives at a loading of 30% on the regression rate of HTPB fuels burning in GOX.....	220
Figure 106. Relative effects of metallic additives at a loading of 30% on the combustion efficiency of HTPB fuels burning in GOX.....	221
Figure 107. Post-combustion fuel ports surfaces for metallized fuels containing (top) 30%, (middle) 20%, and (bottom) 10% concentrations of metals. Motor formulations are shown left to right: baseline HTPB, micro-aluminum, micro-magnesium, micro-titanium, micro-zirconium, nano-aluminum, nano-boron, and magnesium-coated nano-boron.	222
Figure 108. Relative effects of metallic additives on the regression rate (solid black) and fuel mass loss rate (dashed grey) of HTPB fuels burning in GOX at 100 kg/m ² -s.....	224
Figure 109. Measured regression rates for plain HTPB, plain paraffin, and mixed-fuel systems burning in GOX.	226

LIST OF TABLES

	Page
Table 1. The effects of various aluminum and boron additive on HTPB combustion and specific impulse efficiency.	61
Table 2. Material property and combustion performance data for HTPB and pure metals.	99
Table 3. Parameter input values for the hybrid motor burn simulation program.	120
Table 4. Thread dimensions of the injector and nozzle bulkheads.	134
Table 5. Failure modes and effects analysis.	138
Table 6. Key attributes of the metallic additives considered herein.	140
Table 7. Chemical compositions of boron nano-particles measured with EDS analysis. ...	144
Table 8. Chemical compositions of boron nano-particles measured with EDS analysis. ...	150
Table 9. Fuel Density Measurements.	165
Table 10. Performance parameters of baseline and metal-loaded HTPB fuel formulations burning in GOX.	223
Table 11. Summary of relevant regression rate results for HTPB/paraffin binders.	228

1. INTRODUCTION

Chemical rockets for propulsion applications have historically been composed of pure liquid or solid propellant. Rocket propulsion concepts with fuel and oxidizer components stored in different phases are termed hybrid rockets. These three chemical propulsion concepts are visually depicted in Figure 1.

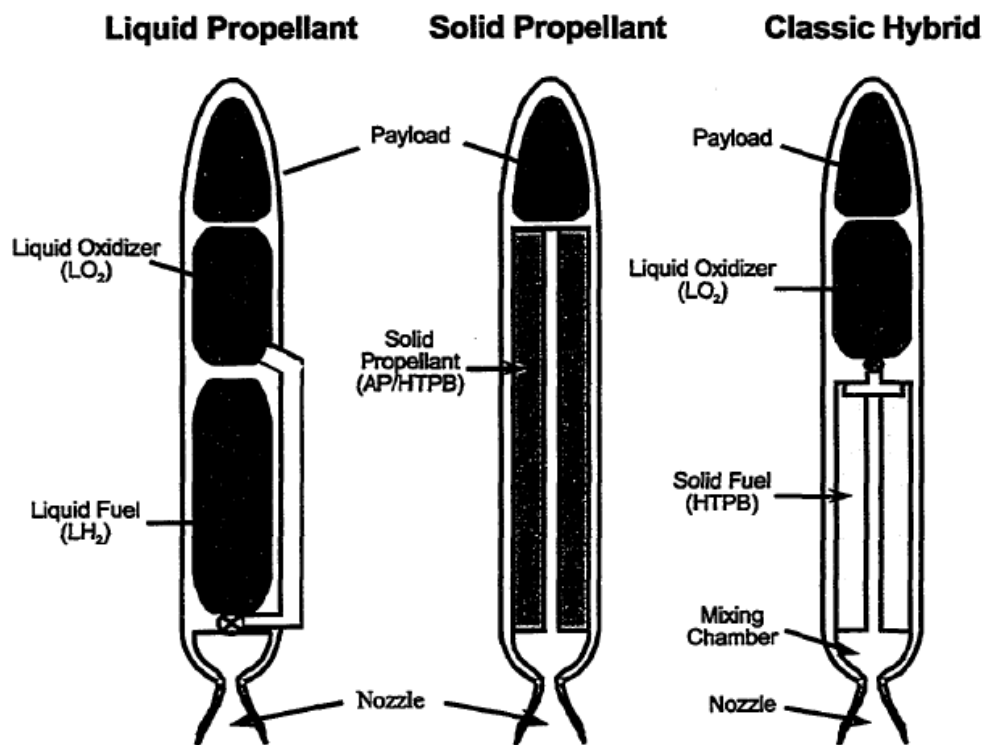


Figure 1. Typical configurations of liquid, solid, and hybrid chemical propulsion concepts. Image taken from Ref. [1].

Material within this chapter has been previously published and is reprinted with permission from “Hybrid Rocket Burning Rate Enhancement by Nano-Scale Additives in HTPB Fuel Grains” by Thomas, J. C., Petersen, E. L., Brady, B. B., and DeSain, J. D., AIAA 2014-3955, 50th AIAA/ASME/SAE/ASEE Joint Propulsion Conference, Cleveland, OH, 2014, Copyright 2014 by James C. Thomas and Eric L. Petersen.

The traditional hybrid rocket configuration is composed of a solid fuel grain and a fluidic oxidizer (Figure 2). In comparison to solid propellants, hybrid propellants are safer, more controllable, and less sensitive to mechanical imperfections. In comparison to liquid rockets, hybrid rockets are safer, have added fuel versatility, and are mechanically simpler. Additionally, hybrid rockets allow for higher specific impulse and density specific impulse than certain solid propellants and liquid bipropellants, respectively. Some disadvantages of hybrid rockets include unavoidable fuel residuals, a variation in mixture ratio during operation, proneness to pressure instabilities, lower combustion efficiencies, and comparatively complicated internal motor ballistics. The most commonly cited drawback of hybrid chemical propulsion is low solid fuel regression rates that ultimately limit motor thrust.

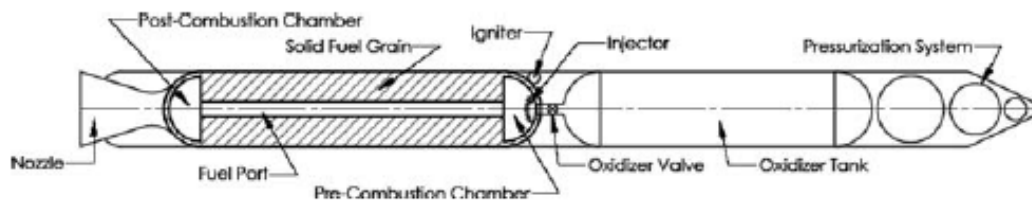


Figure 2. Classical hybrid rocket configuration depicting the separate oxidizer tank and fuel grain. Image taken from Ref. [2].

Combustion processes inside hybrid propulsion systems are inherently different from pure solid or liquid propellant systems. The solid fuel phase must undergo pyrolysis and vaporization before it mixes with the oxidizer flow stream and begins combustion. A thorough review of regression rate theory is given by Chiaverini [2] and is summarized below for the reader. Marxman et al. [3-5] developed a regression rate model based on heat transfer mechanisms which suggested the regression rate is heavily dependent on total

mass flux, weakly dependent on axial location and oxidizer and fuel properties, and not dependent on operating pressure. However, their experimental results showed the regression rate was dependent on pressure, especially at low pressures where they believed that gas-phase chemical kinetics dominate regression processes. [3] Smoot and Price [6-8] demonstrated the regression rate was dependent on oxidizer flow rate and total pressure. Furthermore, they showed regression rates were nearly independent of pressure at low oxidizer mass fluxes, but very dependent on pressure at high oxidizer mass fluxes. [6] Muzzy utilized chemical kinetic calculations to show that at high oxidizer mass fluxes and/or low pressures of non-radiative systems, the regression rate was more dependent on pressure than total mass flux. [9] Muzzy used similar calculations to show that for radiative systems, such as for metallized fuels, the regression rate was very dependent on pressure at low oxidizer mass fluxes. [9] Ramohalli and Stickler argued that fuel wall oxidative depolymerization could account for pressure dependence at low pressures and high oxidizer mass fluxes. [10] These various phenomena that should be accounted for when modeling the regression and combustion of a classical hybrid are visually depicted in Figure 3. In summary, factors affecting the fuel regression rate in hybrids include operating pressure and temperature, fuel/oxidizer composition, oxidizer mass flow rate, combustion port geometry, and axial port location. At very low and high mass fluxes, thermal radiation and gas-phase chemical kinetics mechanisms, respectively, dominate fuel regression behavior in hybrid motors. [11] At moderate oxidizer mass fluxes, turbulent mass diffusion processes dominate fuel regression behavior. [3-5] These generalized trends are depicted in Figure 4.

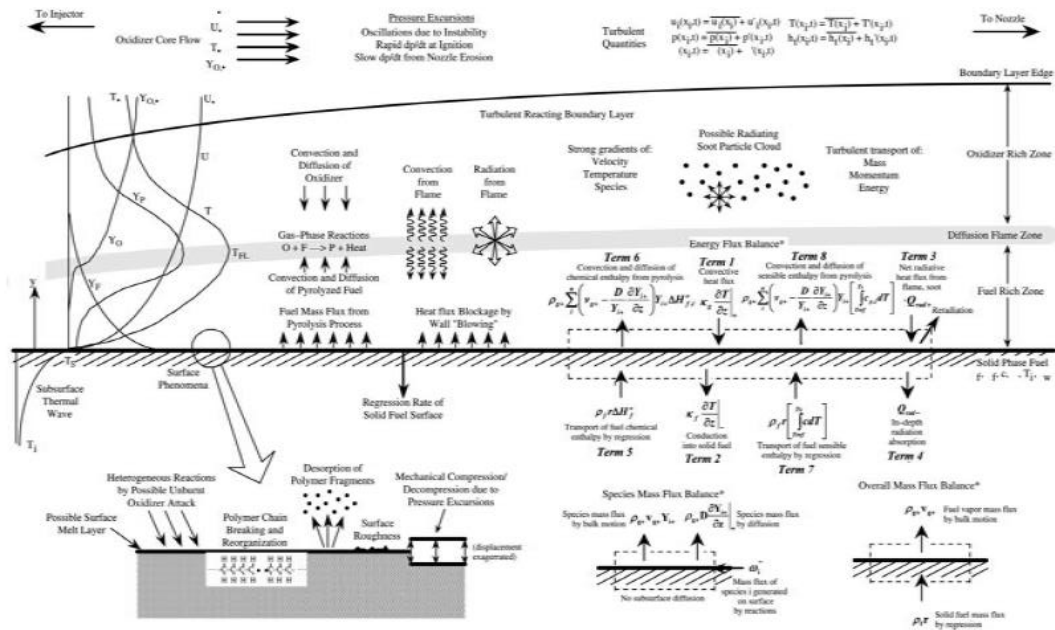


Figure 3. Physical processes involved in the regression and combustion of hybrid rocket fuels. Image taken from Ref. [2].

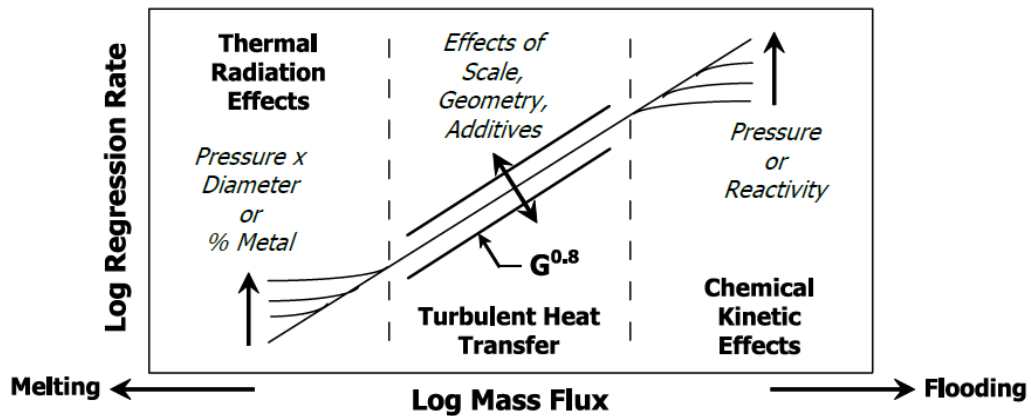


Figure 4. Regression rate regimes and the corresponding effects of key parameters. Image taken from Ref. [2].

For preliminary design or experimentation purposes, aerodynamic, thermochemical, and fluidic effects are typically lumped together into a single parameter.

[11] The resulting equation for regression rate, r , of a solid hybrid fuel grain is given by the traditional power law:

$$r = aG_{ox}^n \quad (1)$$

where a and n are empirically fitted constants, and G_{ox} is the oxidizer mass flux. An alternative form to Equation (1) to account for observed dependency on chamber pressure, P_c , and combustion port diameter, D , is:

$$r = aG_{ox}^n P_c^k D^l \quad (2)$$

where k and l are also empirical constants. Typical values of n , k , and l have been observed to vary between 0.4-0.7, 0-0.25, and 0-0.7, respectively. [11] Equations (1) and (2) are extremely simplified, are typically determined empirically, and their corresponding constants can drastically change when the propellant formulation or design scale or geometry is altered. Numerous investigators have developed rigorous theories for the prediction of regression rates from first-principles theories, and these models are comprehensively detailed by Chiaverini [2].

Hybrid rockets have numerous potential applications which include sounding rockets, auxiliary power units, tactical rockets, space engines, thrust augmentation control, and large launch boosters. Some specific examples where hybrid rockets have been designed, built, or considered for real applications are given as follows:

- A research and development effort by the Air Force in the 1960's led to the first flight of a hybrid propulsion system, the Sandpiper Target Missile, which combusted poly(methyl methacrylate) (PMMA) doped with 10% magnesium additive in a

oxidizer flow stream comprised of 25% nitric oxide (NO) and 75% dinitrogen tetroxide (N_2O_4), termed MON-25. [12] The Sandpiper program led directly to the development of the High Altitude Supersonic Target (HAST) and Firebolt Target.

- NASA and Lockheed Martin developed and launched a hybrid propulsion sounding rocket in 2002 that burned HTPB fuel loaded with >60% aluminum additive in a liquid oxygen (LOX) stream and that was capable of delivering a 360-kg payload to an altitude of 45 km. [13] The flight demonstration also served to increase the concept's technology readiness level (TRL) from 3 to 7 on NASA's TRL scale.
- Italian researchers led by Dr. Luigi DeLuca designed a hybrid propulsion module and mission to remove large debris from low earth orbit (LEO) to avoid future collision scenarios. [14-18]
- Virgin Galactic is currently developing SpaceShipTwo, a fully reusable vehicle launched from a carrier airplane (WhiteKnightTwo) that is designed to provide a suborbital spaceflight experience to space tourists. SpaceShipTwo is powered by RocketMotorTwo, a hybrid propulsion system that burns HTPB or Nylon in a nitrous oxide flow.
- Karabeyoglu et al. [19] have argued that hybrid rocket systems are the perfect candidate to replace upper stage motors on launch vehicles and could provide payload

increases up to 40%. Karabeyoglu et al. [20] also theorized and preliminarily designed a two-stage, air-launched hybrid vehicle capable of placing a 31-kg payload into orbit.

- The Sierra Nevada Corporation designed and tested a hydroxyl-terminated polybutadiene/nitrous oxide (HTPB/N₂O) hybrid rocket system capable of delivering 12,000 lbf of thrust. [21] The hybrid rocket was developed for the orbital maneuvering system onboard the Dream Chaser vehicle as part of NASA's Commercial Crew Development initiative.

- Chandler et al. [22-23] conducted a systems study to demonstrate the feasibility and advantages of utilizing a hybrid rocket propulsion system composed of a paraffin-based fuel and nitrous oxide/oxygen oxidizer for a Mars ascent vehicle as part of a Mars sample return campaign.

- Researchers at JPL are currently evaluating the feasibility of a paraffin/MON30 hybrid rocket with hypergolic additives and deep throttle capabilities for use as a Mars Ascent Vehicle (MAV). [24-35] Hot-fire testing of an 11" full-scale motor by space Propulsion Group is scheduled for 2018.

It is clear that hybrid rocket engines possess several distinct advantages over alternative propulsion systems which make them suitable for numerous applications. However, their disadvantages and a lack of fundamental knowledge have retarded their

widespread integration into flight systems thus far. The objective of this dissertation project was to 1) provide a thorough literature review of hybrid rocket performance enhancement techniques; 2) develop lab-scale hybrid rocket testing capabilities at Texas A&M University in the TEES Turbomachinery Laboratory; 3) evaluate mixed HTPB/paraffin fuel systems as they pertain to hybrid rocket applications; 4) determine the relative effects of pure metal type (aluminum, boron, magnesium, titanium, or zirconium) and loading (0-30%) on the combustion of HTPB/GOX systems; and 5) assess the synergistic performance benefits of bi-metallic fuel formulations in comparison to formulations containing plain boron. The combination of these works should advance the state-of-the-art knowledge of hybrid rockets and potentially mitigate some of their historical disadvantages.

2. LITERATURE REVIEW: HYBRID ROCKET PERFORMANCE ENHANCEMENT STRATEGIES

Hybrid rockets have numerous advantages, but their disadvantages, such as characteristically low regression rates, moderate energy densities, and requirements for large vehicle volumes, has held back their widespread implementation. Various strategies to improve their performance and mitigate their disadvantages have been proposed in the literature. These strategies include ideal selection of the oxidizer and fuel combination, manipulation of the oxidizer flow, augmentation of the combustion port geometry, inclusion of energetic additives, and implementation of unconventional geometries. A review of these enhancement strategies, with emphasis on more relevant areas, is presented in this section of the thesis.

2.1. Oxidizer and Fuel Selection

One advantage of hybrid rockets is the relatively wide selection of fuels and oxidizers available to the propulsion system design team. The selected fuel/oxidizer combination is the most important parameter in determining the rocket's performance. In this section, a general review and comparison of the more common and some unconventional fuel and oxidizer candidates is given.

Material within this chapter has been previously published and is reprinted with permission from "Hybrid Rocket Burning Rate Enhancement by Nano-Scale Additives in HTPB Fuel Grains" by Thomas, J. C., Petersen, E. L., Brady, B. B., and DeSain, J. D., AIAA 2014-3955, 50th AIAA/ASME/SAE/ASEE Joint Propulsion Conference, Cleveland, OH, 2014, Copyright 2014 by James C. Thomas and Eric L. Petersen.

2.1.1. Oxidizers

Estey and Whittinghill [36] performed an early systems analysis and ranked available oxidizers and fuels for an upper stage hybrid rocket system based on performance, cost, availability, and probability of success. Theoretical performance plots for selected oxidizers' combustion with plain and aluminized HTPB are shown in Figure 5. Their calculations and rankings suggested that HTPB/LOX was the best combination of fuel and oxidizer for hybrid rocket systems. Although some oxidizers containing fluorine (LF_2 and FLOX) yield better performance, their high toxicity and the associated costs make them unattractive. Estey and Whittinghill [36] also noted that low-energy, storable oxidizers, such as N_2O , are greatly improved by the addition of aluminum. Karabeyoglu and Arkun [37] recently performed a similar study to determine viable fuel additives and came to a similar conclusion.

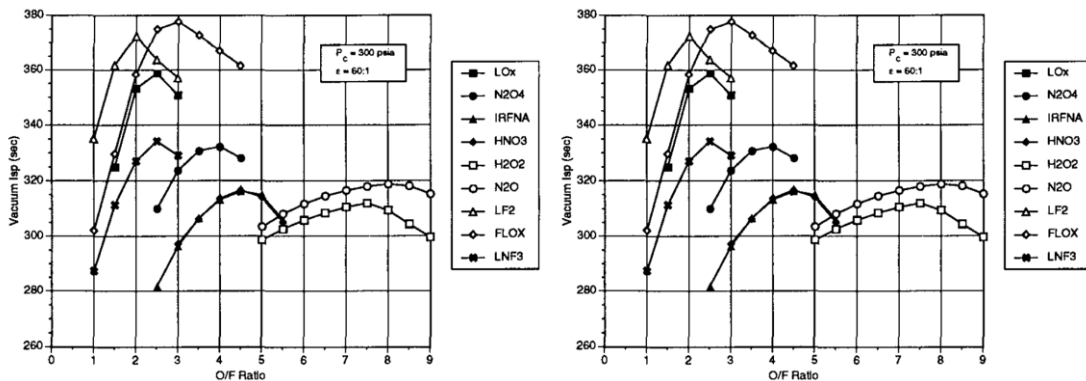


Figure 5. Theoretical specific impulse performance of various oxidizers reacting with (left) plain HTPB and (right) 20% aluminized HTPB at a chamber pressure of 300 psia and nozzle expansion ratio of 60:1. Images taken from Ref. [36].

Several reviews of oxidizer available to the HRE designer [36-38] have been surveyed, and a list of these oxidizers and their corresponding generalized benefits and disadvantages is given, as follows:

- Liquid Oxygen (LOX) – Readily available, affordable, high performance, good stability. Moderate density, cryogenic storage.
- Nitrous Oxide (N₂O) – Self pressurization, good availability, reasonable cost, good stability. Low density, comparatively poor performance.
- Hydrogen Peroxide (H₂O₂) – High density, moderate performance. Toxic with contact, explosive, poor aging.
- Dinitrogen Tetroxide (N₂O₄/NTO) – High density, moderate performance. Expensive, toxic, low-temperature decomposition.
- Others:
 - Liquid Fluorine/Liquid Oxygen mixtures (FLOX) – High Performance, hypergolic. Moderate density, expensive, cryogenic storage, toxic.
 - Inhibited Red Fuming Nitric Acid (IRFNA) – High density. Poor performance, toxic with contact, corrosive.
 - Inhibited White Fuming Nitric Acid (WFNA) – High density. Poor performance, toxic, corrosive.
 - Liquid Fluorine (LF₂) – High performance, high density, hypergolic. Cryogenic, toxic, very reactive with metals.

- Liquid Nitrogen Trifluoride (LNF_3) – Moderate performance, high density, hypergolic. Cryogenic, toxic.

The most commonly evaluated oxidizers are undoubtedly LOX and N_2O . Both oxidizers have good stability, are readily available, and are affordable. LOX has the potential to yield much higher performance, but its application is much more complex due to necessity for cryogenic storage and a pressurization system. Utilization of N_2O yields lower performance, but carries the benefits of self-pressurization properties. Additionally, these two oxidizers interact with fuels very differently during combustion due to alternative chemistries and thermodynamics. For example, Evans et al. [39] performed combustion tests of plain and aluminized HTPB fuels burning in gaseous oxygen and nitrous oxide. The regression rates of these fuels are shown in Figure 6. The collected data indicate that fuels burning in nitrous oxide regress significantly slower than in gaseous oxygen, but that this disadvantage can be mitigated with metallic additive inclusion. Furthermore, the experimental results demonstrate the effects of varying the oxidizer on combustion performance.

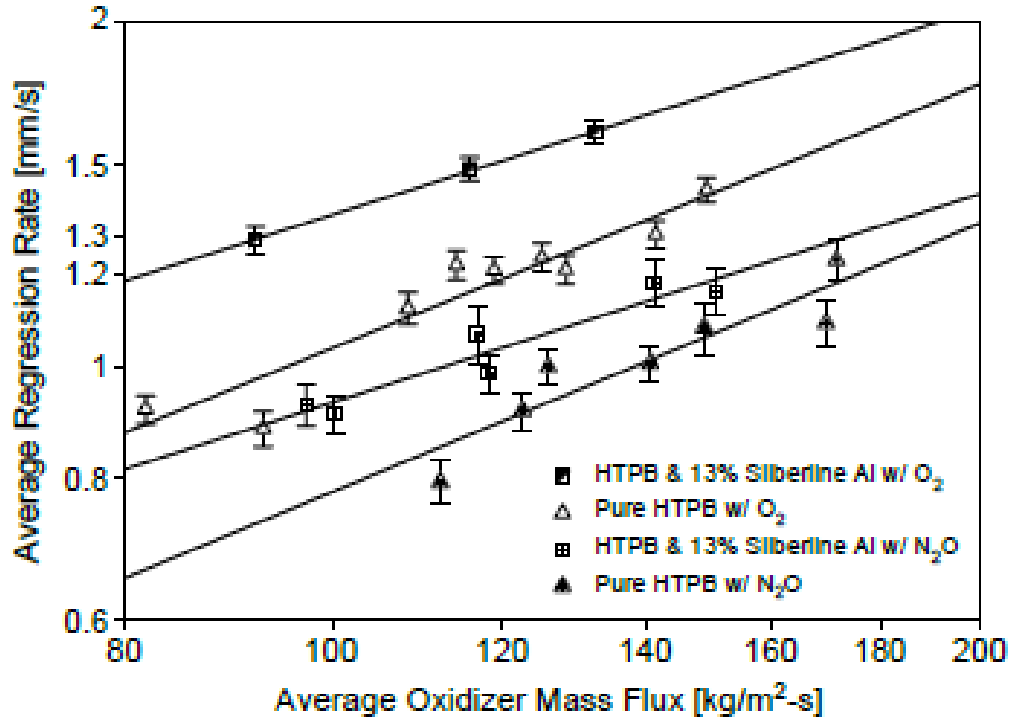


Figure 6. The effects of oxidizer selection (GOX versus N₂O) on plain and aluminized HTPB regression rate. Image taken from Ref. [39].

Oxidizers containing fluorine yield significant performance improvements in comparison to more common oxidizer selections, such as LOX, N₂O, or H₂O₂, but are typically disregarded due to their high toxicity and the associated fielding costs. However, they have been studied in a laboratory setting by several researchers which has yielded some interesting findings. Smoot and Price [7-8] performed combustion experiments with butyl rubber burning in FLOX flows and determined that increasing the amount of fluorine in the oxidizer significantly increased the regression rate. Lips [40-42] performed similar experiments with aluminized polyurethane (PU) and came to the same conclusion. Lips also concluded that higher combustion efficiencies could be achieved with FLOX, rather

than pure oxygen. [42] These findings were attributed to the production of aluminum fluoride (AlF_3) rather than aluminum oxide (Al_2O_3) which has a higher heat of combustion and doesn't accumulate as much on the surface due to a low sublimation temperature.

In addition to the more common oxidizers previously discussed, several unconventional oxidizers have been theorized and evaluated to varying degrees. Some unconventional oxidizers which are worth discussion include Nytrox, MON, and ionic liquid oxidizers.

N_2O and LOX stand out as the most practical propellant oxidizers for various reasons including their historical use, wide availability, low toxicity, easy handling, and low cost. Karabeyoglu [43-45] theorized a new class of oxidizers, termed Nytrox, which is a combination of the two individual chemicals. The nitrous oxide serves as a pressurizing agent, and the liquid oxygen serves as a densifying component. Nytrox exhibits self-pressurization capability, high density and density impulse, non-cryogenic operational temperatures, and efficient gas-phase combustion. [45] Nytrox mixtures have a higher specific impulse than pure nitrous oxide, are more stable than pure oxygen during combustion due to heat release from nitrous oxide decomposition, and allow for independent control of pressure and temperature. [45] Furthermore, Karabeyoglu [45] and Chandler [23] have conducted mission systems studies to show the reduction in total system weight associated with use of Nytrox oxidizers.

Mixtures of liquid nitric oxide (NO) and liquid dinitrogen tetroxide (N_2O_4) are termed MON oxidizers. The introduction of nitric oxide reduces the freezing point of the mixture and additional increases in nitric oxide loading decreases corrosiveness, decreases

oxidation potential, and increases storability of the oxidizer. In addition, MON oxidizers are hypergolic with numerous fuels/additives, which could potentially eliminate the necessity of an ignition system and reduce the complexity of the vehicle design. The first ever hybrid propulsion system to be flown, the Air Force's Sandpiper Target Missile, utilized a 25% NO/75% N₂O₄ mixture (MON-25). [12]

Ionic liquids are defined as salts in the liquid state, and numerous solid oxidizers can be stored in this manner, such as ammonium dinitramide (ADN), ammonium perchlorate (AP), and hydroxyl ammonium nitrate (HAN). These liquid oxidizer candidates typically have high density and can yield high performance, but are sometimes toxic and/or expensive, and are not as well studied or characterized. In addition, these liquids can be catalytically decomposed prior to combustion with the fuel, yielding a simple ignition system. Several HRE systems based on ionic liquids, especially HAN [46-50], are currently being studied and considered for future applications.

2.1.2. Fuels

Early theoretical investigations on the decomposition of polymers was completed by Dekker [51] and Chaiken et al. [52], and focused on poly(methyl methacrylate) (PMMA) and polystyrene (PS). McAlevy and Hansel [53] later completed experimental investigations of these processes. PMMA was one of the first studied fuel systems, but contains a large fraction of oxygen which leads to a reduction in specific impulse performance for HRE applications. [36] The emergence of polybutadiene-based polymers, such as hydroxyl-terminated polybutadiene (HTPB) and carboxyl-terminated polybutadiene (CTPB), as fuel binders in solid propellants led to their adaptation into

hybrid fuel systems. Other notable polymers that have been studied for this purpose include polybutadiene acrylonitrile (PBAN), polybutadiene-acrylic acid (PBAA), polyurethane (PU), and fluoropolymers. [54]

Hydroxyl-terminated polybutadiene (HTPB) is the most widely studied fuel binder utilized to date owing to its historical use in ammonium perchlorate composite propellants (APCPs). HTPB is readily available and a well-known material, and it is the fastest burning polymeric fuel used in hybrids. [37] Drawbacks of HTPB include significantly lower regression rates when compared to recent paraffin fuels and incompatibility with some high-energy additives, such as metal hydrides. Humble [55] has recently reported on the utilization of dicyclopentadiene (DCPD) fuel as a substitute for HTPB due to its slightly improved specific impulse, higher density, comparable mechanical and rheological properties, and compatibility with metal hydride additives. The main drawback of DCPD is a significantly reduced regression rate when compared to HTPB.

Combustion experiments performed by Lips [40-42] on several aluminized polymeric fuels burning in FLOX suggested that the fuel composition plays a large role in determining the regression rate due to differing decomposition processes. Lips noted that some polymers, polyisobuthylene (PIB) and polyethylene (PE), melt faster than they burn, leading to a liquid surface layer that can become entrained in the oxidizer flow and that can inhibit metallic burning through encapsulation. [40-41] The surfaces of unsaturated polybutadienes; including polybutadiene acrylic acid (PBAA), polybutadiene acrylonitrile (PBAN), carboxyl-terminated butadiene and butadiene acrylonitrile copolymer (CTBN), and carboxyl-terminated polybutadiene (CTPB); char during combustion due to low-

temperature gasification stemming from exothermic breaking of double carbon bonds. [41] Polyurethanes can behave like either of the previously described groups, and HTPB behaves like the unsaturated polybutadienes.

Carrick and Larson [56-58] evaluated cryogenic solid fuels as a potential replacement for traditional polymeric fuels. The authors utilized solid n-pentane and ethylene, and measured regression rates that were 2-8 times larger than a typical polymer fuels, such as HTPB and PMMA. Furthermore, the authors attributed the increase in regression rate to the higher blowing coefficients associated with the cryogenic fuels. However, reduced combustion efficiencies were noted due to incomplete burning of the fuel. Follow-on cryogenic fuel testing was completed by St. Clair et al. [59], Gramer et al. [60], and Rice et al. [61-62].

Following these studies, researchers at Stanford University [63-67] began experimenting with long-chain, paraffin-based hydrocarbons with melting temperatures above room temperature. Paraffin-based fuels exhibited regression rates 3-5 times higher than similar polymeric fuels, such as HTPB. Polymeric fuels generally regress purely through gasification, and regression rate enhancement in paraffin-based fuels is due to an alternative mechanism termed entrainment. A liquid surface layer of fuel forms during combustion due to the thermal properties of the fuel. [67] The liquid layer is hydrodynamically unstable and fuel droplets become entrained in the oxidizer stream. [63] The susceptibility of a fuel to this shear-driven instability is directly tied to the melt layer's rheological properties. [64] More explicitly, reduction of the melt layer's viscosity and/or surface tension leads to further regression rate enhancement.

Karabeyoglu et al. [63-64] presented a first-principles theoretical model for the entrainment regression rate. The model was utilized to calculate the regression rate of paraffin and pentane, was compared to paraffin burn data collected at Stanford and pentane burn data collected by Carrick and Larson [56-58], and exhibited good agreement. Karabeyoglu et al. [65] later improved the model to predict regression rates of any normal alkane fuel with reasonable accuracy. Weinstein and Gany [68-69] and Sisi and Gany [70] further expanded the regression rate theory to include liquid flow along the fuel surface into the combustion chamber, which becomes relevant at lower oxidizer mass fluxes. It was suggested that this fuel loss mechanism should be considered because it potentially has significant consequences on the combustion efficiency of the hybrid rocket.

Scale-up tests of paraffin fuels at NASA Ames Center showed the high regression rate characteristics were maintained in larger scale motors. [66] Furthermore, the larger motors burned at NASA Ames were compared to smaller-scale motors burned at Stanford and authors noted that the regression rate did not exhibit dependency on chamber pressure or motor length. [66] The developed fuel technology is currently being utilized to develop and fly a sounding rocket [71-77] and has been proposed for use in the Mars Ascent Vehicle (MAV) for a Mars sample return mission (MSRM) [33-35].

Karabeyoglu and Akron [37] claim the benefits of paraffin fuels include: 1) low cost and high availability; 2) high performance including specific impulse, regression rate, and fuel utilization; 3) non-toxicity; 4) virtually infinite shelf life; and 5) hydrophobic nature which allows for sensitive, high-energy additive incorporation. Karabeyoglu and Arkun [37] also suggested that inclusion of aluminum additives in the fuel greatly

improved the performance when combined with N_2O as an oxidizer, but that the more recent paraffin fuels were still superior to traditional polymeric fuels, such as HTPB.

Kobald et al. [78] evaluated various types of paraffin waxes with a DSC, rheometer, and hybrid combustor. The varying molecular structure of each wax led to differing viscosity-temperature profiles. The authors noted that an increase in viscosity led to a reduction in regression rate and commented that this phenomenon was related to droplet size during the fuel entrainment process. Kobald et al. [79] also performed experiments to visually detect liquid layer entrainment processes and further identified instabilities in the liquid film were related to the Kelvin-Helmholtz instability, as depicted in Figure 7. Evans et al. [80] later determined that this instability allowed aluminum particles trapped in the surface layer of paraffin fuels to also become entrained in the oxidizer flow. More recent paraffin combustion visualization experiments conducted by Kobald et al. [81-82] and Petrarolo et al. [83-91] have focused on quantification of the wave instabilities and successfully related them to the operating conditions and resultant regression rate. Numerous other research teams have focused on flow visualization techniques to better understand these phenomena. [92-97]

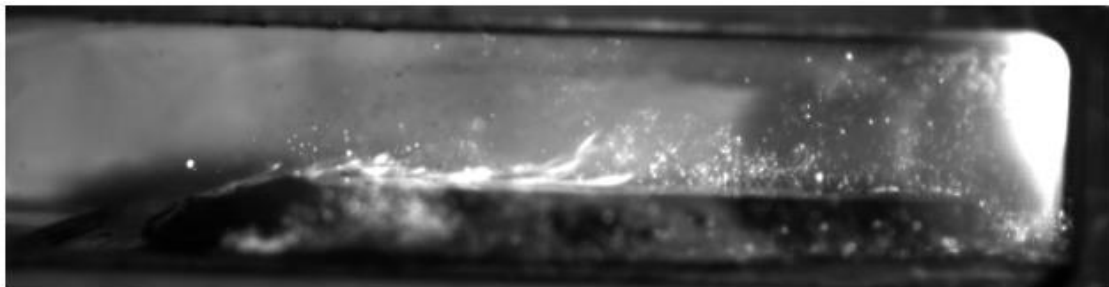


Figure 7. Visualization of paraffin fuel entrainment during combustion in oxygen crossflow. Image taken from Ref. [79].

Kobald et al. [98] also evaluated HDPE and paraffin-based fuel systems containing various loadings of polymer and nano-clay additives which were utilized to manipulate the rheological and mechanical properties of the fuel mixture. Combustion experiments were performed in a gaseous oxygen crossflow to measure regression rates and combustion efficiencies. Kobald et al. [98] were able to successfully correlate the regression rate of all mixtures to a reference condition and their measured viscosity with an empirical power law. Mechanical property experiments showed the inclusion of small mass loadings of polymer or reinforcing nano-clays could significantly increase the strength and elasticity of the fuel, but this improvement was accompanied by a reduction in the regression rate.

Paravan et al. [99] evaluated the ballistic, rheological, and mechanical properties of paraffin-based fuel formulations with various mixtures and grades of wax. The various fuel compositions displayed a wide range of properties. The experimental findings demonstrated that proper blending of paraffinic materials into a homogenous fuel grain allows the designer to tailor the resultant combustion and structural properties. Furthermore, an analysis was completed which related the measured regression rate to the measured viscosity and a reference condition, similar to the analyses performed by Kobald et al. [98].

Dermanci and Karabeyoglu [100] performed viscosity measurements of paraffin fuels containing micro-aluminum suspensions. The fuel viscosity was weakly dependent on aluminum addition, even to a mass loading of 60%, which suggests the high

entrainment regression rates associated with these fuels is retained even at high metallic loadings.

DeSain et al. [101] performed mechanical property testing on paraffin fuel mixtures containing 0-4% low density polyethylene (LDPE) and determined that increasing the loading of LDPE in the fuel led to increases in ultimate strength and ductility. Similar results have been reported by Kim et al. [102-103] who also found that this method lowered resultant regression rate of the fuel. Pal and Kumar [104] evaluated paraffin fuel samples with various loadings of LDPE and micro-aluminum with thermal decomposition, rheological, mechanical, and ballistic experiments. Their results indicated that although the addition of LDPE results in a decrease in regression rate which is exacerbated by further loading, the presence of aluminum in the fuel can readily make up for these detriments. Pal and Kumar [104] also demonstrated the capability to yield regression rates and structural properties over a wide range by simple variation of the additive (LDPE and/or micro-aluminum) loadings.

Research efforts at Central Connecticut State University, led by Dr. Viatcheslav Naoumov, have focused on the evaluation of bio-derived fuels, including paraffin and beeswax, with and without aluminum additives. [105-106] In general, their experimental findings indicate that 1) the purity of the fuel has significant implications on the resultant regression rates, and 2) beeswax is a higher performing fuel than traditional paraffin.

Several researches have proposed mixtures of HTPB and paraffin as a means to tailor the rheological, mechanical, and combustion properties of the resultant fuel. These mixed-fuel systems have been evaluated through thermal degradation [117-121] and

combustion [68, 117, 122-128] experiments by various research groups, but disparate findings have been reported thus far. These fuel mixtures are a large component of the current project and are further discussed in their own subsection later in this section.

There are numerous other fuel choices available to the HRE designer, but some other non-conventional fuels are especially worth noting and are described, as follows. Rastogi and Baijal [129-130] performed ballistic testing on polymers containing boron incorporated into the polymers' backbone chains with B-O or B-C linkages. The boron-containing polymers were synthesized and burned in gaseous oxygen. All three polymers outperformed the baseline formulation in terms of regression rate and displayed high port diameter dependencies. The polymer incorporating boron with B-C linkages outperformed the analogous polymer with B-O linkages.

Risha et al. [131] performed regression rate measurements of HTPB fuel containing a high-nitrogen polymeric additive (Triaminoguanidium azotetrazolate, TAGzT) to loadings of 25% in an opposed flow burner. The high-nitrogen additive can increase the density specific impulse of the fuel and shift the peak O/F to lower values. The formulation containing 25% TAGzT yielded a 25% increase in regression rate over plain HTPB at higher oxidizer mass flowrates which was attributed to the formation of N_2 rather O_2 and an accompanying increase in heat release.

Whitmore et al. [49,132-148], amongst others, have evaluated acrylonitrile butadiene styrene (ABS) as an alternative fuel for hybrid rocket engines. ABS performs similar to HTPB in terms of its combustion performance and properties, but also has

advantages such as compatibility with additive manufacturing technologies and arc-ignition capability.

2.1.2.1. Mixed-fuel (HTPB/Paraffin) Systems

Many research efforts have focused on the evaluation of HTPB/paraffin fuel blends for hybrid rocket applications, mainly through thermal degradation [117-121] and combustion [68, 117, 122-128] experiments. This section of the thesis serves to provide a thorough and comprehensive review of all contributions thus far to the topic.

Sakote et al. [117] investigated TDI-cured HTPB fuel containing 35%, 50%, and 65% paraffin concentrations by mass. Fuel samples were manufactured by mixing of heated HTPB with molten paraffin, and allowing the mixture to cure at 65 °C for 3-5 days. Simultaneous TGA and DTA experiments were performed in a nitrogen atmosphere from 10-500 °C at a heating rate of 10 K/min. All samples exhibited two major stages of mass loss which onset near 200 °C and 425 °C. The first stage of mass loss was more significant, and increased from 56% to 72% with an increased paraffin loading of 35% to 65%. DTA thermograms for all fuel samples displayed similar behavior, and exhibited an endothermic peak near 60 °C, an exothermic peak near 200 °C, an endothermic peak near 325 °C, and a set of two exothermic peaks near 425 °C. The first endothermic peak near 60 °C is due to paraffin melting. The set of exothermic peaks near 425 °C differed between compositions due to differing concentrations of bounded and unbounded paraffin, as confirmed by SEM analysis. Sakote et al. [117] suggested that this set of exothermic peaks, and the differences between each composition at this decomposition stage,

indicates that the HTPB and paraffin are bounded at the molecular scale and that each constituent melts at different temperatures.

Sinha et al. [118] reported on the thermal decomposition of TDI-cured HTPB R45M fuel containing 0-27.75% paraffin as determined through TGA and DSC experiments at heating rates of 3-43 K/min from 30-520 °C in a Helium atmosphere. Mixed-fuel samples were prepared by mixing a slurry of liquid pre-polymer, paraffin, and curative at elevated temperature with subsequent curing at elevated temperature for 5 days and room temperature for 5 days. The pure HTPB fuel samples exhibited two mass loss stages in the TGA and DSC curves, and representative results from the heating rate of 3 K/min are reported, as follows. The first mass loss was comparatively small, occurred near 300 °C, and can be attributed to breaking of the urethane linkages formed during the polymer curing process and subsequent evaporation and decomposition of the curative material. The second mass loss stage occurs near 425 °C and can be attributed to depolymerization and decomposition of the remaining HTPB fuel. In general, increasing the heating rate slightly increased the first stage mass loss; shifted the decomposition onset temperatures of both stages to higher temperatures; and decreased the net exothermicity and endothermicity of the first and second stages, respectively. Mixed-fuel samples, with paraffin fuel included, exhibited similar behavior to pure HTPB samples. The inclusion of paraffin in the fuel system did not significantly affect the last mass loss stage. However, an additional endothermic stage with no corresponding mass loss was present near the paraffin melting temperature of approximately 50 °C. Additionally, the mass loss associated with the next stage significantly increased with an accompanying decrease in

exothermicity, without a significant change in the decomposition onset temperature. These trends were more prevalent with higher paraffin loading, and the first stage mass loss was doubled for the highest paraffin loading of 27.75%. Furthermore, these trends were attributed to the volatilization of paraffin between 300 and 320 °C.

Sinha et al. [119] also measured the heats of combustion of the mixed-fuel systems and reported small increases associated with paraffin inclusion, as expected. Mechanical properties of the fuel specimen were evaluated through DMA experiments and showed significant alterations in stiffness and storage modulus with even the lowest paraffin loading.

Sinha et al. [118] further utilized the collected DSC data to determine thermal degradation kinetic parameters of all evaluated fuel mixtures. The inclusion of paraffin led to a reduction in the activation energy, reaction rate constant, and frequency factor for the first decomposition stage, and these trends were more prevalent with additional paraffin loading. The activation energy and reaction rate were also decreased by the inclusion of paraffin for the second decomposition stage, but the frequency factor was not significantly affected, and additional paraffin loading did not further alter the kinetic parameters. Sinha et al. [119] also measured the temperature-dependent specific heat capacity of these fuel blends during DSC experiments. Paraffin inclusion led to a significant reduction in the fuel blend's specific heat capacity, and the highest paraffin loading of 27.75% led to a 50% decrease from approximately 1.6-0.8 J/g-K at 80 °C. The collected kinetic parameters and specific heat capacity data were coupled and utilized to calculate the pyrolysis rates of fuel samples, according to methods reported by Lengelle

et al. [149-151]. These calculations indicated paraffin inclusion in the mass range of 12.25-27.75% leads to an increase of 5-33% in fuel pyrolysis over pure HTPB fuel in an inert atmosphere. The reported increases are due to a reduction in activation energy and increase in fuel vaporization and should not be confused with the previously mentioned entrainment effect.

Cardoso et al. [120] performed TGA experiments with pure HTPB, pure paraffin, and a mixed-fuel system at heating rates of 5-15 K/min under a 100 mL/min oxidant flow. The mixed-fuel system was prepared by addition of paraffin particles (<0.6 mm) to an HTPB slurry and subsequent curing with IPDI. The pure HTPB samples showed two stages of major mass loss onset at approximately 300 and 425 °C. The first stage can be attributed to breaking of the urethane bonds formed during the curing process, and the second stage can be attributed to depolymerization, cyclization, and crosslinking processes. The pure paraffin sample showed two stages of mass loss onset at approximately 200 and 425 °C, due to elimination of volatile compounds, water, and low molecular weight hydrocarbons, and due to decomposition of higher molecular weight compounds, respectively. The mixed-fuel system, which contained 60% mass loading of paraffin particles, also showed two major mass loss stages. The onset temperature of the first stage was slightly shifted to a lower temperature of approximately 200 °C, and the corresponding mass loss significantly increased from roughly 10% to 35%.

Cardoso et al. [120] also utilized the TGA mass loss data to calculate the activation energy of the fuel samples according to the Ozawa-Wall-Flynn method [152]. The pure HTPB and paraffin samples exhibited single activation energies over the measured

temperature range of approximately 300 and 100 kJ/mol, respectively. However, the mixed-fuel system exhibited an activation energy of 150 kJ/mol at lower temperatures and 300 kJ/mol at higher temperatures. These findings suggest the decomposition of the fuel mixture requires a two-step kinetics model rather than a single-step model that applies for the pure fuel systems. This finding is significant because one of the assumptions made in the evaluation of pyrolysis rates from thermal degradation kinetics is that the degradation reaction is first order [152]. Accordingly, pyrolysis rates of mixed HTPB and paraffin fuel systems may be inaccurate when determined according to these methods.

Hu et al. [121] evaluated HTPB/paraffin fuel blends containing aluminum, magnesium, ammonium perchlorate, and carbon black additives through DSC and TGA experiments at a heating rate of 20 K/min under air and nitrogen gas flows (30 mL/min) at temperatures from 20-750 °C. No information was provided regarding fuel sample preparation and manufacturing procedures. Mixtures without energetic additives were not presented, with the exception of a plain HTPB sample, so direct comparison to other experiments cannot be made. However, a reduction in the HTPB loading and corresponding equivalent increase in the paraffin loading in additive fuel samples led to increased mass loss at the first stage of decomposition, which is in agreement with the previously reported results.

In general, the findings of Cardoso et al. [120] are in good agreement with the experiments completed by Sinha et al. [118-119]. However, Sinha et al. [118] noted a 35% mass loss in the first decomposition stage with the addition of only 27.75% paraffin, while Cardoso [120] noted a 35% mass loss corresponding to a 60% paraffin loading. The two

notable differences between the experiments were that Sinha et al. [118] utilized an inert Helium atmosphere and included paraffin as a dissolved liquid during the fuel mixing process, while Cardoso et al. [120] utilized an oxidant atmosphere and included paraffin as dispersed solid particles during the mixing process. The differences in their results highlight the importance of how atmospheric composition and paraffin inclusion procedures can play a significant role in mixed-fuel system decomposition under heating in quiescent conditions.

Lee and Tsia [122-123] evaluated the combustion of IPDI-cured HTPB loaded with 50%, 70%, and 90% paraffin in GOX and nitrous oxide core flows with axial and swirling flow configurations on a lab-scale hybrid motor. Oxidizer mass fluxes and chamber pressures were tailored through means of a pressure regulator and interchangeable nozzles and were varied in the ranges of 1.4-3.5 MPa and 50-500 kg/m²·s, respectively. Mixed-fuel samples were prepared by mixing molten paraffin and heated HTPB at a temperature of 80 °C, and curing procedures were carried out according to general HTPB curing practices. In addition to spatially and temporally averaged regression rate data, transient regression rate data were deduced from the burn reconstruction method developed by George et al. [153]. The researchers stated the mixed-fuel grains loaded with 70% and 90% paraffin were not structurally sound and resulted in ejection of significant unburned fuel through the nozzle and unstable combustion at higher oxygen mass fluxes. [122] The addition of 50% and 90% paraffin to plain HTPB led to approximate regression rate increases of 10% and 150%, respectively, under non-swirling GOX flow at an

oxidizer mass flux of $250 \text{ kg/m}^2\cdot\text{s}$. This finding suggests that a minimal paraffin loading may be required prior to realization of any useful regression rate enhancement.

Boronowsky [124] evaluated the combustion of plain HTPB, plain paraffin, and HTPB loaded with 15% and 30% paraffin spheres (0.3-0.7 mm) in low GOX flow (15-60 $\text{kg/m}^2\cdot\text{s}$) and low pressures ($<0.7 \text{ MPa}$) on a lab-scale hybrid motor. Boronowsky's intentions for including spherical paraffin in a non-homogenous fuel mixture, instead of liquid paraffin in a homogenous mixture, were to 1) not further complicate the curing process of HTPB fuel, and 2) yield the regression rate benefits of paraffin without compromising the structural integrity of the fuel grain. Utilization of spherical paraffin may also lead to a rougher fuel surface during combustion, once the paraffin spheres are removed from the fuel surface or become entrained into the core flow, and could lead to enhancement of turbulence and heat transfer. Boronowsky made notes on potential modeling complications but did not make a significant effort to model the regression of the mixed-fuel system. In particular, an accurate regression rate model would need to account for alterations in the gas properties due to variations in fuel chemistry, adjustments of the skin friction coefficient due to additional roughness, and modifications to the blocking factor. [124] It is worth noting that after combustion testing was completed on all fuel formulations, regression rate prediction of mixed-fuel compositions was completed through volumetric weighting of the empirical regression rate expressions of the base fuel formulations with some success.

The fuel formulation containing 30% paraffin spheres showed signs of mechanical weakness due to a lack of bonding between the paraffin and HTPB. The addition of 15%

and 30% paraffin spheres to HTPB led to 25% and 40% increases in regression rate, respectively, at the higher evaluated oxidizer fluxes. [124] The measured regression rates for baseline HTPB and paraffin do not agree with literature values and are significantly larger than reported elsewhere. A number of factors could cause this discrepancy including the small motor scale (5×2 cm), but the probable culprit is the average oxidizer mass flux calculation methodology which is not presented within the paper. The reported oxidizer mass flux appears to be calculated through an average of the initial and final oxidizer mass fluxes, which can yield significant error for even small changes in the combustion port diameter [121]. Regardless, the presented results can still be considered on a relative scale to each other, and serve as a proof-of-concept for the proposed enhancement technique.

Boronowsky [124] noted that the 30% paraffin-loaded fuel samples generated an audible noise during combustion testing, but no discrepancies were present in pressure or thrust data traces. Furthermore, Boronowsky suggested this sound may be related due to ejection of unburned paraffin pieces. There likely exists a confounding limit of paraffin sphere size and concentration for stable and efficient combustion, which is also dependent on hybrid motor scale.

Boronowsky [124] also made several homogenous mixed-fuel samples by including liquid paraffin during the curing process. The paraffin concentration was not specified, but was likely similar to other fuel samples and on the order of 15-30%. Although the mixed-fuel samples exhibited good mechanical properties, combustion testing did not show any significant regression rate enhancement. This result is in agreement with the findings of Lee and Tsia [122], and may support the hypothesis that a

minimal paraffin loading may be required prior to realization of any useful regression rate enhancement. It is also worth noting that this experimental observation is in conflict with the thermal degradation studies of Sinha et al. [118-119] and Cardoso [120], in which inclusion of paraffin as a molten liquid led to more significant pyrolysis enhancement than inclusion of paraffin spheres. The combination of these experimental observations may further suggest that the surface roughness increase produced by removal of paraffin spheres at the fuel surface is indeed significantly enhancing turbulence and heat transfer processes.

Weinstein and Gany [68] and Sisi and Gany [125] burned pure paraffin, pure PMMA, and HTPB/paraffin (1:1) mixed-fuel in a nitrous oxide core flow at low oxidizer mass fluxes (20-50 kg/m²·s). Additionally, the mechanical properties of the fuels were evaluated through uniaxial compressive testing at a displacement rate of 5 mm/min. The mixed-fuel specimens were manufactured by mixing paraffin particles (0.5 mm) into pre-polymerized HTPB and allowing for binder curing at room temperature. Mechanical property testing demonstrated that the mixed-fuel system had significantly more elasticity than the pure paraffin fuel. The combustion data were analyzed to yield average regression rates and combustion efficiencies. The regression rate of the mixed-fuel fell in between that of the pure fuels and exhibited an oxidizer mass flux exponent that was reduced from 0.67 for pure paraffin to 0.59 for the mixed-fuel system. Combustion efficiencies on the order of 80-100% were achieved and were generally higher for the mixed-fuel system in comparison to the pure paraffin fuel. Combustion tests with the pure paraffin fuel exhibited residual fuel mass in the post-combustion chamber and larger exhaust plumes

stemming from unburned fuel ejection, but these phenomena were not present in the mixed-fuel system. This burning behavior alteration was attributed to the variation of the fuel systems' mechanical properties [125], but may actually be linked to the lack of a melt layer on the fuel surface.

A group of students at the University of Washington [126-127] designed and built a sounding rocket based on a HTPB/paraffin fuel system burning in a nitrous oxide core flow. The team's fuel was based on paraffin for high regression rates, and 10% HTPB was added as a structural agent. Unfortunately, useful diagnostics were not presented, so no comparison can be made between the motor firing data and other literature.

Research efforts at the SPLab at Politecnico di Milano have also focused on the inclusion of paraffin in HTPB fuel systems. DeLuca et al. [154] applied statistical-thermodynamic modeling and estimated a homogenous paraffin saturation limit between 60 and 70%. Subsequent curing tests showed a loss of mixture stability between 60 and 70% loading, as evidenced by mass loss after mixture curing. Uni-axial tensile testing at a displacement rate of 50 mm/in showed a significant increase in elasticity accompanied by a small reduction in strength due to the addition of 50% paraffin to the plain HTPB fuel. Ignition and combustion evaluations have also been completed, but not yet reported, and indicated no measureable regression rate enhancement with the inclusion of paraffin particles in an HTPB fuel matrix. (Personal Communication, May 19, 2017)

In addition to the previously detailed thermal degradation studies, Sakote et al. [117] also evaluated HTPB fuel loaded with 35%, 50%, and 65% paraffin burning in a swirling GOX core flow at moderate oxidizer mass fluxes ($70\text{-}90\text{ kg/m}^2\cdot\text{s}$). As previously

mentioned, fuel samples were prepared by mixing heated HTPB and molten paraffin and allowing the mixture to cure at 65 °C for 3-5 days. One fuel sample of each formulation was burned at the same initial conditions for a total time of 5 s, and the post-combustion fuel grains were cut and measured with calipers to determine the spatial fuel regression. No baseline HTPB or paraffin motors were burned, so a direct comparison cannot be made. However, average regression rate increases of 10% and 12% were noted when increasing the paraffin content from 35% to 50% and from 50% to 65%, respectively. [117]

From the present authors' group, Thomas et al. [128] evaluated the performance of a HTPB/paraffin fuel blend loaded with 10% paraffin burning in gaseous oxygen (10-150 kg/m²·s) at moderate pressures (<1.5 MPa). The mixed-fuel system was prepared by inclusion of molten paraffin at elevated temperature and led to a 20% increase in regression rate across the tested oxidizer mass flux range.

There is no general consensus on the effects of paraffin inclusion in HTPB on combustion behavior and regression rate enhancement. Combustion studies presented by Lee and Tsai [122-123] indicate that when paraffin is included as a molten liquid, a high loading is necessary for notable regression rate enhancement, which is in agreement with the findings presented by Boronkowsky [124]. Boronkowsky [124] directly compared the combustion of fuel blends containing paraffin included as a molten liquid and as spherical particles, and found that spherical particle inclusion is the only method that leads to regression rate enhancement at low mass loadings (< 30%). Combustion results presented by Sakote et al. [117] and Thomas et al. [128] are in direct conflict with these findings,

and suggest useful regression rate enhancement can occur at lower mass loading, even when included as a molten liquid. The reasons for these discrepancies are not clear, but they could potentially stem from variation in fuel formulation, motor scale, or prescribed operating conditions.

In summary, significant work has been completed towards the evaluation of the thermal degradation of these fuel blends. In general, inclusion of paraffin in an HTPB fuel leads to increased mass loss during the early stages of decomposition, which is more prevalent with further paraffin loading. Several research teams have evaluated the combustion of HTPB/paraffin fuel blends on lab-scale hybrid rockets and under various operating parameters. While some researchers report significant enhancement, others have reported little to no enhancement associated with paraffin inclusion. Discrepancies between both thermal degradation and hybrid rocket combustion studies indicate that a paraffin inclusion limit for noticeable enhancement may exist, highlight the importance of paraffin inclusion methodology (molten liquid versus solid particle), and suggest potential dependencies on operating conditions.

2.1.3. Summary

The preceding section served to provide a general overview of the large effects oxidizer and fuel selection can have on the design of an HRE system. The most commonly utilized oxidizers are LOX and N_2O , but several novel candidates such as Nytrox, MON, and ionic liquids are being considered for future mission. The most common fuels are HTPB and paraffin, and ABS is currently the only promising candidate.

2.2. Oxidizer Flow Manipulation

Early combustion studies performed on aluminized polyurethane in FLOX flow by Lips [42] showed that proper design and implementation of mixing devices and the combustion chamber can significantly improve the combustion efficiency of hybrid propulsion systems. It is now well-known that the oxidizer injection system plays a major role in determining motor combustion efficiency and stability. [155]

Swirling oxidizer flow represents a strategy that can increase both fuel regression rate and combustion efficiency. Paccagnella et al. [156-157] developed and utilized a numerical code to simulate hybrid rocket combustion phenomena involving swirling oxidizer flow. The authors found the tangential component of the oxidizer flow leads to a rotational flow field which enhances the mixing of the reacting chemical species, leads to higher temperatures, and increases regression rates and combustion efficiencies. [156] Increasing swirl number of the flow leads to further increases in the fuel's regression rate due to further increases in mixing efficiency. [156] Increasing the chamber pressure did not affect the flow field shape, but it did increase its intensity which had negligible effect on the performance of the motor. [157] Furthermore, the authors were able to modify the classical empirical regression rate law to empirically predict regression rates based on oxidizer mass flux and swirl number with reasonable accuracy. [156]

Summers and Villarreal [158] evaluated the combustion of HTPB/N₂O motors with swirl injectors of various intensities (0-1.15). The measured regression rates linearly increased with increasing swirl number, and the highest swirl injector (1.15) yielded a 50% increase in regression rate while yielding more uniform burning profiles than the

axial injection case. Shin et al. [159] induced swirl flow in PMMA fuel grains burning in gaseous oxygen by modifying the post's geometrical structure, rather than the injector. The authors' approach led to similar enhancements in regression rate, and a significantly more-uniform axial burn profile.

Significant research efforts have been conducted on hybrid rocket configurations with swirling flows by researchers at Tokyo Metropolitan University [160-180]. These efforts have included direct visualization of swirling flow during the combustion of fuel grains, as shown in Figure 8. Experimental findings have indicated that the swirling flow is much more effective near the injection site and that the flow becomes more axial along the fuel grain's length as mass is injected from the fuel surface. The research team has successfully developed control parameters, based upon the oxidizer viscosity and swirl number, which differed between the leading and downstream regions for the empirical correlation of the regression rates in swirl-flow hybrids, which can be used to predict the performance of swirling flow hybrid systems. Hirata et al. [181], Araki et al. [182], and Ohe et al. [183] later proposed utilizing several swirl injection locations along the hybrid fuel grain's length to yield further enhancement. This method did increase the regression rate and combustion efficiency further, but it also led to uninform burning near the injection sites. Ozawa et al. [184] successfully developed an oxidizer delivery system that was capable of transient variation of the oxidizer flow rate and swirl number to tailor the instantaneous regression rate, O/F ratio, and thrust of a hybrid rocket.

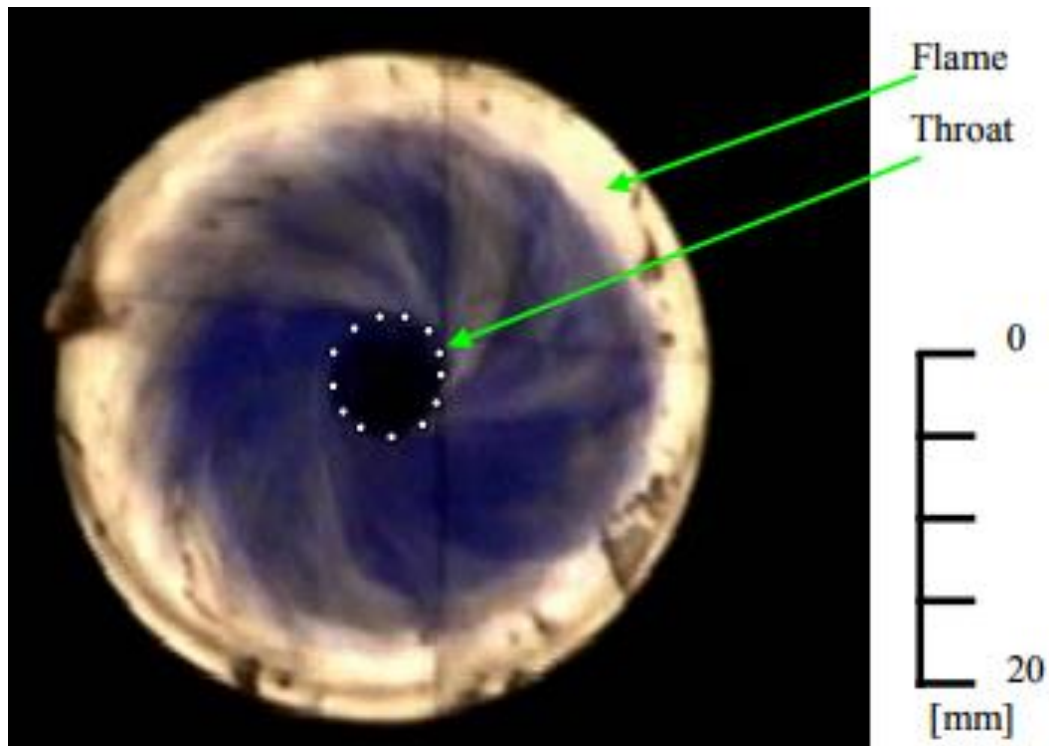


Figure 8. Direct visualization of swirling oxidizer flow during the combustion of a PMMA/GOX hybrid fuel grain. Image taken from Ref. [173].

The research team at Kyushu University [182-185] proposed utilizing several swirl injection locations along the hybrid fuel grain's length to yield further enhancement. This method did increase the regression rate and combustion efficiency further, but it also led to uninform burning near the injection sites. Ozawa et al. [184] successfully developed an oxidizer delivery system that was capable of transient variation of the oxidizer flow rate and swirl number to tailor the instantaneous regression rate, O/F ratio, and thrust of a hybrid rocket.

Tadini et al. [186] reported similar increases in regression rate for HTPB fuel combustion in a swirling gaseous oxygen flow but noted that aluminized formulations did not exhibit significant regression rate enhancement when swirl injection was substituted

for axial injection. Numerous other researchers have investigated swirl flows for hybrid rocket applications and presented similar findings. [92, 187-194]

Boardman et al. [195] advocated for wire screens inside of the combustion chamber to enhance heat transfer and mixing, and increase regression rates and combustion efficiencies. Experimental results in the JIRAD project indicated combustion efficiencies approaching 100%. Osmon [196] incorporated protrusions into fuel grains and noted a slight increase in combustion efficiency. Gany and Timnat [197] utilized phenolic diaphragms to yield combustion efficiencies on the order of 97-98%. Furthermore, the authors noted that altering the location of the diaphragm had a negligible effect on the resultant combustion efficiency. Grosse [198] incorporated numerous diaphragm designs into the combustion chamber to yield improved combustion efficiencies, and also noted corresponding improvements in regression rate.

Kumar and Ramakrishna [199] demonstrated the utilization of a bluff body in gaseous oxidizer flow to induce regression rate enhancement during the combustion of HTPB fuel. The enhancements effects were more prominent at lower oxidizer mass fluxes and shorter motor lengths. Additionally, the enhancement strategy led to a more uniform axial burn profile. Kumar and Ramakrishna [200-201] later reported on the inclusion of rubber and graphite protrusions in the oxygen flow field to yield enhanced regression rate, but this method did not yield as satisfactory uniform burning profiles. Example post-burn profiles of the fuel grains with protrusions at several locations are shown in Figure 9. Numerical computations by Kumar and Kumar [202] indicated that the protrusion's height

plays an important role in enhancement due to alterations in the flame zone height in the downstream recirculation zone.

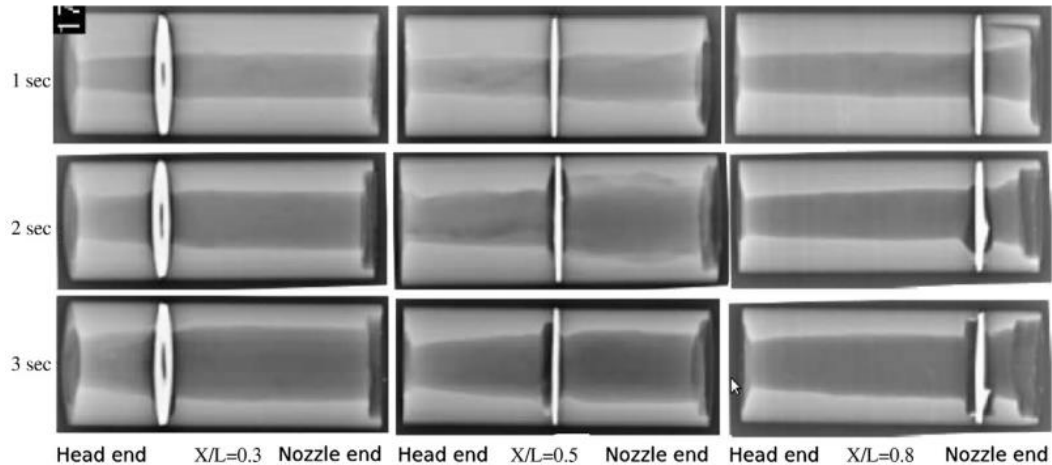


Figure 9. Effect of diaphragms on the regression rate of hybrid fuel grains. Image taken from Ref. [201].

Researchers at the University of Padua and the University of Wuppertal [203-207] numerically and experimentally evaluated the effects of several diaphragm geometries and locations on the combustion behavior of paraffin burning in nitrous oxide. Incorporations of diaphragms yielded enhanced downstream mixing and regression rates, and significantly increased combustion efficiencies. For example, the presence of a four-hole diaphragm located at 1/3 the motor length yielded an 80% increase in regression rate and an absolute increase of 12% in delivered specific impulse.

Kim et al. [208-209] evaluated the effects of tapered fuel ports and a midstream mixing chamber on the performance of HDPE burning in GOX and noted increased regression rates and combustion efficiencies with both methods of enhancement. Similarly, Ishiguro

et al. [210] found that inclusion of a baffle plate amidst the mixing chamber led to regression rate and combustion efficiency enhancements.

Sakashi et al. [211] evaluated hybrid fuel grains with alternating convex-concave surface structures of various sizes and spacings. Although the unique fuel geometries led to enhanced regression rates, significant combustion instabilities were produced.

Yano [212] noted a significant increase in the combustion efficiency of an HTPB fuel grain containing 20% AP burning in aqueous HAN by the replacement of a shower head injector with an impingement type injector head.

In summary, oxidizer injection schemes and combustion chamber design play major roles in determining the delivered performance of a HRE system. Improper design can lead to poor combustion efficiencies. Furthermore, the injector design can be modified through several means to yield alternative fuel regression rates, higher combustion efficiencies, and tailored motor operating conditions.

2.3. Combustion Port Geometry Augmentation

George et al. [213] performed a parametric investigation to determine the effects of cylindrical port grain geometry variations and determined that reduction in port diameter led to large increases in regression rate and increases in port length led to minor increases. The port diameter effect is much larger and is related to the increase in oxidizer mass flux, while the port length effect is related to increases in the local total mass flux.

Evans et al. [214] performed scaling tests with plain and aluminized HTPB fuel grains burning in oxygen. The experimental results, shown in Figure 10, indicate that the larger motor exhibited lower regression rates at comparable oxidizer mass fluxes and that

the effectiveness of the additive aluminum was significantly reduced as the motor's size was increased.

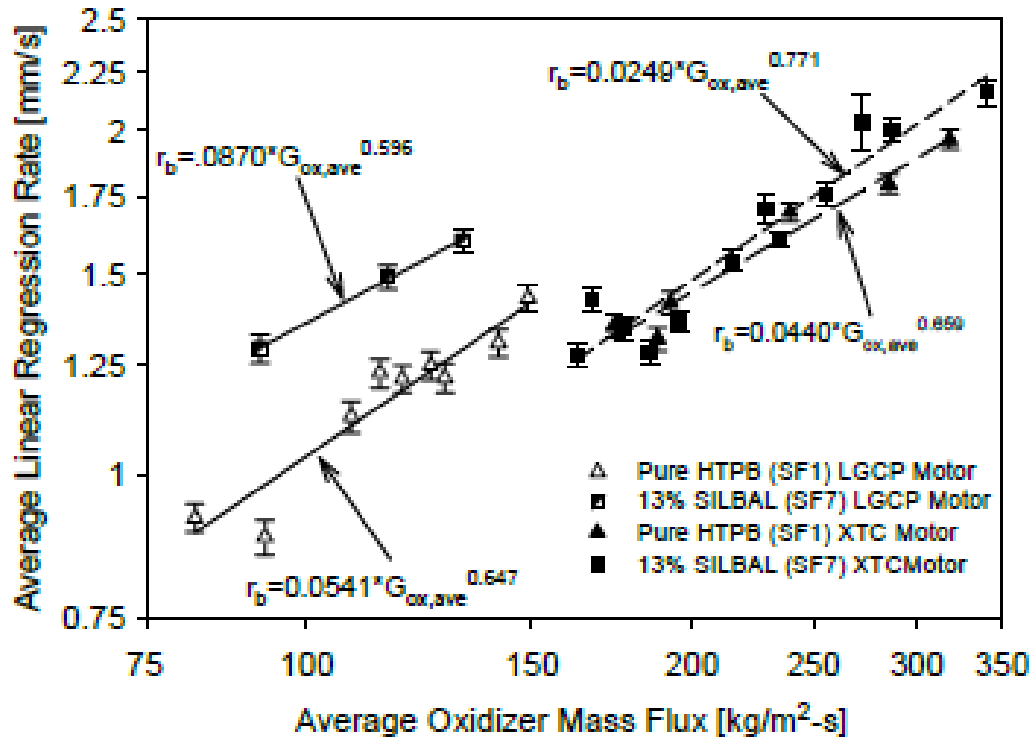


Figure 10. Hybrid fuel grain size effects on regression rate and additive particle effectiveness. Image taken from Ref. [214].

2.3.1. Additive Manufacturing

Fuller et al. [215-218] of the Aerospace Corporation were amongst the first to recognize the potential benefits of additive manufacturing for production of hybrid fuel grains. They designed and burned several epoxy-acrylate fuel grains with helical ports, swept star geometries, and passive flow control structures and burned them in gaseous oxygen as a demonstration of the technology. Recent work by Fuller [218] has focused on

the production of 3D-printed fuel grains which incorporate passive fuel storage inside of the fuel grain and release a secondary liquid fuel during combustion.

Researchers at the Pennsylvania State University (PSU) [219-220] manufactured acrylic grains with various combustion port geometries. Novel geometries were manufactured by printing ABS substrates (swept honeycombs or turbulator vanes) and filling the remaining system with paraffin. In comparison to plain paraffin with a straight combustion port, the novel geometries yielded enhanced regression rates and higher combustion efficiencies

A student team at Purdue University [221] recently designed and built a 3D printer for manufacturing paraffin-based fuel systems. The team successfully printed a lab-scale fuel grain and burned it at Zucrow Laboratories.

Catina et al. [222] utilized additive manufacturing to develop sophisticated grain geometries with flow and injection configurations, as shown in Figure 11. The motors were fabricated with acrylic fuel and burned in gaseous oxygen at the PSU High Pressure Combustion Laboratory. In comparison to the traditional tube motor configuration, the alternative geometry (Figure 11) yielded a 10% increase in chamber pressure and 2.5% increase in combustion efficiency at the same oxidizer flow conditions.



Figure 11. Fuel grain geometries manufactured with internal flow injection structures. Images taken from Ref. [222].

Researchers led by Stephen Whitmore at Utah State University [49, 132-148] have evaluated several 3D-printed hybrid fuel systems based on ABS. Whitmore et al. [132-134] have argued that ABS fuel is similar to HTPB in terms of combustion performance and properties, but is also more versatile since it has better mechanical properties and print capabilities. Whitmore et al. [134-140] have also designed an arc ignitor compatible with ABS/GOX, and numerous other fuels and oxidizers, that allows for dependable restart capability and which has been incorporated into several fully designed hybrid rocket systems [135, 141-144].

Whitmore et al. [145-146] evaluated 3D-printed ABS fuel grains with helical port structures, as shown in Figure 12. The helical combustion port structures yielded significant regression rate enhancement, which is reduced over time as the fuel grain

‘straightens’ during combustion. The improved regression rates were attributed to higher skin friction coefficients and enhanced convection heat transfer stemming from reduced wall blowing due to centrifugal forces from the helical flow.

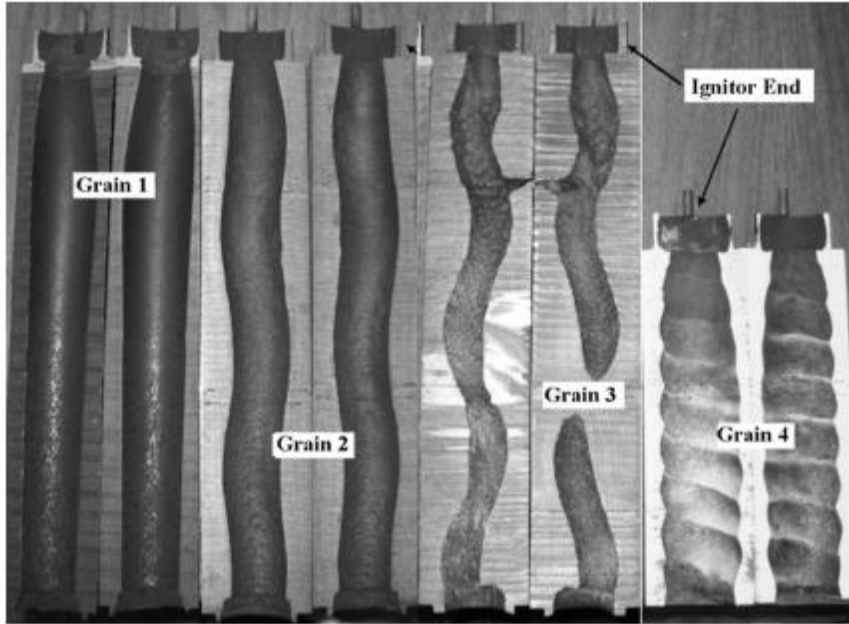


Figure 12. Post-combustion images of ABS fuel grain with helical fuel structures. Image taken from Ref. [145].

McCulley et al. [223] printed an ABS mesh structure which was infilled with paraffin wax to yield enhanced regression rates and surprisingly good combustion stability, with a non-constant thrust profile. Eilers et al. [141, 144] 3D-printed an ABS pancake-type motor that was built into a cubesat system which included vortex flow, N_2O regenerative cooling, a truncated aerospike nozzle, and secondary fluid injection.

Whitmore et al. [143] developed a thruster which is entirely printed and then coated with Nickel, and they demonstrated its combustion performance capability. Whitmore et al. [147] has also suggested the use of consumable 3D printed hybrid

chambers in the structure of small satellite for deorbiting maneuvers, similar to the design proposed by Remson et al. [224].

Elliott et al. [225] recently demonstrated a process for additive manufacturing of fuel grains with 10% micro-aluminum loading through stereolithography. Jones [226] has patented a similar method that incorporates 5% polymer-capped nano-aluminum into a thermoplastic fuel system which is 3D-printed by fused deposition modeling. This technology is currently being employed under a DARPA contract by Rocket Crafters, Inc. to develop the two-stage Intrepid-1 hybrid rocket launch vehicle. Discussions with John DeSain of the Aerospace Corporation indicate that their Propulsion Science Department has developed a similar technique for printing thermoplastic fuels loaded with 10% micro- or nano-aluminum by fused deposition modeling. (Personal Communication, 2016) Johnson et al. [227] have demonstrated an additive manufacturing method capable of producing HTPB fuel samples with up to 80% solids loadings of micro-aluminum, although the system, method, and its performance have not been detailed.

2.4. Energetic Additives

Inclusion of energetic additives can improve theoretical specific impulse and fuel density, attenuate acoustic instabilities, and increase mass generation. [37] However, disadvantages of additives can include increased cost of materials and processing, poor aging performance, additional hazards, and decreased efficiency from slower chemical kinetics and two-phase losses. [37] The introduction of additives can also include additional complexities, such as a change in the optimum O/F during operation, alteration of the fuel's mechanical and rheological properties, introduction of regression rate

dependency on pressure, slag formation during operation, increased nozzle erosion rates, increased toxicity, and compatibility issues. [37] Experimental efforts towards production, inclusion, and characterization of additives in solid fuels are reviewed in this section.

2.4.1. Oxidizer Inclusion

Raghunandan et al. [228] utilized 25% ammonium perchlorate ($\text{NH}_4\text{ClO}_4/\text{AP}$) loading in polyester fuel burning in air to yield smooth combustion and easy ignition in solid fuel ramjet experiments. George et al. [213] performed combustion experiments on plain HTPB fuel grains burning in GOX and with fuel grains including 8% AP, and both aluminum and AP. The inclusion of AP led to significant increases in regression rate, and further enhancement was seen with the additional inclusion of aluminum.

Humble [55] included 2% potassium perchlorate (KClO_4) in polydicyclopentadiene (DCPD) fuels burning in hydrogen peroxide (H_2O_2) to increase pressure dependence and regression rate. The additive fuel grain exhibited a 15% increase in average regression rate over the plain DCPD fuel grain but also exhibited evidence of burn-through at several axial locations.

Experimental work by Frederick et al. [229] evaluated HTPB fuel seeded with 0-30% AP and 0-5% burn rate catalyst (Fe_2O_3) burning in GOX. The introduction of AP into the fuel grain led to pressure-dependent regression behavior. The inclusion of 27.5% AP and 2.5% catalyst led to a 450% increase in regression rate over plain HTPB. Furthermore, additive fuel grains remained extinguishable through termination of oxidizer flow.

Marothiya et al. [230] reported on HTB fuel grains containing micro-aluminum, AP, and iron oxide (Fe_2O_3) or copper chromite ($\text{Cu}_2\text{Cr}_2\text{O}_5$) burn rate catalysts. The authors

noted that an AP loading limit exists above which the fuel grain is not extinguishable through termination of oxidizer flow. Combustion experiments in a lab-scale hybrid burner were carried out on a formulation containing 35% micro-aluminum and 15% AP. Inclusion of these additives led to regression rate enhancement at low-moderate oxidizer mass fluxes ($<20 \text{ kg/m}^2\text{-s}$). Reduction of the AP size and inclusion of the burn rate catalysts led to further regression rate enhancement. Furthermore, the inclusion of the burn rate catalysts increased the oxidizer mass flux dependency, with copper chromite outperforming iron oxide.

Wernimont et al. [231] investigated the utilization of a consumable sodium borohydride (NaBH_4) catalyst bed system in a hybrid motor configuration with polyethylene (PE) and hydrogen peroxide (H_2O_2) as the binder, and oxidizer, respectively. The inventors' intention was to utilize the combustion products for ignition and subsequent combustion of a downstream fuel grain.

Yano [212] performed combustion experiments with an 80% AP/HTPB fuel grain burning in 90% HAN/water solution crossflow. Experimental results indicated high combustion efficiency, stable combustion, and that fuel regression was pressure dependent and not a function of mass flux. Yano also noted that injector type played a large role in combustion efficiency performance. Similar experiments performed by Takashita and Teramoto [232] with 60% AP/HTPB propellant burning in inhibited white fuming nitric acid exhibited comparable combustion efficiencies ($>95\%$).

The NASA PHUS [233] program aimed to develop a gas cycle hybrid engine based on 60% AP/HTPB propellant burning in 90% hydrogen peroxide flow. The low loading

of AP allowed for the team to classify the system as a 1.4C explosive, which allowed for retention of the hybrid's touted safety advantages. Laboratory-scale experiments revealed the combustion behavior was dependent upon injector type, binder type, fluidic oxidizer level and type, and solid oxidizer particle size. Furthermore, the fuel exhibited pressure-dependent burning behavior and little mass flux dependency. Scale-up tests with sub-scale motors demonstrated predictable fuel regression rates, high combustion efficiencies (>98%), and controllable extinguishment.

Numerous other researchers, including the works by Radinsky et al. [234] and Lee and Lee [235] have also evaluated fuel systems containing solid oxidizer with similar results. It is evident from these experimental undertakings that inclusion of oxidizers within the solid fuel matrix can yield improved performance in terms of specific impulse, regression rate, and combustion efficiency without removing the benefits of superior safety associated with hybrid rockets; however, oxidizer inclusion can significantly alter the already complex combustion response yielding additional regression rate dependency behavior.

An alternative oxidizer incorporation method was recently developed by Matthews et al. [236-237] which entails an ultrasonic emulsification method to yield stable liquid-fuel-in-solid-fuel-binder colloidal dispersions. This method could potentially be utilized to incorporate numerous energetic liquid oxidizers or additives into the solid fuel matrix, but the authors' work has been limited to ethanol thus far.

2.4.2. Metal-Based Additives

Risha et al. [54] include an extensive review of energetic additives utilized in hybrid rocket and solid fuel ramjet (SFRJ) systems as well as the history of their development. Metallic particles, both on a micro- and nano-scale, are one of the most well-studied inclusions in hybrid motors owing to their capability to increase regression rates and serve as a dense, high-energy fuel source. The addition of metallic additives to solid fuel grains can result in higher specific impulse performance, higher volumetric heat of oxidation, improved adiabatic flame temperature and heat of combustion, and enhanced radiation heat transfer processes. [54] Figure 13 shows a comparison of the gravimetric and volumetric heats of combustion with oxygen for HTPB with common metallic fuels. [54] The highest specific-energy materials are aluminum, boron, and beryllium which can be used to increase performance in mass- and volume-limited applications. Beryllium has the highest gravimetric heat of oxidation, but the high toxicity of its oxide has kept it from becoming a viable additive. Boron has the highest volumetric heat of oxidation, but difficulties with its ignition and complete combustion have hindered its adaptation. Aluminum is the most well-studied and adapted metallic particle for performance enhancement in hybrids but has its own complications.

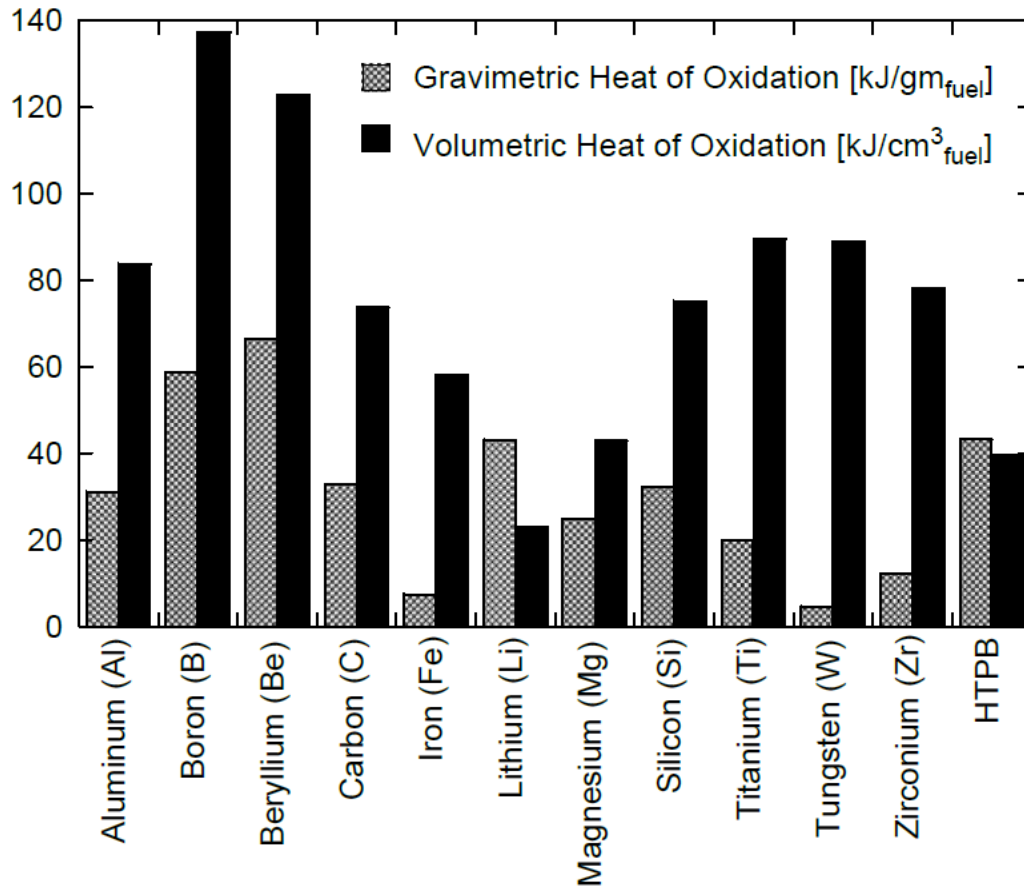


Figure 13. Comparison of heats of combustion with oxygen of several fuels. Image taken from Ref. [54].

An alternative method for comparing the metals as potential additives in rocket propellants is presented by Karabeyoglu [37] and shown in Figure 14. The metals are ranked according to their heat of combustion during combustion with oxygen per total propellant mass, including the oxidizer mass. On this basis, total propellant mass for comparison, lithium out performs all other metals except the highly toxic beryllium.

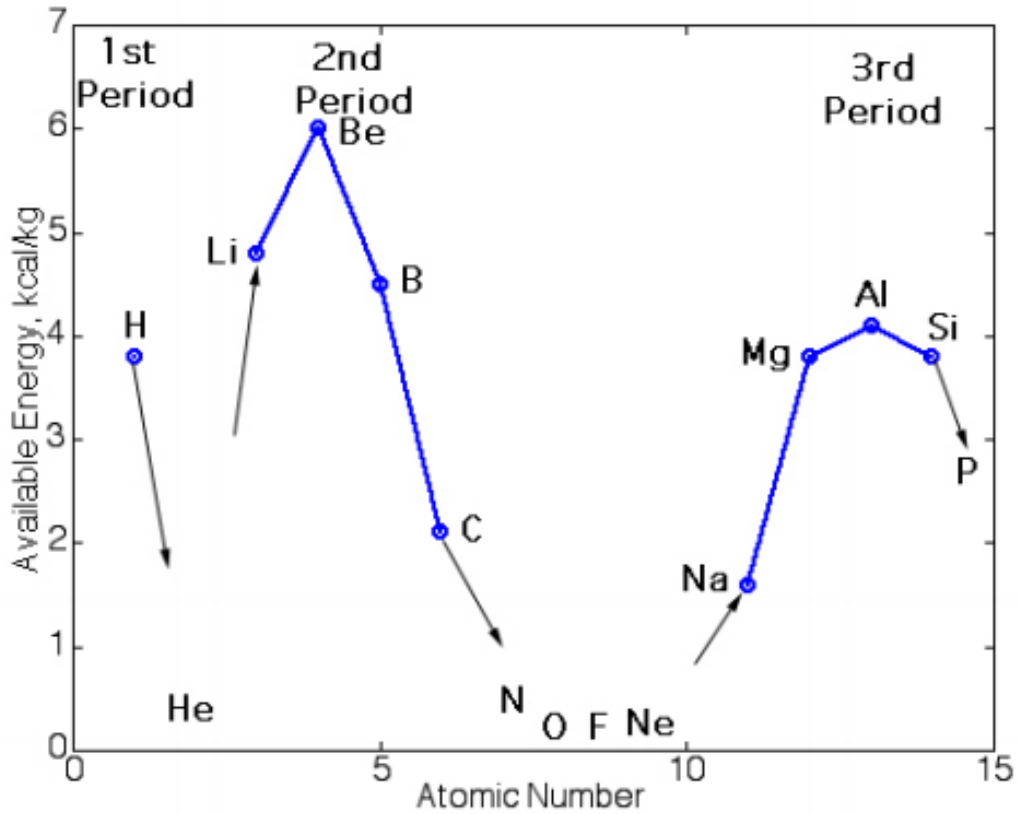


Figure 14. Comparison of available energy per total propellant mass for metals combusting with oxygen. Image taken from Ref. [37].

Karabeyoglu and Arkun [37] performed a comprehensive assessment of fuel additives for hybrid rocket engines based on an open literature review and corresponding chemical equilibrium calculations. The selected additives were ranked according to their capability to increase performance; availability and cost; increase in hazards; storability; and potential for immediate adaptation into current designs. The key results of the study were 1) metallic additives are not an effective means to increase regression rate of solid fuels; 2) aluminum additives are excellent for increasing specific impulse and density specific impulse performance, especially when used with energy-deficient oxidizers; 3)

aluminum hydride (AlH_3) delivers the best performance benefits, but is not commonly available and has long-term storability issues; and, 4) boron-based additives do not have a major impact on hybrid rocket performance due to incomplete combustion. The authors also noted that boron-hydride compounds, such as decaborane and ammonia borane, could potentially be useful in hybrid systems, if improvements in combustion efficiency could be made.

Aluminum is the most researched additive for solid fuel formulations due to its relatively high heat of oxidation, high density, and ease of ignition. Micro-scale aluminum increases solid grain regression rates through energy release from metal oxidation and enhanced radiation heat fluxes from the diffusion flame zone back to the fuel surface. [54] Radiative heat transfer enhancement in aluminized hybrids stems from higher gas phase temperatures and radiating metallic particles. Nano-particle additives have been shown to yield better combustion efficiencies, enhanced heat transfer processes, and shorter ignition delay and burning times when compared to their micro-particle counterparts. [54] The drawbacks of nano-additives include higher cost, difficult synthesis and processing, and decreased safety. Nano-scale aluminum has the same radiative effect as micro-aluminum, but also has much lower ignition temperatures and times, due to a high specific surface area, resulting in energy release closer to the fuel surface. [54] However, most aluminum nano-particles have a significantly higher unreactive, oxide mass fraction which is dependent on the additive's production and processing. A state-of-the-art review of aluminum-based nanoparticles for energetic applications, especially related to solid propellants, is provided by DeLuca [238].

Boron has received significant attention as a fuel additive for hybrid rockets and SFRJ systems due to its high volumetric and gravimetric heats of combustion. However, boron has not yet yielded its performance potential in chemical propulsion systems due to difficulties with ignition and complete combustion. Ignition difficulties stem from the presence of boron oxide, B_2O_3 , at the metal particle surface which inhibits ignition, and inefficient combustion is derived from the formation of HOBOR compounds in systems containing hydrogen.

The following section serves to provide a thorough review of experimental investigations focused on the incorporation of metal-based additives in solid fuels for HRE and SFRJ applications. Plain metal particles, especially aluminum and boron, are well studied and are discussed in detail. Metal hydrides are also discussed in detail due to their recent and widespread attention in the HRE literature. Advanced metal-based additives manufactured through various means are also considered; however most of the state-of-the-art additives have been evaluated in solid propellant combustion rather than solid fuel combustion.

2.4.2.1. Pure Metals

The Air Force's Sandpiper Target Missile's development program was amongst the first to demonstrate hybrid motor firings with metal additives and included combustion testing of PMMA fuel loaded with several metallic powders burning in MON-25 oxidizer. [12, 239] Experimental results indicated that the addition of a magnesium additive led to regression rate enhancement, and increased loading (5, 10, and 20%) led to further regression rate enhancement but less-efficient combustion. [239]

Lips [40-42] was among the first researchers to comprehensively investigate aluminum additives in hybrid rockets propulsion systems. Lips performed combustion experiments of highly aluminized (60-80%) fuels burning in FLOX to evaluate the effects of binder composition; metal type and concentration; and oxidizer composition. Lips found that increasing the aluminum loading leads to further regression rate enhancement but reduces the observed combustion efficiency. [42] The regression rate enhancement effect seen with increased aluminum loading is shown in Figure 15. [42] The increase in regression associated with the increase in aluminum loading is evidence that some portion of the aluminum additive is combusting in the near-surface region and contributing to heat feedback. [54] Furthermore, Lips evaluated other metals including silicon, boron, and magnesium. The experimental results suggested that aluminum slightly outperformed silicon and boron in terms of regression rate and magnesium exhibited significantly larger regression rate enhancements than aluminum. [41] The higher regression rates exhibited by magnesium-loaded fuel were attributed to rapid vapor-phase combustion of the metal. Lastly, the aluminum particle size was varied in the micrometer range, with negligible alteration to performance. [40-41]

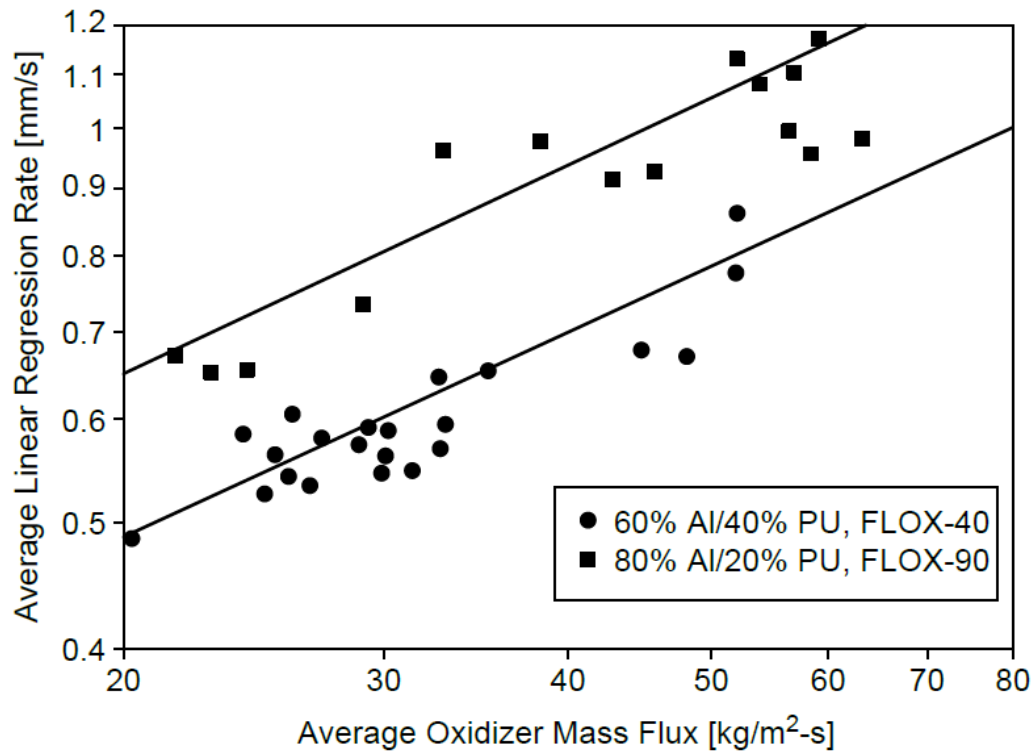


Figure 15. Enhancement of regression rate seen with increased aluminum loading in HTPB fuels burning in FLOX. Image taken from Ref. [42].

Strand et al. [240-242] performed combustion studies of HTPB with and without micro-aluminum and coal particles burning in GOX on single- and double-slab burners. The combustion events and regressing fuel surfaces were characterized with high-speed video data acquisition. Strand noted a surface melt layer that contained binder and agglomerated additive that would periodically detach from the combustion zone. Reducing the aluminum particle size in the micrometer range did not reduce agglomeration size, which was on the order of 1 mm, and had negligible effects on performance. At higher oxidizer fluxes, the melt layer transitioned to a steady regression of carbonaceous ash stemming from rapid decomposition of the HTPB due to increased

surface heat flux. [240] This finding resulted in pressure dependency at lower oxidizer mass fluxes and suggested that at higher oxidizer mass fluxes, the rate-limiting step is mass diffusion. The effect of adding a second slab to the experimental apparatus is shown in Figure 16. Inclusion of the second slab during combustion had no effect on plain HTPB regression, but it significantly increased aluminized fuel regression which is evidence of the role of radiation heat transfer in the regression process.

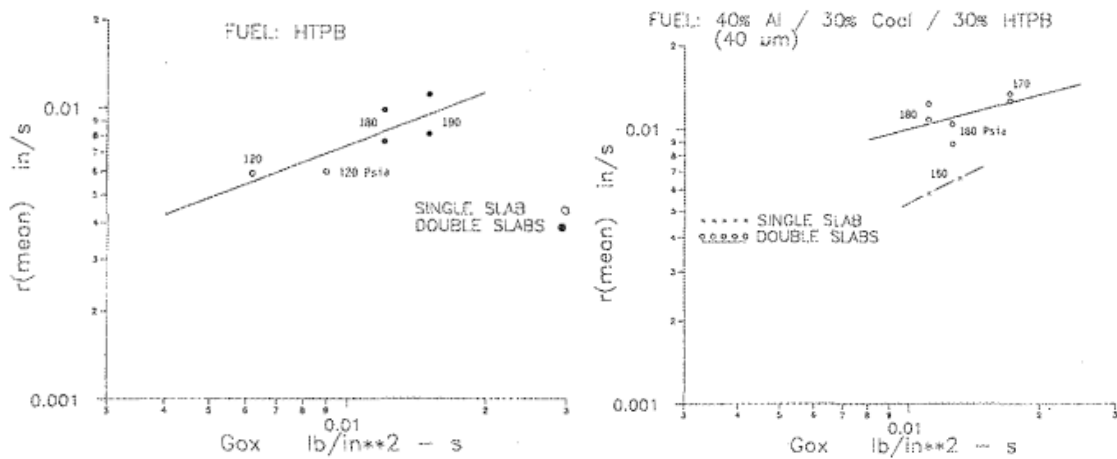


Figure 16. Regression rate behavior of (left) plain HTPB and (right) aluminized HTPB with coal burning in gaseous oxygen in a single and double slab burner configuration. Images taken from Ref. [240].

George et al. [213] completed combustion testing of plain and 20% aluminized HTPB fuel grains burning in gaseous oxygen and found significant increases in regression rate for the aluminized fuel, especially at higher oxidizer mass fluxes.

Some of the most comprehensive work on metallic additives has been completed by researchers at Pennsylvania State University under the supervision of Dr. Kenneth Kuo and Dr. Vigor Yang. [1, 80, 39, 214, 243-276] Early investigations by Chiaverini et al. [1, 243-247] reported on the combustion behavior of HTPB fuels loaded with carbon black

and micro- and nano-scale aluminum. Experiments were performed in a double-slab burner configuration, where one slab was composed of pure HTPB and the second included additive particles. The inclusion of nano-aluminum led to higher regression rate enhancement than micro-aluminum. The regression rate enhancement for micro-aluminum is attributed to increased radiative heat transfer and combustion gas temperature. The further enhancement from the addition of nano-aluminum is attributed to the higher rate of exothermic reactions in the near-surface region. The effects on nano-aluminum (100-150 nm) addition are shown in Figure 17. Increasing regression rate enhancement is noted with increasing additive loading. Chiaverini et al. [245-246] also conducted hot disk pyrolysis experiments under rapid heating conditions (>100 K/s) for plain HTPB specimen and fuel samples loaded with 20% micro- and nano-aluminum. The Arrhenius regression rate parameters were not altered by the addition of aluminum, which supports their previous conclusions from hybrid rocket experiments.

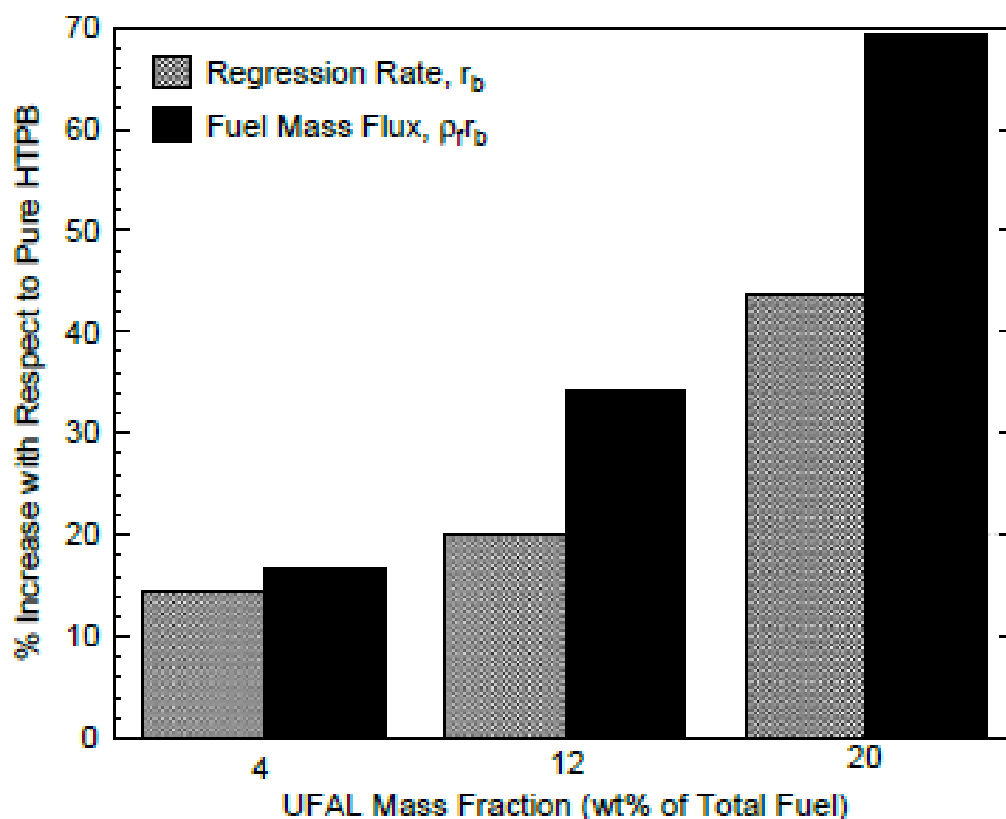


Figure 17. The effects of nano-aluminum addition to HTPB fuels burning in gaseous oxygen. Image taken from Ref. [248].

Risha et al. [249-253] included numerous aluminum- and boron-based additives in HTPB fuel grains burning in gaseous oxygen. The additive particles were purchased from several commercial entities and preliminary characterized by thermal gravimetric analysis (TGA), dynamic scanning calorimetry (DSC), Brauner-emmet-teller (BET) analysis, base hydrolysis, and scanning electron microscope (SEM) methodologies to determine their respective composition, size, and morphology. Regression rate results for aluminum- and boron-based additives are shown in Figures 18 and 19, respectively, and the effects on

combustion and specific impulse efficiency of these additives are shown in Table 1.

Experimental findings are summarized as follows:

- 1) The regression rate enhancement and combustion efficiency associated with aluminum or boron addition is dependent upon the particle size, type, geometry, composition, and loading.
- 2) Decreasing the size of the aluminum additive particles leads to enhanced regression rates stemming from fast and efficient combustion processes in the near-surface region and enhanced heat transfer processes.
- 3) Increasing the additive content in the propellant increases the regression rate; however, additional loading at high contents leads to less-efficient combustion in the near-surface region and periodic surface-layer shedding, so that a practical loading limit exists.
- 4) Passivation techniques that alter the oxide layer and coat the additive in an alternative, protective chemical layer, such as a fluorinated compound, can successfully lead to further regression rate enhancement and increased combustion efficiency.
- 5) Combustion and specific impulse efficiency losses are more prevalent in boron compounds than aluminum compounds due to the inherent difficulty associated with igniting boron and additional two-phase flow losses in the nozzle.

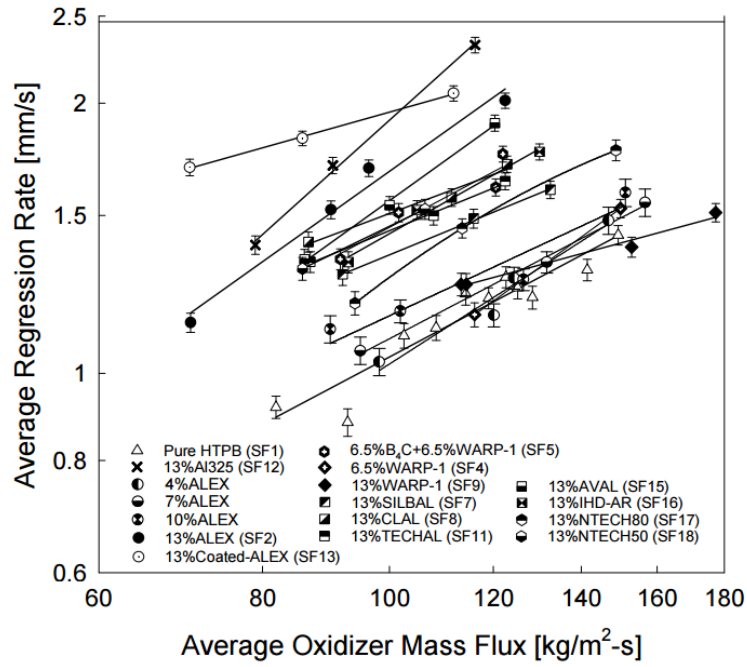


Figure 18. The effects of various aluminum additives on HTPB regression rate. Image taken from Ref. [254].

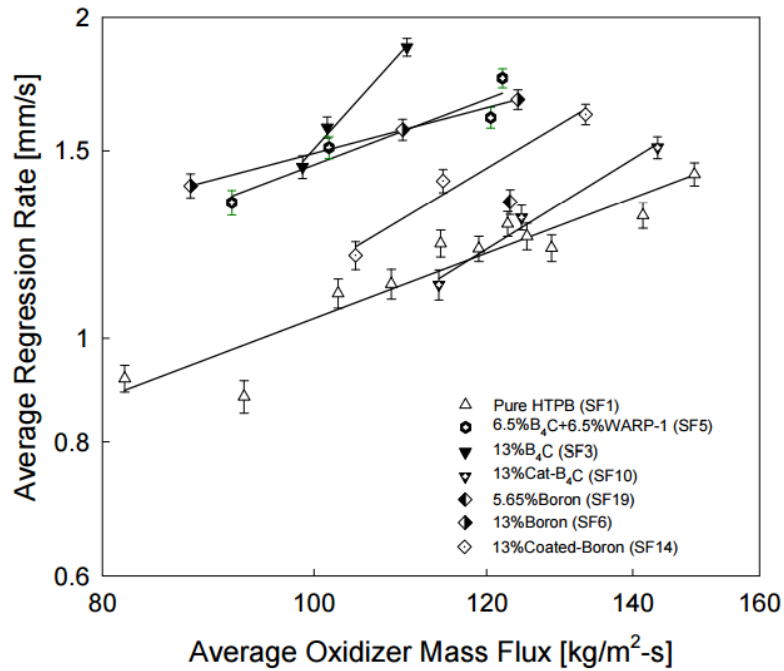


Figure 19. The effects of various boron additives on HTPB regression rate. Image taken from Ref. [254].

Table 1. The effects of various aluminum and boron additive on HTPB combustion and specific impulse efficiency. Image taken from Ref. [254].

Solid Fuel	Additive (by wt%)	C* Combustion Efficiency [%]	I_{sp} Efficiency [%]
SF1	None	72 – 91	73-88
SF2	13%Alex [®]	77 – 89	59-72
SF3	13%B ₄ C	60 – 81	50-84
SF4	6.5%WARP-1	73 – 81	47-54
SF5	6.5% B ₄ C/ and 6.5%WARP-1	71 – 80	51-68
SF6	13%BORON	78 – 81	63-69
SF7	13%SILBAL	72 – 80	65-68
SF8	13%CLAL	83 – 85	61-64
SF9	13%WARP-1	69 – 89	81
SF10	13%Cat-B ₄ C	76 – 82	64-71
SF11	13%TECHAL	81 – 94	70-80
SF12	13%Al-325	81 – 85	71-78
SF13	13%C-Alex	88 – 92	71-86
SF14	13%C-Boron	76 – 81	69-76
SF15	13%AVAL	87 – 98	75-82
SF16	13%IHD-AR	73 – 78	68-73
SF17	13%NTECH-80	80 – 90	74-77
SF18	13%NTECH-50	76 – 87	77-78
SF19	5.65%BORON	83	83

Evans et al. [39, 80, 214, 248, 254-255] went on to study the effects of aluminum additive in paraffin fuels and scalability of the previously observed enhancements. Experimental observations suggested that aluminum additives agglomerating on the surface of paraffin fuels can become encapsulated and entrained in oxidizer flow, which

leads to further increases in regression rate and combustion efficiency when compared to HTPB. [80] Larger HTPB fuel grains, scaled up by a factor of 3, were burned in a follow-up set of experiments. [214] The regression rate of plain HTPB was decreased by approximately 15% which was attributed to decreases in heat flux associated with the larger port diameter. The regression rate enhancement due to aluminum addition exhibited by the smaller motor was not retained in the larger motor. The authors speculated that this finding is most likely associated with 'flake' geometry of the evaluated aluminum and stipulate that further work should be completed to identify scaling difficulties associated with metallic additives.

Further researcher at PSU [266-269] focused on the evaluation of boron-based fuels for SFRJ applications which included numerical simulations, laser ignition experiments, and solid-fuel combustion experiments for various propellant systems. Solid-fuel combustion experiments were performed in subsonic and supersonic air flows with varying boron concentrations, sizes, and purity; oxygen mass fraction; oxidizer temperature; and chamber pressure. The addition of boron particles to HTPB fuel led to an increase in regression rate at nearly all operating conditions. However, higher loadings (>10%) showed decrements in regression rate with the densest fuel (50% B) yielding a regression rate below that of plain HTPB. The increase in regression rate at low loadings of boron is derived from heat generated during particle burning in the diffusion flame and a corresponding increase in heat transfer back to the fuel surface. The diminishing returns associated with additional boron loading was attributed to a combination of unreacted boron particles absorbing heat which reduces the gas-phase temperature and boron

accumulation on the fuel surface which leads to a blocking effect. Reduction of particle size, increasing the purity, or magnesium coatings on the boron additive led to further enhancements in regression rate. The effects of boron were also more prevalent at higher freestream temperatures.

A network of Italian-based researchers have been working towards improving the performance and understanding of hybrid rocket propulsion systems. [277] A significant amount of experimental work regarding energetic additives in hybrid fuel systems has been conducted at the Politecnico di Milano under the leadership of Dr. Luigi DeLuca. [14-18,186,278-296] The research team thereat has developed a typical cylindrical burner apparatus in conjunction with a time-resolved optical measurement system to visualize the transient combustion behavior of fuels burning in solid fuel samples.

Galfetti et al. [278] evaluated the addition of nano-aluminum in gelled- and solid-wax fuel formulations. Interestingly, the nano-aluminum additive was found to be significantly more effective in the gelled wax as compared to the solid wax, most likely since the plain, gelled-wax regression rate was much lower than that of the plain, solid wax.

DeLuca et al. [279] and Paravan et al. [280] reported on aluminum particle size effects in HTPB fuels burning in gaseous oxygen. Reduction of particle size from micro- to nano- and then further in the nano-regime led to further increases in regression rate which was attributed to more-rapid exothermic reactions closer to the fuel surface. Experimental results from tensile testing of fuel samples showed micro-particles led to better reinforcement than nano-particles, which was attributed to aggregate formation

associated with the nano-particles. Furthermore, sonication treatments to reduce aggregation in the fuel samples containing nano-particles were able to improve the fuel's mechanical properties.

A cooperative researcher effort performed by the Israel Institute of Technology and the Naval Postgraduate School [297-302] examined the combustion of HTPB fuels loaded with boron and boron carbide particles burning in air crossflow for solid fuel ramjet (SFRJ) applications. The authors noted that the boron particles tended to form larger agglomerates on the fuel surface and that particle removal from the surface occurred by two distinct methods: 1) ejection of a fuel surface piece from shear forces or 2) a burst of particles due to oxidizer impingement and local pressure build up. [297] Regardless of the particle-removal phenomenon, the particles did not have sufficient residence times or oxidizer concentration to burn rapidly prior to nozzle ejection. Installation of a post-combustor bypass air system allowed for significant combustion efficiency enhancements by increasing the local oxidizer concentration around the already burning particles and increasing particle residence times. [299] Improvement of combustion efficiency with boron-loaded solid fuels by the introduction of bypass air is a well-established result. [303]

Fluorine is an extremely electronegative element and can be utilized as an oxidizing agent in the oxidation of fuels, including metallic particles. The most common form of fluorine inclusion for metallic particle combustion purposes is Polytetrafluoroethylene (PTFE), a fluorocarbon that contains 75% Fluorine by mass. [304] PTFE/metal systems have also been evaluated in numerous capacities as pyrolant mixtures, and a thorough review is given by Koch [305]. One representative study was

completed by Shidlovskii and Gorbunov [306] who measured the burning rates of PTFE pellets loaded with micro-boron, magnesium, and titanium at various pressures. In all cases, the inclusion of each metal led to an increase in burning rate of the system, with titanium and boron yielding the best and worst results, respectively. Furthermore, each PTFE/metal system had an optimum fuel loading that yielded the highest burning rate value.

Connell et al. [307-308] recently reported on utilization of a polytetrafluoroethylene ((C₂F₄)_n/PTFE) binder containing 20% boron as a high-density solid fuel for hybrid rocket applications. The fuel's regression rate exhibited high pressure dependency and negligible mass flux dependency. High combustion efficiencies (>95%) were achieved at higher motor operating pressures (>15 MPa). The authors attributed the high combustion efficiency of the boron additive to the local presence of fluorine which enhances the removal rate of the passivating boron oxide surface layer and the lack of hydrogen which avoids production of metaboric acids (HBO₂). Connell also provides an extensive review of research completed on boron combustion and the effects of fluorine oxidizing environments, all of which suggest that the presence of fluorine can lead to more-rapid and efficient ignition and combustion of boron additives.

Connell et al. [309-310] evaluated PTFE and 20% boron as a potential hybrid fuel candidate and completed combustion testing with gaseous oxygen in a lab-scale rocket, and in oxygen and nitrogen environments in a strand burner. The authors noted that the presence of fluorine was expected to enhance the removal rate of boron oxide leading to enhanced ignition, while the lack of hydrogen in the system would mitigate the formation

of metaboric acid and other boron hydrides leading to enhanced combustion efficiency. The fuel formulation exhibited pressure dependency and burned similar to a solid propellant above the low-pressure, self-deflagration limit, but burned similar to a classical hybrid below this limit.

Young et al. [322] evaluated the combustion of boron-containing PTFE fuel samples in an opposed flow burner configuration. Theoretical chemical equilibrium calculations suggest this fuel system is capable of significant performance improvements over plain HTPB (~ 460 s I_{sp}), but high flame temperatures (>3000 K) could limit their application. The opposed-flow ballistic testing showed the regression rates of PTFE/boron fuels are lower than that of plain HTPB, but the higher density of the system yielded comparable mass flow rates. Lab-scale hybrid rocket testing was characterized by odd burning behavior and suggested possible pressure and oxidizer mass flux dependencies.

2.4.2.2. Metal Hydrides

Metal hydrides represent a class of metal-based additives that can significantly improve the specific impulse of hybrid rocket propulsion systems, but one major difficulty with the incorporation of metal hydrides is their high reactivity with water and humid air. This complication makes utilization of some binders, such as HTPB, impractical due to outgassing and water penetration, but other binders, such as paraffin and DCPD, have shown good compatibility with metal hydrides. Lithium-based particles, such as lithium aluminum hydride, have relatively low volumetric heats of oxidation, but exhibit high gravimetric heats of oxidation and are extremely reactive due to their electropositive outer

shell. Another key advantage of metal hydride additives is the potential to remove the ignition system because they can be hypergolic with some oxidizers.

Detailed theoretical chemical calculations for HTPB fuels loaded with numerous metals and metal hydrides burning in oxygen has been completed by the research team at Politecnico di Milano. [281-283] Impulse performance variation with the inclusion of these additives is shown in Figure 20. These calculations demonstrated that aluminum hydride (AlH_3) has the greatest potential for specific impulse improvement amongst the surveyed metal hydrides.

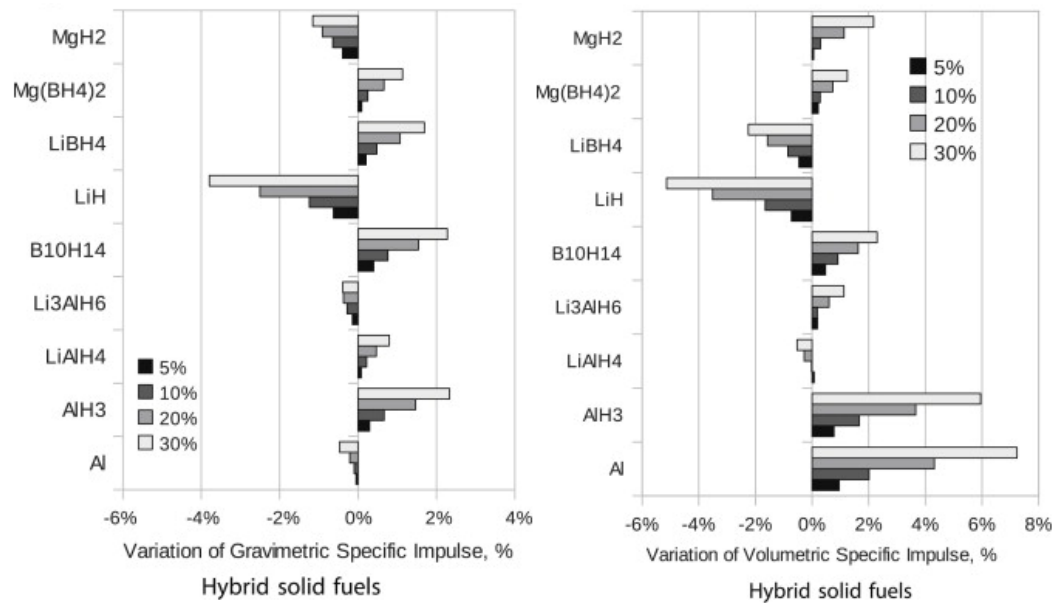


Figure 20. (left) Gravimetric and (right) volumetric specific impulse performance variation with the inclusion of various metal hydrides in comparison to plain HTPB burning in oxygen. Images taken from Ref. [283].

Smoot and Price [7-8] performed laboratory-scale combustion experiments of butyl rubber seeded with 0-90% lithium hydride (LiH) burning in pure oxygen, pure fluorine, and FLOX flows. Their experimental results are shown in Figure 21. These

experiments showed that the addition of LiH to rubber increased the regression rate, and that increasing the mass loading of LiH led to further regression rate enhancement, especially at higher oxidizer mass fluxes. Furthermore, increasing the amount of lithium additive reduced high-flow-rate pressure dependence. The transition from mass flow dependent behavior to pressure-dependent behavior was speculated to correspond to a shift from a diffusion-controlled regime to a chemical kinetics-controlled regime.

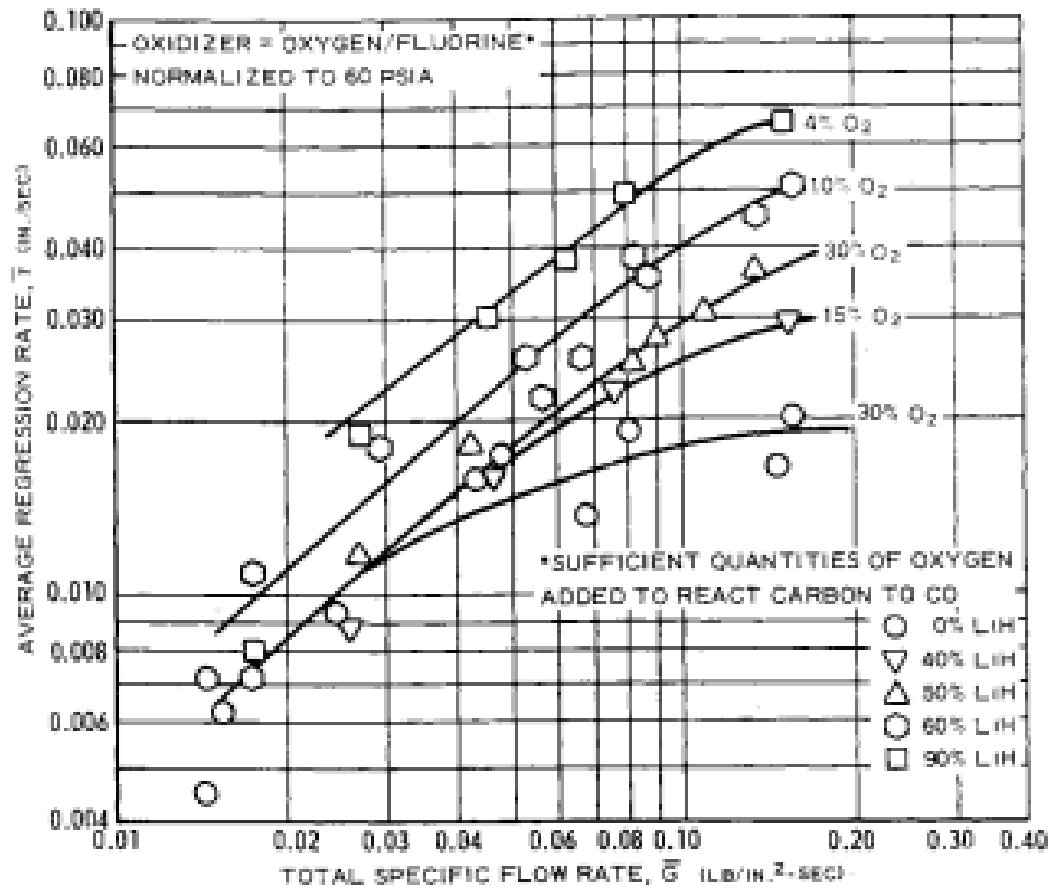


Figure 21. Regression rate dependence on lithium hydride (LiH) loading in butyl rubber burning in oxygen. Image taken from Ref. [7].

Osmon [196] performed combustion experiments of polyethylene (PE) fuel seeded with 95% lithium aluminum hydride (LiAlH_4) burning in 90% liquid hydrogen peroxide (H_2O_2). The fuel grains exhibited increased regression rate in comparison to plain PE. Osmon noted non-uniform burning consisting of more-significant regression at the fuel port entrance and further downstream locations. Humble [55] incorporated 50% lithium aluminum hydride (Li_3AlH_6) into dicyclopentadiene (DCPD) fuel burning in hydrogen peroxide (H_2O_2). Theoretical thermochemical equilibrium calculations were performed to demonstrate the capability of the additive to significantly improve the specific impulse of hybrid systems. The additive fuel's combustion gases were much hotter than expected and eroded the nozzle quickly, but early test data indicated a significant increase in chamber pressure and temperature, fuel regression, and thrust production corresponding to the introduction of the additive. Corpening et al. [323] performed combustion experiments of dicyclopentadiene (DCPD) fuel seeded with 50-80% lithium aluminum hydride (LiAlH_4) burning in 98% liquid hydrogen peroxide (H_2O_2). Chemical equilibrium calculations confirmed the additive was capable of significantly improving specific impulse, but the test motors exhibited only moderately increased regression rate and poor combustion efficiencies.

DeSain et al. [324] demonstrated the stability of lithium aluminum hydride (LiAlH_4) additives in paraffin-fuel binders for long shelf lives, under humid conditions, during recasting, and even in water submersion. Furthermore, the authors theorized and demonstrated the potential use of the additive as a hypergolic ignition source under crossflow of strong acidic oxidizers, such as nitric acid (HNO_3), potassium nitrate (KNO_3),

and dinitrogen tetroxide (N_2O_4 /NTO). Recent work by Stober et al. [325-327] is also focused on hypergolic ignition experiments through similar additive methods. Larson et al. [328] performed a follow-up set of combustion experiments with paraffin fuel seeded with 10-28% lithium aluminum hydride ($LiAlH_4$) additive burning in gaseous oxygen. The experimental results indicated higher regression rates with increasing additive loading, similar to those seen by Smoot and Price [7]. Theoretical chemical calculations correlated large chamber pressure increases accompanying increased additive loading, not only to increased mass flux, but also to increasing combustion gas temperature and decreasing molecular weight. The authors also investigated triethylaluminum ($Al_2(C_2H_5)_6$) and diisobutylaluminum hydride ($C_8H_{19}Al$) as potential performance enhancers in single motor firings; both additives showed promise, but further work is required. [328]

Galfetti et al. [278, 284-286] performed mechanical, rheological, and ballistic evaluations of paraffin fuels containing carbon black, nano-aluminum, magnesium hydride (MgH_2), lithium aluminum hydride ($LiAlH_4$), polyurethane (PU) foam, and thermoplastic polymers. Findings suggested that the additive effects on viscosity dominated the corresponding regression rate due to the dependency of entrainment processes on this rheological property. All additive formulations exhibited enhanced mechanical properties and regression rates when compared to baseline paraffin. In terms of regression rate, lithium aluminum hydride outperformed magnesium hydride, and increasing the mass loading of either additive led to further regression rate enhancement. In contrast, follow-up investigations by Boiocchi et al. [329] determined that some wax-based formulations including structural additives (SEBS-MA) exhibited poor

compatibility with lithium aluminum hydride which decreased the regression rates in ballistic testing.

Paravan et al. [280] performed combustion experiments of fuels burning in gaseous oxygen with additives including micro- and nano-aluminum and magnesium-coated boron. Experimental results indicated that all additives led to regression rate enhancement, but Paravan et al. noted that a low loading of magnesium-coated boron (2.8%) led to significantly more enhancement than moderate loadings (10%) of nano-aluminum in both HTPB and paraffin fuels. Fanton et al. [287] later extended the study to include additional additives, such as carbon black, titanium dioxide (TiO_2), nano-aluminum coated with palmitic acid ($\text{C}_{16}\text{H}_{32}\text{O}_2$), and magnesium hydride (MgH_2). The regression rate measurements are presented in Figure 22. The addition of carbon black led to significant enhancement, especially at higher oxidizer mass fluxes and regardless of other additive constituents. The introduction of titanium dioxide (TiO_2) was detrimental to performance. This finding suggests carbon black's role in regression rate enhancement is not as an opacifier in the subsurface solid fuel, but that it contributes directly to combustion processes. The coated nano-aluminum did not outperform the uncoated additive. Finally, the combination of low loadings of magnesium hydride (2.5%) and magnesium-coated boron (1.4%) yielded the largest regression rate enhancement. However, previous experimental work completed by the research team [281-282, 288] indicates that the inclusion of aluminum hydride (AlH_3) leads to significantly better regression rate enhancement than magnesium hydride (MgH_2), as shown in Figure 23.

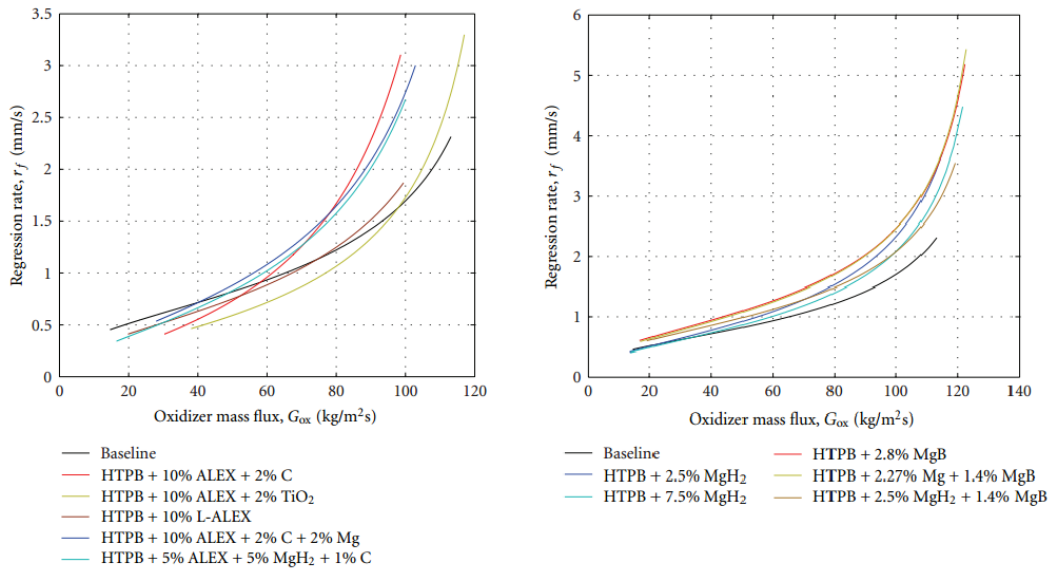


Figure 22. Regression rate measurements of HTPB fuels with metallic additives burning in gaseous oxygen. Images taken from Ref. [118].

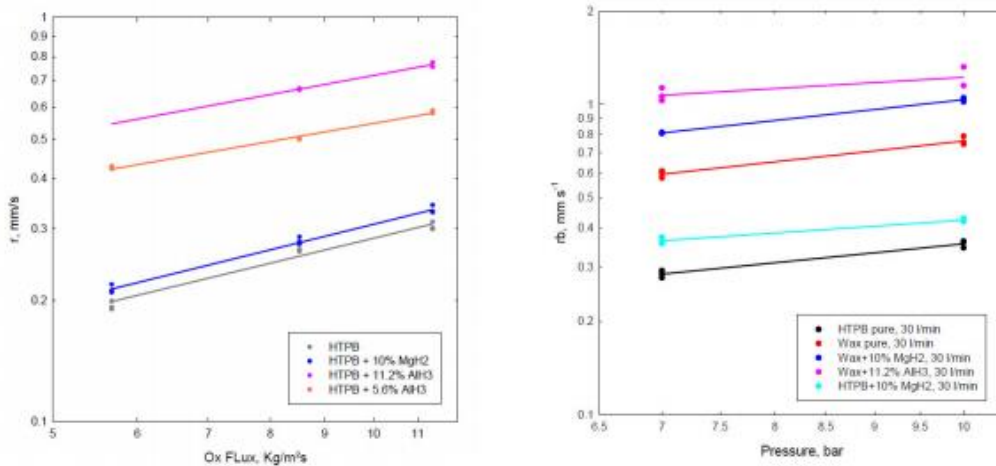


Figure 23. Regression rate comparisons of fuel formulations containing MgH₂ and AlH₃. Images taken from Ref. [288].

Qin et al. [289-290] studied the ignition of HTPB fuels with and without metals in a quiescent oxygen atmosphere. Metallic formulations included aluminum, magnesium, magnesium-coated boron, and an iron/yttrium/aluminum alloy. The ignition delay time

was reduced at higher pressures with the presence of any of the metals. Furthermore, the formulation containing plain magnesium exhibited the shortest ignition delay times.

Recent work at Purdue University led by Dr. Steve Son [330-338] has focused on evaluation of metal hydrides and borane additives as potential additives in hybrid propulsion systems. Sippel et al. [133], followed by Shark et al. [331-334], focused on characterization of dicyclopentadiene (DCPD) fuel containing uncoated nano-aluminum, PTFE-coated nano-aluminum, aluminum hydride (AlH_3), and sodium borohydride (NaBH_4) burning in gaseous oxygen and hydrogen peroxide (H_2O_2) flows. Their unique optical cylindrical combustor (OCC) apparatus allows for clear visualization of the flame and combustion processes during operation. Evaluation of aged heats of combustion demonstrated the stability and lack of stability of the compounds in DCPD and HTPB fuel binders, respectively. Fuel grains containing 25% sodium borohydride (NaBH_4) and 25% uncoated or coated nano-aluminum had comparable regression rates which were elevated in comparison to the plain DCPD fuel. Reduction of the sodium borohydride (NaBH_4) particle size in the micro-range did not have an appreciable effect on the observed regression rate, but increasing the additive's mass loading led to further regression rate enhancement and reduction in the combustion efficiency. The aluminum hydride (AlH_3) additive outperformed the sodium borohydride (NaBH_4) additive in terms of regression rate but exhibited a comparable combustion efficiency at all evaluated experimental conditions.

The unique design of an optical chamber combustor [331] allows for visualization of a cylindrical hybrid sample during combustion and has been utilized to visual flame

height for the previously described additives. The flame heights of DCPD fuels containing aluminum additives were comparable to the plain DCPD, but addition of sodium borohydride (NaBH_4) led to an increase in flame height. This finding was attributed to an increase in flame thickness accompanying hydrogen diffusion into the flame zone and enhanced heat feedback.

Young et al. [335] measured the ignition temperatures of alane (AlH_3) in air, oxygen, and CO_2 environments and found they increased with heating rate, were insensitive to oxygen concentration, and were comparable to that of nano-aluminum (900-1500 K). Young et al. [336] also studied solid HTPB fuel formulation containing micro-aluminum, nano-aluminum, and alane at loadings of 10, 20, and 40% burning in GOX on an opposed-flow burner. The alane-based formulations moderately outperformed the aluminized and plain HTPB formulations in the opposed-flow burner configuration, but they did not yield any measurable regression rate enhancement in the lab-scale hybrid experiments.

Weismiller et al. [337] reported that the addition of ammonia borane (NH_3BH_3) can significantly increase specific impulse and performance through an increase in chamber temperature and reduction in combustion product molecular weight. Experimental results performed with paraffin burning in gaseous oxygen indicated that the addition of 10% additive led to regression rate enhancement, but additional loading actually decreased fuel regression rate. Furthermore, all tested formulations containing the additive exhibited increased characteristic velocity and combustion efficiency. Subsequent investigations by Pfeil et al. [338-339] and Ramachandran et al. [340] led to

the identification of amine boranes, such as ethylenediamine bisborane ($C_2H_{14}B_2N_2$), as a class of air-stable, rapid-ignition fuel additives that induce hypergolicity with nitric acids and improve regression rates.

2.4.2.3. Metal Blends

Vadala et al. [293] reported on the characterization of bimetallic blends of nano-aluminum and copper. DSC/TGA analyses determined the presence of copper leads to a reduction in oxidation onset temperature and energy release, which is further intensified with increasing loading. Combustion tests of HTPB-loaded fuels in a gaseous oxygen flow revealed faster regression with bimetallic blends, compared to pure-aluminum-loaded fuel. Furthermore, increases in copper/aluminum ratios led to reductions in the regression rate sensitivity to changes in oxidizer mass flux. Further research efforts into these phenomena involving aluminum alloys are currently being undertaken and will be reported in future publications. [295]

Farbar et al. [341] burned HTPB fuel formulations in a 90% hydrogen peroxide core flow. Additive fuel formulations contained 60% metallic loading of either micro-Al ($3 \mu m$) or a 50/50 blend of micro-Al and Mg ($120 \mu m$). The aluminized formulation performed comparably to the baseline HTPB formulation, while the formulation containing the Al/Mg mixture regressed faster than the baseline and the aluminized formulation and reduced the amount of slag accumulation. Both metallized formulations resulted in a small decrease in combustion efficiency, which is impressive considering the high loading of particles in the system. However, the authors make note that a non-

traditional method was utilized to estimate the combustion efficiency, since significant nozzle erosion was present during motor firings.

Liu et al. [342] evaluated the combustion of mixtures of boron and magnesium micro-particle mixtures prepared with a mortar and pestle. Ballistic testing was completed in a windowed combustor with CO₂-laser ignition in air at atmospheric pressure. Addition of magnesium led to a reduction in ignition delay time at low loadings, with the best performance exhibited by the 20% magnesium loading and a return to nominal performance at higher loadings (50%). The combustion efficiency of boron in the particulate samples was evaluated by residue titration. Increasing magnesium content consistently led to an increase in boron combustion efficiency. Complementary TGA/DSC studies were completed in air flow and showed the onset temperature of oxidation decreased with increasing magnesium loading.

Obuchi et al. [343] assessed the effects of magnalium (50/50 Mg/Al, 20 μm) addition on the combustion of boron (1.8 μm) particles in a series of experiments. TGA/DSC experiments showed the oxidation onset temperature for Mg:Al was similar to that of boron, but occurred much more rapidly, and that the addition of magnalium to boron at a loading of 50% led to more-rapid oxidation. Ignition experiments were conducted in a furnace at a pre-conditioned temperature. Magnalium exhibited the lowest ignition delay times and enhanced the ignition of boron particles by lowering their ignition delay time and allowing for boron ignition at lower temperatures where plain boron would not ignite. Ballistic experiments were performed in a ducted rocket configuration at low pressures (<0.5 MPa) with boron and magnalium incorporated into an AP/HTPB (70/30)

propellant formulation. Inclusion of the Mg:Al particles within the system led to significant increases in combustion efficiencies of the secondary combustor which were more prominent with higher concentrations of magnalium. The highest loading of magnalium (70/30/20/20 AP/HTPB/B/Mg:Al) yielded a relative increase in combustion efficiency of 70% over the formulation with only boron (70/30/20 AP/HTPB/B). Similar experiments were conducted by Negishi and Kuwahara [343] which showed comparable increases in combustion efficiency with increased Mg:Al particle loading. Hara et al. [344] measured the burning times of Mg:Al particles in a pre-conditioned, pressurized furnace system and found that burning times decreased sharply with increasing pressure and slightly with increasing temperature.

Mitsuno et al. [345] performed ballistic experiments with HTPB and CTPB fuel containing AP, micro-B (5 μm), and micro-Mg/Al alloy (50/50, 30 μm) in a ram-air combustor. The propellant formulation containing the Mg/Al alloy burned significantly faster (~20%) and more efficiently (~5%) than the formulation containing B. The combustion efficiencies of each propellant were found to increase with increasing ram-air temperature, and the combustion efficiency of formulations containing B improved (~15%) by the incorporation of low loadings (5-10%) of the Mg/Al alloy.

Carmicino et al. [346-347] reported on experimental efforts at the University of Naples that showed regression rate enhancement in HTPB fuels burning in gaseous oxygen with nano-aluminum additive at moderate mass loadings (10%) and significantly more enhancement with magnesium hydride (MgH_2) at lower mass loadings (5%). Follow-up experiments included micro-aluminum, uncoated and Viton-coated nano-

aluminum, magnesium, magnesium hydride (MgH_2), iron, and a blend of magnesium and iron. [347] Although more experimental data should be collected for completeness, preliminary findings yielded interesting results regarding regression rate enhancement. The fuel seeded with micro-aluminum outperformed virgin nano-aluminum and was comparable to PTFE-coated nano-aluminum. The best results were realized with the fuel mixture containing both magnesium and iron. This finding was attributed to the low melting temperature of iron oxide (Fe_2O_3) which allowed for quicker combustion near the fuel surface and further released heat input that assisted in melting the magnesium oxide (MgO) coating.

2.4.2.4. Boron Carbide

Pein and Vinnemeier [348-349] performed ballistic testing of HTPB-based fuels containing up to 40% boron or boron carbide (B_4C) with axial or swirl air flow. Fuels containing boron carbide exhibited higher combustion efficiencies than fuels containing plain boron. Increasing the loading of either additive led to a reduction in combustion efficiency. Incorporation of swirl flow led to relative enhancements of 50% and 100% in the combustion efficiencies of fuels containing boron and boron carbide, respectively.

Nabity et al. [350] evaluated the combustion of fuels loaded with boron carbide (B_4C) burning in air crossflows for SFRJ applications. Experimental measurements included combustion efficiencies and post-combustion particle size distributions at various operating conditions. Higher combustion efficiencies were noted with higher equivalence ratios (shorter grain lengths) and air temperatures.

The experimental work completed by Risha [249-253] which evaluated numerous aluminum and boron particles loaded in HTPB and burning in GOX also included B₄C. In comparison to the plain and PTFE-coated boron fuel formulations, the B₄C formulation exhibited a higher regression rate but lower combustion efficiencies.

2.4.2.5. Metal Borides

Korotkikh et al. [351-354] have performed thermochemical equilibrium calculations and laser-ignition studies to compare the performance of solid propellants based on AP/AN/HTPB mixtures containing pure metals and metal borides. Ignition studies in a combustion chamber at atmospheric pressure showed the replacement of micro-aluminum at a mass loading of 30% in the propellant with aluminum borides (AlB₂ or AlB₁₂) led to a 50% reduction in the ignition delay time. Follow-on ignition studies indicated that amorphous boron was more effective than the aluminum boride compounds at reducing the ignition delay time, and that titanium boride (TiB₂) was not effective for this measure of performance. It is worth noting that the boron particles were on the nano-scale (≈ 200 nm, 99.5% purity), while the aluminum boride compounds were on the micro-scale ($\approx 1-5$ μm).

Oleg et al. [355] measured the burning rate and boron combustion efficiency of composite propellant formulations based upon an energetic binder and AP which contained various loadings of micro-boron and several additives (AlB₂, mixed micro-Al and B, and AlB₂ coated in fluorine-substituted alloxysilane at low pressures ($P < 2.5$ MPa)). Boron combustion efficiency measurements were completed by collection, treatment, and analysis of condensed-phase products. In general, the burning rates of formulations

containing high loadings (40%) of boron or additives were similar, but the calculated combustion efficiency of the plain boron formulation was highest. It is also interesting to note that calculated combustion efficiency of the propellant formulation increased with increasing boron content, while the measured regression rate decreased.

Researchers at Tomsk State University [356-358] have detailed the potential of metal borides in energetic systems, developed micro-particle synthesis procedures for several systems, and evaluated their performance through TGA/DSC studies. In general, the heat of combustion for metal borides is high, and their onset temperatures of oxidation are significantly reduced in comparison to amorphous micro-boron.

Researchers at Tomsk Polytechnic University [359-364] have reported on the passivation and stabilization of nano-scale aluminum with aluminum diboride (AlB_2). The research team has developed a process for the production of nano-aluminum by the explosion of wire method which yields AlB_2 -passivated particles with 78% Al content and 18% AlB_2 content, which is quite good considering the nominal particle size (≈ 2 nm). The synthesized AlB_2 -passivated nano-aluminum particles yielded significant improvements over similarly synthesized ALEX in DTA/TGA experiments. [360-361]

Liu et al. [365] evaluated the ignition and combustion of several micro-scale (1 μm) magnesium boride compounds (MgB_5 , MgB_8 , MgB_{12} , and MgB_{20}) in a windowed combustor at low pressures (< 2 MPa). TGA/DSC studies at atmospheric pressure indicated the onset of the oxidation reaction for the boride particle was higher than that of amorphous boron. Combustion experiments indicated the ignition delay times of the

boride compounds were also longer than for amorphous boron, but this trend was diminished at the higher evaluated pressures.

2.4.2.6. Advanced Particle Synthesis Strategies

Specific activation processes can be performed on metallic additives to gain increased ignition and combustion performance without reducing the particle size to the sub-micrometric range. These processes include mechanical milling, metallic deposition coating, passivation techniques, and chemical weakening of the surface oxide shell. A comprehensive review of these techniques and their effects is outside of the scope of this paper, but specific examples related to metallic combustion and, especially, performance improvement in hybrid propulsion systems is given, as follows.

Mechanical milling processes, also termed mechanical alloying, alter the particle morphology and/or chemistry through high-energy impact with processing spheres and chemicals. More explicitly, this process can decrease diffusion distances and increase surface area and reactivity. [366] A detailed survey of mechanical alloying and milling processing and parameters is given by Suryanarayana [366].

Dr. Edward Dreizin's research group at the New Jersey Institute of Technology has developed arrested reactive milling (ARM) techniques to produce metallic alloys or nanocomposite powders. [367-395] The referenced nanocomposite powders comprise micron-sized powders in which each particle represents a metal matrix with nano-sized inclusions. [367] The research team has evaluated mechanical alloys encompassing numerous systems which have included metals (Al, Hf, Li, Mg, Ni, W, Zn, Zr); metalloids (B, C, S, Si); metal oxides (Bi_2O_3 , CuO , Fe_2O_3 , MoO_3 , SrO_3 , WO_3); metal hydrides

(MgH₂); oxidizers (CaI₂O₆, NaNO₃, I), and hydrocarbons (paraffin, PE). A significant amount of these research efforts have been aimed at the production of enhanced thermites. Potential materials of particular interest for hybrid rocket applications include Al composites containing Fe [368], Li [369], Mg [370-382], Ni [368], Ti [383-388], Zn [368], and PTFE [389-390]; and B composites containing Mg [371], Ti [367, 372, 377, 391-393], W [393], and Zr [394]. For further information on these techniques, the reader is referred to detailed reviews given by Dreizin [395-396].

SEM and XRD analyses are typically performed to characterize the powder morphology and composition. Combustion experiments have consisted of constant-volume explosion testing in a variety of environments where the maximum overpressure and pressurization rate are numerical indicators of energetic and efficient combustion. Microscopic analysis of combustion residue has also yielded further insight into combustion mechanisms and oxidation efficiency. Alternative constant-volume combustion experiments have measured ignition times and powder combustion rates initiated by laser. Shock-tube experiments achieve ignition behind a reflected shock wave have focused on measurements of ignition delay time, particle combustion rate, emission spectra, and combustion temperature. Ignition temperatures of powder systems are commonly measured by the wire-heating method. Ballistic results have been coupled with thermal decomposition experiments to better understand the mechanisms involved in the observed enhancement.

In general, the mechanical alloys produced through ARM have outperformed similar powder blends or pure metals. The observed performance enhancements are

typically derived from lowered ignition temperatures and more-efficient self-heating processes stemming from added metal-metal or metal-metalloid reactions, or from new metal-oxidizer reactions at the surface of aluminum or boron. For example, investigations of a mechanically alloyed 2B-Ti powder completed by Trunov et al. [367] demonstrated improvement in terms of rapid ignition, combustion rate, and combustion efficiency in comparison to a similar powder blend or plain aluminum powder in dry and wet gaseous environments. The observed enhancements were attributed to a significant increase in the interface surface area between B and Ti which yields rapid, nearly adiabatic heating stemming from the metal-metalloid reaction. In another investigation, Aly et al. [397] demonstrated the capability to produce Al-Mg nanocomposites with selectable composition and size, all of which exhibited ignition temperatures near that of magnesium and much lower than that of similar aluminum particles. Dreizin and Schoenitz [396] provide a detailed review of mechanochemically alloying techniques and results for their own work as well as for other investigators.

White et al. [398] performed mechanical activation of Al-Ni mixtures and showed that it significantly reduces the exothermic reaction onset temperature, leading to increased reactivity. Filimonova et al. [399] further showed that these mixtures exhibited a reduction in ignition temperature and activation energy. Similar experiments performed by Mason et al. [400] showed the activation process of equi-atomic Al/Ni mixtures led to increased combustion velocities and flame temperature, and further demonstrated the dependency of these results on the milling procedure parameters. Combustion experiments performed by Hahma et al. [401] suggest the nickel coating catalyzes aluminum nitride

formation. Similar mechanical activation experiments with low loadings of secondary metals including Fe, Zn, and Ni in aluminum particles have exhibited reduced ignition temperatures and increased low-temperature oxidation reactivity. [368] The experiments performed by Hahma et al. [401] indicated aluminum particles coated with nickel exhibited quicker and more efficient combustion in comparison to cobalt.

Sippel et al. [402-405] utilized mechanical milling to increase particle surface area and selectively include PTFE in the surface oxide layer. The activated particles exhibited two pre-ignition exothermic reactions and a corresponding increase in combustion enthalpy and reduction in ignition temperature. Furthermore, this increased reactivity has been attributed to the very high volumetric and gravimetric heat releases resulting from fluorination of the aluminum instead of oxidation. [402, 405-408] The boiling point of metal-fluorides occurs at significantly lower temperatures compared to their respective oxides, which leads to enhanced ignition and gas production, and reduced condensed-phase products. [402, 408] Various other experiments with inclusions of fluoro-polymers into the aluminum oxide structure have yielded similar results. [406-412] Osborne and Pantoya [410] noted similar exothermic reactions and reduced ignition temperatures, and showed that the benefits derived from these mechanical activation processes with PTFE are more pronounced in nano-aluminum. Furthermore, the particle size phenomenon was further probed by Pantoya and Dean [413] which showed the lower-temperature exothermic reaction becomes more pronounced as the aluminum particle size is decreased, suggesting the specific surface area of the particle plays a critical role in the fluorination reaction. Combustion experiments performed by Hahma et al. [401] showed fluoride

coatings on aluminum particles accelerated combustion, especially in a carbon dioxide atmosphere, and even promoted combustion in an inert nitrogen atmosphere.

Dossi et al. [291, 294, 414-416] performed mechanical activation of micro-aluminum with PTFE and combusted the additive in HTPB fuel mixtures burning in gaseous oxygen at a mass loadings of 10%. A 10% loading of PTFE on the activated aluminum yielded negligible performance augmentation, while a 30% loading led to some regression rate enhancement but still less than the virgin micro-aluminum additive. Further experimentation showed that the activation process was more effective on nano-aluminum. [415] Current investigations are probing aluminum activated with magnesium additives.

An alternative means to increasing the reactivity of metal particles is through chemical coatings or passivation methods. Rosenband and Gany [417] developed a chemical deposition technique to coat aluminum particles with nickel, which were burned in nitrogen and air atmospheres. The coated particles did not agglomerate upon heating, unlike the plain aluminum particles, and they exhibited a lower ignition temperature which decreased with increasing nickel content (1-15%). Rosendband and Gany [418] also developed methods to coat aluminum particles with iron and to produce highly porous micro-particles with enhanced reactivity.

Liu et al. [419] measured burning rates and ignition delay times of AP/HTPB solid propellant samples containing 8% magnalium and 37% boron. The micro-boron particles were coated in LiF, Viton A, and silane. All three coatings led to reductions in burning rates, especially at lower pressures, but decreased the ignition delay time, which was most

prominent with the LiF-coated boron particles. Li and Jin [420] performed TGA/DSC studies coupled with optical ignition experiments on AP/HTPB-based propellants containing boron particles at atmospheric pressure to evaluate the effects of magnesium addition and coatings comprised of AP, KP, and LiF. The addition of magnesium was found to reduce the propellant ignition temperature, while the LiF-coated boron formulation outperformed all others in terms of burning rate and ignition delay time. Liu et al. [421] showed that fluorinated graphite could effectively increase the burning rates of AP/HTPB propellants containing boron micro-particles, which was strongly dependent on the additive particle size.

Experimental work completed at Purdue University [200-204] evaluated the combustion of DCPD containing nano-aluminum, PTFE-coated nano-aluminum, aluminum hydride (AlH_3), and sodium borohydride (NaBH_4) burning in gaseous oxygen and hydrogen peroxide (H_2O_2) flows. The PTFE-coated aluminum fuel samples did not yield any significant increase in regression rate over those loaded with uncoated aluminum. In contrast, lab-scale experiments conducted by Carmicino et al. [346-347] on HTPB fuels burning in GOX suggest that PTFE-coated nano-aluminum outperforms virgin nano-aluminum in terms of regression rate.

As previously discussed, Oleg et al. [355] evaluated the combustion of several composite solid propellant formulations containing various additives (AlB_2 , mixed micro-Al and micro-B, and AlB_2 coated in fluorine-substituted alloxisilane) at low pressures ($P < 2.5$ MPa). The coated additive formulation exhibited the lowest combustion efficiency and similar burning rates to the plain boron formulation.

Dr. Dreizin's group at NJIT has investigated numerous particle-coating technologies to enhance metal combustion processes. [394, 422-424] Vummidi et al. [422] evaluated a Ni-coated aluminum powder through constant-volume combustion experiments and thermal decomposition analyses, and they found that the coating yielded significantly reduced ignition delays, enhanced combustion rates, and increased oxidation efficiency. Zhang et al. [394] utilized reactive milling techniques to produce highly active, cyclooctane-coated aluminum particles which burned faster than similar oxide-coated particles, and exhibited significantly reduced ignition temperatures in a variety of atmospheric environments. Chintersingh et al. [423] modified the surface of boron particles by rinsing them in acetonitrile to dissolve the oxidized and hydrated surface layers and subsequently washing them with solutions to produce alternative protective coatings. The surface-modified boron particles were burned in an air-acetylene flame and exhibited similar burning times to the as-received particles but significantly shorter ignition delay times. Liu et al [424] further demonstrated that the surface-modified boron particles exhibited significantly reduced activation energies through thermal decomposition experiments.

Mach I Chemicals has developed proprietary methods to produce Mg-coated boron particles via reactive milling or vapor deposition processes. [425-426] Magnesium efficiently heats the boron particles and reduces the concentration of boron oxide at the particle surface. [426] Pace et al. [275] studied the combustion of HTPB fuels containing magnesium-coated boron particles in oxygen crossflow. Fuels containing the coated boron exhibited higher regression rates than plain boron due to heating from magnesium

oxidation at the boron surface. The coating's effects were prevalent at low pressures, but diminished at higher pressures due to the decrease in the relative amount of heat feedback generated from surface reactions. Furthermore, higher-magnesium-content coatings (10-20%) led to further enhancement of regression rate.

Paravan et al. [280] and Fanton et al. [287] performed hybrid rocket ballistic studies with both HTPB and paraffin fuels burning in GOX with various additives (micro-Al, nano-Al, Mg-coated B, C, TiO₂, palmitic acid-coated Al, and MgH₂), as previously discussed. The coated nano-aluminum did not outperform the plain nano-aluminum. The inclusion of magnesium-coated boron (2.8%) led to significantly more enhancement than moderate loadings (10%) of nano-aluminum in both fuels. The combination of low loadings of magnesium hydride (2.5%) and magnesium-coated boron (1.4%) yielded the largest regression rate enhancement. Qin et al. [289-290] evaluated HTPB loaded with the same magnesium-coated boron, as well as micro-scale magnesium and aluminum, and noted that all additive yielded a reduction in the ignition delay at higher pressures.

Sossi et al. [292] characterized polymeric fuels containing plain nano-aluminum and several types of coated nano-aluminum. Most of the aluminum was passivated with dry air and subsequently coated through a chemical suspension processes. Coating chemicals included octadecanoic acid; hexadecanoic acid; 1H,1H-perfluoro-1-undecanol (10:1 fluorotelomer alcohol); and Fluorel, a copolymer of vinylidene fluoride and hexafluoropropylene, combined with ester from esterification of 1H,1H-perfluoro-1-undecanol with furan-2,5-dione. Dynamic Scanning Calorimetry (DSC) and Thermal Gravimetric Analysis (TGA) experiments revealed some of the fluoride-based coatings

led to greater and more-efficient energy release. Combustion experiments in a hybrid rocket apparatus showed the fluoropolymer-coated aluminum formulations exhibited the highest regression rate enhancements. Furthermore, coating and suspension-separation processes for maximum combustion performance were identified. Gromov et al. [427] performed a similar DSC/TGA study with various non-inert coatings including nitrocellulose, oleic acid, stearic acid, boron, nickel, fluoropolymer, and ethanol. Gromov noted that non-oxide coatings can increase reactivity and combustion enthalpy but reduce the overall fuel content in the additive aluminum. The experimental results suggested boron-coated aluminum outperformed all others, but contradicted previous studies by suggesting fluoropolymers were ineffective in promoting reactivity.

2.4.2.7. Summary

In general, the combustion of solid fuels loaded with metal-based additives has been studied extensively. Pure metals, especially aluminum and boron, represent additives that can increase the energy density, and in most cases they have been reported to increase the mass generation and regression rates of fuel systems. Metal hydrides are more-reactive additives that have been more recently explored and show great promise in yielding high energy densities and combustion rates, but they are currently too expensive for implementation. Advanced synthesis strategies, such as reactive milling or chemical coating technologies, are currently being developed through various approaches and have the potential to significantly increase the viability of many metal-based additives.

2.5. Unconventional Geometries

An alternative means to ‘enhance’ a hybrid rocket design is to significantly alter its architecture by implementing an unconventional geometry. For instance, Lorente et al. [207, 428] designed a double-tube hybrid system with coaxial inner tube injectors distributed along the longitudinal axis, as shown in Figure 24. The hybrid motor fuel grain (HDPE) was burned in gaseous oxygen with the novel injection pattern and compared to a standard showerhead injector configuration. The inner-tube injector led to a 100% increase in regression rate and more-stable combustion but also yielded some uneven burning near the injector orifices.

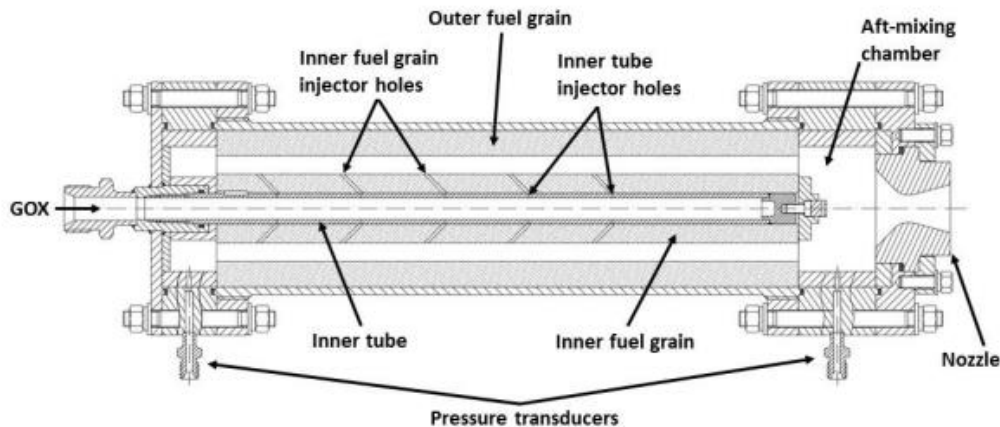


Figure 24. Double tube hybrid motor with internal distributed injection pattern. Image taken from Ref. [428].

Knuth et al. [429-431] evaluated the combustion of the vortex hybrid rocket engine configuration which is characterized by a coaxial, co-swirling, counter-flowing vortex combustion field, as shown in Figure 25. Ballistic testing was completed on a lab-scale rocket with HTPB/GOX which demonstrated regression rates that were 650% higher than classical hybrid systems. The observed regression rate enhancements were attributed to

significant increases in the heat transfer rates, as determined by an analysis of Stanton number ratios. The authors also demonstrated throttling and restart capabilities; observed no combustion instabilities; and developed theoretical and empirical models to predict regression rates in vortex hybrids.

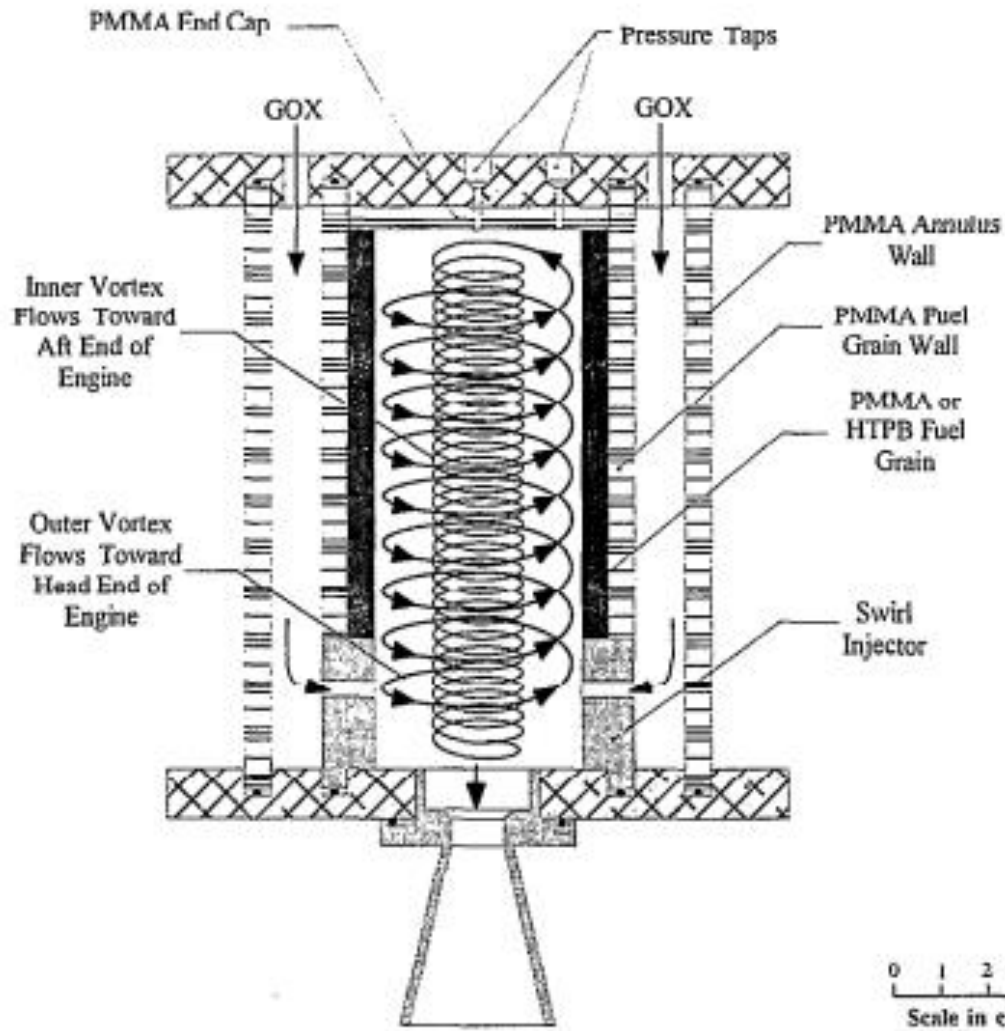


Figure 25. Schematic representation of the VH-20 vortex flow hybrid rocket engine. Image taken from Ref. [429].

Paravan et al. [432-433] have designed and built a lab-scale vortex flow pancake (VFP) hybrid rocket motor, as depicted in Figure 26. Paravan et al. [432] also give a state-of-the-art review regarding vortex combustion in HREs. The lab-scale rocket has been fired with both HTPB and paraffin fuels; has been utilized to determine the relative effects of oxidizer mass flow rate, pressure, and fuel slab height; and is currently being utilized to analyze forced, transient-burning phenomena.

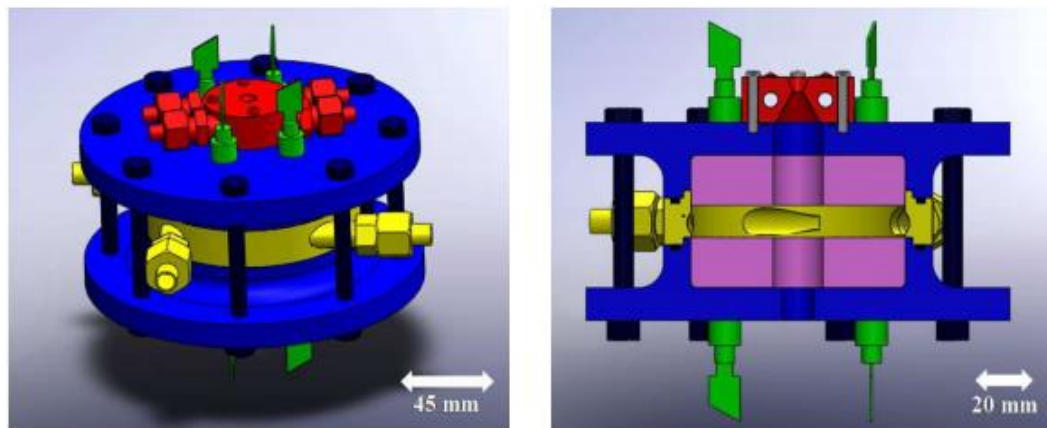


Figure 26. External and cross-section representation of the lab-scale vortex flow pancake hybrid developed at SPLab. Image taken from Ref. [432].

Chen et al. [434-440] have developed a numerical simulation capable of predicting the performance of VFP hybrids and validated it against experimental motor firings. The simulation has since been utilized to predict the performance of several oxidizer/fuel systems in the VHP hybrid configuration and to design a sounding rocket system.

Eilers et al. [141, 144] 3D-printed an ABS pancake-type motor that was built into a cubesat system which included vortex flow, N_2O regenerative cooling, a truncated aerospike nozzle, and secondary fluid injection. The as-built system for testing purposes is shown in Figure 27, has been test fired six times, and successfully demonstrated

performance capabilities. The system is capable of large impulse ΔV and small impulse attitude control maneuvers when designed into cubesat and nanosat systems.

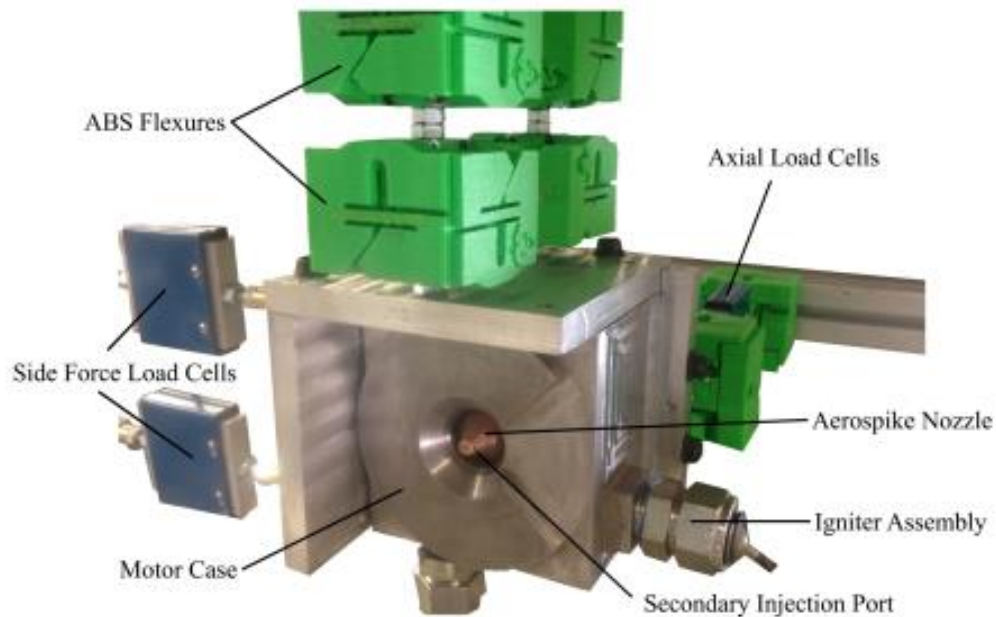


Figure 27. 3D-printed ABS pancake type motor with vortex flow, N_2O regenerative cooling, a truncated aerospike nozzle, and secondary fluid injection. Image taken from Ref. [141].

The end-burning, axial-flow hybrid configuration, shown in Figure 28, has been investigated by several researchers. [441-443] In this configuration, the oxidizer port diameter is sufficiently small such that the flame does not propagate along its longitudinal axis but burns at the aft-end. The end-burning configuration has large potential in hybrid rocket applications since it is more controllable, burns evenly, and yields high volumetric efficiency.

Researchers at Hokkaido University [442-448] have investigated the combustion behavior of end-burning hybrids at various operating conditions to evaluate conditions of

flame spreading, blowoff, and stable end-burning combustion. The authors have successfully demonstrated motor firings under numerous operating conditions, established the capability for thrust augmentation, and developed a model for prediction of fuel flow based upon the granular diffusion flame model which calculates the regression rate's dependency based upon chamber pressure rather than oxidizer mass flow.

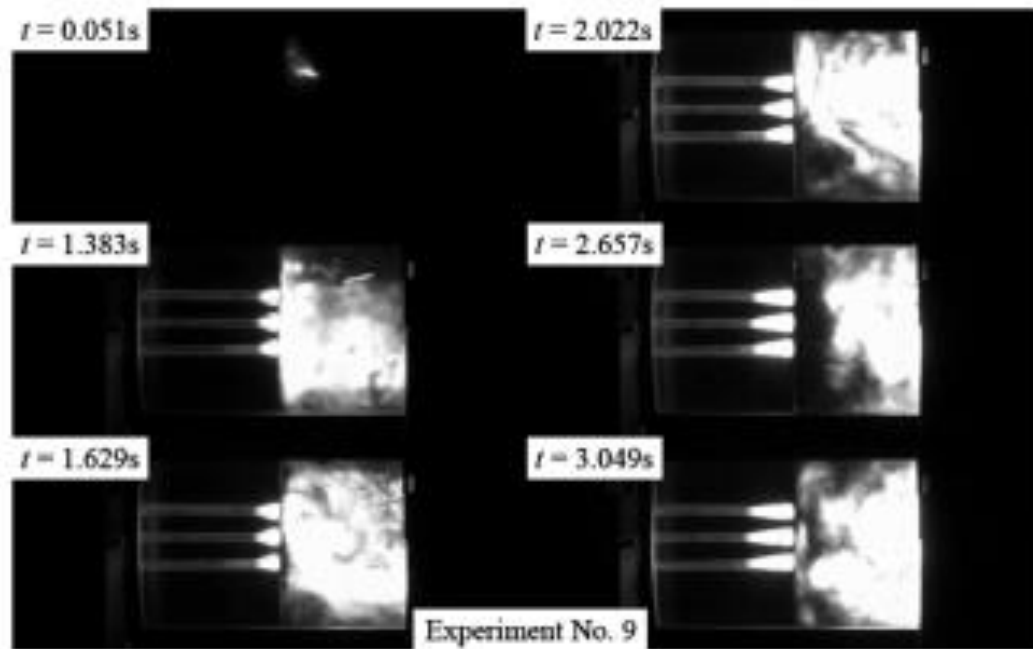


Figure 28. End-burning, axial flow hybrid rocket motor configuration during combustion. Image taken from Ref. [441].

Li et al. [441] fired several end-burning motors based on PMMA in gaseous oxygen to study the flame spreading, blowoff, and regression rate behavior. Li et al. [441] determined that the combustion behavior transitions from side-burning, to opposed-propagating, and to end-burning modes as the oxygen velocity is increased above critical values. Li et al. [441] also noted that the regression rates measured in their system were significantly lower than those measured for traditional hybrid rocket configurations.

Hitt and Frederick [449-453] of the University of Alabama Huntsville evaluated the combustion behavior of a similar end-burning hybrid motor configuration but with porous fuel grains instead of grains with small fuel ports. Small-scale, porous polyethylene fuel grains were burned in gaseous oxygen and nitrous oxide flows. Experimentally measured regression rates were up to 350% larger than the nominal hybrid motor configuration. A granular diffusion flame model was adapted to simulate the combustion mechanism of the fuel grains, and the results indicated diffusion, and not kinetics, dominates the combustion process.

Fuller [215-218] of the Aerospace Corporation was amongst the first to work with 3D-printed fuel grains for hybrid rocket applications. Recent work by Fuller [218] has focused on the production of 3D-printed fuel grains which incorporate passive fuel storage inside of the fuel grain and release a secondary fuel during combustion. An example of such a geometry is shown in Figure 29.

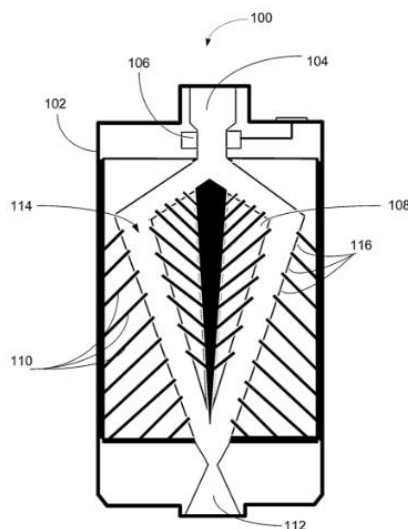


Figure 29. 3D-printed fuel grain with secondary liquid fuel storage compartments for passive thrust control. Image taken from Ref. [218].

3. THEORETICAL PERFORMANCE ANALYSES

3.1. Stoichiometric Combustion

The stoichiometric reactions of plain HTPB, pure metals, and mixtures thereof with pure oxygen are considered within this section. For any reaction, the heat of reaction, ΔH_R^0 , is defined as the energy released or absorbed when products are formed from reactants at standard reference conditions (25 °C, 1 atm). The heat of reaction can be negative or positive which indicates an exothermic or endothermic reaction, respectively. Additionally, the heat of reaction can be calculated for reactions occurring at non-standard temperatures and pressure by accounting for changes in the enthalpy of the reactants and products due to these variations in conditions. In general, the heat of reaction at standard conditions is written as the total enthalpy of the products minus the reactants:

$$\Delta H_R^0 = \sum(n_i \Delta H_{f,i}^0)_{Products} - \sum(n_i \Delta H_{f,i}^0)_{Reactants} \quad (3)$$

where n_i and $\Delta H_{f,i}^0$ are the stoichiometric coefficient and heat of formation of the i th species, respectively. The heat of formation, ΔH_f^0 , of a substance is the energy released or absorbed when 1 mol of the substance is formed from its constituent elements at standard reference conditions (25 °C, 1 atm). Heats of formation are typically determined experimentally, but can also be theoretically computed for some compounds.

In general, idealized stoichiometric combustion reactions involving hydrocarbons and metals reacting with oxygen (O_2) yield product species including only H_2O , CO_2 , and M_xO_y with no residual oxygen. M_xO_y represents a generalized metal oxide consisting of x atoms of the metal, M , and y atoms of oxygen, O . The heat of combustion, ΔH_c^0 , of a

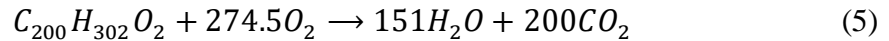
substance is the energy released when the substance undergoes complete, stoichiometric combustion with oxygen at standard conditions. The heat of combustion is a measure of specific energy production (per mass, volume, or mole of reactant) for a given substance and can be written as:

$$\Delta H_c^0 = -\Delta H_R^0 \quad (4)$$

where a positive or negative value indicates an exothermic or endothermic reaction, respectively.

3.1.1. Plain HTPB Reacting with Oxygen

The polymer fuel utilized herein is HTPB R-45M produced by Cray Valley. The molecular weight, density, and heat of formation of HTPB is dependent upon the manufacturer, variant, and curative, among other factors, and the reported values for these properties vary within the literature. The ‘model’ version of HTPB utilized for theoretical calculations herein is represented by the chemical formula $C_{200}H_{302}O_2$ with a density and heat of formation of 900 kg/m^3 and -240 kJ/mol , respectively. Therefore, the stoichiometric combustion equation for HTPB is given by:



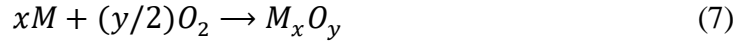
The heat of combustion is then given by:

$$\Delta H_c^0 = (\bar{h}_{f,C_{200}H_{302}O_2}^0 + 274.5\bar{h}_{f,O_2}^0) - (151\bar{h}_{f,H_2O}^0 + 200\bar{h}_{f,CO_2}^0) \quad (6)$$

and is calculated to be 42.0 kJ/g or 37.8 kJ/cm^3 .

3.1.2. Plain Metals Reacting with Oxygen

The stoichiometric combustion reaction for a generalized metal, M , yielding a generalized metal oxide, M_xO_y , is given by:



The heat of combustion of this generalized metal combustion reaction is given by:

$$\Delta H_c^0 = -(1/x)\bar{h}_{f,M_xO_y}^0 \quad (8)$$

since the standard heat of formation of oxygen gas and pure metals are zero at the standard reference conditions.

In general, the oxide of a metal can take several forms, but has a preferential form at standard conditions. The heats of combustion of selected metals have been calculated with Equation (8) by assuming stoichiometric combustion with oxygen yielding the corresponding preferential metal oxide, and are shown in Table 2 alongside that of HTPB. Additionally, the molecular weight, density, melting temperature, and boiling temperature of the metals, and the density, melting temperature, and boiling temperature of the metal oxides have been compiled from JANNAF and NIST databases, and are shown in Table 2. These specific parameters are important to consider in combustion applications because they can drive the theoretical and delivered performance of metal-loaded fuel systems.

Table 2. Material property and combustion performance data for HTPB and pure metals.

Form	Fuel				Final Oxide				Performance				
	MW (g/mol)	ρ (g/cm ³)	T _m (K)	T _b (K)	Form	ρ (g/cm ³)	T _m (K)	T _b (K)	ΔH_f^0 (kJ/mol)	$\Delta H_{\text{Combustion}}$ (kJ/mol)	(kJ/g)	(kJ/cm ³)	
Aluminum	Al	26.98	2.70	933	2792	Al ₂ O ₃	3.99	2327	3253	-1676	838	31.1	83.8
Boron	B	10.81	2.37	2348	4273	B ₂ O ₃	2.55	723	2133	-1272	636	58.8	139.4
Beryllium	Be	9.01	1.85	1560	2742	BeO	3.01	2780	4170	-608	608	67.5	124.9
Carbon	C	12.01	2.27	3925	-	CO ₂ (g)	0.002	217	195	-394	394	32.8	74.3
Chromium	Cr	52.00	7.19	2180	2944	Cr ₂ O ₃	5.220	2708	4270	-1135	567	10.9	78.5
Cobalt	Co	58.93	8.90	1768	3200	CoO	6.440	2206	-	-238	238	4.0	35.9
Copper	Cu	63.55	8.96	1358	2835	Cu ₂ O	6.00	1505	2070	-171	85	1.3	12.0
Iron	Fe	55.85	7.87	1811	3134	Fe ₂ O ₃	5.24	1825	-	-824	412	7.4	58.1
Lithium	Li	6.94	0.53	454	1603	Li ₂ O	2.01	1711	2870	-599	299	43.1	23.0
Magnesium	Mg	24.31	1.74	923	1380	MgO	3.60	3098	3870	-601	601	24.7	43.0
Manganese	Mn	54.94	7.21	1519	2334	Mn ₃ O ₄	4.86	1840	3120	-1387	462	8.4	60.7
Nickel	Ni	58.69	8.91	1728	3003	NiO	6.67	2228	-	-240	240	4.1	36.4
Silicon	Si	28.09	2.33	1687	3538	SiO ₂	2.65	1986	3220	-911	911	32.4	75.5
Tin	Sn	118.71	7.27	505	2875	SnO ₂	6.90	1900	2120	-578	578	4.9	35.4
Titanium	Ti	47.87	4.51	1941	3560	TiO ₂	4.23	2116	3245	-945	945	19.7	89.0
Tungsten	W	183.84	19.35	3695	6203	WO ₃	7.16	1746	1970	-843	843	4.6	88.7
Vanadium	V	50.94	6.00	2183	3680	VO	5.76	2062	2900	-432	432	8.5	50.9
Zinc	Zn	65.38	7.14	693	1180	ZnO	5.61	2248	2360	-350	350	5.4	38.3
Zirconium	Zr	91.22	6.52	2128	4650	ZrO ₂	5.68	2988	4570	-1097	1097	12.0	78.4
HTPB	C ₂₀₀ H ₃₀₂ O ₂	2738.54	0.90	514	-	-	-	-	-	-	114980	42.0	37.8

The relative heats of combustion of the selected metals and HTPB are shown in the top chart of Figure 30. The solid and striped bars represent the gravimetric and volumetric heats of combustion of each compound, respectively. The volumetric heat of combustion of most metals is larger than that of HTPB and the gravimetric heat of combustion is larger for some metals (B, Be, and Li). Accordingly, including metals in fuel formulations with HTPB not only leads to higher specific impulse at some O/F ratios (from increased energy release and flame temperature), but also higher density impulse.

The relevant melting and boiling temperatures of the selected metals and HTPB are shown in bottom chart of Figure 30. The melting and boiling temperature of pure metals and the melting and boiling temperatures of their respective metal oxides are represented by solid, striped, dotted, and dashed bars, respectively. The melting and boiling temperature of some metals and/or their respective metal oxides is significantly

higher than others. High melting and boiling temperature of either the metal or its respective oxide can inhibit efficient ignition and combustion of the metal. Hence, it is important to consider these when evaluating the theoretical performance of metal combustion, as well.

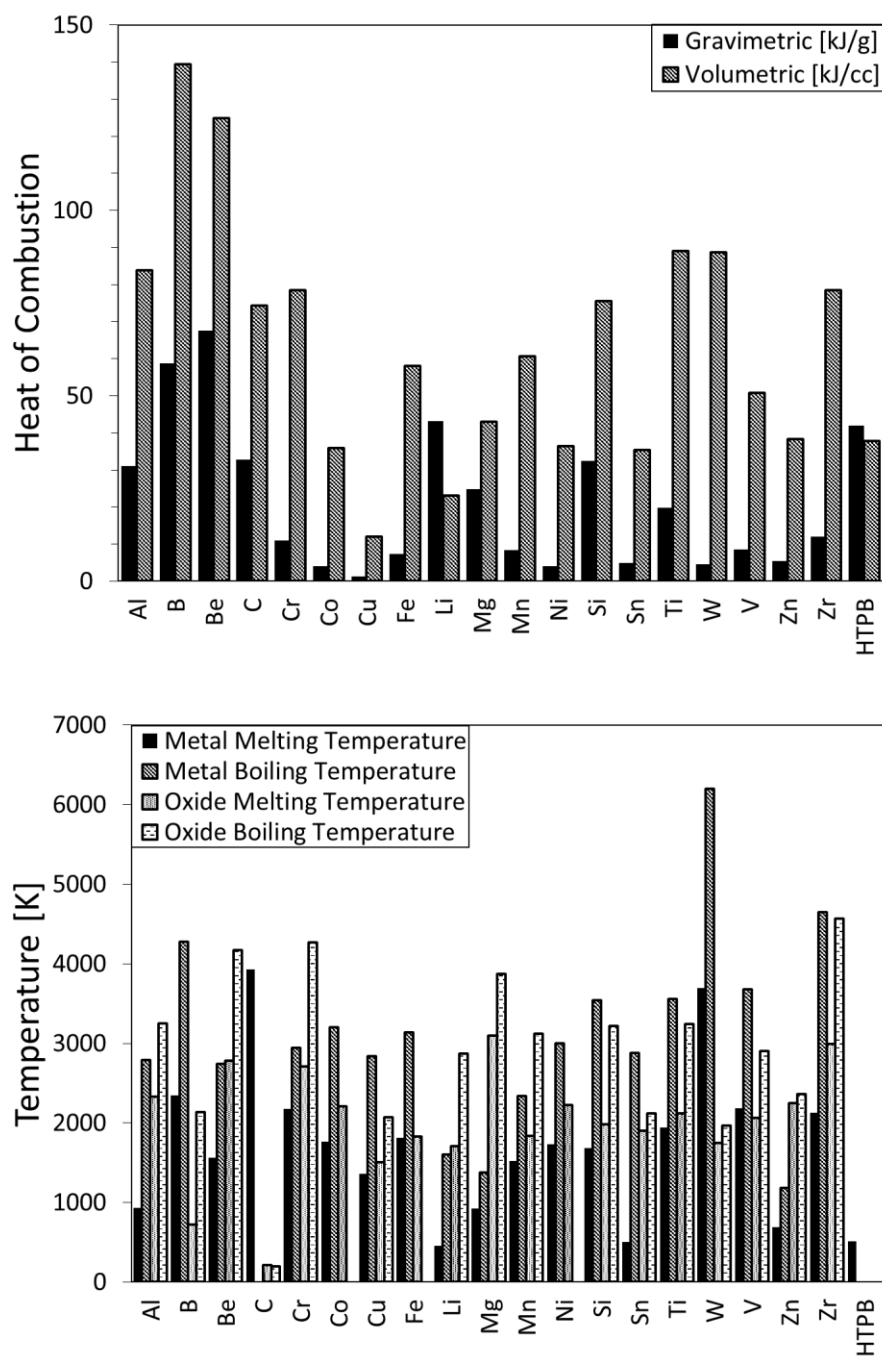
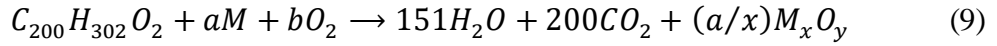


Figure 30. Theoretical performance for HTPB and pure metals combusting with stoichiometric oxygen. Charts depict (top) gravimetric and volumetric heat of combustion and (bottom) melting and boiling temperature of pure metals and their respective oxides.

3.1.3. Metal-Loaded HTPB Reacting with Oxygen

Stoichiometric combustion equations can be derived for HTPB fuel loaded with metals by combining the two previously given reaction equations. This process is generalized for HTPB loaded with a metal (M), as follows. The generalized stoichiometric combustion equation for HTPB loaded with a metal at a mass loading of α_M (i.e. for 50% loading, $\alpha_M = 0.50$) is given by:



where a and b can be written as:

$$a = [\alpha_M/(1 - \alpha_M)](\mathfrak{M}_{HTPB}/\mathfrak{M}_M) \quad (10)$$

$$b = (ay + 549)/2x \quad (11)$$

where \mathfrak{M}_{HTPB} and \mathfrak{M}_M are the molecular weights of HTPB and M , respectively, which are given in Table 2. The heat of combustion of this reaction is then given by:

$$\Delta H_c^0 = (\bar{h}_{f,C_{200}H_{302}O_2}^0 + a\bar{h}_{f,M}^0 + b\bar{h}_{f,O_2}^0) - [151\bar{h}_{f,H_2O}^0 + 200\bar{h}_{f,CO_2}^0 + (a/x)\bar{h}_{f,M_xO_y}^0] \quad (12)$$

which can be reduced to:

$$\Delta H_c^0 = \bar{h}_{f,C_{200}H_{302}O_2}^0 - (a/x)\bar{h}_{f,B_2O_3}^0 \quad (13)$$

since the heats of formation of M , O_2 , H_2O , and CO_2 are zero at the standard reference conditions. The stoichiometric oxidizer-to-fuel mass ratio, $(O/F)_s$, can be written as:

$$\left(\frac{O}{F}\right)_s = \left(\frac{m_{ox}}{m_f}\right)_s = \left[\frac{N_{O_2}\mathfrak{M}_{O_2}}{(N_{HTPB}\mathfrak{M}_{HTPB} + N_B\mathfrak{M}_B)}\right]_s \quad (14)$$

where m_{ox} and m_f are the masses of oxidizer and fuel involved in the reaction, respectively; N_{O_2} , N_{HTPB} , and N_M are the moles of O_2 , HTPB, and M involved in the

reaction, respectively; and \mathfrak{M}_{O_2} is the molecular weight of O_2 (32.00 g/mol).

Accordingly, the stoichiometric oxidizer-to-fuel mass ratio can be written as:

$$\left(\frac{O}{F}\right)_s = \frac{b\mathfrak{M}_{O_2}}{(\mathfrak{M}_{HTPB} + a\mathfrak{M}_M)} \quad (15)$$

The fuel densities, stoichiometric O/F ratios, and gravimetric and volumetric heats of combustion for aluminum-loaded and boron-loaded HTPB fuels burning in pure oxygen are shown in the top and bottom plots of Figure 31, respectively. The fuel densities for both metal-loaded formulations increase with increasing metal loading due to the comparatively high densities of the metals. The stoichiometric O/F ratios decrease with increasing metal loading, indicating less oxygen is required to yield complete combustion metal-loaded fuels. The volumetric and gravimetric heats of combustion increase and decrease with increasing aluminum loading, respectively, since these parameters are greater than and less than that of HTPB, respectively. Both the gravimetric and volumetric heat of combustion increases with increasing boron loading. This trend is more prevalent in the volumetric heat of combustion due to the high density of boron (2.37 g/cm³) in comparison to HTPB (0.90 g/cm³). It is worth noting that a similar set of trends can be derived for most metal-loaded HTPB fuels which results in analogous trends.

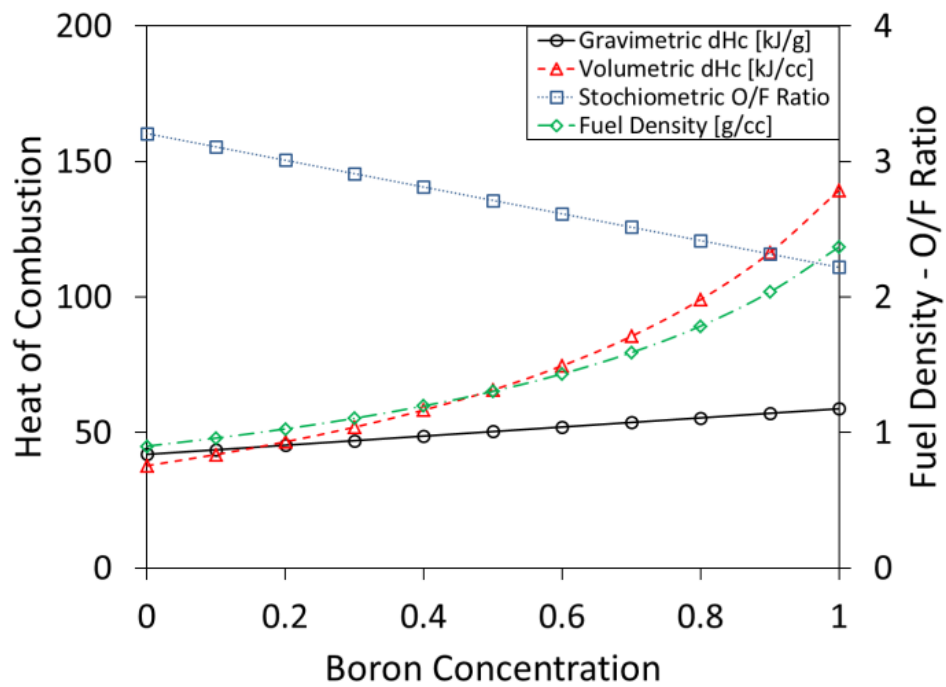
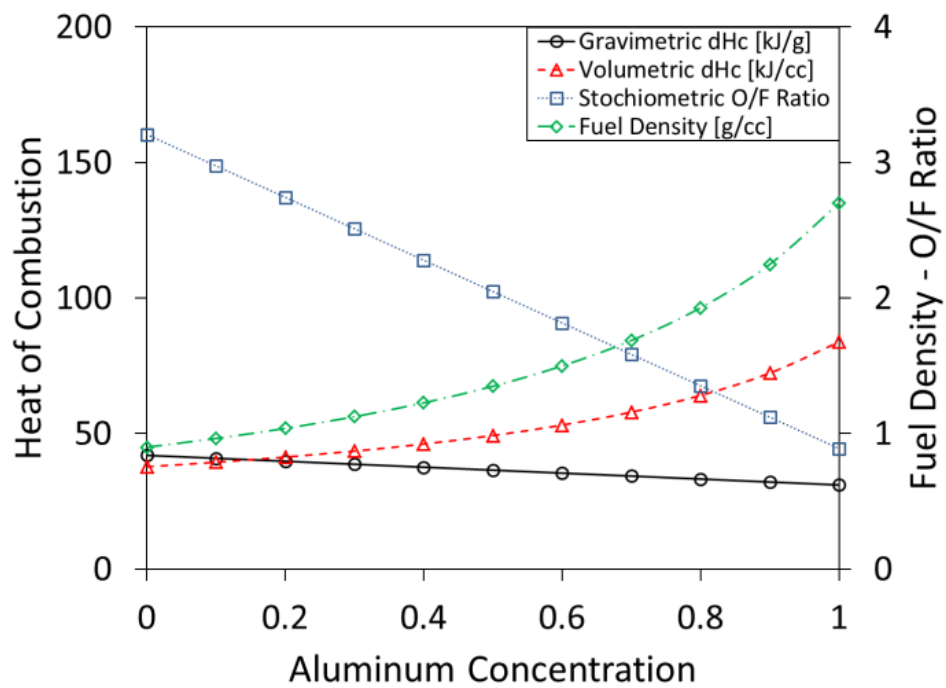


Figure 31. Theoretical heat of combustion and stoichiometric O/F ratios for (top) aluminum-loaded and (bottom) boron-loaded HTPB burning in pure oxygen.

3.2. Chemical Equilibrium Analyses

In real-world combustion systems, complete combustion is not achieved because many other species are formed during reactions. Chemical equilibrium of a reacting system is the state at which the forward reaction rate of forming products is equal to the reverse reaction rate of forming reactants from the products. Chemical equilibrium analyses can be utilized to compare the theoretical performance of propellant formulations and combinations. These computations are typically performed by minimizing the Gibbs free energy of a reacting system and are capable of yielding the theoretical composition and thermodynamic condition of the system at equilibrium. Chemical equilibrium computations presented herein were completed with NASA's CEA which references a large thermodynamic and transport property database containing over 2,000 chemical species. [454-455]

The performance parameters of interest discussed herein include the specific impulse and density impulse. The specific impulse of a propellant, I_{sp} , is the total impulse (*Thrust Force x Time*) per unit weight and is a common figure of merit of performance in rocket propulsion systems. The theoretical specific impulse of propellants are determined through chemical equilibrium analyses, which can be utilized to compare alternative propellant formulations and combinations. The density impulse of a propellant, I_d , is the total impulse per unit volume and can be a more applicable figure of merit for volume-limited propulsion applications. The density specific impulse of a propellant is given by:

$$I_d = \delta_p I_{sp} \quad (16)$$

where δ_p is the specific gravity of the propellant combination. The density of a metal-loaded fuel containing HTPB and some metal, M , is given by:

$$\rho_f = \left[\frac{1-\alpha_M}{\rho_{HTPB}} + \frac{\alpha_M}{\rho_M} \right]^{-1} \quad (17)$$

where ρ_{HTPB} and ρ_M are the density of HTPB and the metal, respectively. The density of the fuel/oxidizer combination, or the propellant density, can be determined in a similar manner. The oxidizer density, ρ_{ox} , is taken as the density of liquid oxygen (LOX, 1141 kg/m³) or nitrous oxide (N₂O, 1976 kg/m³) herein. The density impulse can then be written as:

$$I_d = \frac{\delta_{ox}\delta_f(1+O/F)}{\delta_f(O/F)+\delta_{ox}} I_{sp} \quad (18)$$

where δ_{ox} and δ_f are the specific gravity of the oxidizer and fuel system, respectively.

In the following sections, the theoretical performance of HTPB loaded with various metals, with special emphasis on aluminum and boron, is analyzed through chemical equilibrium computations. Firstly, the theoretical performance is compared for HTPB fuel loaded with selected metals at a mass concentration of 50% reacting with pure oxygen or nitrous oxide, and general conclusions are drawn about the potential for these metals in HRE and SFRJ applications. Further computations are completed regarding the theoretical performance of HTPB fuel loaded with aluminum or boron at various concentrations to elucidate some important trends.

3.2.1. HTPB Loaded with Selected Metals

The performance parameters of plain HTPB and HTPB fuels loaded with metals at a concentration of 50% burning in oxygen at a pressure of 1,000 psia with frozen

composition have been computed and the vacuum specific impulse, density impulse, characteristic velocity, and adiabatic flame temperature of these propellant systems is plotted against the O/F ratio in Figure 32. Each fuel formulation is represented by a unique line in these plots, as indicated in the figure legends. In general, the addition of metals to HTPB burning in oxygen leads to: 1) a decrease in the maximum specific impulse, 2) an increase in the maximum density impulse, 3) a decrease in the maximum characteristic velocity, and 4) an increase in maximum adiabatic flame temperature. The notable exception to this general trend is lithium, which leads to a decrease in all of these performance measures. The addition of metals also shifts the maximum performance condition to lower O/F ratios, which could potentially allow for smaller oxidizer tanks in vehicle designs. The greatest density impulse values are obtained for fuels containing zirconium (Zr), titanium (Ti), aluminum (Al), tungsten (W), boron (B), chromium (Cr), nickel (Ni), beryllium (Be), silicon (Si), magnesium (Mg), and lithium (Li), in that respective order.

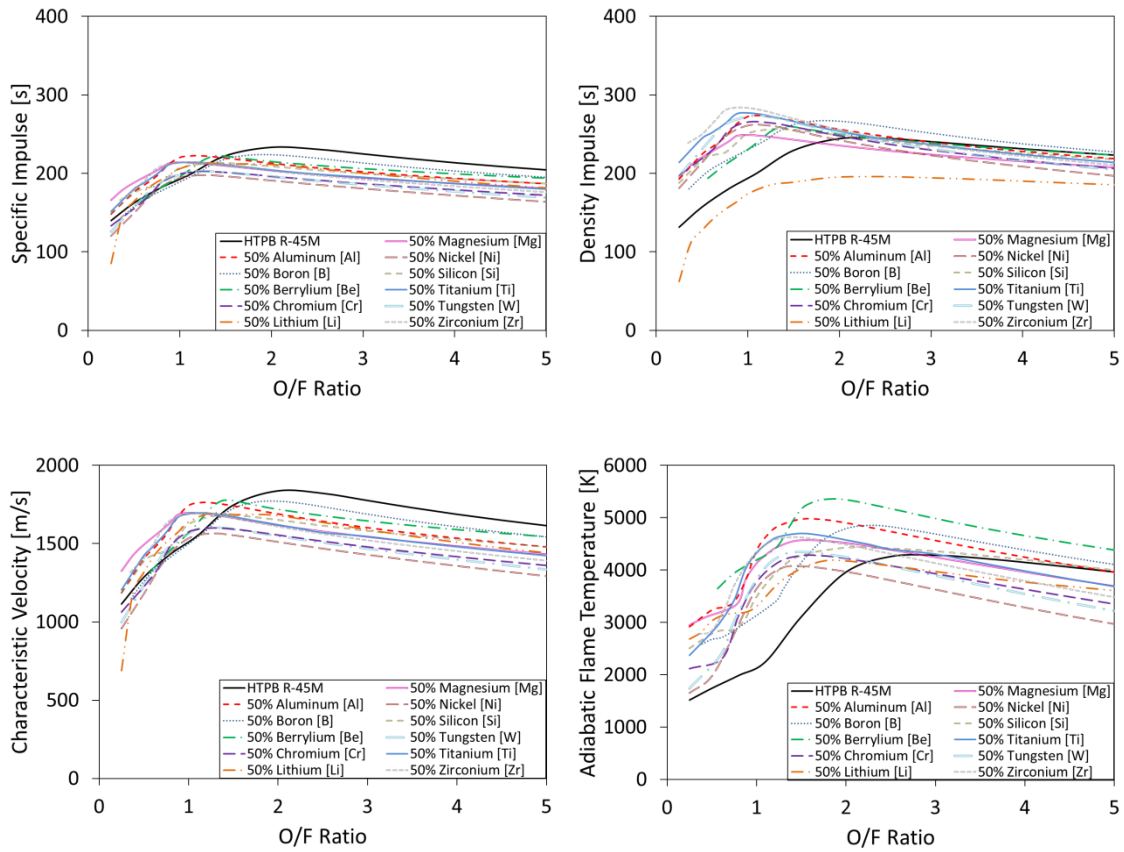


Figure 32. Theoretical performance of HTPB R-45M fuel loaded with selected metals at a mass concentration of 50% burning in oxygen gas (O_2). Plots depict (top left) specific impulse, (top right) density impulse, (bottom left) characteristic velocity, and (bottom right) adiabatic flame temperature as calculated with NASA’s CEA at 1,000 psia.

An analogous set of calculations has been completed for plain HTPB and HTPB fuels loaded with metals at a concentration of 50% burning in nitrous oxide at a pressure of 1,000 psia with frozen composition and the performance parameters of these propellant systems is plotted against the O/F ratio in Figure 33. In general, the addition of metals to HTPB burning in oxygen leads to: 1) an increase or decrease in the maximum specific impulse, 2) an increase in the maximum density impulse, 3) an increase or decrease in the maximum characteristic velocity, and 4) an increase in maximum adiabatic flame

temperature. The notable exception to this general trend is lithium, which leads to a decrease in all of these performance measures. Once again, the addition of metals also shifts the maximum performance condition to lower O/F ratios, which could potentially allow for smaller oxidizer tanks in vehicle designs. The greatest density impulse values are obtained for fuels containing beryllium (Be), boron (B), zirconium (Zr), aluminum (Al), titanium (Ti), tungsten (W), chromium (Cr), nickel (Ni), silicon (Si), magnesium (Mg), and lithium (Li), in that respective order.

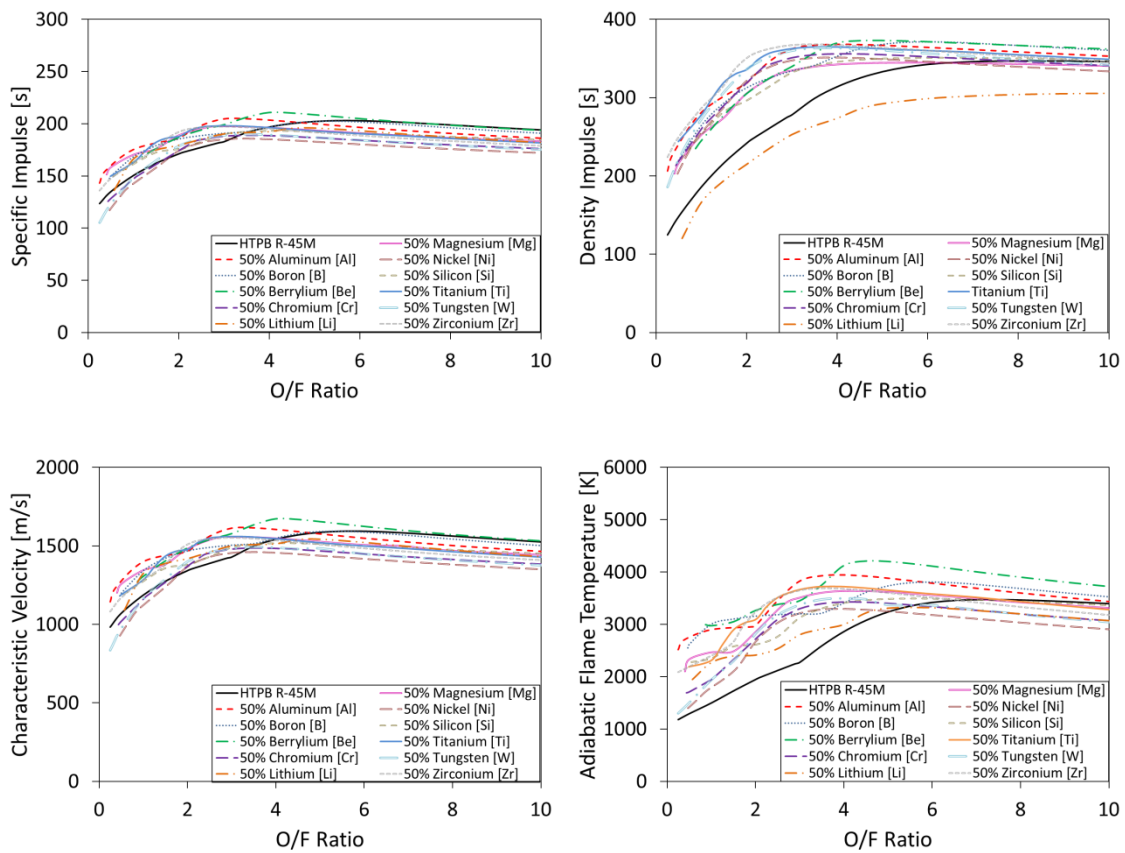


Figure 33. Theoretical performance of HTPB R-45M fuel loaded with selected metals at a mass concentration of 50% burning in nitrous oxide (N_2O). Plots depict (top left) specific impulse, (top right) density impulse, (bottom left) characteristic velocity, and (bottom right) adiabatic flame temperature as calculated with NASA’s CEA at 1,000 psia.

3.2.2. HTPB Loaded with Aluminum or Boron

The maximum specific impulse and density specific impulse, and the corresponding O/F ratios at which they occur, have been calculated for HTPB loaded with various concentrations of aluminum or boron burning in oxygen at a pressure of 1,000 psia with frozen composition. The maximum obtainable performance parameters are plotted against metal concentration for aluminum- and boron-loaded HTPB in the top plots of Figures 34 and 35, respectively. Although the maximum specific impulse decreases with increasing metal loading, the maximum density specific impulse increases due to the higher density of the metals in comparison to HTPB. The corresponding O/F ratios at which the maximum performance parameters occurs is plotted against metal concentration for aluminum- and boron-loaded HTPB in the bottom plots of Figures 34 and 35, respectively, along with the stoichiometric O/F ratio. The required O/F ratio to yield maximum performance decreases with increasing metal loading which translates to lower required oxidizer tank mass for a given vehicle design. This trend is more pronounced with aluminum-loaded HTPB.

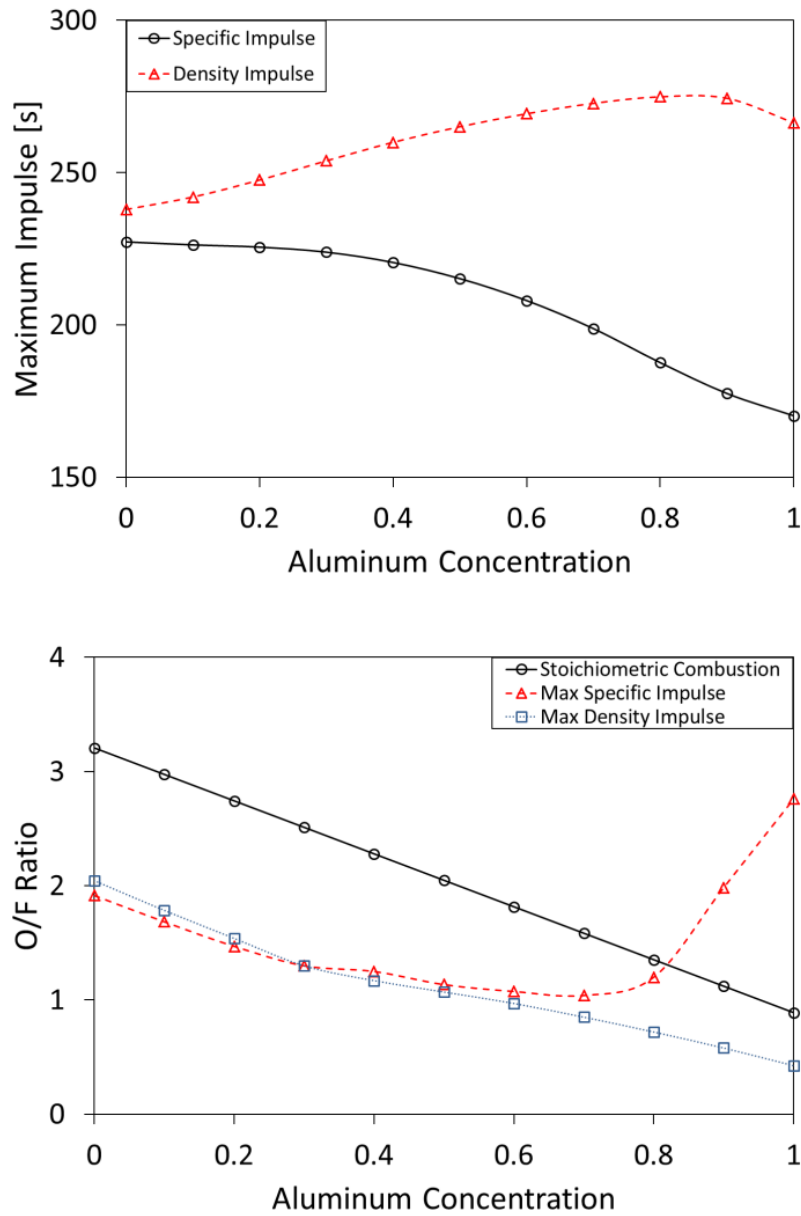


Figure 34. Theoretical performance of HTPB R-45M fuel loaded with various concentrations of aluminum burning in oxygen gas (O_2). Plots depict (left) the maximum specific and density impulse, and (right) oxidizer-to-fuel ratios corresponding to the maximum performance condition for several merits of performance. Calculations were completed with NASA's CEA at 1,000 psia.

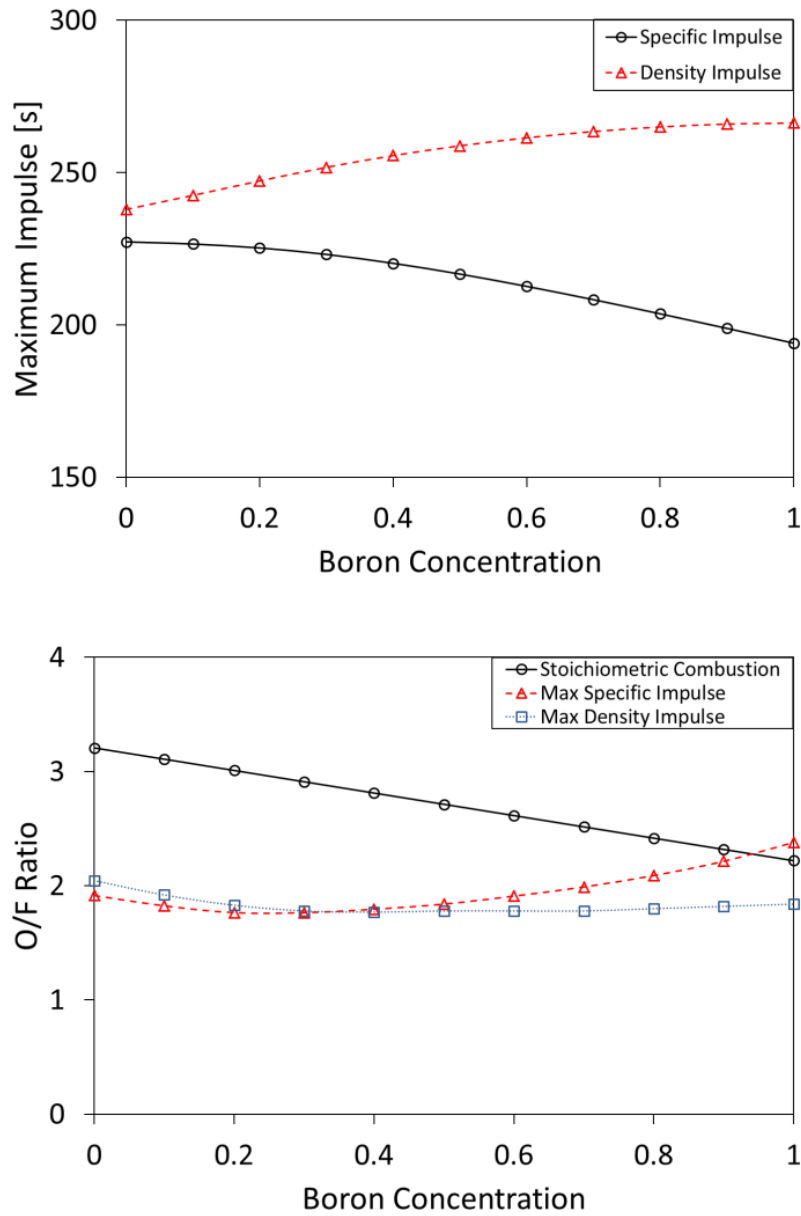


Figure 35. Theoretical performance of HTPB R-45M fuel loaded with various concentrations of boron burning in oxygen gas (O_2). Plots depict (left) the maximum specific and density impulse, and (right) oxidizer-to-fuel ratios corresponding to the maximum performance condition for several merits of performance. Calculations were completed with NASA's CEA at 1,000 psia.

4. HYBRID ROCKET PERFORMANCE MODEL

To size the experimental fuel grain designed herein, a state-of-the-art hybrid rocket performance model based on first principles has been developed and is derived, as follows. The basic geometry of the hybrid rocket design under analysis is shown in Figure 36. In the hybrid rocket diagram, P_T is the pressure of the oxidizer tank, \dot{m}_{ox} is the oxidizer mass flow rate, ρ_f is the density of the solid fuel which undergoes pyrolysis at a fuel mass loss rate of \dot{m}_f , r_f is the radius of the cylindrical combustion port which increases at the radial regression rate of \dot{r} , T_c and P_c are the temperature and pressure of the combustion products inside of the rocket chamber, L_f is the length of hybrid motor fuel grain, A_c is the cross-sectional area of the combustion port, A_b is the surface area of the combustion port, A_t and A_e are the cross-sectional areas of the nozzle throat and exit, and \dot{m}_e is the total mass flow rate of combustion products exhausting through the nozzle. The oxidizer mass flow rate and chamber pressure can be precisely controlled through detailed design of the injector and oxidizer tank systems. These two quantities are considered constant throughout a motor firing for modeling purposes. The cross-sectional and surface area of the combustion port are given by:

$$A_c = \pi r_f^2 \quad (19)$$

$$A_b = 2\pi r_f L_f \quad (20)$$

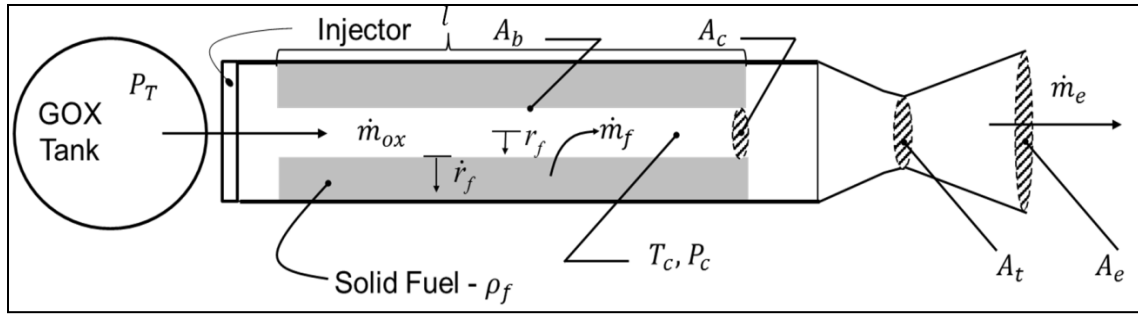


Figure 36. Diagram of a hybrid rocket propulsion system with key features illustrated.

The propulsive thrust force in chemical rockets is derived from accelerating and ejecting combustion products through a nozzle. A detailed derivation of a chemical rocket's thrust force is given by Sutton and Biblarz [11] and can be written as:

$$F = F_f + F_p = \dot{m}_e V_e + (P_e - P_{atm})A_e \quad (21)$$

where F_f and F_p represent the thrust force developed by mass flow and pressure, respectively; \dot{m}_e is total propellant mass flow rate; V_e is the exit velocity of exhaust products; P_e and P_{atm} are the exit and atmospheric pressures, respectively; and A_e is the exit area of the nozzle.

Equation (21) can be manipulated to render it in a more useful form. The ideal rocket model is used for our analysis which assumes the working substance, or chemical combustion products, are homogenous; all of the species of the working fluid are in the gas phase and obey the ideal gas law; the flow is adiabatic; friction and boundary layers effects are negligible; there are no shockwaves or discontinuities in the flow; propellant flow is steady and constant; exhaust gases are uniform across any cross-sectional area; all flow is axially directed; chemical equilibrium is established in the combustion chamber and is frozen in the nozzle flow; and stored propellants are at room temperature. [54]

Assuming that the rocket behaves in a quasi-steady state manner, so that expansion is uniform and steady and transient effects can be neglected, allows the mass flow rate through the system to be defined as:

$$\dot{m} = \dot{m}_e = \dot{m}_t = \dot{m}_f + \dot{m}_{ox} = \frac{A_t V_t}{v_t} \quad (22)$$

where A_t is the nozzle throat area, V_t is the flow velocity at the nozzle throat, and v_t is the specific volume of the working fluid at the nozzle throat. Accordingly, Equation (21) can be written as:

$$F = \frac{A_t V_t V_e}{v_t} + (P_e - P_{atm}) A_e \quad (23)$$

Flow through the nozzle is assumed to be isentropic and choked at the throat, so that many useful isentropic flow relations can be invoked. For this case, the exit velocity of the flow is given by:

$$V_e = \sqrt{\left(\frac{2\gamma}{\gamma-1}\right) RT_c \left[1 - \left(\frac{P_e}{P_c}\right)^{\frac{\gamma-1}{\gamma}}\right]} + V_c^2 \quad (24)$$

where R and γ are the ideal gas constant and specific heat ratio for the combustion product mixture, respectively, and V_c is the velocity of the combustion products within the combustion chamber. The velocity of the combustion products within the combustion chamber will be small relative to that within the nozzle, so that V_c can be neglected in Equation (24). The specific volume and velocity of the flow at the nozzle throat are given by isentropic relations and are written as:

$$v_t = v_c \left(\frac{\gamma+1}{2}\right)^{\frac{1}{\gamma-1}} \quad (25)$$

$$V_t = \sqrt{\frac{2\gamma}{\gamma+1} RT_c} \quad (26)$$

It is worth noting that since the flow is choked at the nozzle throat, the Mach number at this point is one and the velocity is equal to the speed of sound in the combustion products. Other useful isentropic flow equations for analysis of the rocket system are the pressure and area ratios across the diverging section of the nozzle which are given by:

$$\frac{P_c}{P_e} = \left[1 + \frac{\gamma-1}{2} (M_e)^2 \right]^{\frac{\gamma}{\gamma-1}} \quad (27)$$

$$\epsilon = \frac{A_e}{A_t} = \left(\frac{1}{M_e} \right) \left\{ \frac{2}{\gamma+1} \left[1 + \frac{\gamma-1}{2} (M_e)^2 \right] \right\}^{\frac{\gamma+1}{2(\gamma-1)}} \quad (28)$$

where M_e is the exit Mach number and ϵ is defined as the nozzle expansion ratio. Recall that the combustion products are assumed to behave as an ideal gas, which is reasonable given their high temperatures. Accordingly, the ideal gas relation applies and is written as:

$$P_c = \rho_c RT_c \quad (29)$$

Combining Equations (24)-(26) and (28) with Equation (23) and rearranging yields:

$$F = A_t P_c \sqrt{\left(\frac{2\gamma^2}{\gamma-1} \right) \left(\frac{2}{\gamma+1} \right)^{\frac{\gamma+1}{\gamma-1}} \left[1 - \left(\frac{P_e}{P_c} \right)^{\frac{\gamma-1}{\gamma}} \right]} + (P_e - P_{atm}) A_e \quad (30)$$

The thrust coefficient is a dimensionless value that can be used to analyze rocket performance as a function of the specific heat ratio, nozzle area ratio, and pressure ratio across the nozzle and is defined by:

$$C_F = \frac{F}{P_c A_t} = \sqrt{\left(\frac{2\gamma^2}{\gamma-1} \right) \left(\frac{2}{\gamma+1} \right)^{\frac{\gamma+1}{\gamma-1}} \left[1 - \left(\frac{P_e}{P_c} \right)^{\frac{\gamma-1}{\gamma}} \right]} + \left(\frac{P_e - P_{atm}}{P_c} \right) \frac{A_e}{A_t} \quad (31)$$

The theoretical characteristic velocity is a thermodynamic property and is only dependent on fuel formulation and operating conditions. However, similar to the specific impulse, the actual characteristic velocity suffers from losses associated with combustion inefficiency and rocket chamber non-idealities. The theoretical and actual characteristic velocities are given by:

$$c^*_{ideal} = \frac{\sqrt{\gamma RT_c}}{\gamma \sqrt{\left[\frac{2}{\gamma+1}\right]^{\frac{\gamma+1}{\gamma-1}}}} \quad (32)$$

$$c^*_{actual} = \frac{P_c A_t}{\dot{m}} \quad (33)$$

The ratio of the actual characteristic velocity to the ideal characteristic velocity, η_c , is termed the c^* (pronounced “cee-star”) efficiency and is a measure of how efficiently propellant is combusted inside of the rocket chamber. This performance measure is a function of propellant characteristics and combustion chamber design, and is independent of the nozzle characteristics. This allows it to be used as a figure of merit when designing the propellants and combustion chamber. For purposes of this analysis, the c^* efficiency is assumed to be 90%. Utilizing the definitions of thrust coefficient, characteristic velocity, and c^* efficiency, the thrust can be written in a useful form:

$$F = \dot{m} C_F c^* \eta_c \quad (34)$$

which is much more convenient to calculate from measurable and empirical values.

Theoretical methods for determining the fuel regression rate, \dot{r} , do exist, but are very complex and require the implementation of many more assumptions. For this analysis, an empirical power law relation was assumed for the regression rate which is written as:

$$\dot{r} = aG_{ox}^n \quad (35)$$

where a and n are empirical constants, and G_{ox} is the oxidizer mass flux which is given by:

$$G_{ox} = \frac{\dot{m}_{ox}}{A_c} \quad (36)$$

The empirical regression rate constants utilized herein were taken from Evans et al. [254]. The oxidizer/fuel ratio (O/F) of the combustion reaction inside of the rocket chamber is determined by the equation:

$$O/F = \frac{\dot{m}_{ox}}{\dot{m}_f} \quad (37)$$

and the fuel mass loss rate is given by:

$$\dot{m}_f = A_s \rho_f \dot{r}_f \quad (38)$$

For a given oxygen/fuel ratio and chamber pressure, the chamber gas properties, including characteristic velocity and specific heat ratio, are fixed. To determine the molecular weight and specific heat ratio for the mixture of combustion products, it was assumed that the products were in chemical equilibrium, and that the pressure of the products was quasi-static. While it is possible to assume a set number of product species and solve using multiple equilibrium mechanism constants, several programs are available that allow the computation to be completed more quickly and accurately than could be done by hand.

NASA's CEA was used in this analysis to evaluate the combustion chemistry over the operating range of oxidizer/fuel ratios for two propellant formulations: plain HTPB and HTPB with 30.9% pure crystalline aluminum by mass. Specifically, the program was

used to create tables for the ratio of specific heats, γ , and the characteristic velocity, c^* , as functions of the oxidizer-to-fuel ratio, (O/F) , which are used as inputs in the hybrid rocket performance code. Figure 37 shows performance comparisons for the plain HTPB and aluminized HTPB propellant formulations evaluated at 75 psia.

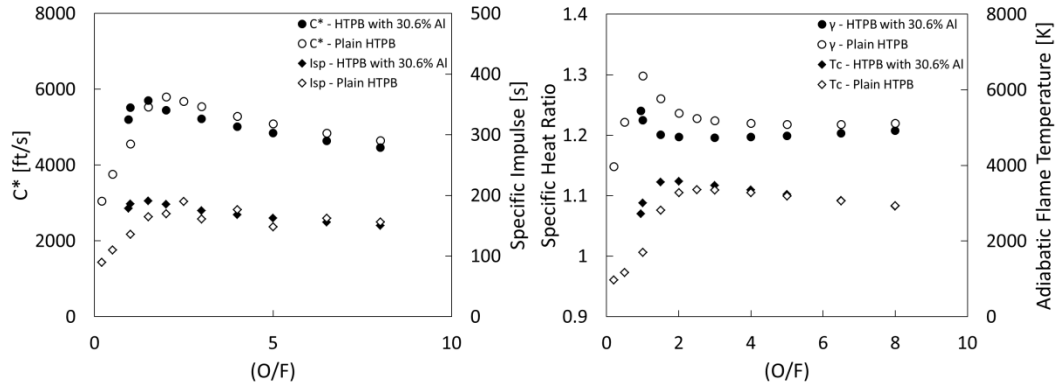


Figure 37. Characteristic velocity, c^* , specific impulse, I_{sp} , specific heat ratio, γ , and adiabatic flame temperature, T_c , calculated by CEA for each formulation over the operating (O/F) range and a pressure of 75 psia.

Unless otherwise noted, the parameters in all of the equations presented within this section vary with time during a hybrid motor firing. The combustion port radius of the hybrid motor can be discretized in time as per:

$$r_f(t + dt) = r_f(t) + \dot{r} dt \quad (39)$$

which allows all other parameters to vary with time as well. The previously presented set of equations are solved simultaneously at every time step, dt , for a total burn time, t_b , to yield transient rocket performance. To accomplish this task, a simulation program and two functions were written in MATLAB and meshed together. The specific calculation algorithm process implemented, which runs for plain and aluminized motor formulations, is shown in Figure 38.

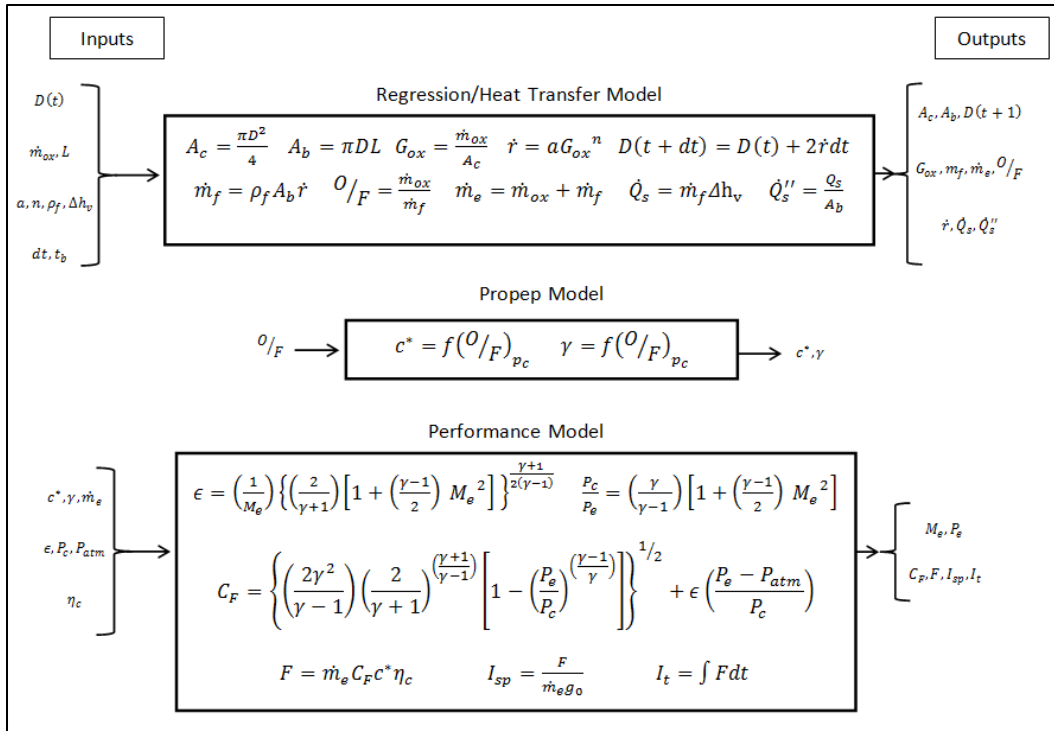


Figure 38. Calculation algorithm for hybrid rocket motor performance model.

The program was utilized to evaluate the operating conditions of a lab-scale hybrid rocket motor and determine the optimal dimensions, oxidizer mass flow rate, and chamber pressure for a small-scale stand capable of evaluating various fuel additives in a timely and cost effective manner. The final operating conditions are given in Table 3.

Table 3. Parameter input values for the hybrid motor burn simulation program.

Rocket Properties	
$D(0) = 0.2 \text{ cm}$	
$\dot{m}_{ox} = 4.46 \text{ g/s}$	
$l = 5 \text{ cm}$	
$P_c = 75 \text{ psi}$	
$P_{atm} = 14.7 \text{ psi}$	
Fuel Properties	
HTPB	HTPB + 30.6% Crystalline Aluminum
$a = 0.240$	$a = 0.343$
$n = 0.647$	$n = 0.596$
$\rho_f = 930 \text{ kg/m}^3$	$\rho_f = 1480 \text{ kg/m}^3$
$\Delta h_v = 1.8 \text{ MJ/kg}$	$\Delta h_v = 4.61 \text{ MJ/kg}$
$n_c = 1$	$n_c = 1$

The burn simulation program produces a set of plots which can be used to evaluate operating conditions throughout the hybrid rocket, determine combustion gas properties inside of the rocket chamber, assess rocket performance throughout the motor burning process, and ensure that the simulation is following fundamental and empirical trends for each fuel formulation in the calculation process. The entirety of the MATLAB code developed to simulate hybrid rocket combustion and its full output are given in Appendices A and B, respectively, and relevant plots are shown below for discussion purposes. Figures 39 and 40 show the oxidizer mass flux and regression rate for the hybrid motor fuel grains as a function of burn time. When combustion is initiated inside of the motor, the port diameter is small, leading to a small surface area and a high oxidizer mass flux. Accordingly, the initial regression rate of each hybrid motor is also high. As combustion processes continue, the diameter of the combustion port expands, so that with a constant oxidizer mass flow rate, the oxidizer mass flux decreases. The decrease in oxidizer mass flux begins rapidly because the regression rate of the motor is high at the beginning of the process, but decreases at a slower rate as the burn continues and the regression rate drops. The oxidizer mass flux for the plain HTPB motor is larger than that of the aluminized formulation for the entirety of the burn, with the exception of the initial ignition time, because the aluminized motor regresses faster. The regression rate of the aluminized motor formulation is higher than that of the plain HTPB formulation for the entirety of the burn, even though the oxidizer mass flux is lower. This is because of the regression rate enhancement due to the aluminum additive inclusion.

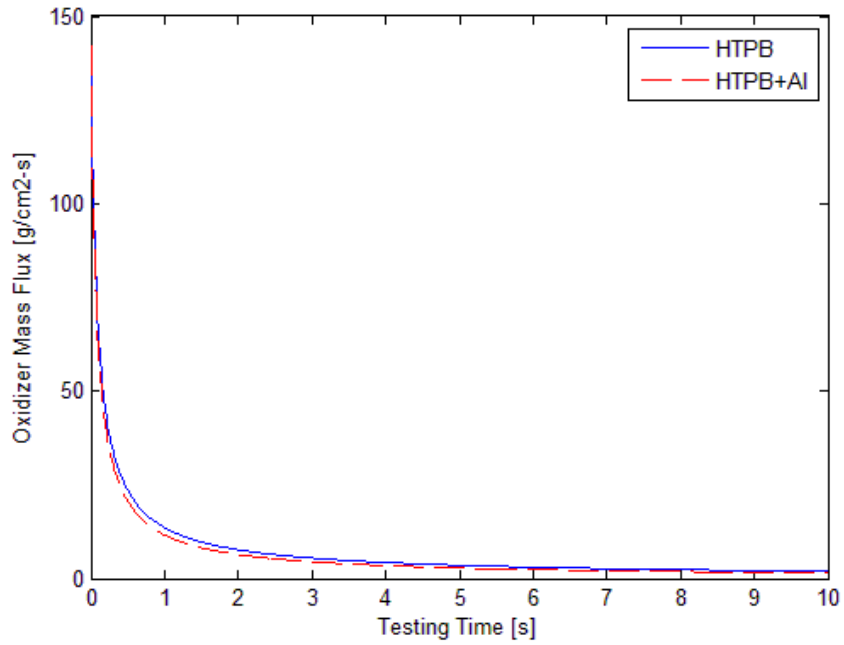


Figure 39. Oxidizer mass flux for plain and aluminized motor formulations versus burn time.

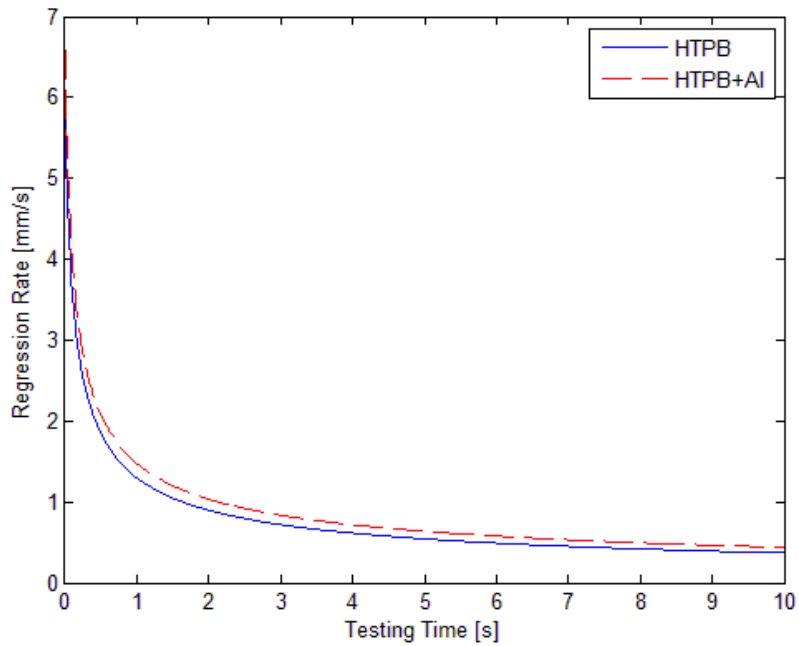


Figure 40. Motor radial regression rate for plain and aluminized motor formulations versus burn time.

Figures 41 and 42 are performance plots illustrating the variation of propulsive thrust force and specific impulse for the two motor formulations throughout motor burning. The thrust force and specific impulse of each motor decrease throughout the burn as the regression rate and fuel mass loss rate decrease and the oxidizer to fuel ratios shift away from peak performance points. Both the thrust force and specific impulse of the aluminized motor formulation are higher than that of the plain HTPB formulation. The fuel mass loss rate, which is shown in Figure B.2, is higher for the aluminized formulation throughout the burn time because the regression rate and fuel density are higher. Accordingly, more mass is being ejected through the nozzle at high velocity, which results higher propulsive thrust force. Additionally, the rocket input dimensions were optimized so that operation occurs near peak performance for aluminized motor formulations, so the specific impulse of the aluminized formulation is higher throughout the burn time.

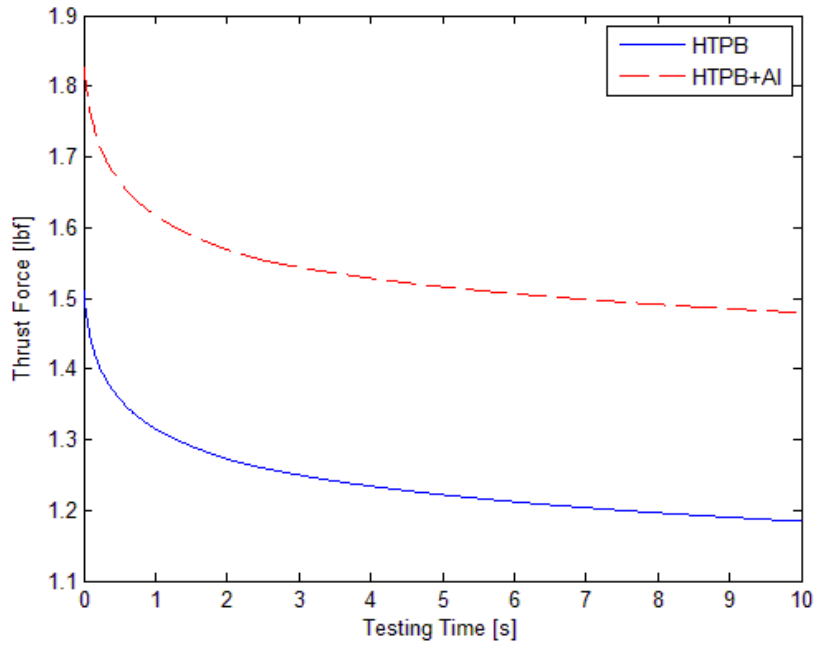


Figure 41. Propulsive thrust force for plain and aluminized motor formulations versus burn time.

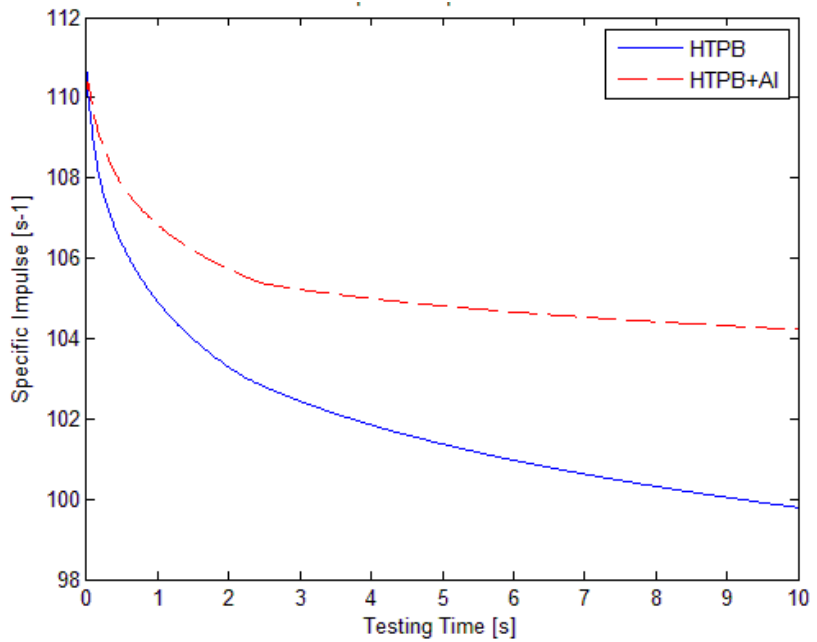


Figure 42. Specific impulse for plain and aluminized motor formulations versus burn time.

5. BALLISTIC STAND DESIGN

The ballistic test stand consists of several interconnected subsystems which are depicted in Figure 43. The oxidizer delivery system transports oxidizer to the rocket chamber. Burning of the hybrid rocket fuel grain takes place in the combustion chamber once oxidizer is delivered and ignition is initiated. The diagnostics system consists of two pressure transducers for measuring the pressure in the oxidizer feed system and the combustion chamber, a mass flow controller for setting oxidizer flow, and a load cell for measuring the thrust force produced by the rocket. The data acquisition (DAQ) system records the outputs of the pressure transducers, mass flow controller, and load cell. The power system provides electrical power to all components of the thrust stand.

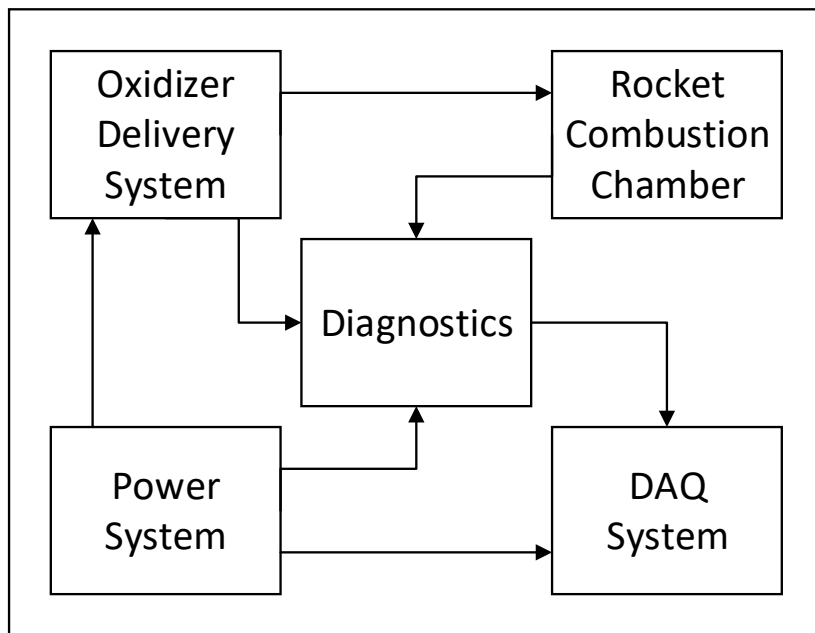


Figure 43. Subsystems of the hybrid rocket ballistic test stand.

Material within this chapter has been previously published and is reprinted with permission from "Design and Characterization of a Lab-Scale Hybrid Rocket Test Stand" by Thomas, J. C., Stahl, J. M., Morrow, G. R., and Petersen, E. L., AIAA 2016-4965, 52nd AIAA/ASME/SAE/ASEE Joint Propulsion Conference, Salt Lake City, UT, 2016, Copyright 2016 by James C. Thomas.

The hybrid rocket test stand is shown in Figure 44. Important individual components are highlighted including the oxidizer blowdown tank, upstream oxidizer and chamber pressure transducers, mass flow controller, injection port, load cell, igniter, combustion chamber, and a plate for condensed combustion product (CCP) collection.

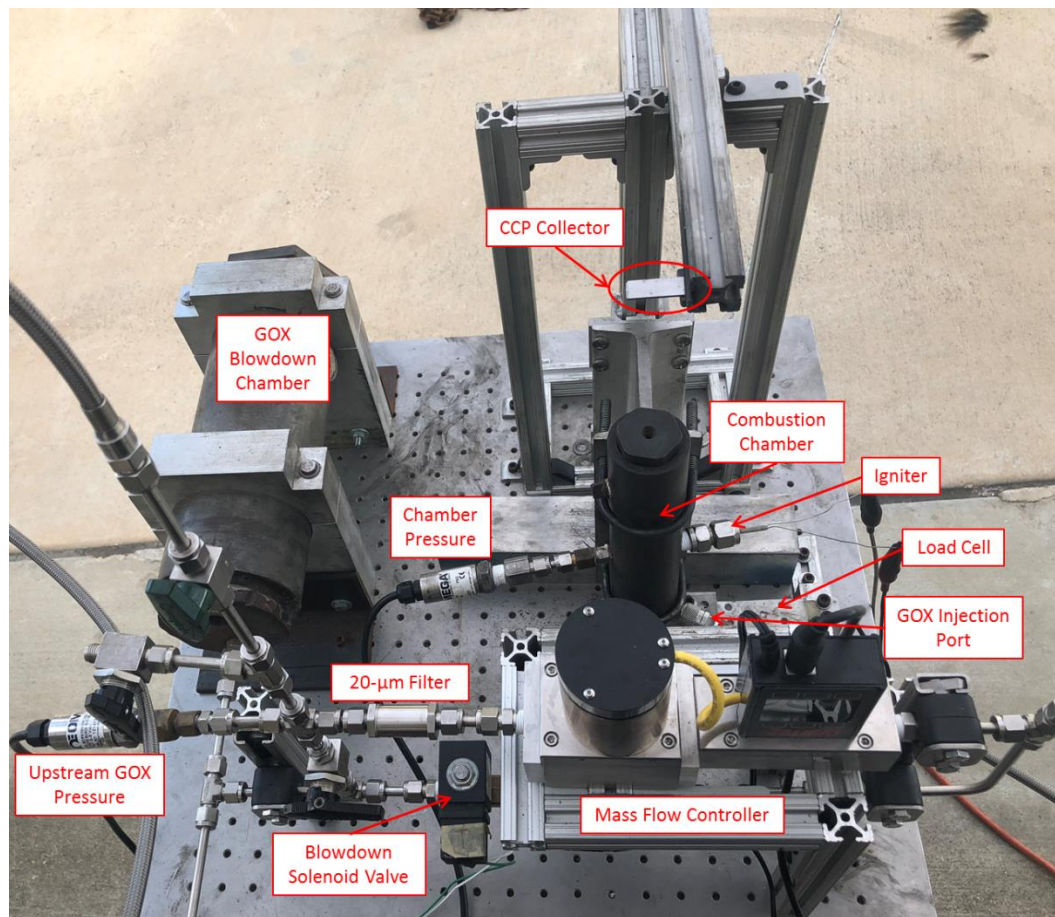


Figure 44. Hybrid rocket ballistic test stand. Key components are highlighted.

5.1. Fuel Grain and Chamber Sizing

To size the combustion chamber and motor fuel grain, a state-of-the-art performance prediction program was developed and has been previously described in

Chapter 4 of the thesis. The program is based on fundamental engineering concepts and utilizes thermochemical analysis databases and empirical correlations given in the literature.

This program was utilized to perform a parametric evaluation of motor fuel grain dimensions including the combustion port initial diameter and length. The constraints of the project included: 1) small motors for economical evaluation of numerous additives, 2) achievable oxidizer mass fluxes as high as $150 \text{ kg/m}^2\text{-s}$, 3) experimental turn-around time of less than 10 minutes for time-efficient testing, and 4) modular design for easy variation of numerous parameters in future testing. The author settled on a combustion port diameter of 2 mm and a motor length of 5 cm. For the prescribed system, the performance program predicts a thrust force of 1.5 lb_f (6.7 N) and oxidizer mass fluxes as high as $200 \text{ kg/m}^2\text{-s}$ for short-duration burns of baseline HTPB motors burning in gaseous oxygen. Detailed results of the performance prediction program are given in Appendix B for baseline and aluminized formulations.

5.2. Combustion Chamber

The combustion chamber section of the hybrid rocket thrust stand includes an injector bulkhead, an injector insert, a pressurized constant-volume chamber, and a nozzle bulkhead. Solid and wireframe Solidworks models of the combustion chamber assembly are shown in Figure 45. Detailed design drawings of the injector bulkhead, injector insert, combustion chamber, and nozzle bulkhead are given in Appendix C. All of these components were manufactured with 1018 steel.

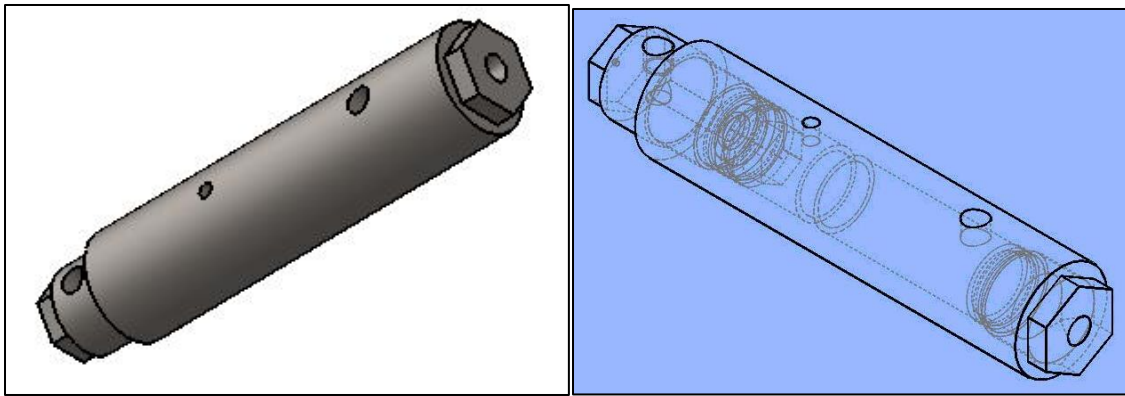


Figure 45. Solid (left) and wireframe (right) Solidworks models of the combustion chamber assembly.

When the hybrid rocket stand is used for motor firing, several components are added to the system. High-temperature silicone O-rings (#121) are utilized in the injector bulkhead, injector insert, and nozzle bulkhead to create high-pressure seals at either end of the rocket chamber. O-rings are mounted in internal radial slots which were machined according to the specifications of ISO 3601. Teflon tape is utilized on the threads of the injector bulkhead and nozzle section as a back-up sealing mechanism. A Swagelok quick-connect system is utilized at the injector port for timely disassembly and reassembly of the motor. A pressure transducer is threaded into the injector side of the chamber for monitoring of chamber pressure during firing and utilizes a similar quick-connect system. A ceramic igniter bulkhead is threaded into the same side of the combustion chamber to initiate motor combustion. The igniter apparatus is further detailed later in this section of the thesis. The motor fuel grain is loaded into the nozzle end of the combustion chamber and is held in place by a steel spacer during motor firing. Figure 46 shows all of these components and how they are assembled for rocket testing.

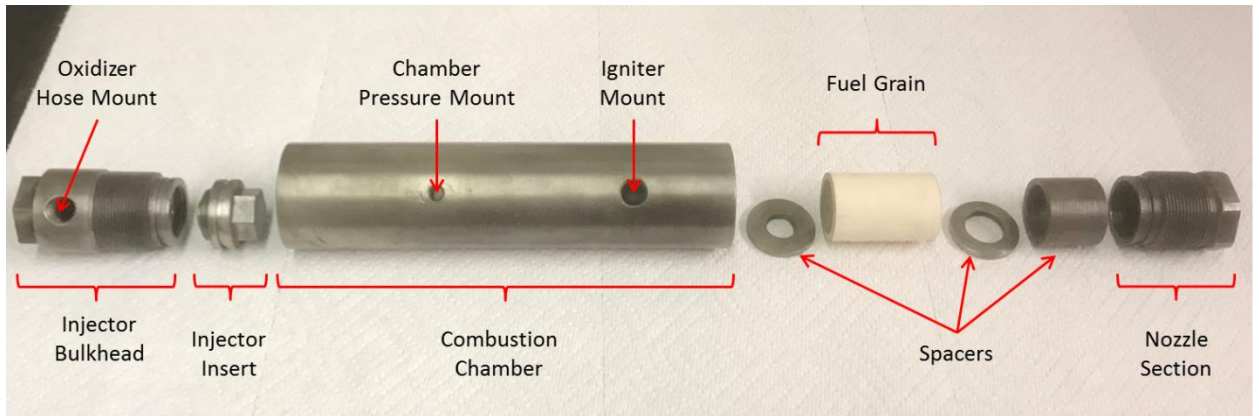


Figure 46. Components of the combustion chamber section.

The ignition system is shown in Figure 47. A high-pressure, probe-sealing assembly was acquired from Conax technologies. Two 1-mm steel lead wires are internally sealed in the probe assembly by a Viton plug. The probe assembly is sealed to the combustion chamber with Teflon tape and 1/4" NPT threads. A composite AP/HTPB solid propellant sample (~1 g) is mounted onto a Nichrome wire strand and hooked onto the steel probe leads, which serves as an ignition booster. Ignition of the solid propellant sample is initiated by passing a high current through the probe leads via a variable power source, which in turn ignites the hybrid motor fuel grain when the oxidizer is flowing. The ignition power system is further detailed in the power and DAQ section of this chapter.

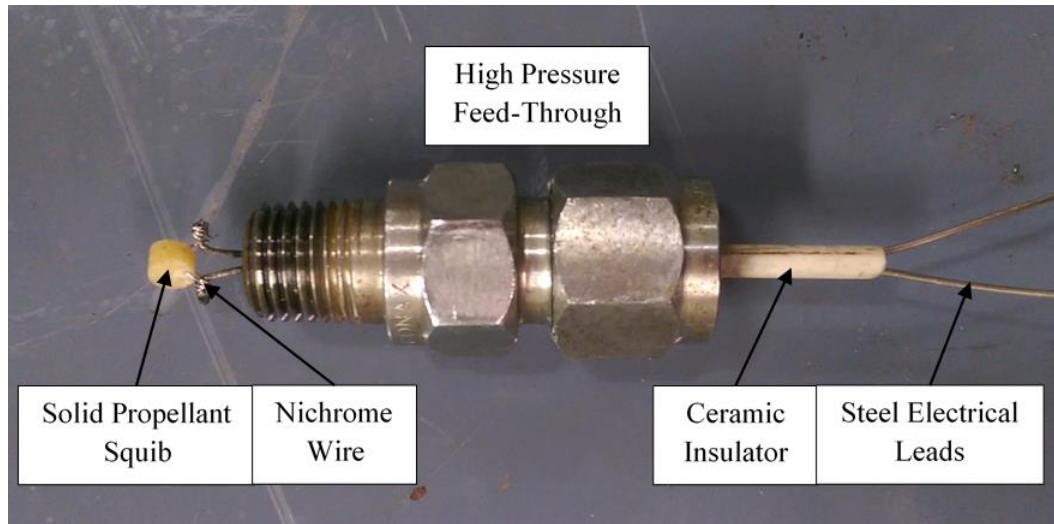


Figure 47. Ignition bulkhead assembly and mounted solid propellant sample.

5.3. Chamber Stress Analysis

It is important to analyze the mechanical stresses inside of the combustion chamber to ensure that structural failure does not occur during motor firing. Structural failure can occur at the wall of the combustion chamber or at threaded connections such as the injector bulkhead, nozzle bulkhead, pressure transducer port, and igniter feed-through port. The tangential, radial, and longitudinal stresses inside of a cylindrical pressure vessel are given by Equations (40)-(42), respectively:

$$\sigma_t = \frac{P_i r_i^2 - P_o r_o^2 - r_i^2 r_o^2 (P_o - P_i) / r^2}{r_o^2 - r_i^2} \quad (40)$$

$$\sigma_r = \frac{P_i r_i^2 - P_o r_o^2 + r_i^2 r_o^2 (P_o - P_i) / r^2}{r_o^2 - r_i^2} \quad (41)$$

$$\sigma_l = \frac{P_i r_i^2}{r_o^2 - r_i^2} \quad (42)$$

where P_i and P_o are the pressures inside and outside of the pressure vessel, respectively; r_i and r_o are the inner and outer radii of the pressure vessel, respectively; and r is the

chamber radius where the mechanical stress is present. [456] The inner and outer radii of the combustion chamber were selected as 1.67 cm (0.66 in) and 2.54 cm (1.00 in), respectively. Preliminary results showed that the combustion chamber pressure for plain HTPB motors is approximately 90 psi. The stress distributions inside of the pressure chamber's walls for an internal pressure of 100 psi and atmospheric pressure outside of the vessel are shown in Figure 47. The largest stress is the circumferential stress at the inner wall of the chamber, which is 201 psi when the operating chamber pressure is 100 psi. As the chamber pressure increases, so do the mechanical stresses in the chamber walls.

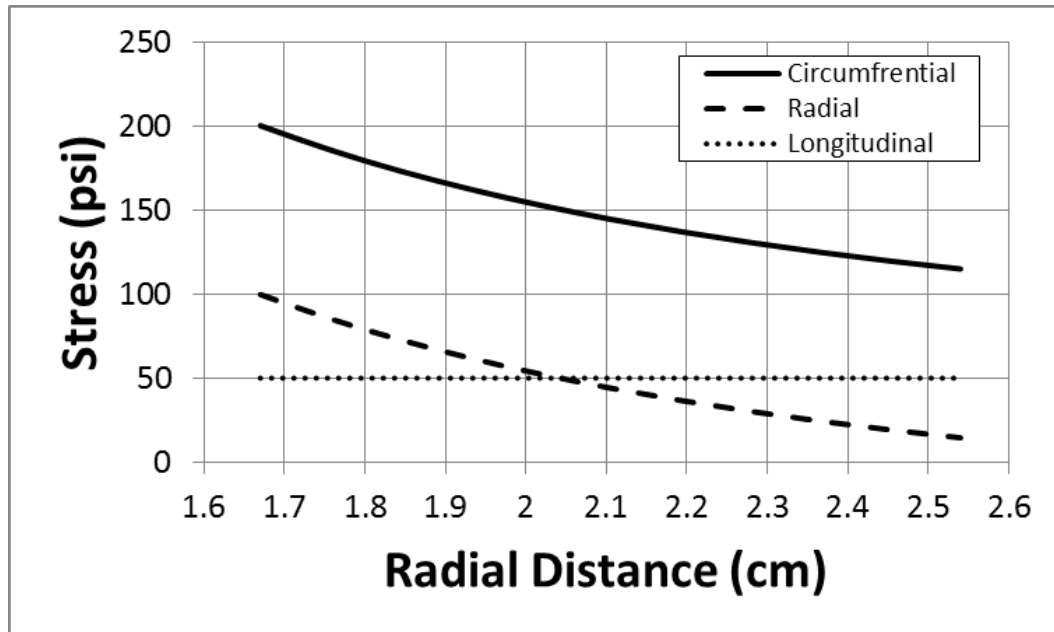


Figure 47. Stress distributions inside of the chamber walls with an internal pressure of 100 psi and atmospheric pressure outside of the vessel.

The factor of safety of a given design system with mechanical stress is defined as:

$$k_s = \frac{\sigma_f}{\sigma_{real}} \quad (43)$$

where σ_f is the failure stress and σ_{real} is the real mechanical stress occurring in the component under consideration. The yield stress of 1018 steel is approximately 45,000 psi [456] and was defined as the failure stress for the combustion chamber. The factor of safety of the chamber design is 224 at an operating chamber pressure of 100 psi; which illustrates how oversized the system is. This factor of safety is plotted against chamber pressure in Figure 48. The factor of safety decreases with increasing operating pressure because the mechanical stresses present are larger at higher operating pressures. The factor of safety of the chamber design at an operating chamber pressure of 1,000 psi is 18, which is still acceptable; so testing at much higher chamber pressures is allowable under the design criteria of chamber wall thickness.

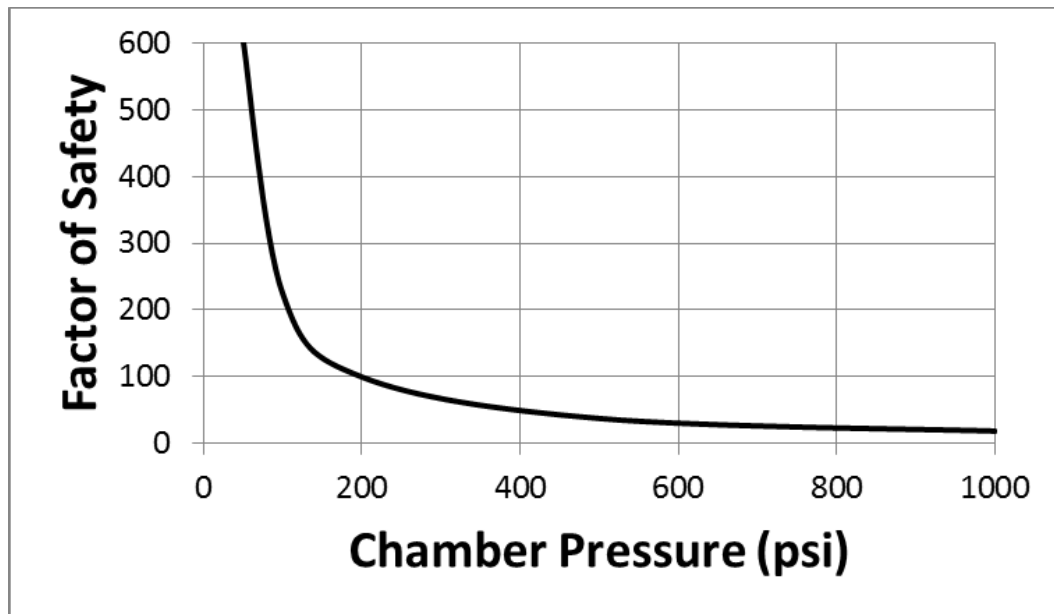


Figure 48. Factor of safety of chamber wall thickness versus chamber operating pressure.

The mechanical stresses in the threaded connections of the injector and nozzle bulkheads are much more difficult to evaluate. To calculate these stresses, the shear area of the thread must be determined and is given by:

$$A_s = \pi n L_e D_{min} \left(\frac{1}{2n} + 0.577735(D_{pitch} - D_{min}) \right) \quad (44)$$

where n is the number of threads per inch, L_e is the length of thread engagement, D_{min} is the minimum diameter of the thread, and D_{pitch} is the pitch diameter of the thread. This equation was empirically determined and is given in Federal Standard #FED-STD-H28/2B. Performing a static force balance on the bolt yields the shear stress acting on the threads:

$$\tau_s = P_i \left(\frac{A_b}{A_s} \right) \quad (45)$$

where P_i is the internal chamber pressure and A_b is the cross-sectional area of the bolt connection. The bolt cross-sectional area can be readily calculated with the outer and inner bolt diameters. The failure shear stress is once again taken as the yield stress and is related to the tensile yield stress for metals by:

$$\tau_y = 0.5777 \sigma_y \quad (46)$$

Thread dimensions for each connection are given in Table 4, and the corresponding shear area has been calculated according to Equation (44). The shear stress acting on each connection can be calculated with Equation (45) and utilized to evaluate the factor of safety at a given operating pressure, similar to the chamber stress analysis previously presented. At an operating pressure of 100 psi, the factors of safety of the injector and nozzle bulkheads are approximately 2,200. At an operating pressure of 1,000 psi, the

factors of safety of the injector and nozzle bulkheads are approximately 225. These large factors of safety once again demonstrate how oversized the pressure chamber is for its operating conditions.

Table 4. Thread dimensions of the injector and nozzle bulkheads.

Connection		Ignition Bulkhead	Nozzle Bulkhead
Thread Type		UNF 1-1/2"	UNF 1-1/2"
Threads per Inch	$n \text{ (in}^{-1}\text{)}$	12	12
Minimum Diameter	$D_{\min} \text{ (in)}$	1.40	1.40
Pitch Diameter	$D_{\text{pitch}} \text{ (in)}$	1.50	1.50
Engagement Length	$L_e \text{ (in)}$	2.54	2.54
Shear Area	$A_s \text{ (in}^2\text{)}$	13.27	13.27
Inner Bolt Diameter	$D_b \text{ (in)}$	0.04	0.08
Outer Bolt Diameter	$D_b \text{ (in)}$	1.40	1.40
Bolt Area	$A_b \text{ (in}^2\text{)}$	1.54	1.54

5.4. Thrust Measurement System

A system consisting of a linear bearing and load cell was designed to measure the thrust of the hybrid rocket and is shown in Figure 44. The rocket combustion chamber is secured to an aluminum I-beam by standard U-bolts and flange nuts for quick disassembly and reassembly. The I-beam has been custom manufactured to fit an aluminum t-slot linear bearing. The injector bulkhead at the front end of the rocket chamber has a small stud which fits snugly into a hole which has been drilled into 1/4" steel bar stock. A 1/4" steel angle iron piece is secured to the stand table by standard bolts. The load cell is mounted to both the bar stock and angle iron by M6 fasteners. When the rocket is operational, the thrust force produced is directly translated to the load cell by this apparatus. The load cell utilized on this thrust stand is an Omega Engineering LCAE-6KG single point model. The

output signal is amplified by an Omega Engineering DMD-465WB fast response amplifier model before being recorded by the system's oscilloscope.

5.5. Oxidizer Delivery System

The hybrid rocket motor system has safety advantages over its pure solid and liquid counterparts because its oxidizer is stored separately from the fuel. The solid fuel grain is contained in the combustion chamber and the oxidizer is contained in an isolated tank. The purpose of the oxidizer feed system is to deliver the oxidizer to the rocket chamber for combustion with the solid fuel grain.

A schematic of the oxidizer delivery and DAQ systems is given in Figure 49, and the actual manifold is shown in Figure 44. The bulk of the system is made up of Swagelok 1/4" stainless steel tubing rated up to 3,000 psi and various Swagelok fittings rated up to 5,000 psi. Ball valves are installed throughout the system to allow for isolation of any subcomponent. Three manual exhaust valves are installed in for pressure relief in the case of a failed solenoid valve or clogged nozzle scenario. Oxidizer and inert gas can be delivered to the combustion chamber during motor firing by remote operation of the solenoid valves or the mass flow controller. The solenoid valves selected for this assembly are Omega Engineering SV121 high-pressure models which are rated to a maximum pressure of 1,450 psi. The mass flow controller utilized herein is a custom-designed Alicat Scientific MCRQ-100SLPM-D-20X32 model capable of flowing 2.5 g/s of GOX and withstanding inlet pressures of up to 325 psia. The MFC also has diagnostics for recording the oxidizer upstream pressure, temperature, and mass flowrate. Pressures at the outlets of the oxygen and inert gas tanks are set by standard pressure regulators with outlet

capabilities of 2,500 psia. The pressure in the delivery manifold and the rocket chamber are monitored by Omega Engineering PX309-1KG5V model pressure transducers, which are rated up to 1,000 psi.

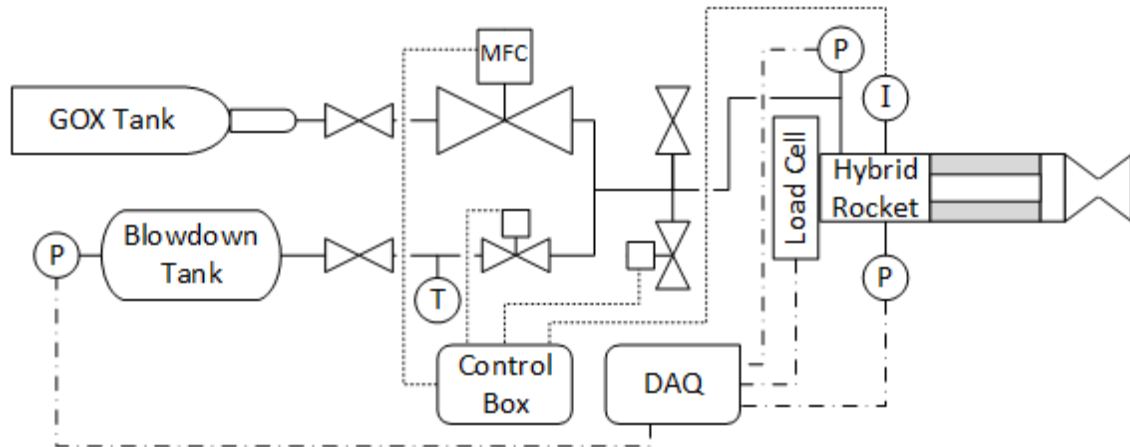


Figure 49. Schematic of the oxidizer delivery and DAQ subsystems.

The hybrid rocket can be operated in several modes: steady, transient, and blowdown oxidizer flow. In the steady mode, the oxygen pressure regulator is set to a pressure compatible with the MFC, and the MFC is set to a constant mass flow rate. In the transient mode, the oxygen pressure regulator is set to a pressure compatible with the MFC, and variable flow conditions (such as stop/start or deep throttle) are implemented within the MFC's software. In the blowdown mode, the attached oxidizer tank is filled to a desired pressure and allowed to blowdown during motor firing. Each mode has unique advantages.

5.6. Power and Data Acquisition System

The power and DAQ system is responsible for providing electrical power to all components of the test stand and for recording measurement voltages of the pressure

transducers and load cell. All components of the system are powered by a 120-VAC power source in the testing facility building. Twelve VDC transformers are utilized to power the pressure transducers and the MFC. The variable power transformer employed to power the ignition system is a GW Instek model GPR-1810HD. The oscilloscope used to record data is a GW Instek model GDS-2064. The remote control box has two switches which control the oxygen solenoid valve and the ignition system power supply.

5.7. Failure Modes and Effects Analysis

To evaluate the safety of the testing apparatus and operations, and quantify the likelihood of all potential failures and their consequences, a failure modes and effects analysis has been conducted. This analysis is presented in Table 5. The most severe failures are further detailed below.

Table 5. Failure modes and effects analysis.

Failure Mode	Probability (1-5)	Consequence (1-5)	Risk (1-5)	Details
Mechanical Failure of the Combustion Chamber (Walls)	1	5	1.0	In the event of a mechanical failure of the combustion chamber's wall, the consequences could be dangerous. Metal shrapnel could be expelled at high velocities. Combustion gases would rapidly exhaust from the failure interface and a possible motor explosion could take place. However, the high factor of safety of this component means this failure mode has an extremely low risk. This failure mode also poses a threat to loss of testing data.
Mechanical Failure of the Combustion Chamber (Threads)	1	5	1.0	In the event of a mechanical failure of the combustion chamber's threads, the consequences could be dangerous. The injector or nozzle bulkhead could be expelled from the system at high velocity. Combustion gases would rapidly exhaust from the failure interface which could lead to a fire hazard. However, the high factor of safety of this component means this failure mode has an extremely low risk. This failure mode also poses a threat to loss of testing data.
Mechanical Failure of a Diagnostic Port (Threads)	1	5	1.0	In the event of a mechanical failure of the combustion chamber's threads at a diagnostic port (injector hose, pressure tap hose, igniter feed-through, or post-combustion chamber plug), the consequences could be dangerous. The failed component could be ejected from the system at high velocity. Combustion gases would rapidly exhaust from the failure interface which could lead to a fire hazard. This failure mode is more likely than mechanical failure of the chamber because NPT threads are utilized instead of UNF threads, but it is still very unlikely when the threads are properly tightened. This failure mode also poses a threat to loss of testing data.
Mechanical Failure of Oxidizer Delivery Component	5, 1	1, 5	1.0, 1.0	The oxidizer delivery system is made up of numerous tubes, regulators, valves, and fittings and each component has a potential for failure. A failure at a valve/tube or fitting/tube interface is likely, but not dangerous and can be easily fixed by tightening or replacing the connection. The failure of a valve would lead to a system leak or unpredictable flow which is not significantly dangerous, but should be fixed by replacing the valve, so that accurate testing data can be recorded. The most significant threat is posed if the pressure regulator at the high-pressure oxidizer or nitrogen tanks fails which would lead to an uncontrolled blowdown of the entire gas bottle. This could lead to unsafe conditions near the testing rig via high pressure gas exhaust or by mechanical failure of the rig's components due to over pressurization.
Structural Failure of O-Ring Pressure Seals	5	1	1.0	The O-rings utilized to pressure seal the combustion chamber are made for high temperature environments, but the combustion gases are extremely hot. After numerous tests the O-rings can and will encounter structural failure. Visual inspections of each O-ring's integrity should be made prior to each test. When an O-ring fails a combustion gas bleed-through will occur and hot gas will be expelled from the system. This even does not pose a significant fire hazard, but will invalidate testing pressure data.
Mechanical Failure of Linear Bearing Assembly Components	1	3	0.6	The linear bearing assembly includes the t-slot aluminum bolted to the main table, the bearing itself, the I-beam bolted to the bearing, the U-bolts securing the rocket to the I-beam, and all corresponding structural joints. In the event that any one of these individual components fail, then the rocket could potentially fly free from the stand. The rocket is not designed for flight purposes and would not travel at a high velocity, but would still pose a fire hazard and a loss of testing data. However, all load bearing components are overdesigned for the small thrust force the rocket will produce (1.5 lb), so this event is very unlikely.
Mechanical Failure of Load Cell Apparatus Components	2	1	0.4	The load cell apparatus includes the load cell itself, the steel bar stock which interfaces the load cell with the rocket, the steel angle iron which interfaces the load cell with the table, and all corresponding structural joints. In the event that any one of these individual components fail, then the rocket/linear bearing assembly would be able to slide forward, but not leave the table. This failure mode is possible because of the unthreaded connection of the load cell/bar stock interface, but only presents a consequence of lost data and damaged equipment.
Structural Failure of the Stand Table	1	3	0.6	In the event that an individual leg or bolt on the stand table itself fails, the table should still be standing; but if several fail, then the table could fall over. This failure mode is extremely unlikely due to the low thrust force produced by the rocket, the high weight of the table, and the low center of gravity of the table. This failure mode would lead to a potential fire hazard and loss of testing data.
Sealing Failure of Oxidizer Delivery System	1	5	1.0	If a single fitting in the oxidizer delivery system is loose, then a leak of oxidizer to the atmosphere would occur. For short time scales, this failure mode is not dangerous. However, if the system were left pressurized over an extended period of time with an oxidizer leak, then a catastrophic event could occur if an unanticipated ignition source were encountered. This entire failure mode can be avoided by ensuring the fittings are tightened properly prior to testing and the risk of a catastrophic event can be completely avoided by ensuring the oxidizer tank is closed in between tests and at the end of testing days.
Electrical Failure (Diagnostic)	2	3	1.2	Electrical failure to diagnostic equipment (pressure transducers and load cell) is possible due to a loose electrical connection or power loss. This failure mode can lead to a loss of testing data. If operators approach the stand while it is pressurized, but the DAQ is not measuring the pressure, then significant injury could occur. Accordingly, the system should be purged prior to approach if this failure mode occurs.
Electrical Failure (Igniter)	2	1	0.4	Electrical failure to the ignition system is possible due to a loose electrical connection, incorrect fitting of the nichrome ignition wire, or power loss. This failure mode poses no significant risk except loss of testing data.
Electrical Failure (Oxidizer Solenoid Valve)	2	4	1.6	Electrical failure to a solenoid valve is possible due to a loose electrical connection or power loss. Prior to testing, loss of power to the oxidizer solenoid valve poses no potential risk. If power to the valve is lost during testing, then an uncontrolled blowdown of the oxidizer tank would occur. The motor fuel grain would burn to completion and excess oxygen oxidizer would be leaked to the atmosphere. Testing staff should wait for conditions to clear before approaching the testing rig after such a failure.
Electrical Failure (Nitrogen Solenoid Valve)	2	1	0.4	Electrical failure to a solenoid valve is possible due to a loose electrical connection or power loss. Prior to testing, loss of power to the nitrogen solenoid valve poses no potential risk. If power to the valve is lost during testing, then an inert purge can not be accomplished and testing staff should wait for conditions to clear before approaching the testing rig.
Fire	4	2	1.6	The rocket chamber exhausts hot combustion products to the atmosphere during testing. The test stand is close to the ground and testing will take place on a grass field, so the probability of a potential fire near the stand is relatively high. However, the area around the stand will be conditioned for this risk prior to testing and fire extinguishers will be kept on hand during testing, so the risk of this event is low.

The highest risk events from the failure modes and effects analysis are the uncontrolled blowdown of oxidizer through the system due to a loss of electrical power to the oxidizer solenoid valve during testing and an uncontrolled fire caused by the expulsion of hot combustion exhaust onto the testing location's ground.

If an uncontrolled blowdown occurs during testing, the motor fuel grain will burn until no fuel is left. The oxidizer tank would be allowed to blow down and exhaust to the atmosphere. Testing staff would remain in the control room and monitor the conditions remotely through pressure transducers in the oxidizer delivery system and visually. After the blowdown is completed, the conditions should be given time to clear before the testing staff approaches the testing apparatus.

The uncontrolled fire hazard can be mitigated by conditioning the testing area prior to motor burning. In the event that a fire does occur, testing procedures should take place as planned until the test has been completed. After the test is complete, fire extinguishers kept inside the control room can be utilized to put out the fire.

5.8. Summary

A ballistic test stand for evaluating regression rates and combustion efficiencies of hybrid rockets has been developed at Texas A&M University. State-of-the-art prediction methodologies have been utilized to predict the conditions and performance of the rocket system. Thorough analysis has been conducted to ensure the stand is functional and safe.

6. EXPERIMENTAL METHODOLOGY: ADDITIVE CHARACTERIZATION

The size, purity, composition, and morphology of metallic additives can all have profound effects on the resultant combustion behavior in solid fuel combustion. Accordingly, efforts have been taken to characterize and document these attributes within this section of the thesis. The additives selected for the current project are shown in Table 6 and include micro-aluminum, nano-aluminum, nano-boron, micro-magnesium, micro-titanium, micro-zirconium, and magnesium-coated nano-boron. A summary of the additives' key characteristics (average particle size, purity, and geometry) and their respective manufacturers are also given in Table 6 for comparison. Experimental methods for microscopy analyses are given in the next two sections, and results of the additive particle characterization are subsequently presented.

Table 6. Key attributes of the metallic additives considered herein.

Additive	Manufacturer	ID	Size (μm)	Purity (%)	Geometry
micro-Al (μAl)	Valimet, Inc.	H-30	20-30	99.7	Spherical
nano-Al ($n\text{Al}$)	US Research Nanomaterials, Inc.	US-1043	0.1	99.9	Spherical
nano-B ($n\text{B}$)	SB Boron Corporation	SB-95	0.7	92.1-96.0	Irregular
micro-Mg (μMg)	US Research Nanomaterials, Inc.	US-1060	40	99.9	Flake
micro-Ti (μTi)	US Research Nanomaterials, Inc.	US-1038M	45	99	Irregular
micro-Zr (μZr)	US Research Nanomaterials, Inc.	US-1040M	75	99	Irregular
nano-MgB ($n\text{MgB}$)	Mach I Specialty Chemicals, Inc.	-	0.7	88	Irregular

6.1. Scanning Electron Microscopy

Scanning Electron Microscopy (SEM) images of the micro-additive particles were taken on a Tesca Vega 3 SEM, located in Texas A&M University's Microscopy and Imaging Center, to confirm additive particle sizes. SEM samples were prepared by placing

a piece of double-sided carbon tape on an aluminum sample holder. Additive particles were carefully sprinkled across the tape's surface.

6.2. Transmission Electron Microscopy

Transmission Electron Microscopy (TEM) images of the nano-additive particles were taken on a JEOL JEM-2010 Transmission Electron Microscope, located in Texas A&M University's Microscopy and Imaging Center, to confirm additive particle sizes and evaluate the surface chemistry. TEM samples were prepared by dispersing additive particles in an aqueous solution of nitromethane solvent at a mass concentration of 5% and subjecting the mixture to a 15-minute ultra-sonication treatment. The sample was diluted in a 5:1 volumetric ratio with additional solvent and suspended on a carbon film, 400-mesh copper grid. The nitromethane was evaporated off the grid at atmospheric conditions. TEM images were taken at various magnifications for representative particle network and fundamental particle sizing. In addition to particle imaging, Energy Dispersive X-Ray Spectroscopy (EDS) was utilized to map the surface chemistry and quantitatively evaluate the composition of the nano-B and nano-MgB particles.

6.3. Additive Characterization Results

All of the additives shown in Table 6 have been imaged through the previously described methods. The following sections serve to report manufacturer specifications, measured particle sizes, and EDS analyses completed herein.

6.3.1. Micro-Aluminum Particles

The aluminum micro-particles utilized herein (H-30) were obtained from Valimet, Inc. The manufacturer indicates the purity of the aluminum is 99.7% minimum with trace

amounts of volatile (<0.1%), oil and grease (<0.2%), and iron (<0.2%). Average particle size is reported as 20-30 μm with minimum pass-throughs of 99.5% and 85.0% on 200- and 325-mesh sieves, respectively.

SEM images of the aluminum micro-particles at increasing magnification are shown in Figure 50. The average particle size is on the order of 20-30 μm , and the geometry is spherical.

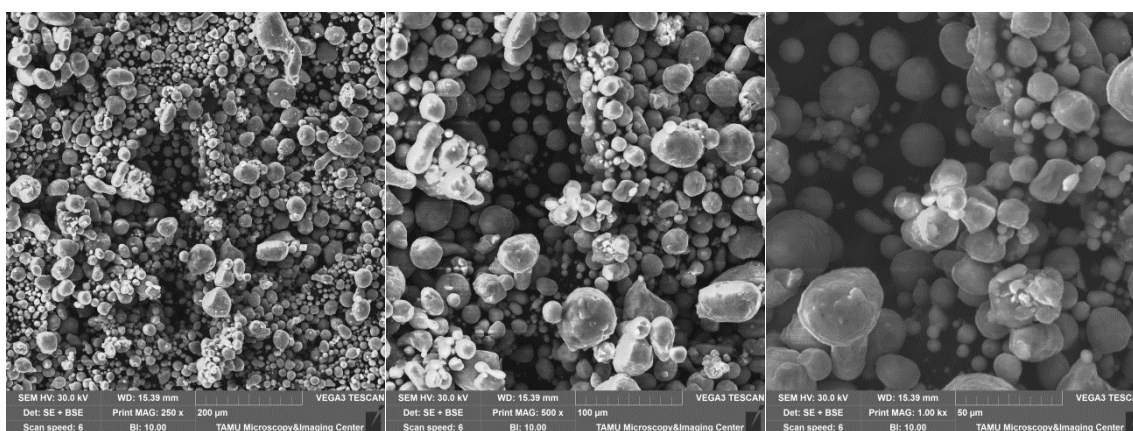


Figure 50. SEM images of aluminum micro-particles at increasing magnification.

6.3.2. Nano-Aluminum Particles

The aluminum nano-particles utilized herein (US-1043) were obtained from US Research Nanomaterials, Inc. and were produced by the electric explosion of wire method. The manufacturer indicates the purity of the aluminum is 99.9% minimum. Particles are reported to be spherical, have an average particle size of 100 nm, and a specific surface area of 10-20 m^2/g .

TEM images of the aluminum nano-particles at increasing magnification are shown in Figure 51. The nano-aluminum particles are all spherical and have a fundamental particle size of approximately 100 nm. However, the particles tended to form aggregate

chains which ranged in size from 0.2-2 μm in length. Measurements of the oxide layer thickness are shown in Figure 51 and indicate a thickness of approximately 3 nm.

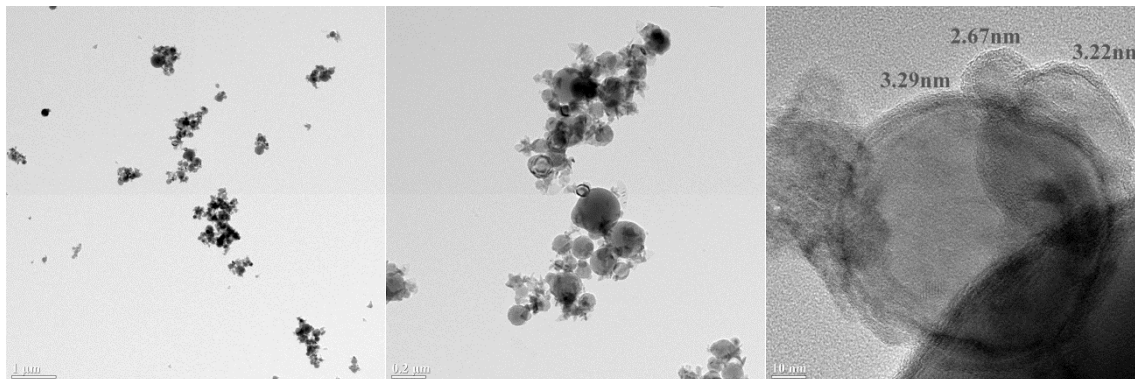


Figure 51. TEM images of aluminum nano-particles at increasing magnification.

6.3.3. Nano-Boron Particles

The boron nano-particles utilized herein (SB-95) were obtained from SB Boron Corporation. The manufacturer reports a purity of 92.1-96.0% with trace amounts of magnesium (<3.0%); iron (<0.10%); nitrogen (<0.10%); manganese (<0.08%); calcium, silicon, and sodium (<0.04%); aluminum, lead, and nickel (<0.01%); and barium, bismuth, cadmium, and copper (<0.005%). The average particle size is reported as 0.7 μm .

TEM images of the boron nano-particles at increasing magnification are shown in Figure 52. The boron particles exhibit various morphologies including spheres and flakes. The spherical particles are on the order of 100 nm in diameter and vary in size. The boron flakes are much larger and were typically several 0.3-3 μm in length.

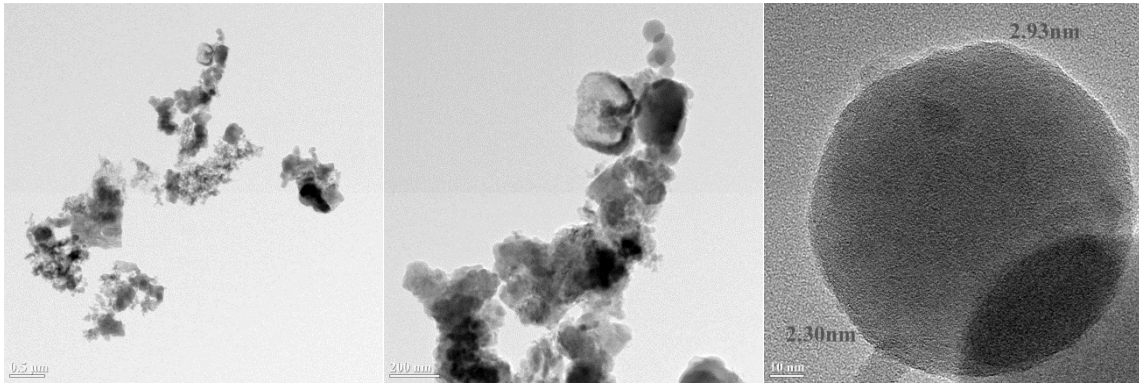


Figure 52. TEM images of boron nano-particles at increasing magnification.

EDS analysis was utilized at five different sites within the boron nano-particle sample to determine the average particles' composition, and the results are presented in Table 7. The particles are mostly composed of amorphous boron (~95%) with notable concentrations of oxygen (~2%) and magnesium (~2%), and trace amounts of iron, silicon, and cobalt. The EDS spectra collected also contained traces of several other elements (aluminum, barium, calcium, cadmium, chlorine, cobalt, copper, manganese, nitrogen, sodium, nickel, and lead) which were below the threshold of the composition measurement (0.1%).

Table 7. Chemical compositions of boron nano-particles measured with EDS analysis.

Element	Concentration (wt %)
B	95.2 ± 1.9
Mg	2.3 ± 1.1
O	2.1 ± 0.7
Fe	0.3 ± 0.3
Si	0.1 ± 0.1
Co	0.1 ± 0.1

Atomic maps of a single boron particle's surface are shown in Figure 53 for (b) boron, (c) oxygen, (d) magnesium, and (e) iron. In general, the contaminant atoms are

evenly spread across the surface of the boron particle. The atomic maps were also able to identify the location of the trace contaminants previously mentioned, which were also evenly spread across the particle's surface.

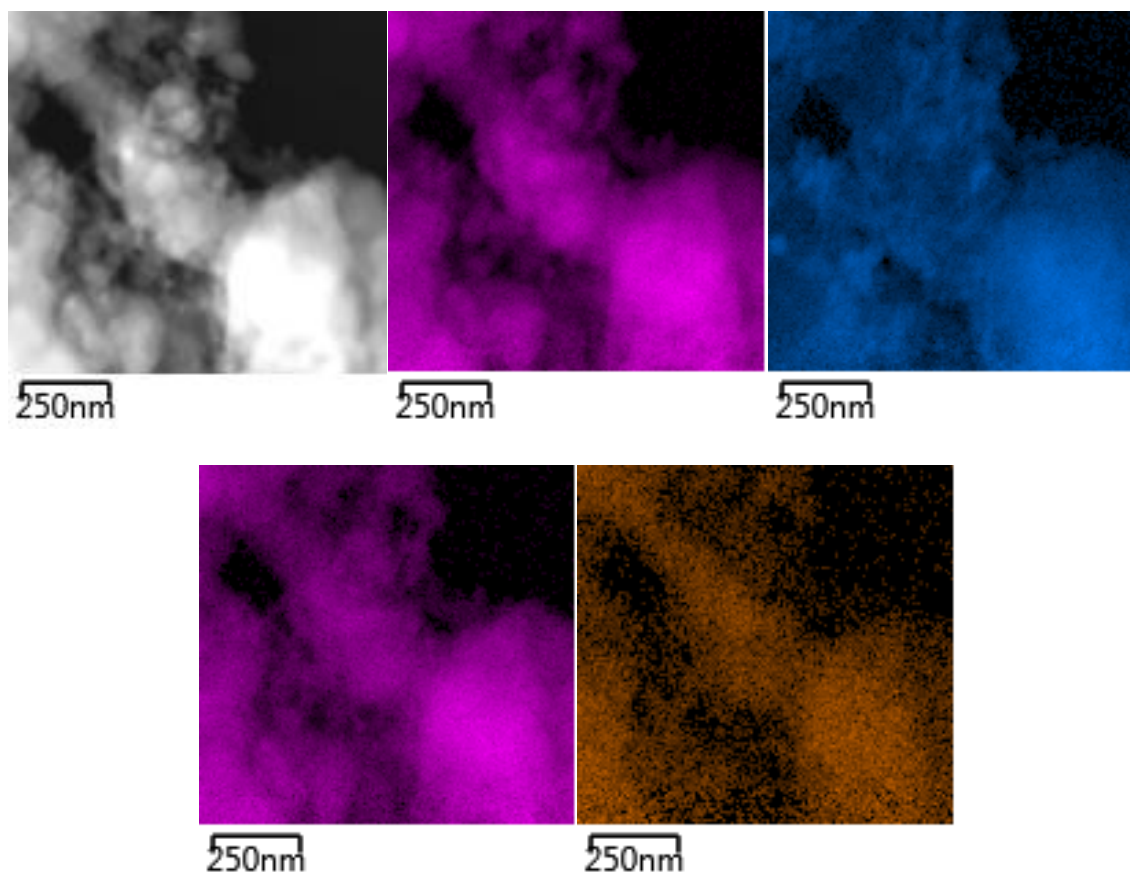


Figure 53. Atomic surface maps of a single boron nano-particle. (a) plain particle surface, (b) atomic boron [B] map, (c) atomic oxygen [O] map, (d) atomic magnesium [Mg] map, and (e) atomic iron [Fe] map.

6.3.4. Micro-Magnesium Particles

The magnesium micro-particles utilized herein (US-1060) were obtained from US Research Nanomaterials, Inc. The manufacturer indicates the purity of the magnesium is 99.9% minimum with trace amounts of copper (<0.02%); manganese, potassium, and

sodium (<0.01%); nitrogen and oxygen (<0.006%); iron, silicon, and sulfur (<0.005%); carbon (<0.003%); nickel and cobalt (<0.002%); and aluminum, calcium, and lead (<0.001%). Particles are reported to be irregular with an average particle size of 40 μm .

SEM images of the magnesium micro-particles at increasing magnification are shown in Figure 54. The magnesium particles have an average particle size on the order of 40 μm with a narrow distribution and flake-like geometries.

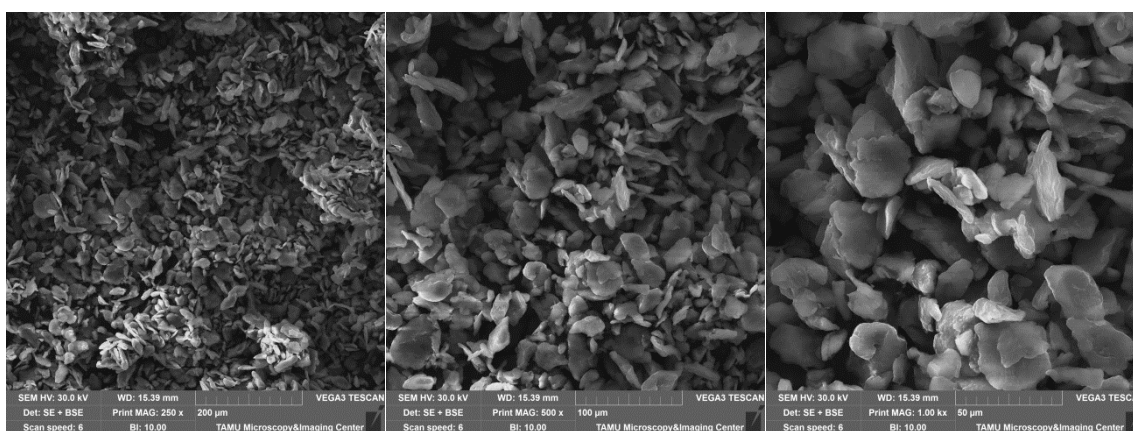


Figure 54. SEM images of magnesium micro-particles at increasing magnification.

6.3.5. Micro-Titanium Particles

The titanium micro-particles utilized herein (US-1038M) were obtained from US Research Nanomaterials, Inc. The manufacturer indicates the purity of the titanium is 99% minimum with trace amounts of iron (<0.05%); nickel (<0.038%); carbon and silicon (<0.028%); molybdenum (<0.002%); and aluminum (<0.0033%). Average particle size is reported as 45 μm , but no morphology is indicated.

SEM images of the titanium micro-particles at increasing magnification are shown in Figure 55. The titanium particles have an average particle size on the order of 45 μm with a wide distribution and irregular geometries.

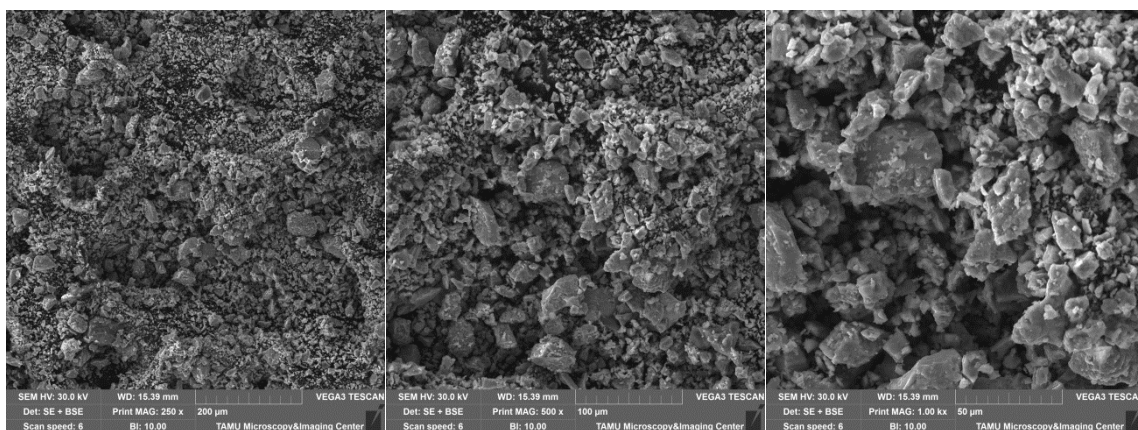


Figure 55. SEM images of titanium micro-particles at increasing magnification.

6.3.6. Micro-Zirconium Particles

The zirconium micro-particles utilized herein (US-1040M) were obtained from US Research Nanomaterials, Inc. The manufacturer indicates the purity of the zirconium is 99% minimum with trace amounts of tin (<0.3%); iron (<0.2%); hydrogen and magnesium (<0.1%); silicon (<0.08%); aluminum (<0.05%); and calcium and chlorine (<0.02%). Average particle size is reported as 75 μm , but no morphology is indicated.

SEM images of the zirconium micro-particles at increasing magnification are shown in Figure 56. The zirconium particles have an average particle size on the order of 75 μm with a wide distribution and irregular geometries.

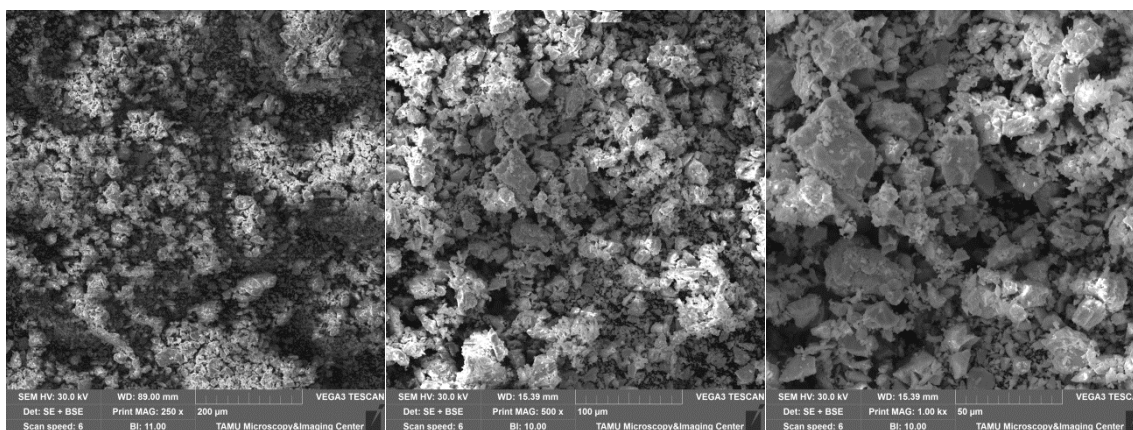


Figure 56. SEM images of zirconium micro-particles at increasing magnification.

6.3.7. Magnesium-Coated Nano-Boron Particles

The magnesium-coated boron (MgB) nano-particles utilized herein (US-1040M) were donated by Mach I Specialty Chemicals, Inc. and were recently developed in their R&D department. Their proprietary process begins with virgin SB95 boron nano-particles, which were previously discussed, and coats them in a 20% atomic loading (36% by mass) of magnesium.

TEM images of the MgB nano-particles at increasing magnification are shown in Figure 57. In general, the MgB particle sizes and morphologies appear similar to that of the virgin SB95 boron nano-particles.

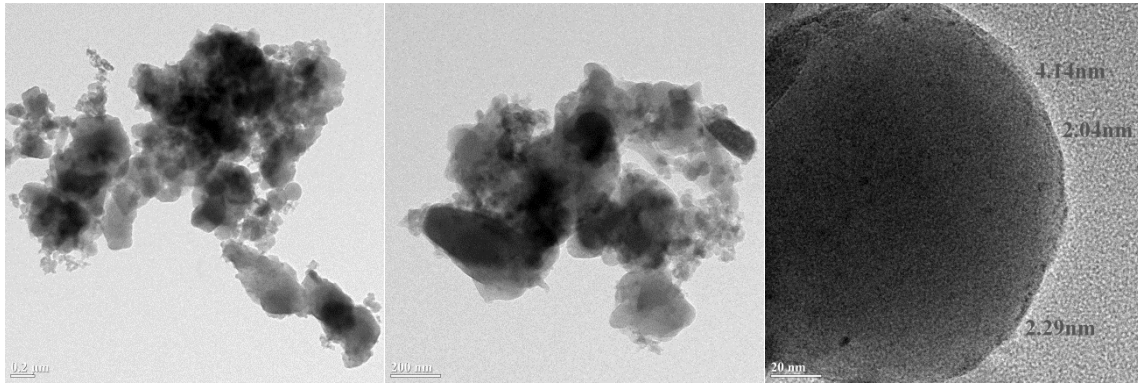


Figure 57. TEM images of magnesium-coated boron nano-particles at increasing magnification.

EDS analysis was utilized at three different sites within the MgB nano-particle sample to determine the average particles' composition and the results are presented in Table 8. The particles are mostly composed of amorphous boron (~63%) and magnesium (~24%) with a notable concentration of oxygen (~10%), and trace amounts of cobalt, iron, calcium and silicon. The EDS spectra collected also contained traces of several other elements (aluminum, barium, calcium, cadmium, chlorine, cobalt, copper, manganese, nitrogen, sodium, nickel, and lead) which were below the threshold of the composition measurement (0.1%). In comparison to the SB95 boron nano-particles, the MgB nano-particles have a significantly higher concentration of magnesium, as expected, but also have a significantly higher concentration of absorbed oxygen (2%→10%).

Table 8. Chemical compositions of boron nano-particles measured with EDS analysis.

Element	Concentration (wt %)
B	63.3 ± 14.7
Mg	23.8 ± 6.4
O	10.3 ± 5.8
Co	1.3 ± 1.2
Fe	1.2 ± 1.2
Ca	0.2 ± 0.1
Si	0.1 ± 0.1

Atomic maps of a single MgB particle's surface are shown in Figure 58 for (b) boron, (c) magnesium, and (d) oxygen. In general, the contaminant atoms are evenly spread across the surface of the boron particle. The atomic maps were also able to identify the location of the trace contaminants previously mentioned, which were also evenly spread across the particle's surface.

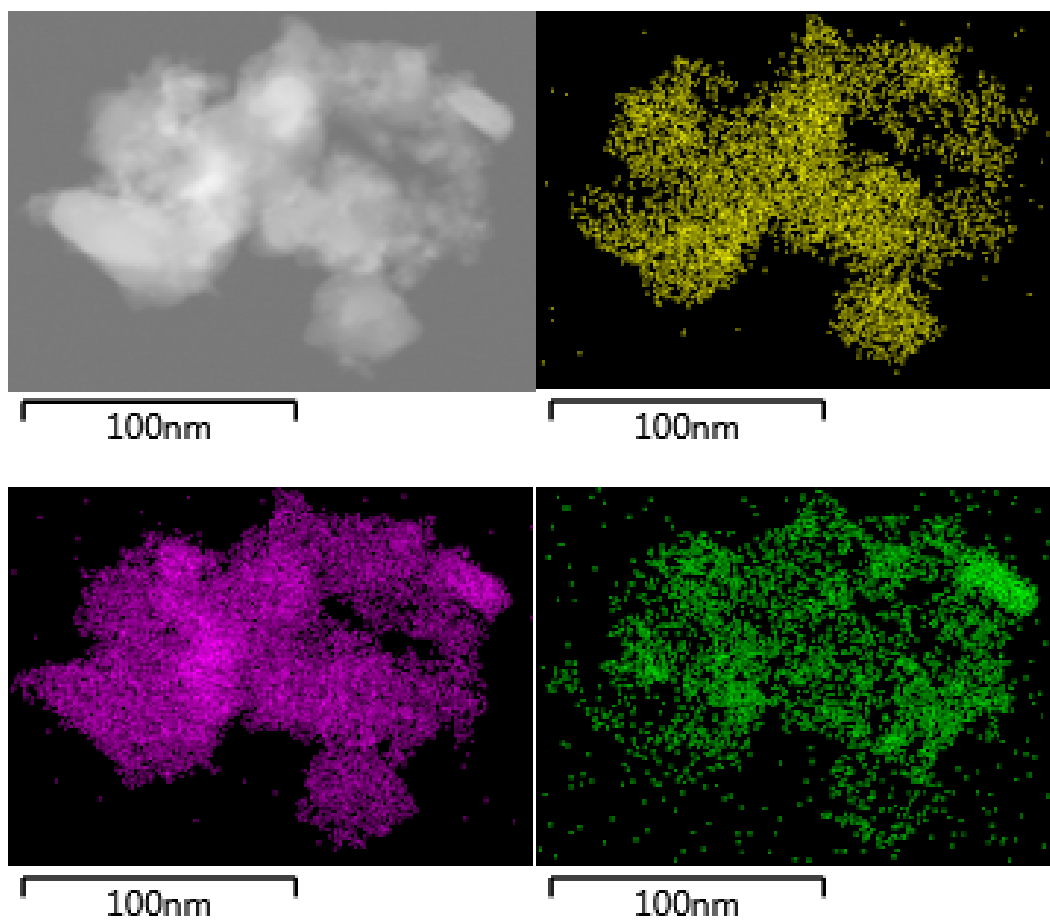


Figure 58. Atomic surface maps of a single boron nano-particle. (a) plain particle surface, (b) atomic boron [B] map, (c) atomic magnesium [Mg] map, and (d) atomic oxygen [O] map.

7. EXPERIMENTAL METHODOLOGY: FUEL GRAIN MANUFACTURING

Fuels grains manufactured herein are composed of HTPB R45M, isophorone diisocyanate (IDPI), paraffin, and metallic additives. The HTPB R45M pre-polymer, IPDI curative, and paraffin wax (FR 3032) were obtained from Firefox Enterprises LLC, Sigma Aldrich, and the CanleWic Company, respectively. The metallic additives have been previously characterized and discussed in Chapter 6 of the thesis.

Each fuel grain type (baseline, mixed-fuel, or metal-loaded) requires a unique set of manufacturing methods to achieve high-quality, void-free specimen for ballistic testing. This section of the thesis serves to document the calculations utilized in formulating fuel composition and the processes utilized in their manufacturing.

7.1. Curing Calculations

The fuel formulations herein consist of an isocyanate curative, hydroxyl-terminated polymer, and metallic fuels. The chemical cure ratio, r_c , is defined as the number of isocyanate reactive groups (-NCO) in the curative to the number of hydroxyl reactive groups (-OH) in the polymer. The mechanical properties of the cured polymer are largely dependent on the degree of crosslinking [457-458] which is determined by the polyfunctional groups in the polyurethane [459-463] and the chemical cure ratio of the composite system [460, 462]. Fuel systems manufactured herein utilized a chemical cure ratio of 1.00, which has been shown to yield a high fuel strength and ductility. [460, 462]

The equivalent weight, EW , of the curative and polymer is defined as the mass of each compound that delivers one mole of reactant groups to the curing reaction, and is

typically provided by the manufacturer. The mass curative ratio, r_m , is the mass ratio of polymer to curative and can be written in terms of the equivalent weights of each of these components:

$$r_m = \frac{m_{polymer}}{m_{curative}} = \frac{EW_{polymer}}{EW_{curative}} \times r_c^{-1} \quad (47)$$

The equivalent weight of IPDI is 113.4 and the equivalent weight of the HTPB R45M utilized herein is 1184, yielding a mass curative ratio of 10.44. During the fuel grain manufacturing procedure, which is described in the following section, the ingredients are measured and mixed in order of polymer, curative, and metallic additive. The mass of curative required for a given mass of polymer is given by:

$$m_{curative} = r_m^{-1} \times m_{polymer} \quad (48)$$

The total fuel system, binder (polymer and curative mixture), and metal additive mass can be written, respectively, as:

$$m_{Total} = m_{binder} + m_{metal} \quad (49)$$

$$m_{binder} = m_{polymer} + m_{curative} = m_{polymer} \times (1 + r_m^{-1}) \quad (50)$$

$$m_{metal} = \alpha_{metal} \times m_{Total} \quad (51)$$

where α_{metal} is the mass loading of the metal additive in the final fuel system. The total mass of metal for a given binder or polymer mass is then given by:

$$m_{metal} = \left(\frac{\alpha_{metal}}{1 - \alpha_{metal}} \right) \times m_{binder} = \left(\frac{\alpha_{metal}}{1 - \alpha_{metal}} \right) \times (1 + r_m^{-1}) \times m_{polymer} \quad (52)$$

Equation (52) can be generalized to all other additives, as well, and is not particular to metallic additives. Equations (28) and (52) are typically utilized for convenience during fuel mixing processes, which are further described in the following section.

7.2. Manufacturing Procedures

Optimum in-house motor manufacturing procedures of hydroxyl terminated polybutadiene (HTPB) hybrid fuel grains, with and without various additives, have been developed at Texas A&M University through a combination of previous experience with solid propellants, a detailed review of commercial and university manufacturing methods, and a trial-and-error testing process. This section of the thesis serves to detail these manufacturing processes and is separated into three sections which describe manufacturing of baseline fuel specimen (plain HTPB), fuel specimen containing metallic additives, and mixed-fuel specimen (HTPB and paraffin). Fuel formulation and curing calculations have been previously presented and are not given within this section. Sets of representative mixed-fuel and metal-loaded fuel grains are shown in Figures 59 and 60, respectively.



Figure 59. Representative mixed-fuel grains. (left to right) Plain HTPB, HTPB containing 0%, 10%, 25%, 50%, 75% paraffin, and plain paraffin.

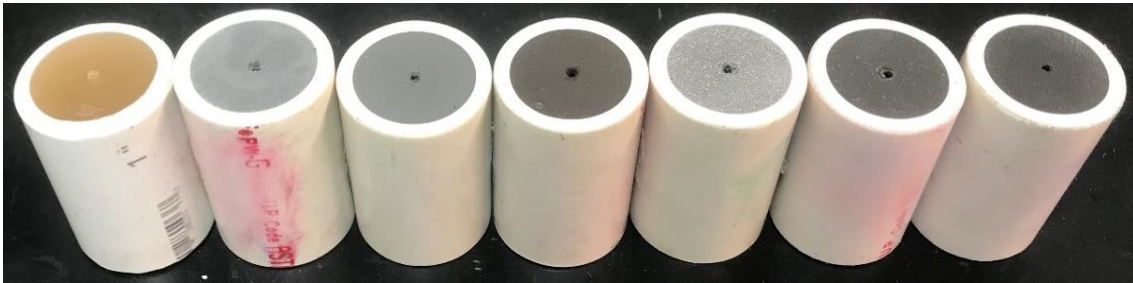


Figure 60. Representative metal-loaded fuel grains. (left to right) Plain HTPB and HTPB containing 10% micro-Al, nano-Al, nano-B, micro-Mg, micro-Ti, and micro-Zr particles.

7.2.1. Baseline (HTPB) Fuel Specimen

This section details the manufacturing procedures for fuel specimen composed of plain HTPB. The motor mold includes several 1" schedule 40 PVC components (pipe, coupling, and end-cap) and sheets of Saran wrap and wax paper, all of which are shown in Figure 61.

7.2.1.1. Pre-Mixing Mold Preparation

- 1) Cut a 1" schedule 40 PVC pipe to ~10" in length on a horizontal band saw. Sand both ends to a smooth finish on a bench-top sander. Slightly chamfer the outer edges of the PVC pipe by hand with a piece of sand paper.
- 2) Clean a 1" schedule 40 PVC coupling and the PVC pipe from step 7.2.1.1.1 with soap and water. Thoroughly dry all components with a paper towel.
- 3) Insert a 1" schedule 40 PVC end-cap into the PVC coupling.
- 4) Cut a 3"×3" square of Saran wrap and wax paper. Place the Saran wrap square on top of the open side of the PVC coupling. Place the wax paper square on top of the Saran wrap square.

- 5) Slowly insert the PVC pipe into the coupling, on the side covered by the Saran wrap and wax paper squares, in a twisting motion. Care should be taken not to tear or rip the Saran wrap and wax paper sheets.



Figure 61. Unassembled mold components for baseline (plain HTPB) fuel specimen.

7.2.1.2. Fuel Mixing

- 1) Clean a 250-mL glass beaker and a glass stirring rod with soap and water, and dry thoroughly with a paper towel.
- 2) Clean the beaker and stirring rod with acetone, and dry thoroughly with a lint-free wipe.
- 3) Measure out HTPB pre-polymer (~70 g) on a high-resolution scale (≤ 0.01 g resolution).
- 4) Add the required amount of curative to the pre-polymer.
- 5) Mix thoroughly (~10 minutes).
- 6) Vacuum out entrained air. (See Figure 62)
 - 1) Place the mixture inside of a vacuum chamber.
 - 2) Increase vacuum level (via needle valve) until the mixture is near the top of the beaker.
 - 3) Rapidly decrease the vacuum level (open to atmosphere).

- 4) Repeat steps 7.2.1.2.6.2 – 7.2.1.2.6.3 until the maximum vacuum level can be applied without the fuel mixture overflowing the beaker.
- 5) Allow adequate time for all entrained air bubbles to be removed from the fuel.
- 6) Remove sample from the vacuum chamber.



Figure 62. (left) Fuel mixture after mixing containing entrained air bubbles in atmosphere, (middle) fuel mixture containing entrained air bubbles under vacuum, and (right) fuel mixture containing no entrained air bubbles.

7.2.1.3. Post-Mixing Mold Preparation

- 1) Tilt the motor mold at an angle of $\sim 45^\circ$ and slowly pour the processed fuel mixture into the mold. Care should be taken to minimize the amount of air that becomes entrained during pouring. The fuel mixture should be poured to a height just above 6".
- 2) Vacuum out entrained air. (See step 7.2.1.2.6)

7.2.1.4. Fuel Curing

- 1) Place the motor mold containing the vacuumed fuel mixture upright inside of an oven at 63 °C.
- 2) Allow adequate time (~1 week) for the motor to fully cure before removing it from the oven.
- 3) Allow the motor adequate time to cool (~1 hour) before post-processing.

7.2.1.5. Post-Curing Mold Preparation

- 1) Place the top portion of the motor (without the PVC coupling) snugly in a vise.
- 2) Remove the PVC coupling with channel locks by applying an upward force with a twisting motion.
- 3) Cut the end of the PVC without fuel off on a horizontal band saw.
- 4) Cut the motor into multiple fuel grains of desired length (~5 cm).
- 5) Sand both ends of each fuel grain to a smooth finish on a bench-top sander. Slightly chamfer the outer edges of the PVC pipe by hand with a piece of sand paper.
- 6) Drill a 2-mm hole through the center of the motor on a lathe.

7.2.2. Mixed (HTPB/Paraffin) Fuel Specimen

This section details the manufacturing procedures for mixed-fuel specimen composed of HTPB and paraffin. The motor mold is the same as in the previous section outlined for baseline fuel specimen composed of plain HTPB, and is shown in Figure 61. It is worth noting that no vacuum cycle is required for the final mixed-fuel mixtures, as deaeration at atmospheric pressure is sufficient for air removal.

7.2.2.1. Pre-Mixing Mold Preparation

- 1) See steps 7.2.1.1 – 7.2.1.5.

7.2.2.2. Fuel Mixing

- 1) Clean (2) 250-mL glass beakers and a glass stirring rod with soap and water, and dry thoroughly with a paper towel.
- 2) Clean the beakers and stirring rod with acetone, and dry thoroughly with a lint-free wipe.
- 3) Measure out HTPB pre-polymer on a high-resolution scale (≤ 0.01 g resolution).
- 4) Add the required amount of curative to the pre-polymer.
- 5) Mix thoroughly (~10 minutes).
- 6) Vacuum out entrained air. (See step 7.2.1.2.6)
- 7) Measure out more than the required amount of paraffin in a separate beaker.
- 8) Heat both beakers on a hot plate to a temperature above the melting point of the paraffin (~75 °C). Allow the mixtures to sit at this temperature until all of the paraffin has melted.
- 9) Add the required amount of molten to the HTPB/curative mixture.
- 10) Mix thoroughly (~10 minutes) atop the hot plat to maintain the high temperature.

7.2.2.3. Post-Mixing Mold Preparation

- 1) Tilt the motor mold at an angle of $\sim 45^\circ$ and slowly pour the processed fuel mixture into the mold. Care should be taken to minimize the amount of air that becomes entrained during pouring. The fuel mixture should be poured to a height just above 6".

7.2.2.4. Fuel Curing

- 1) Place the motor mold containing the fuel mixture upright inside of an oven at 63 °C.
- 2) Allow adequate time (~1 week) for the pre-polymer to fully cure before removing it from the oven.
- 3) Allow the motor adequate time to cool (~1 hour) before post-processing.

7.2.2.5. Post-Curing Mold Preparation

- 1) See steps 7.2.1.5.1 – 7.2.1.5.6

7.2.3. Metal-Loaded Fuel Specimen

This section details the manufacturing procedures for fuel specimen composed of plain HTPB and metallic additives. The motor mold includes several 1" schedule 40 PVC components (pipe and threaded end-caps) and threaded metal fastener system, all of which are shown in Figure 63.

7.2.3.1. Pre-Mixing Mold Preparation

- 1) Cut a 1" schedule 40 PVC pipe to ~6" in length on a horizontal band saw. Sand both ends to a smooth finish on a bench-top sander. Slightly chamfer the outer edges of the PVC pipe by hand with a piece of sand paper.
- 2) Clean two 3/4" threaded schedule 40 PVC end-caps and the PVC pipe from step 3.1.1 with soap and water. Thoroughly dry all components with a paper towel.
- 3) Thoroughly coat the threads of one of the 3/4" threaded schedule 40 PVC end-caps with quick-dry silicone. Insert the end-cap into one side of the PVC pipe. Clean away excess silicone.



Figure 63. (top) Unassembled and (bottom) mold components for mixed-fuel (HTPB/paraffin) specimen.

7.2.3.2. Fuel Mixing

- 1) Clean a 250-mL glass beaker and a glass stirring rod with soap and water, and dry thoroughly with a paper towel.
- 2) Clean the beaker and stirring rod with acetone, and dry thoroughly with a lint-free wipe.
- 3) Measure out HTPB pre-polymer (~ 70 g) on a high-resolution scale (≤ 0.01 g resolution).
- 4) Add the required amount of metal additive to the mixture.
- 5) Mix thoroughly (~ 5 minutes). Ultrasonicate the mixture to decrease additive agglomeration (~ 5 minutes). Mix thoroughly (~ 5 minutes).
- 6) Vacuum out entrained air. (See Figure 62)

- 1) Place the mixture inside of a vacuum chamber.
- 2) Increase vacuum level (via needle valve) until the mixture is near the top of the beaker.
- 3) Rapidly decrease the vacuum level (open to atmosphere).
- 4) Repeat steps 7.2.3.2.6.2 – 7.2.3.2.6.3 until the maximum vacuum level can be applied without the fuel mixture overflowing the beaker.
- 5) Allow adequate time for all entrained air bubbles to be removed from the fuel.
- 6) Remove sample from the vacuum chamber.
- 7) Add the required amount of curative to the mixture.
- 8) Mix thoroughly (~10 minutes).
- 9) Vacuum out entrained air. (See step 7.2.3.2.6)

7.2.3.3. Post-Mixing Mold Preparation

- 1) Tilt the motor mold at an angle of $\sim 45^\circ$ and slowly pour the processed fuel mixture into the mold. Care should be taken to minimize the amount of air that becomes entrained during pouring. The fuel mixture should be poured to a height just below the top of the PVC pipe.
- 2) Insert the second threaded 3/4" schedule 40 PVC end-cap into the open side of the PVC pipe. Firmly press the end-cap down. Utilize the threaded fastener system (Figure 63) to fully insert the threaded end-cap into the pipe. Remove the fastener system.

- 3) Excess fuel should overflow and should be cleaned. Allow adequate time for the excess fuel to overflow (~10 minutes) before continuing.
- 4) Seal the end-cap with quick-dry silicone. Allow adequate time for the silicone to dry (~10 minutes).
- 5) Seal the entire motor mold within a Ziploc bag. Reapply the fastener system.

7.2.3.4. Fuel Curing

- 1) Place the motor mold horizontally on top of the roller (Figure 64) inside of an oven at 63 °C. the roller is utilized to avoid additive settling during the curing process.
- 2) Allow adequate time (~1 week) for the motor to fully cure before removing it from the oven.
- 3) Allow the motor adequate time to cool (~1 hour) before post-processing.



Figure 64. Roller assembly utilized to mitigate additive particle settling effects during fuel curing. Fully processed motors are shown.

7.2.3.5. Post-Curing Mold Preparation

- 1) Cut both end-caps off of the PVC on a horizontal band saw.
- 2) Cut the motor into multiple fuel grains of desired length (~5 cm).
- 3) Sand both ends of each fuel grain to a smooth finish on a bench-top sander. Slightly chamfer the outer edges of the PVC pipe by hand with a piece of sand paper.
- 4) Drill a 2-mm hole through the center of the motor on a lathe.

7.3. Fuel Density Measurements

The density of a motor's fuel, ρ_f , is given by:

$$\rho_f = \frac{m_f}{V_f} = (D_i^2 - D_p^2)^{-1} \left[\frac{4m_T}{\pi L_f} - \rho_{PVC} (D_o^2 - D_i^2) \right] \quad (53)$$

where m_f is the fuel mass in the motor, V_f is the fuel volume of the motor, L_f is the measured length of the motor (~5 cm), D_i is the inner diameter of the PVC tube or outer diameter of the fuel volume (2.61 cm), D_p is the combustion port diameter (2.0 mm), m_m is the measured mass of the motor, ρ_{PVC} is the density of the PVC pipe (~1.375 g/cm³), and D_o is the outer diameter of the PVC tube (3.34 cm). The fuel density is generally measured prior to drilling the combustion port, so that this value is set equal to zero in Equation (53).

The measured fuel densities of all fuel formulations manufactured herein are given in Table 9. The measurement uncertainty of the fuel density has been evaluated through a Kline-McClintock (root-sum-of-squares) uncertainty analysis, which is presented in Appendix D, and ranges from 3.5-4 kg/m³.

Table 9. Fuel Density Measurements.

Formulation	Additives	Density (kg/m ³)		Theoretical Maximum Density	
		Average	Standard Deviation	(kg/m ³)	(%)
Baseline	-	914	7	930	98
H90	10% Paraffin	892	17	924	97
H75	25% Paraffin	888	6	914	97
H50	50% Paraffin	882	17	898	98
H25	75% Paraffin	917	9	881	104
P100	100% Paraffin	852	10	865	98
μAl-10	10% micro-Al	999	8	995	100
μAl-20	20% micro-Al	1069	1	1070	100
μAl-30	30% micro-Al	1149	6	1158	99
μAl+nB-10	3.5% micro-Al, 6.5% nano-B	995	1	992	100
nAl-10	10% nano-Al	969	18	995	97
nAl-20	20% nano-Al	1043	10	1070	97
nAl+nB-10	3.5% nano-Al, 6.5% nano-B	1007	4	992	102
nB-10	10% nano-B	989	0	990	100
nB-20	20% nano-B	1043	19	1059	99
nB-30	30% nano-B	1144	0	1137	101
μMg-10	10% micro-Mg	972	5	975	100
μMg-20	20% micro-Mg	1008	7	1025	98
μMg-30	30% micro-Mg	1079	3	1081	100
μMg+nB-10	3.5% micro-Mg, 6.5% nano-B	970	11	985	98
μTi-10	10% micro-Ti	1001	3	1010	99
μTi-20	20% micro-Ti	1096	2	1105	99
μTi-30	30% micro-Ti	1207	4	1221	99
μTi+nB-10	3.5% micro-Ti, 6.5% nano-B	1015	1	997	102
μZr-10	10% micro-Zr	1011	5	1017	99
μZr-20	20% micro-zr	1099	11	1122	98
μZr-30	30% micro-Zr	1225	10	1252	98
μZr+nB-10	3.5% micro-Zr, 6.5% nano-B	999	0	999	100
nMgB-10	10% nano-MgB	989	1	986	100
nMgB-20	20% nano-MgB	1052	-	1049	100

8. EXPERIMENTAL METHODOLOGY: BALLISTIC TESTING

The design of the ballistic test stand has been described in Chapter 5 of the thesis, and this chapter serves to document ballistic testing procedures and data reduction methods. Several steps precede motor firing in the rocket chamber. All pressure transducers and the load cell are calibrated, and all mechanical connections on the test stand are checked for their integrity. The solenoid valve, mass flow controller, and ignition power system are checked to ensure they are working properly. The testing site is secured by testing personnel to ensure no one is in the vicinity of the testing rig during motor firing.

Immediately preceding motor firing, the rocket chamber is prepared. The fuel grain is loaded into the chamber, and all chamber connections and diagnostic ports are tightly sealed. The chamber is secured to the linear bearing with U-bolts and flange nuts. The injector hose, chamber pressure hose, and ignition leads are connected to their corresponding components. Testing personnel return to the control room which is isolated from the testing stand.

The test is initiated when the oxidizer solenoid valve is remotely opened (blowdown orientation) or the mass flow controller is engaged (steady flow orientation), which allows oxidizer to flow through the system. The oxidizer flow triggers the oscilloscope which begins recording data. After a short time, approximately 1 second, the ignition system is powered and the motor begins to burn. After a predetermined testing

time, between 2-10 seconds, oxidizer flow is terminated and the motor extinguishes. The testing site is secured and checked for testing anomalies.

8.1. Data Reduction

One motor firing produces a significant amount of data, that when properly analyzed can yield useful information about the fuel composition's combustion behavior. A representative set of transient data for a baseline HTPB fuel grain burning in GOX with a constant oxidizer mass flow rate is shown in Figure 65. The upstream oxidizer pressure, combustion chamber pressure, oxidizer mass flowrate, and thrust force are indicated by the magenta, red, green, and blue lines, respectively. Important events in the testing process are highlighted in this figure. The spike in combustion chamber pressure and thrust at approximately 1 second correspond to ignition of the motor. The steady-state chamber pressure is indicated by a dashed line at approximately 75 psia. The oxidizer flow is terminated at approximately 3.5 seconds when the oxidizer mass flowrate sharply decreases. However, the motor firing is not considered 'complete' until the chamber pressure drops below 75% of the steady state value. The motor burn time is taken between this point and the time of ignition.

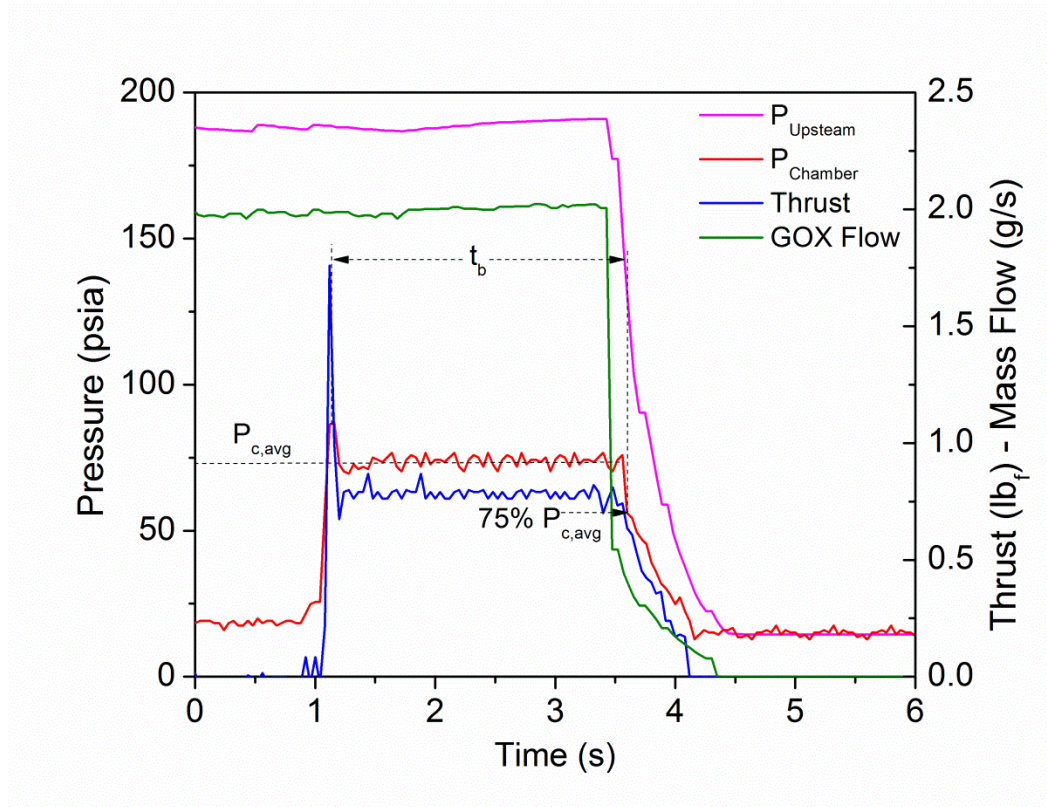


Figure 65. Representative set of transient data traces for plain HTPB burning in GOX.

The mass of the motor and diameter of the combustion port are recorded before and after each test for data reduction. Telescoping gauges and a digital caliper can be utilized to make measurements of the port diameter at several locations along the length of its axis. In the current studies, the final diameter of the combustion port after each motor firing was not directly measured, but was calculated according to:

$$D_f = \left[\frac{4(m_i - m_f)}{\pi \rho_f L_f} + D_i^2 \right]^{1/2} \quad (54)$$

where m_i and m_f are the initial and final mass of the motor, respectively, and D_i is the initial diameter of the combustion port. The average regression rate for the motor firing can be calculated according to:

$$\bar{r} = \frac{D_f - D_i}{2t_b} \quad (55)$$

where D_f is the final combustion port diameters and t_b is the burn time of the motor firing. The initial and final combustion port diameters are spatially averaged and the regression rate computed is spatially and temporally averaged.

When the stand is operated in the blowdown oxidizer flow configuration, the oxidizer mass flow rate decreases during the motor firing, and the average oxidizer mass flux is given by the ideal gas law applied to the oxidizer tank:

$$\bar{m}_{ox} = \frac{\Delta m_{ox}}{t_{ox}} = \frac{MV(P_{ox,i} - P_{ox,f})}{R_u T_0 t_{ox}} \quad (56)$$

where Δm_{ox} the change in mass in the oxidizer tank, t_{ox} is the total time of oxidizer flow, V is the volume of the oxidizer tank, and $P_{ox,i}$ and $P_{ox,f}$ are the initial and final pressures in the oxidizer tank, respectively. The transient oxidizer mass flux is evaluated according to choked flow equations and an empirically determined discharge coefficient. In the current study, the ballistic stand was only operated in the steady-flow mode, and the oxidizer mass flowrate was measured by the mass flow controller.

The average oxidizer mass flux, \bar{G}_{ox} , can be computed through several different methods. Karabeyoglu et al. [464-465] showed that the evaluation method can have a significant effect on the final value and that utilizing the average diameter of the combustion port yields the most accurate results. Accordingly, the average oxidizer mass flux is given by:

$$\bar{G}_{ox} = \frac{16\bar{m}_{ox}}{\pi(D_i + D_f)^2} \quad (57)$$

where \bar{m}_{ox} is the average oxidizer mass flow rate and \bar{A}_c is the average cross-sectional area of the combustion port. The average fuel mass loss rate is given by:

$$\bar{m}_f = \frac{m_i - m_f}{t_b} \quad (58)$$

The average oxidizer-to-fuel mass ratio is then given by:

$$\frac{O}{F} = \frac{\bar{m}_{ox}}{\bar{m}_f} \quad (59)$$

The time-averaged characteristic velocity of the motor burn can be calculated with the chamber pressure data according to:

$$\bar{c}^* = \frac{1}{t_b} \int c^* dt \cong \frac{\bar{P}_c A_t}{t_b (\bar{m}_{ox} + \bar{m}_f)} \quad (60)$$

where \bar{P}_c is the average chamber pressure. Note that the approximately equal to sign has been used because utilizing the average properties in this calculation introduces some error. The theoretical characteristic velocity for the motor burn, c_{th}^* , is evaluated with thermochemical equilibrium programs at the average chamber pressure and oxidizer-to-fuel ratio. The characteristic velocity or combustion efficiency is then given by:

$$n_{c^*} = \frac{\bar{c}^*}{c_{th}^*} \quad (61)$$

The characteristic chamber length, L^* , is defined as the length a post-combustion chamber of the same volume would have if it were a straight tube and had no converging nozzle section. [11] It can be written as:

$$L^* = \frac{V_c}{A_t} \quad (62)$$

where V_c is the post-combustion chamber volume which includes the converging section of the nozzle and A_t is the throat area. For the experimental apparatus described herein,

the post-combustion chamber volume includes the converging section of the nozzle, a cylindrical section whose diameter is set by the chamber spacer and whose length is set by the length of the fuel grain being tests, and the combustion port itself. Only one-half of the combustion port volume is considered herein since this is the average volume that ejected fuel atoms experience during the motor firing. The post-combustion chamber volume can be written as:

$$V_c = \frac{\pi}{4} \left[D_c^2 (L_c - L_f) + \frac{(D_c^3 - D_t^3)}{6} + \frac{L_f (D_i + D_f)^2}{8} \right] \quad (63)$$

where D_c is the diameter of the combustion chamber spacer (2.80 cm), L_c is the length of the combustion chamber (10.65 cm), L_f is the length of the fuel grain ($\cong 5$ cm), D_t is the throat diameter (3.175 mm), and D_i and D_f are the initial and final combustion port diameters, respectively. Accordingly, the characteristic chamber length can be written as:

$$L^* = \frac{1}{D_t^2} \left[D_c^2 (L_c - L_f) + \frac{(D_c^3 - D_t^3)}{6} + \frac{L_f (D_i + D_f)^2}{8} \right] \quad (64)$$

Typical values for the post-combustion chamber length and characteristic chamber length, assuming a fuel grain length of 5 cm and disregarding the combustion port volume contribution, are 37.7 cm³ and 476 cm, respectively. The residence time of the propellant combustion products, t_r , is the average value of time spent by each molecule or atom within the chamber volume and is given by:

$$t_r = \frac{V_c \rho_c}{\dot{m}_T} \quad (65)$$

where ρ_c is the average density of the combustion products and \dot{m}_T is the total mass flow rate through the nozzle. The combustion product density, similar to the characteristic

velocity, evaluated with thermochemical equilibrium programs at the average chamber pressure and oxidizer-to-fuel. The residence time can be rewritten as:

$$t_r = \frac{\pi \rho_c}{4(\dot{m}_{ox} + \dot{m}_f)} \left[D_c^2 (L_c - L_f) + \frac{(D_c^3 - D_t^3)}{6} + \frac{L_f (D_t + D_f)^2}{8} \right] \quad (66)$$

In addition to the average property calculations previously outlined, two separate burn reconstruction algorithms are implemented in some cases to analyze the transient combustion data. An in-house developed burn reconstruction code, based primarily on the hybrid rocket model previously outlined in Chapter 4, assumes the regression rate is well-known based upon the measured empirical constants and allows for evaluation of a transient combustion efficiency during the burn. The alternative algorithm, developed by George et al. [213] assumes the combustion efficiency is constant and allows for evaluation of the transient regression rate. The transient combustion efficiency and regression rate reconstruction techniques utilize the measured change in diameter and mass, respectively, to converge to the computation to applicable values. The details of these algorithms are not discussed herein since they are not applied to the current datasets.

9. RESULTS AND DISCUSSION: METAL LOADED FUEL SYSTEMS

Solid fuel grains composed of plain HTPB and HTPB loaded with metallic additives have been manufactured according to the procedures detailed in Chapter 7. A minimum of two solid fuel grains were manufactured for each metallic additive (micro-aluminum, micro-magnesium, micro-titanium, micro-zirconium, nano-aluminum, nano-boron, and magnesium-coated nano-boron) at three separate loadings (10%, 20%, and 30%). This combination of fuel compositions allowed for the independent parametric evaluation of the effects of each metallic additive and their relative loading on the solid fuels' ballistic performance. Additionally, solid fuel grains containing a mixture of each additive and nano-boron were also manufactured at a loading of 10% (6.5% nano-boron and 3.5% other) to evaluate the synergistic effects of each additive on nano-boron combustion performance.

Each solid fuel grain was fired in GOX a minimum of three times, and the regression rates and combustion efficiencies were computed according to the data reduction methods described in Chapter 8. Additionally, the condensed combustion products ejected through the nozzle were collected for the motor firings of fuel compositions containing a mass loading of 30%. The collected combustion residue was analyzed with SEM and EDS diagnostics to determine the general chemistry of the specimen.

9.1. Micro-Aluminum Fuels

The regression rates of plain HTPB and HTPB loaded with micro-aluminum burning in GOX are shown in Figure 66. Motor firings of plain HTPB are represented by open black circles, and motor firings of HTPB loaded with 10%, 20%, and 30% micro-aluminum are represented by solid blue squares, solid green triangles, and solid red diamonds, respectively. Error bars are shown for both the baseline and 30% loading formulations in the regression rate plot, as is the case for all regression rate plots given in this section of the thesis. These error bars are derived from a Kline-McClintock (root-sum-of-squares) uncertainty analysis which is further detailed in Appendix D. The regression rate data of each formulation have been correlated with a traditional power law, Equation (1), and the corresponding empirical coefficients are given in the regression rate plot and in Table 10 at the end of this section.

In general, the inclusion of micro-aluminum in the solid fuel reduced the observed regression rate. This trend is more observable at higher oxidizer mass fluxes and higher additive loadings. This finding is in direct conflict with most of the data available in the literature which indicate the inclusion of micro-aluminum yields regression rate enhancement in solid fuel combustion.

The reaction time of aluminum particles has been shown to be dependent on pressure [466] which could play a significant role in the observed trends. More explicitly, the data collected herein were for motor firings at approximately 75-100 psia, which is lower than previous investigations where regression rate enhancement due to aluminum inclusion was observed. For example, Strand et al. [240-242], George et al. [213],

Chiaverini et al. [243], Risha et al. [249-253], and Evans et al. [248, 254-25] observed regression rate enhancement for ballistic testing at pressures of approximately 170-180, 290, 170-800, 335-665, and 315-615 psia, respectively. These regression rate enhancements are generally attributed to energy release from metal oxidation near the surface of the fuel and enhanced radiation heat fluxes. [54] However, if the aluminum is not reacting rapidly enough due to the lower-pressure environment, oxidation and combustion may not take place in the combustion port fuel grain and instead in the post-combustion chamber.

Strand et al. [240-242] observed that micro-aluminum additives included in HTPB burning in GOX would agglomerate on the fuel surface and periodically detach from the surface. This accumulated surface layer acts as a thermal isolator and hinders heat transfer from the diffusion flame to the solid fuel, which is termed the blowing effect. Increased loading of micro-aluminum led to further decreases in the observed regression rate. This trend is likely due to accumulation of more agglomerations and additive mass on the fuel surface which further decreases the heat flux that reaches the virgin fuel.

At moderate oxidizer mass fluxes, mass diffusion processes dominate the fuel regression rate behavior, but at lower oxidizer mass fluxes, thermal radiation processes dominate the regression behavior. [11] The reduced regression rates accompanied by micro-aluminum addition are more observable at higher oxidizer mass fluxes which results in a decreased oxidizer mass flux exponent (n). This observation may indicate that there is some combustion of the aluminum in the combustion port yielding enhanced radiation heat transfer.

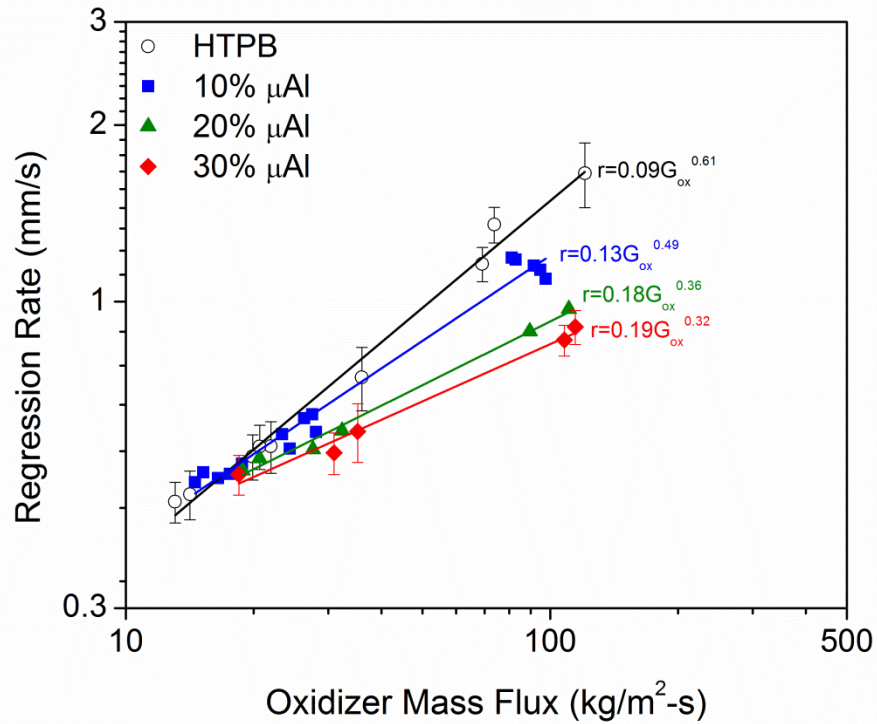


Figure 66. Regression rates of plain HTPB and fuel samples loaded with 10%, 20%, and 30% micro-aluminum.

The combustion efficiencies of plain HTPB and HTPB loaded with micro-aluminum burning in GOX are shown in Figure 67. Once again, motor firings of plain HTPB are represented by open black circles, and motor firings of HTPB loaded with 10%, 20%, and 30% micro-aluminum are represented by solid blue squares, solid green triangles, and solid red diamonds, respectively. Error bars are shown for the baseline formulation in the combustion efficiency plot, as is the case for all combustion efficiency plots given in this section of the thesis. These error bars are derived from a Kline-McClintock (root-sum-of-squares) uncertainty analysis which is further detailed in Appendix D.

Generally, the measured combustion efficiencies of hybrid rocket experiments are plotted against the average O/F ratio. However, these types of plots yielded no general trends in the current investigation. Alternatively, the measured combustion efficiencies of all motor firings are plotted against the residence time of the fuel reaction. In general, the combustion efficiency of all motor firings increases with increasing residence time, as expected. Furthermore, the combustion efficiencies of the plain and all of the micro-aluminized motors collapse onto a single trend which approaches a combustion efficiency of 100% near a residence time of 75 ms. These observations suggest that although chemistry (O/F ratio) probably does play a role in determining the combustion efficiency of hybrid rockets, the residence time is the more dominant factor. Furthermore, given the simplistic design of the current ballistic stand, the current results also suggest that high combustion efficiencies can be achieved without post-combustion mixing devices if sufficient post-combustion chamber volume is included in the HRE design.

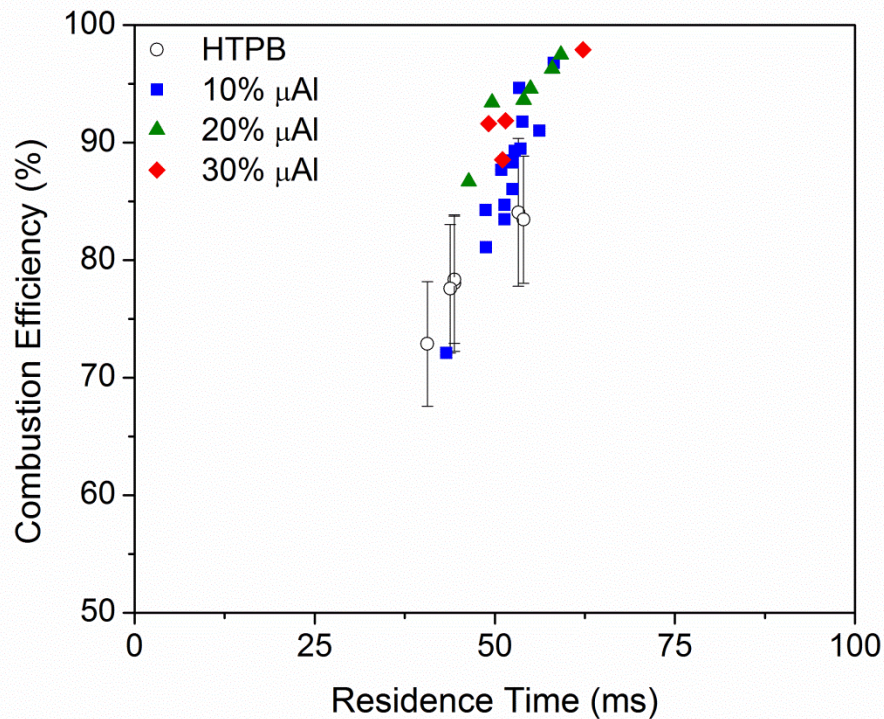


Figure 67. Combustion efficiencies of plain HTPB and fuel samples loaded with 10%, 20%, and 30% micro-aluminum.

SEM images of the combustion residue collected for an HTPB fuel loaded with 30% micro-aluminum burning in GOX at an average O/F ratio of 2.4 is shown in Figure 68. Due to the large amount of mass collected on the specimen, individual particles are not discernible and these particles appear to have agglomerated and sintered into a single layer. EDS analysis was performed on the collected residue layer, and the resultant aluminum, oxygen, and carbon atomic maps are shown in Figure 69. In general, the oxygen (64%) and aluminum (33%) atoms account for most of the surface layer and completely encompass the map, which suggests that the majority of the aluminum is reacted. Elemental compositional analysis of the EDS spectra showed that the ratio of

O/Al is 1.9 which is greater than the ratio in the standard aluminum oxide (Al_2O_3 – O/Al = 1.5) indicating efficient combustion. This finding is in agreement with the high measured combustion efficiency (92%) for the motor firing.

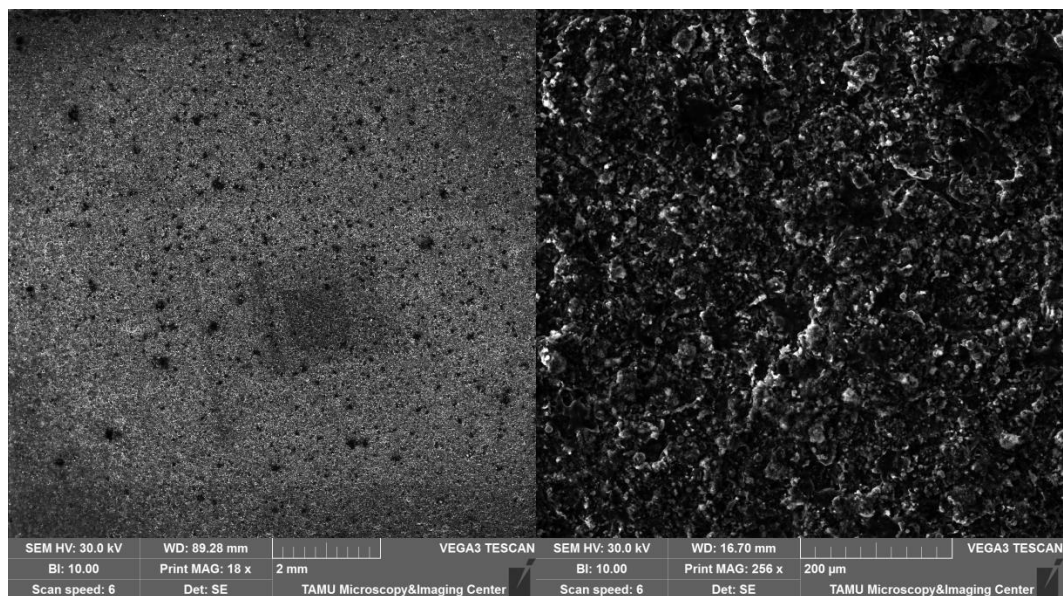


Figure 68. SEM analysis of the combustion residue collected during the motor firing of HTPB loaded with 30% micro-aluminum burning in GOX.

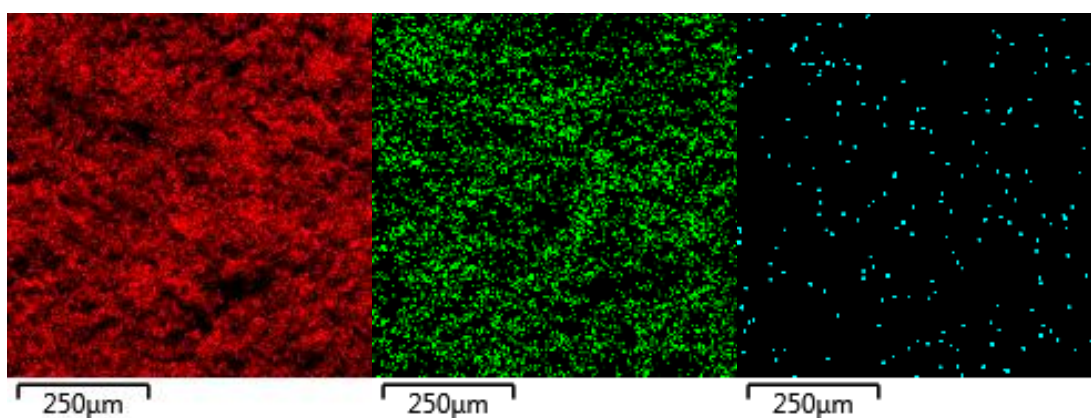


Figure 69. EDS analysis of the combustion residue collected during the motor firing of HTPB loaded with 30% micro-aluminum burning in GOX. Atomic maps show the overlay of (red) aluminum, (green) oxygen, and (blue) carbon.

9.2. Micro-Magnesium Fuels

The regression rates and combustion efficiencies of plain HTPB and HTPB loaded with micro-magnesium burning in GOX are shown in Figures 70 and 71, respectively. Once again, motor firings of plain HTPB are represented by open black circles, and motor firings of HTPB loaded with 10%, 20%, and 30% micro-magnesium are represented by solid blue squares, solid green triangles, and solid red diamonds, respectively

In general, the inclusion of micro-magnesium in the solid fuel reduced the observed regression rate. Once again, this trend is more observable at higher oxidizer mass fluxes and higher additive loadings. These observations are attributed to slow metal additive reactions which likely mostly take place in the post-combustion chamber and an increased accumulation of mass on the fuel surface.

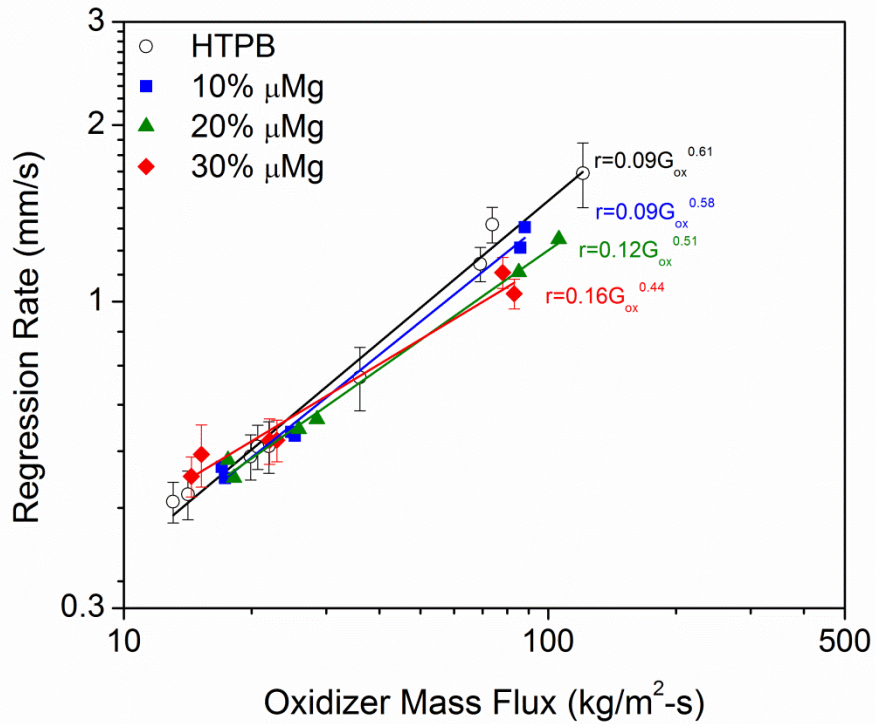


Figure 70. Regression rates of plain HTPB and fuel samples loaded with 10%, 20%, and 30% micro-magnesium.

The combustion efficiency of HTPB fuels loaded with micro-magnesium increases with increasing residence time. Although the combustion efficiency data shown in Figure 71 appear to collapse onto a single trend within the measurement uncertainty of the experiment, the data suggest that higher loadings of micro-magnesium require longer residence times to combust efficiently.

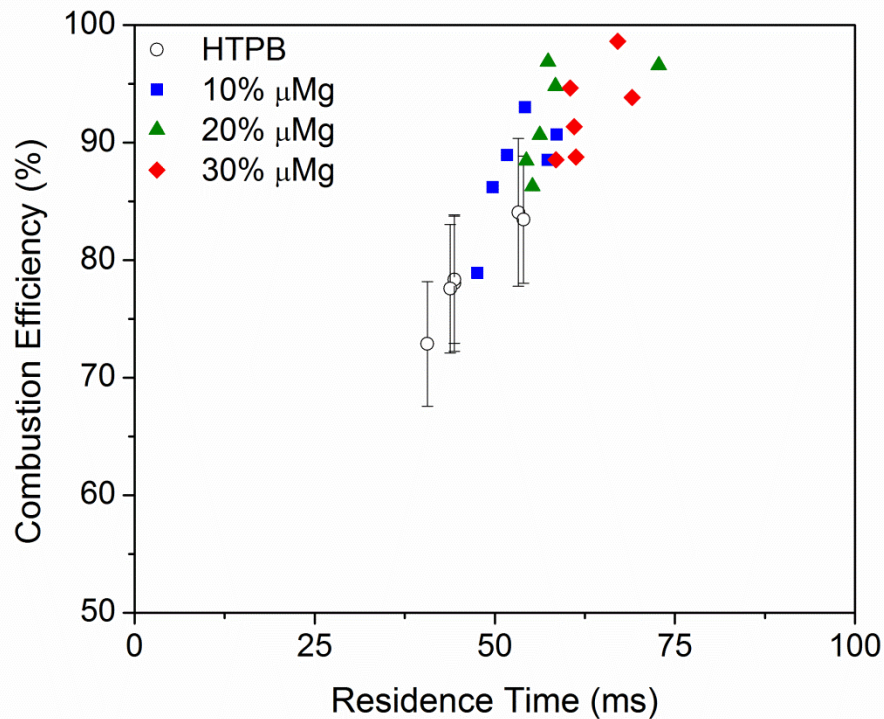


Figure 71. Combustion efficiencies of plain HTPB and fuel samples loaded with 10%, 20%, and 30% micro-magnesium.

SEM images and atomic maps derived from EDS analyses of the combustion residue collected for an HTPB fuel loaded with 30% micro-magnesium burning in GOX at an average O/F ratio of 2.0 are shown in Figures 72 and 73, respectively. Once again, due to the large amount of mass collected on the specimen, individual particles are not discernible and these particles appear to have agglomerated and sintered into a single layer. In general, the oxygen (58%) and magnesium (33%) atoms account for most of the surface layer and completely encompass the map, which suggests that the majority of the magnesium is reacted. Elemental compositional analysis of the EDS spectra showed that the ratio of O/Mg is 1.8 which is greater than the ratio in the standard magnesium oxide

($\text{MgO} - \text{O/Mg} = 1.0$) indicating efficient combustion. This finding is in agreement with the high measured combustion efficiency (95%) for the motor firing. However, close inspection of Figure 73 shows that some of the larger particles, which appear brighter in Figure 72, have not fully reacted and are not completely covered in an oxide layer.

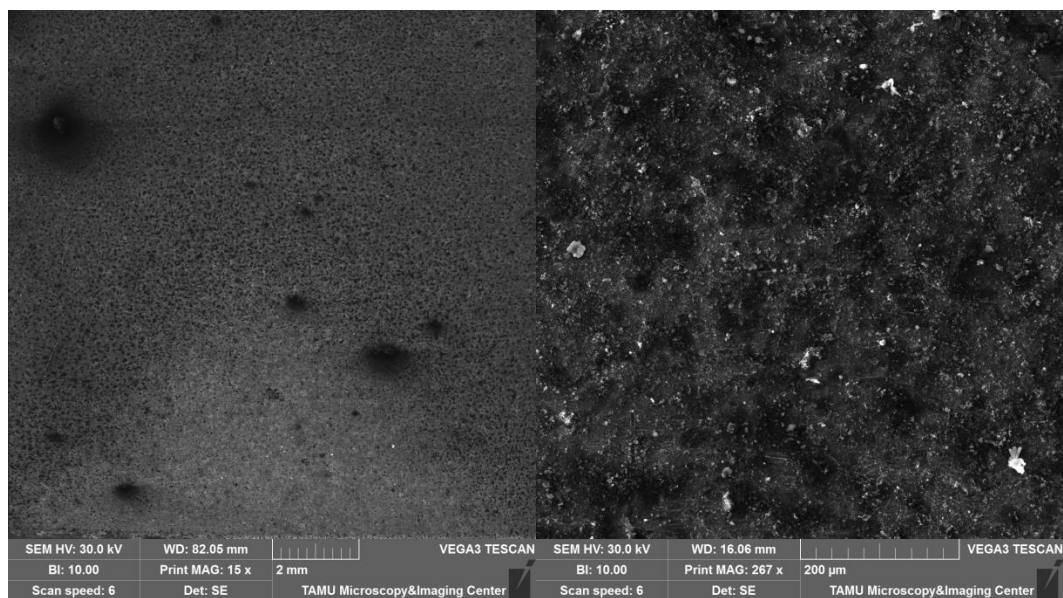


Figure 72. SEM analysis of the combustion residue collected during the motor firing of HTPB loaded with 30% micro-magnesium burning in GOX.

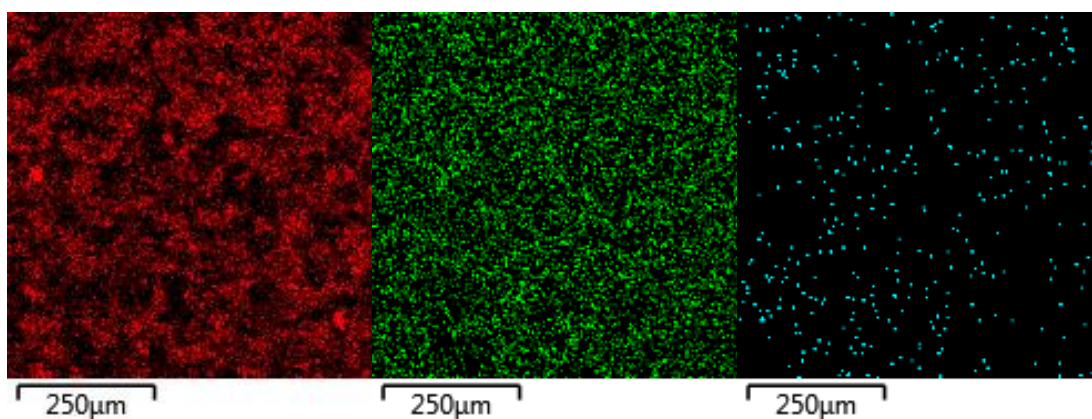


Figure 73. EDS analysis of the combustion residue collected during the motor firing of HTPB loaded with 30% micro-magnesium burning in GOX. Atomic maps show the overlay of (red) magnesium, (green) oxygen, and (blue) carbon.

9.3. Micro-Titanium Fuels

The regression rates and combustion efficiencies of plain HTPB and HTPB loaded with micro-titanium burning in GOX are shown in Figures 74 and 75, respectively. Once again, motor firings of plain HTPB are represented by open black circles, and motor firings of HTPB loaded with 10%, 20%, and 30% micro-titanium are represented by solid blue squares, solid green triangles, and solid red diamonds, respectively

In general, the inclusion of micro-titanium in the solid fuel reduced the observed regression rate. Once again, this trend is more observable at higher oxidizer mass fluxes and higher additive loadings. These observations are attributed to slow metal additive reactions which likely mostly take place in the post-combustion chamber and an increased accumulation of mass on the fuel surface.

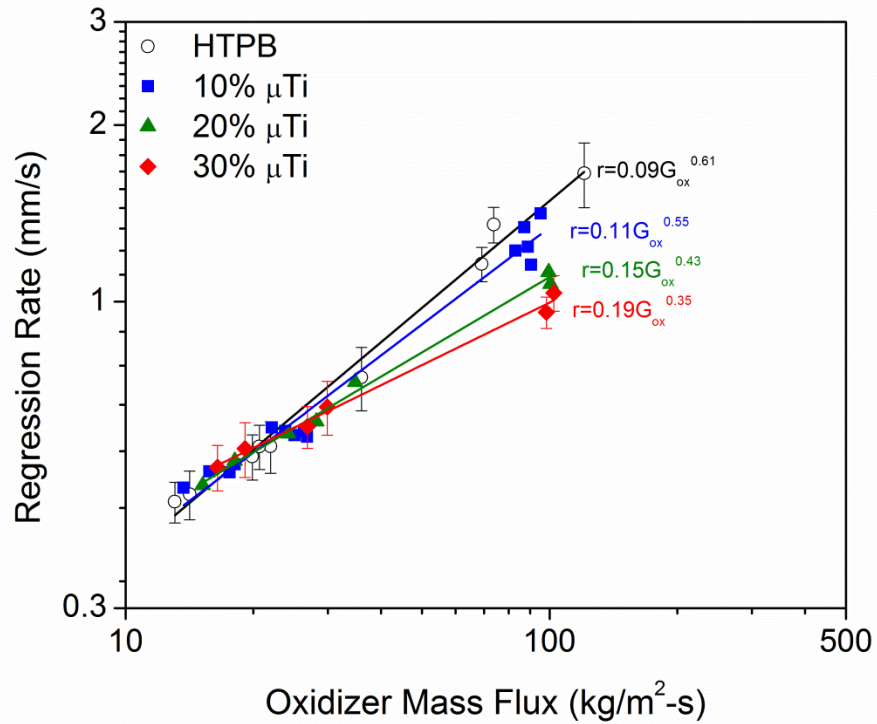


Figure 74. Regression rates of plain HTPB and fuel samples loaded with 10%, 20%, and 30% micro-titanium.

The combustion efficiency of HTPB fuels loaded with micro-titanium increases with increasing residence time. The combustion efficiency data shown in Figure 75 appear to collapse onto a single trend within the measurement uncertainty of the experiment.

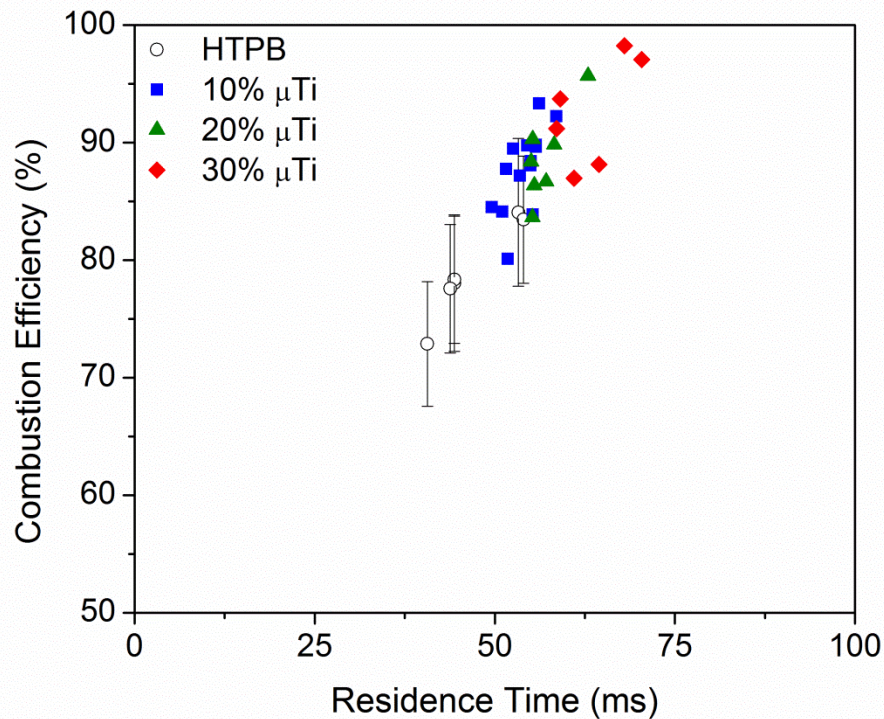


Figure 75. Combustion efficiencies of plain HTPB and fuel samples loaded with 10%, 20%, and 30% micro-titanium.

SEM images and atomic maps derived from EDS analyses of the combustion residue collected for an HTPB fuel loaded with 30% micro-titanium burning in GOX at an average O/F ratio of 2.2 are shown in Figures 76 and 77, respectively. Once again, due to the large amount of mass collected on the specimen, individual particles are not discernible and these particles appear to have agglomerated and sintered into a single layer. In general, the oxygen (70%) and titanium (26%) atoms account for most of the surface layer and completely encompass the map, which suggests that the majority of the magnesium is reacted. Elemental compositional analysis of the EDS spectra showed that the ratio of O/Ti is 2.7 which is greater than the ratio in the standard titanium oxide (TiO_2

– O/Ti = 2.0) indicating efficient combustion. This finding is in agreement with the high measured combustion efficiency (94%) for the motor firing.

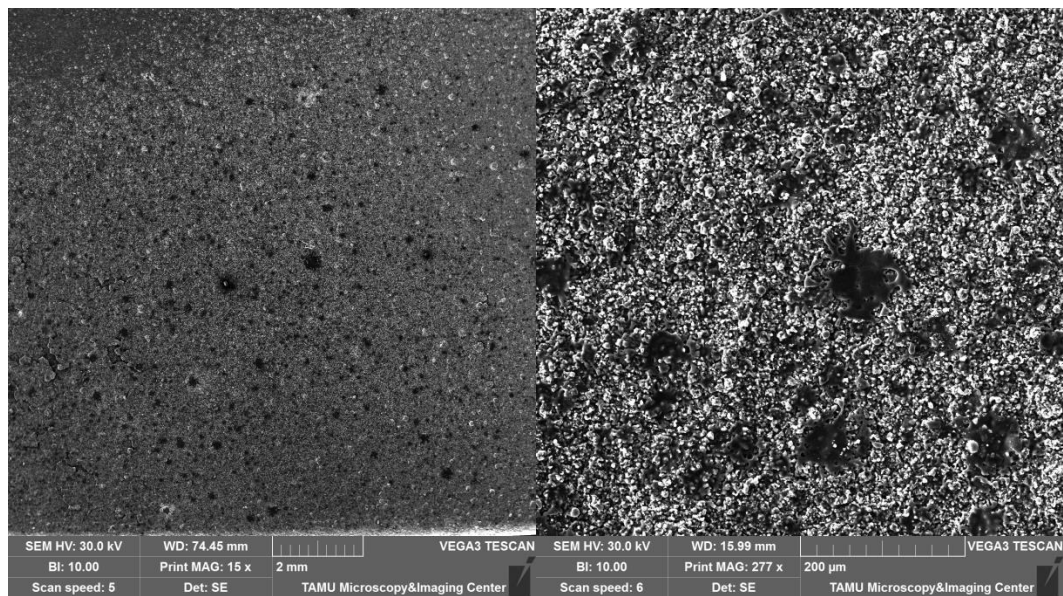


Figure 76. SEM analysis of the combustion residue collected during the motor firing of HTPB loaded with 30% micro-titanium burning in GOX.

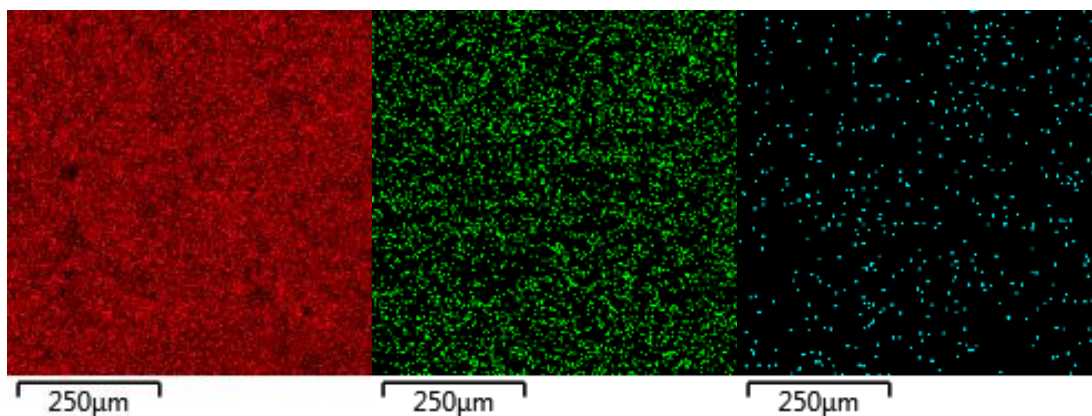


Figure 77. EDS analysis of the combustion residue collected during the motor firing of HTPB loaded with 30% micro-titanium burning in GOX. Atomic maps show the overlay of (red) titanium, (green) oxygen, and (blue) carbon.

9.4. Micro-Zirconium Fuels

The regression rates and combustion efficiencies of plain HTPB and HTPB loaded with micro-zirconium burning in GOX are shown in Figures 78 and 79, respectively. Once again, motor firings of plain HTPB are represented by open black circles, and motor firings of HTPB loaded with 10%, 20%, and 30% micro-zirconium are represented by solid blue squares, solid green triangles, and solid red diamonds, respectively

The inclusion of micro-zirconium at a loading of 10% led to a moderate increase in the fuel's regression rate (10-20%). However, the inclusion of micro-zirconium at higher loadings reduced the observed regression rate. Once again, the observed trends are more prevalent at higher oxidizer mass fluxes, resulting in an increased oxidizer mass flux exponent (n) for the 10% loading formulation and a decreased exponent for the 20% and 30% loading formulations.

As previously discussed, at higher oxidizer mass fluxes, turbulent mass diffusion processes, and not thermal radiation processes, dominate the fuel's regression rate. [11] These observations indicate that the metal additives are likely reacting in a diffusion flame within the combustion port, but increased mass accumulation at the fuel surface leads to the blocking effect, retarding thermal radiation enhancement at higher mass loadings.

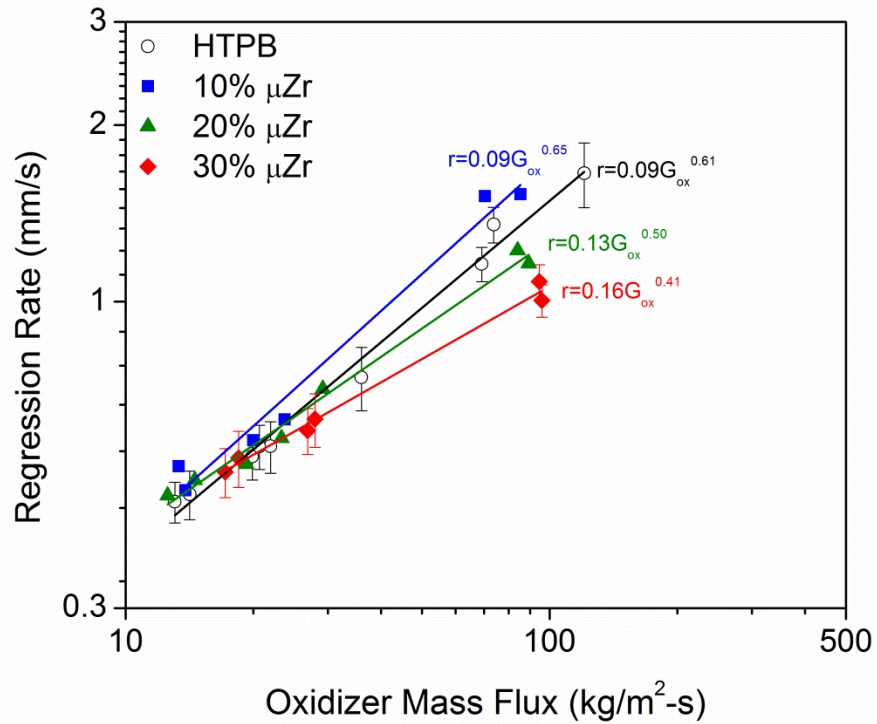


Figure 78. Regression rates of plain HTPB and fuel samples loaded with 10%, 20%, and 30% micro-zirconium.

The combustion efficiency of HTPB fuels loaded with micro-zirconium increases with increasing residence time. Although the combustion efficiency data shown in Figure 79 appear to collapse onto a single trend within the measurement uncertainty of the experiment, the data suggest that higher loadings of micro-zirconium require longer residence times to combustion efficiently.

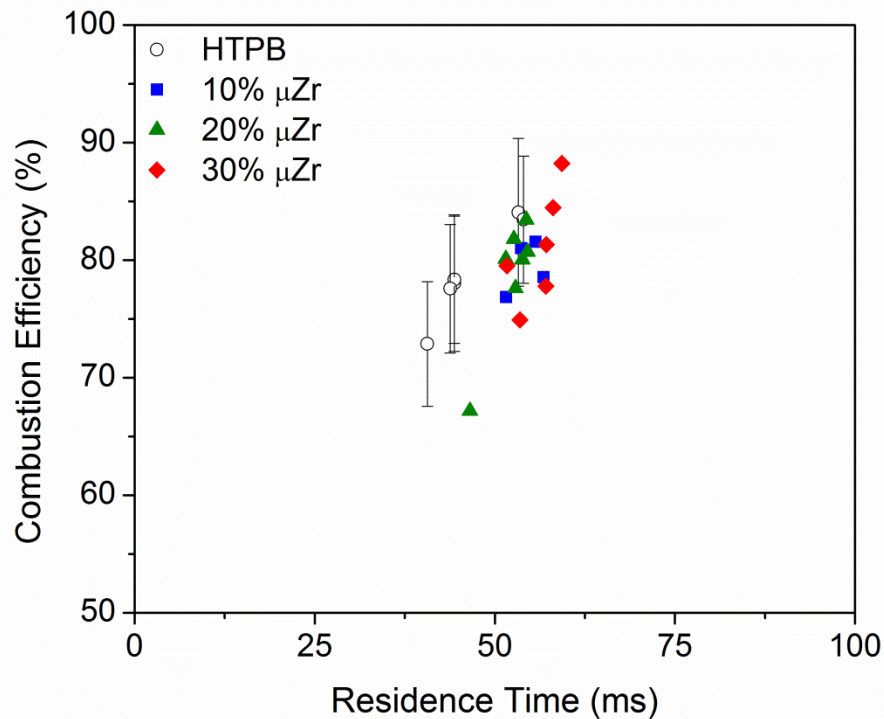


Figure 79. Combustion efficiencies of plain HTPB and fuel samples loaded with 10%, 20%, and 30% micro-zirconium.

SEM images and atomic maps derived from EDS analyses of the combustion residue collected for an HTPB fuel loaded with 30% micro-magnesium burning in GOX at an average O/F ratio of 2.0 are shown in Figures 80 and 81, respectively. Once again, due to the large amount of mass collected on the specimen, individual particles are not discernible and these particles appear to have agglomerated and sintered into a single layer. In general, the oxygen (59%) and zirconium (13%) atoms account for most of the surface layer and completely encompass the map, which suggests that the majority of the zirconium is reacted. However, a large concentration of carbon (28%) was observed in the surface layer, suggesting a substantial fraction of the zirconium is forming a carbide or

carbonate compound. Elemental compositional analysis of the EDS spectra showed that the ratio of O/Zr is 4.5 which is greater than the ratio in the standard zirconium oxide ($ZrO_2 - O/Zr = 2.0$) indicating efficient combustion. This finding is in agreement with the high measured combustion efficiency (88%) for the motor firing. However, close inspection of Figure 81 shows that some of the larger particles, which appear brighter in Figure 80, have not fully reacted and are not completely covered in an oxide layer.

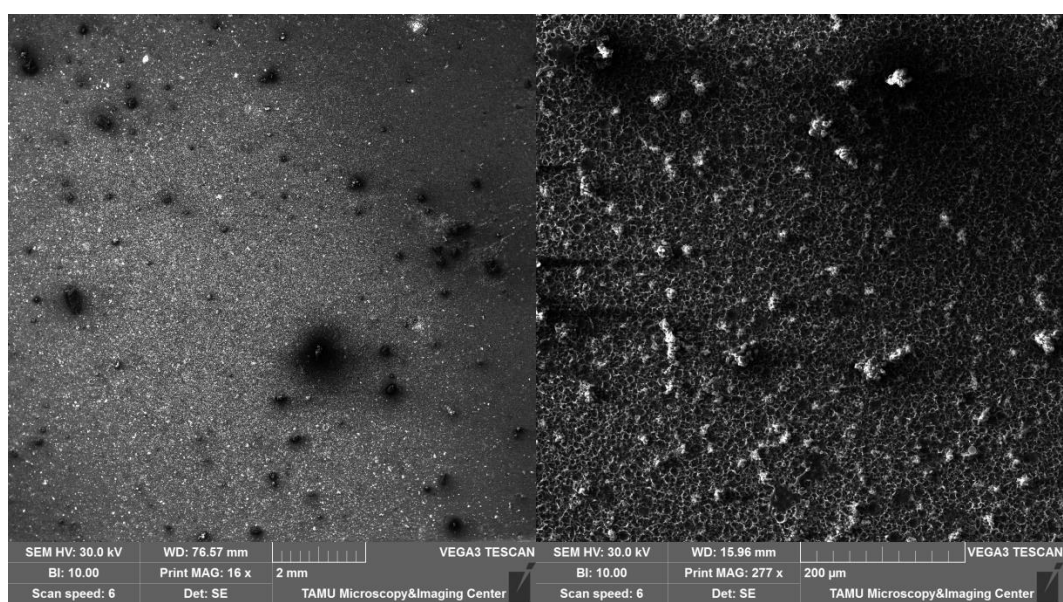


Figure 80. SEM analysis of the combustion residue collected during the motor firing of HTPB loaded with 30% micro-zirconium burning in GOX.

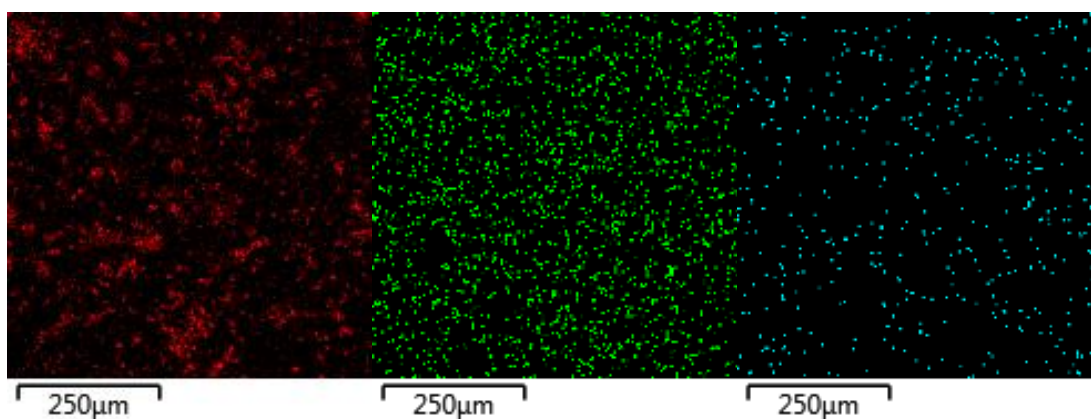


Figure 81. EDS analysis of the combustion residue collected during the motor firing of HTPB loaded with 30% micro-zirconium burning in GOX. Atomic maps show the overlay of (red) zirconium, (green) oxygen, and (blue) carbon.

9.5. Nano-Aluminum Fuels

The regression rates and combustion efficiencies of plain HTPB and HTPB loaded with nano-aluminum burning in GOX are shown in Figures 82 and 85, respectively. Motor firings of plain HTPB are represented by open black circles, and motor firings of HTPB loaded with 10% and 20% nano-aluminum are represented by solid blue squares and solid green triangles, respectively

In general, the inclusion of nano-aluminum in the solid fuel reduced the observed regression rate. This trend is more observable for the 10% loading formulation at higher oxidizer mass fluxes. This observation is attributed to slow metal additive reactions which likely mostly take place in the post-combustion chamber and an increased accumulation of mass on the fuel surface.

The fuel formulations containing 20% nano-aluminum did not exhibit stable combustion during secondary motor firings (i.e. after the first motor firing). An example transient pressure data trace for a secondary firing of an HTPB fuel loaded with 20% nano-

aluminum burning in GOX is shown in Figure 83. The chamber pressure exhibits large excursions from the average steady-state value. Video analysis of the rocket plume indicated that these pressure excursions were accompanied by large ejections of mass, which appeared to be aluminum and/or aluminum oxide particles.

As previously mentioned, Strand et al. [240-242] have observed that micro-aluminum additives included in HTPB burning in GOX would agglomerate on the fuel surface and periodically detach from the surface. Similarly, Risha et al. [249-253] noted that higher loadings of metallic additives led to periodic surface layer shedding. Similar results have been reported for highly-loaded fuels containing boron. [266-276, 297] Although this phenomenon does not appear to be prevalent with any of the previously discussed metal additives (micro-aluminum, micro-magnesium, micro-titanium, and micro-zirconium) at any of the evaluated metal loadings (10%, 20%, or 30%), it becomes problematic in the formulations containing nano-aluminum at relatively low loadings (20%). This observation may be due in part to the variation in rheological properties associated with nano-additives versus micro-additives, and more specifically increases in liquid viscosity and surface tension. Furthermore, post-combustion examination of the fuel grains containing 20% nano-aluminum showed approximately a 1.2-mm thick layer of molten material accumulated on the fuel's surface (Figure 84). Accordingly, the regression rate data for secondary motor firings of the 20% nano-aluminum formulation, i.e. $G_{ox} < 100 \text{ kg/m}^2\text{-s}$, should be treated qualitatively, rather than quantitatively.

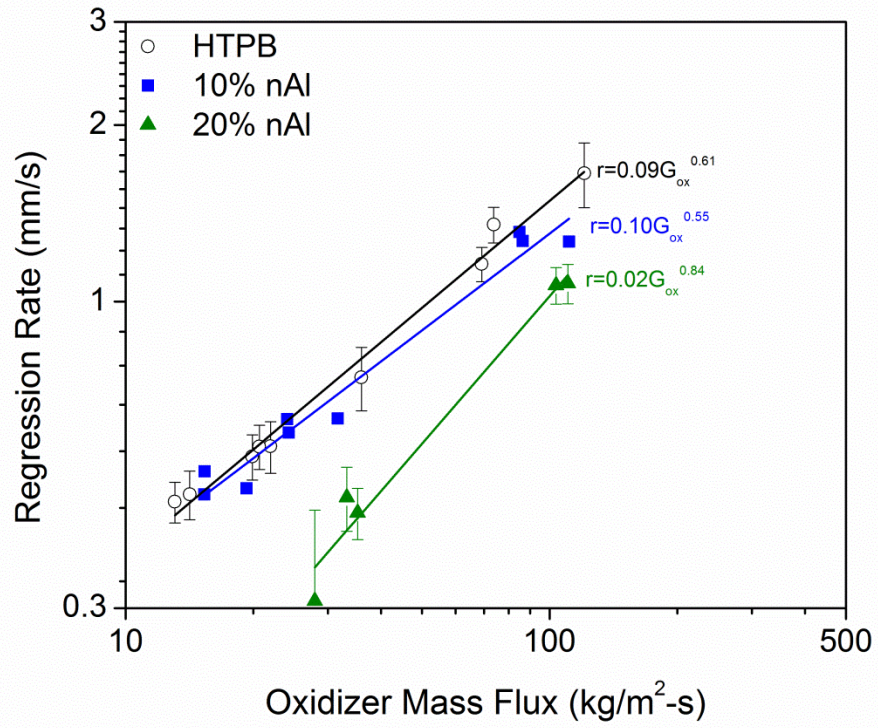


Figure 82. Regression rates of plain HTPB and fuel samples loaded with 10% and 20% nano-aluminum.

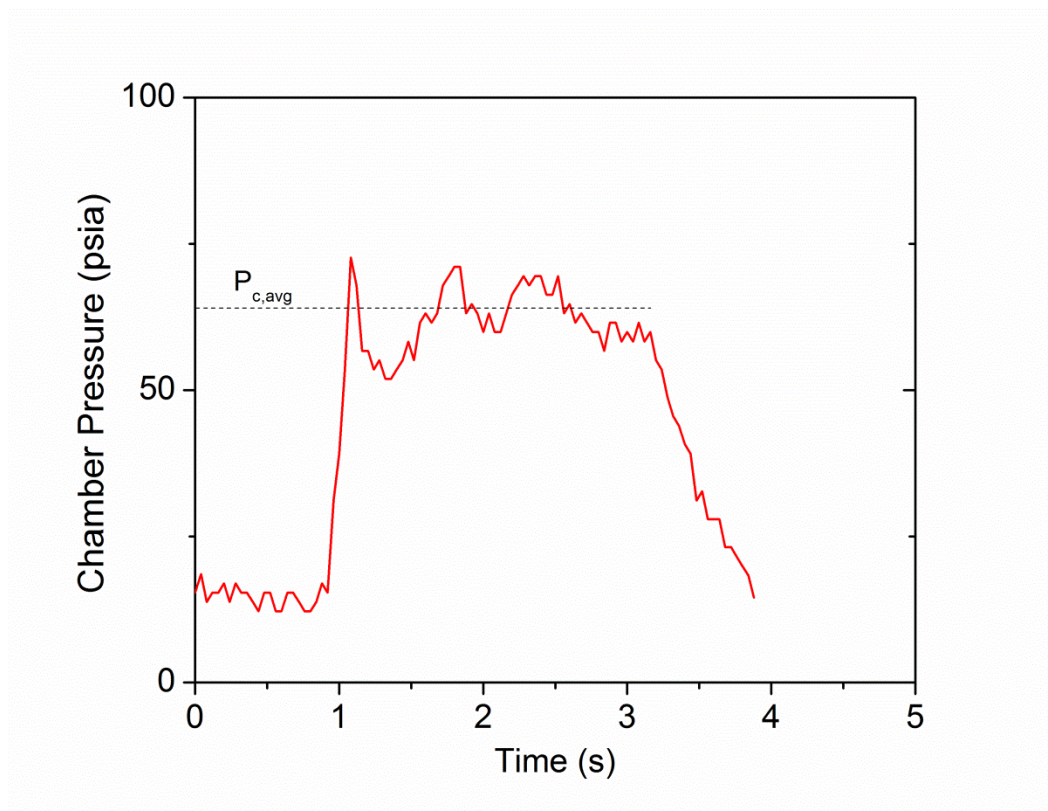


Figure 83. Transient pressure data trace for a 20% nano-aluminum fuel burning in GOX exhibiting large pressure excursions.

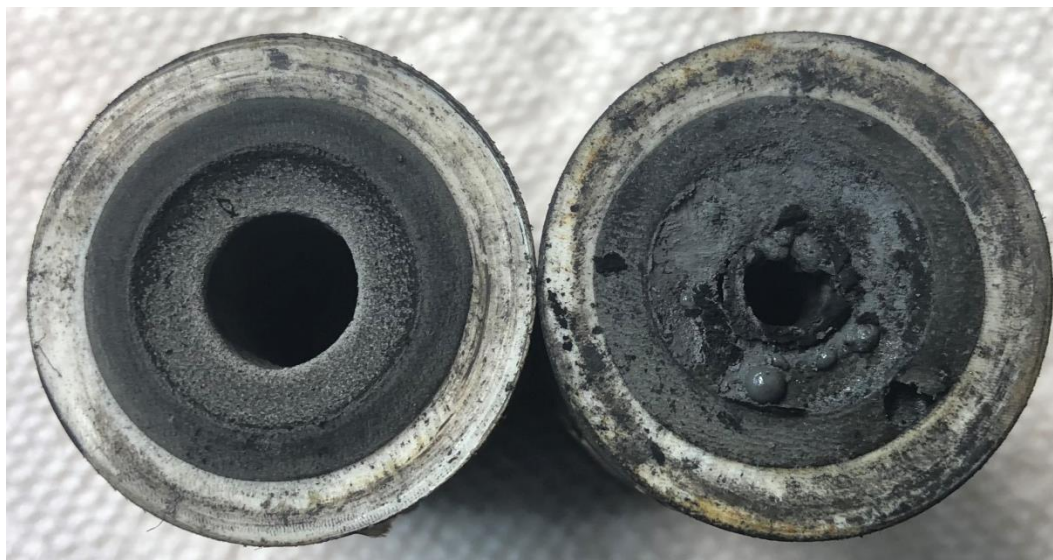


Figure 84. Fuel grains loaded with (left) 20% micro-aluminum and (right) 20% nano-aluminum. A layer of molten material accumulated on the combustion port surface of fuel containing 20% nano-aluminum.

The combustion efficiency of HTPB fuels loaded with nano-aluminum increases with increasing residence time. The combustion efficiency data shown in Figure 85 appear to collapse onto a single trend within the measurement uncertainty of the experiment.

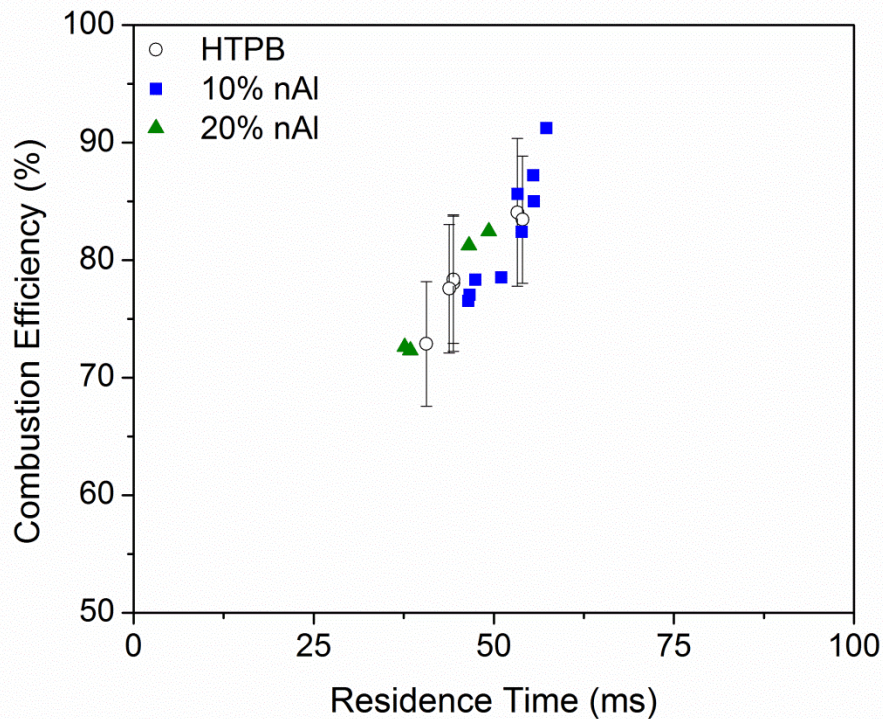


Figure 85. Combustion efficiencies of plain HTPB and fuel samples loaded with 10% and 20% nano-aluminum.

9.6. Nano-Boron Fuels

The regression rates and combustion efficiencies of plain HTPB and HTPB loaded with nano-boron burning in GOX are shown in Figures 86 and 88, respectively. Once again, motor firings of plain HTPB are represented by open black circles, and motor firings of HTPB loaded with 10%, 20%, and 30% nano-boron are represented by solid blue squares, solid green triangles, and solid red diamonds, respectively

In general, the inclusion of nano-boron in the solid fuel reduced the observed regression rate. This trend is more observable for the 10% loading formulation at higher oxidizer mass fluxes. This observation is attributed to slow metal additive reactions which

likely mostly take place in the post-combustion chamber and an increased accumulation of mass on the fuel surface.

Similar to the fuel specimen containing nano-aluminum, the fuel formulations containing 20% or 30% nano-boron did not exhibit stable combustion during secondary motor firings (i.e. after the first motor firing). Post-combustion examination of the fuel grains containing 20% and 30% nano-boron showed approximately 0.9-mm and 1.8-mm thick layers of molten material, respectively, accumulated on the fuels' surface (Figure 87). Accordingly, the regression rate data for secondary motor firings of the 20% nano-aluminum formulation, i.e. $G_{ox} < 40 \text{ kg/m}^2\text{-s}$, should be treated qualitatively, rather than quantitatively.

The author considered that the poor secondary firings and larger surface accumulations with nano-additive formulations could be an artifact of the start-stop testing methodology. Accordingly, a long-duration burn (12 s) of a fuel grain containing 20% nano-boron was completed, but no significant change in behavior was noted.

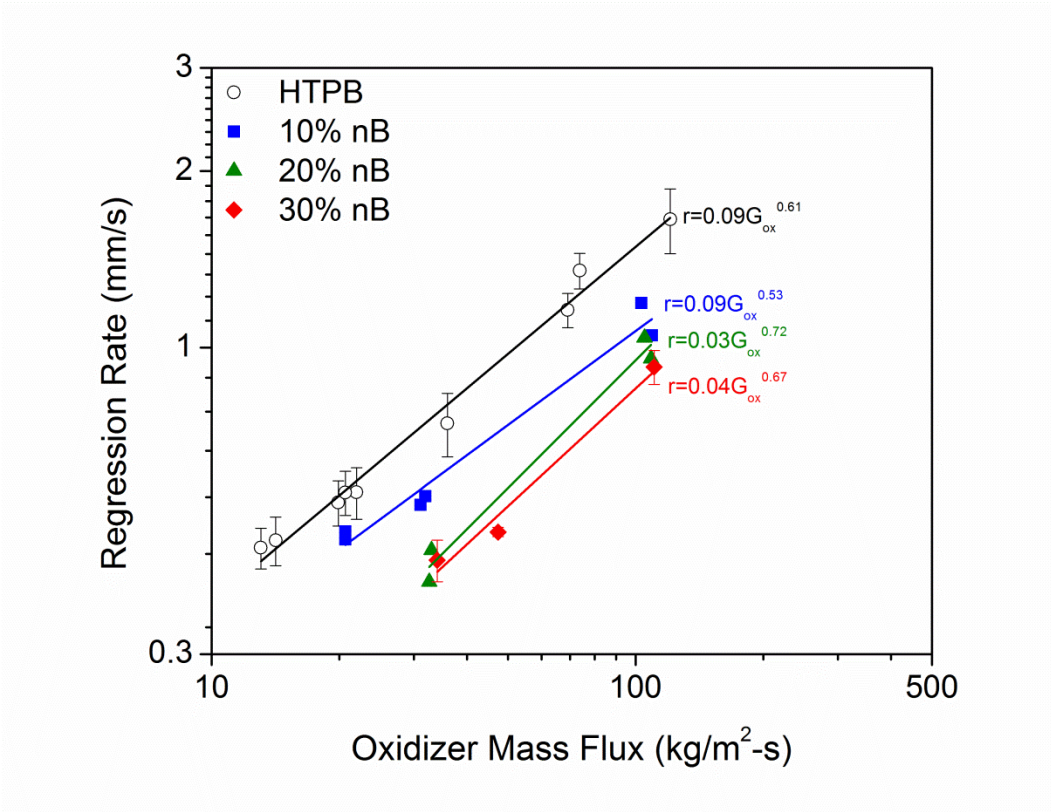


Figure 86. Regression rates of plain HTPB and fuel samples loaded with 10%, 20%, and 30% nano-boron.

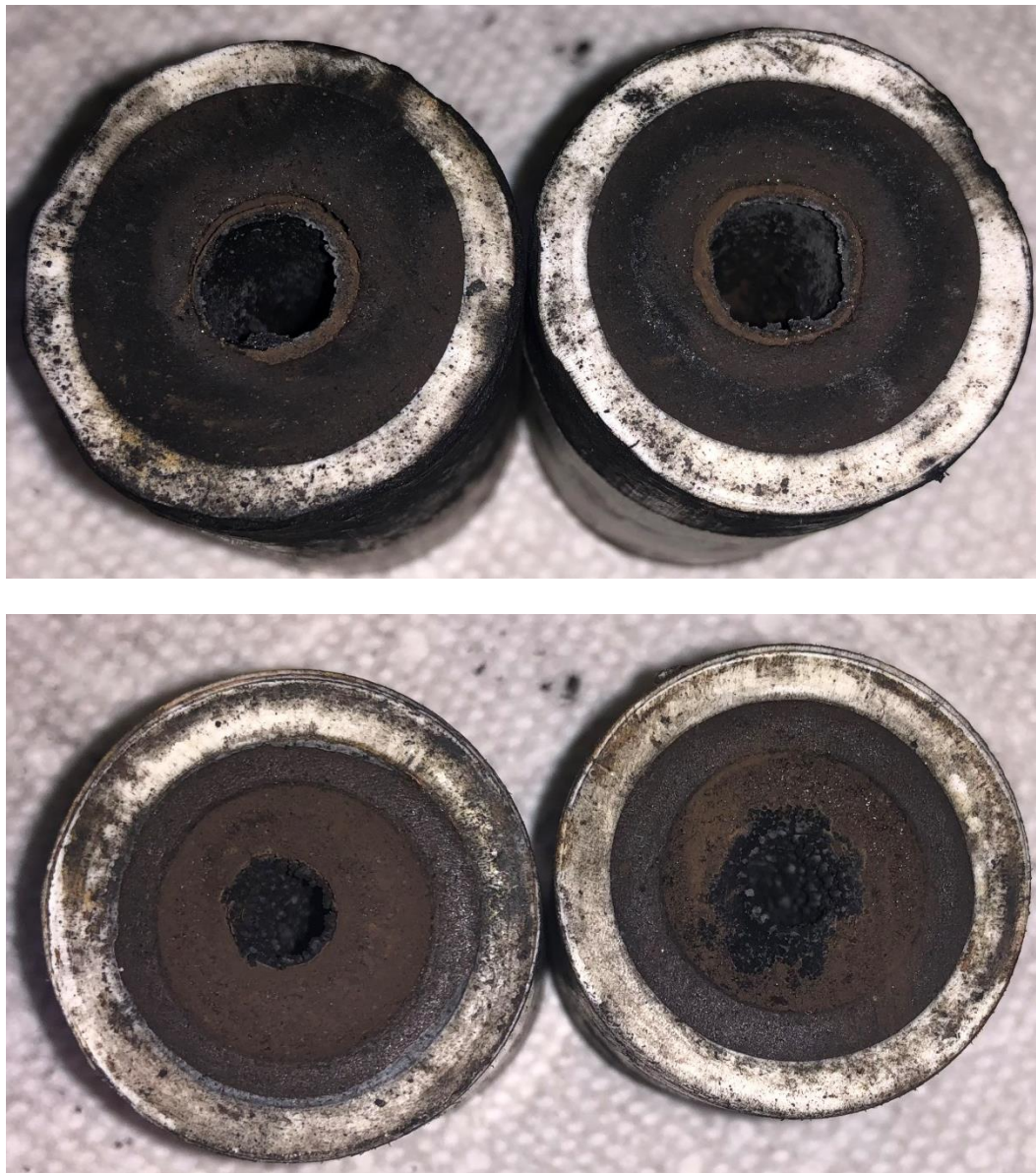


Figure 87. (top) Injector- and (bottom) nozzle-side views of fuel grains containing (left) 20% and (right) 30% nano-boron. A layer of molten material accumulated on the combustion port surfaces.

The combustion efficiency of HTPB fuels loaded with nano-boron increases with increasing residence time. The combustion efficiency data shown in Figure 88 appear to collapse onto a single trend within the measurement uncertainty of the experiment.

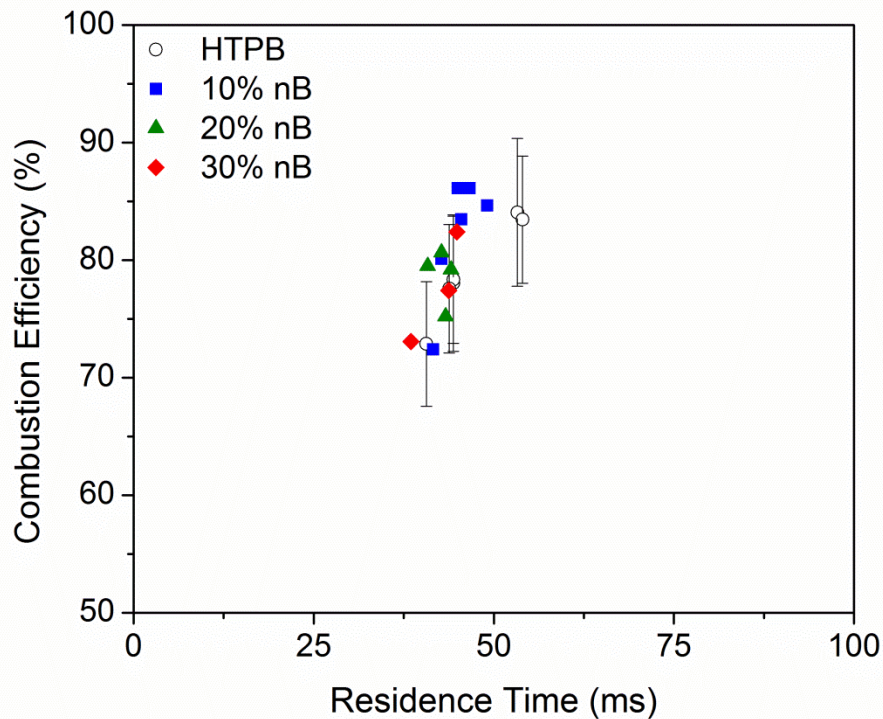


Figure 88. Combustion efficiencies of plain HTPB and fuel samples loaded with 10%, 20%, and 30% nano-boron.

SEM images and atomic maps derived from EDS analyses of the combustion residue collected for an HTPB fuel loaded with 30% nano-boron burning in GOX at an average O/F ratio of 3.2 are shown in Figures 89 and 90, respectively. Once again, due to the large amount of mass collected on the specimen, individual particles are not discernible and these particles appear to have agglomerated and sintered into a single layer. In general, the oxygen (25%) and boron (43%) atoms account for most of the surface layer and completely encompass the map, which suggests that the majority of the boron is reacted. However, a large concentration of carbon (31%) was observed in the surface layer, suggesting a substantial fraction of the boron is forming a carbide or carbonate compound.

Elemental compositional analysis of the EDS spectra showed that the ratio of O/B is 41.7 which is greater than the ratio in the standard boron oxide ($B_2O_3 - O/B = 1.5$) indicating efficient combustion. This finding is in agreement with the high measured combustion efficiency (73%) for the motor firing.

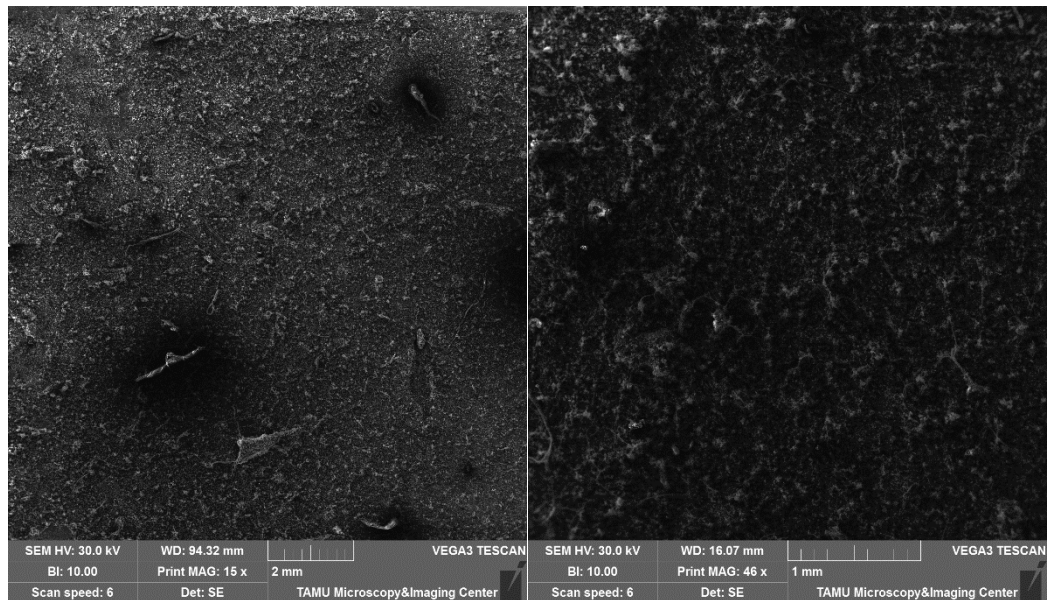


Figure 89. SEM analysis of the combustion residue collected during the motor firing of HTPB loaded with 30% nano-boron burning in GOX.

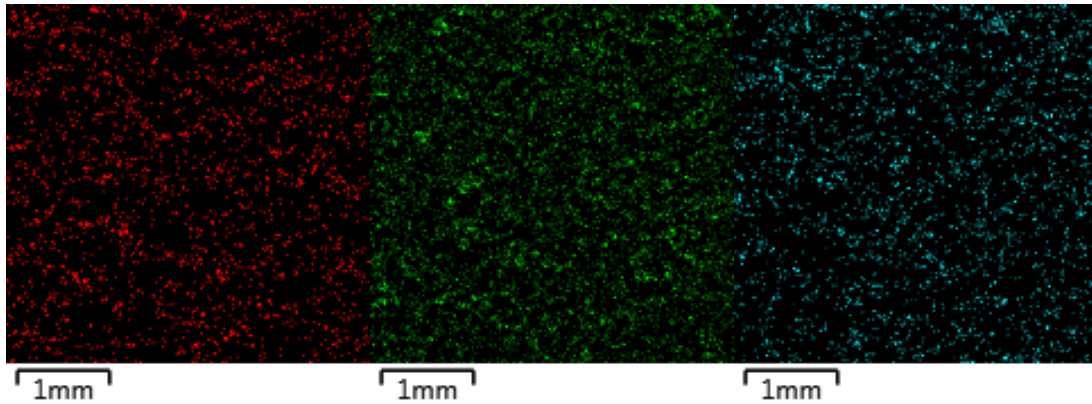


Figure 90. EDS analysis of the combustion residue collected during the motor firing of HTPB loaded with 30% nano-boron burning in GOX. Atomic maps show the overlay of (red) boron, (green) oxygen, and (blue) carbon.

9.7. Magnesium-Coated Nano-Boron Fuels

The regression rates and combustion efficiencies of plain HTPB and HTPB loaded with magnesium-coated nano-boron burning in GOX are shown in Figures 91 and 92, respectively. Once again, motor firings of plain HTPB are represented by open black circles, and motor firings of HTPB loaded with 10% and 20% magnesium-coated nano-boron are represented by solid blue squares and solid green triangles, respectively.

In general, the inclusion of magnesium-coated nano-boron in the solid fuel reduced the observed regression rate. Once again, this trend is more observable at higher oxidizer mass fluxes and higher additive loadings. These observations are attributed to slow metal additive reactions which likely mostly take place in the post-combustion chamber and an increased accumulation of mass on the fuel surface. In comparison to the uncoated nano-boron, the 10% loaded formulation regressed at approximately the same rate, while the 20% loaded formulation regressed slightly faster. Furthermore, post-combustion analysis

of the port surface indicated the magnesium-coated nano-boron did alter the surface accumulation layer, but did not significantly change its thickness.

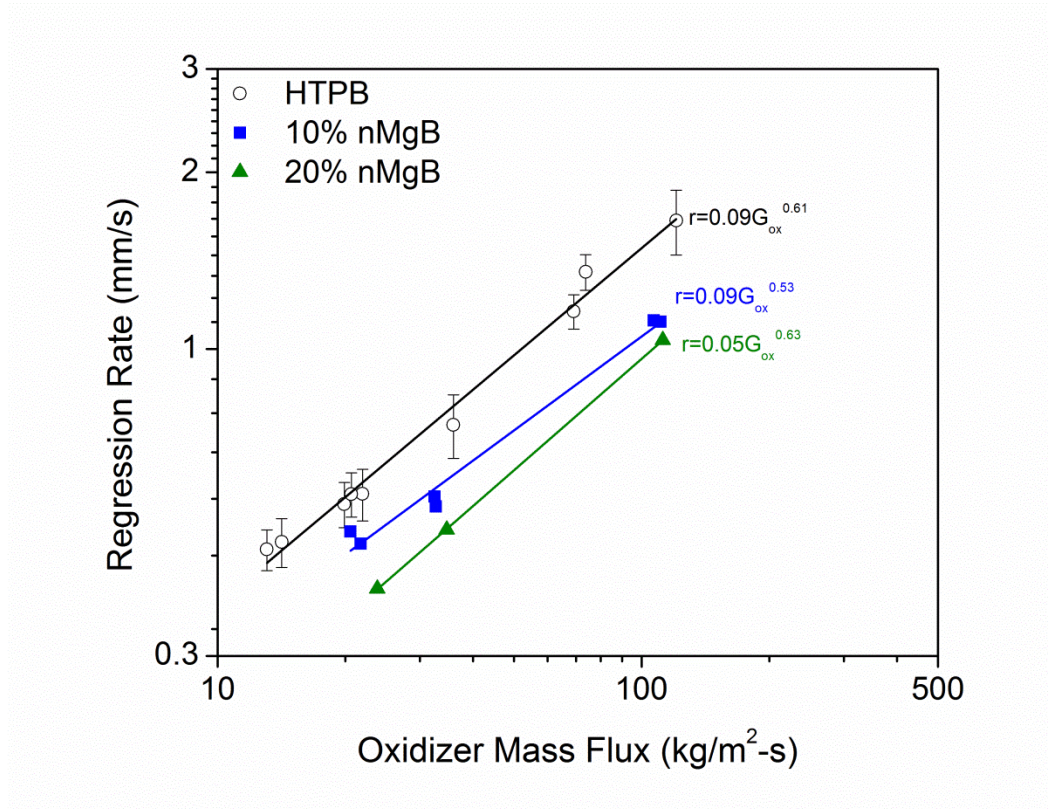


Figure 91. Regression rates of plain HTPB and fuel samples loaded with 10% and 20% magnesium-coated nano-boron.

The combustion efficiency of HTPB fuels loaded with magnesium-coated nano-boron increases with increasing residence time. The combustion efficiency data shown in Figure 87 appear to collapse onto a single trend within the measurement uncertainty of the experiment.

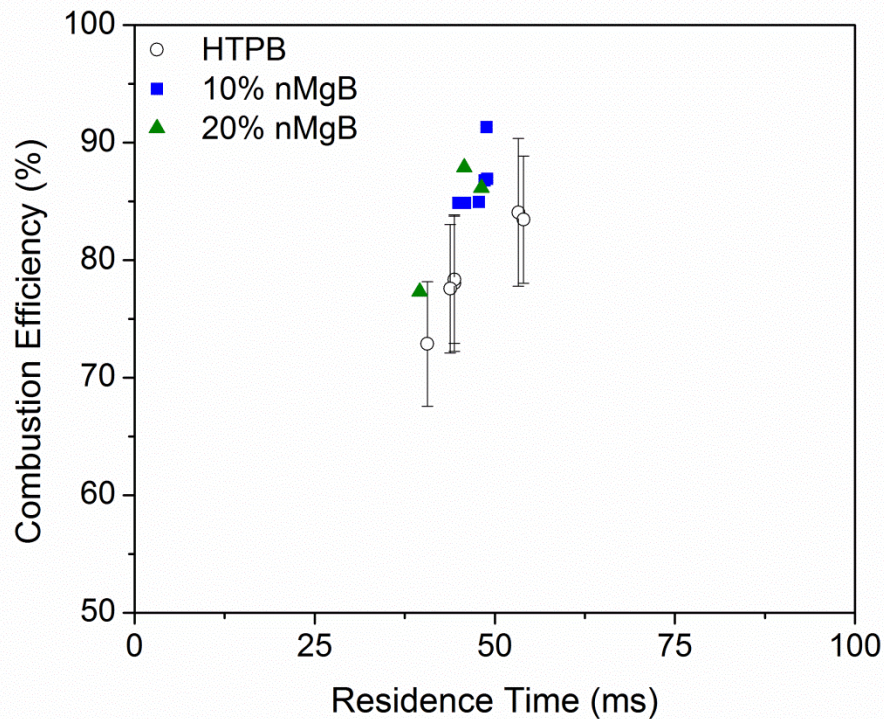


Figure 92. Combustion efficiencies of plain HTPB and fuel samples loaded with 10% and 20% magnesium-coated nano-boron.

9.8. Bimetallic Fuels

To evaluate the possible synergetic effects of bimetallic blends of plain metals on the combustion of HTPB fuels, and nano-boron, burning in GOX, formulations containing mixtures of the previously described at a loading of 10% were prepared. As previously described in Chapter 6, the magnesium-coated nano-boron additive contains an approximate mass ratio of B/Mg of 65/35. Bimetallic blends incorporated in HTPB fuel were also prepared at this ratio for consistency and to allow for direct comparison.

The regression rates and combustion efficiencies of plain HTPB, HTPB loaded with 10% micro-aluminum, 10% nano-boron, and a 10% 35/65 blend of micro-aluminum

and nano-boron burning in GOX are shown in Figures 93 and 94, respectively. Motor firings of plain HTPB, HTPB loaded with micro-aluminum, HTPB loaded with nano-boron, and HTPB loaded with a 10% blend of the two additives are represented by open black circles, solid blue squares, solid green triangles, and solid red diamonds, respectively. Interestingly, the fuel containing a bimetallic blend of micro-aluminum and nano-boron regressed faster than the other formulations at higher oxidizer mass fluxes, suggesting a synergistic effect. The combustion efficiency data appear to collapse onto a single trend line within the experimental uncertainty.

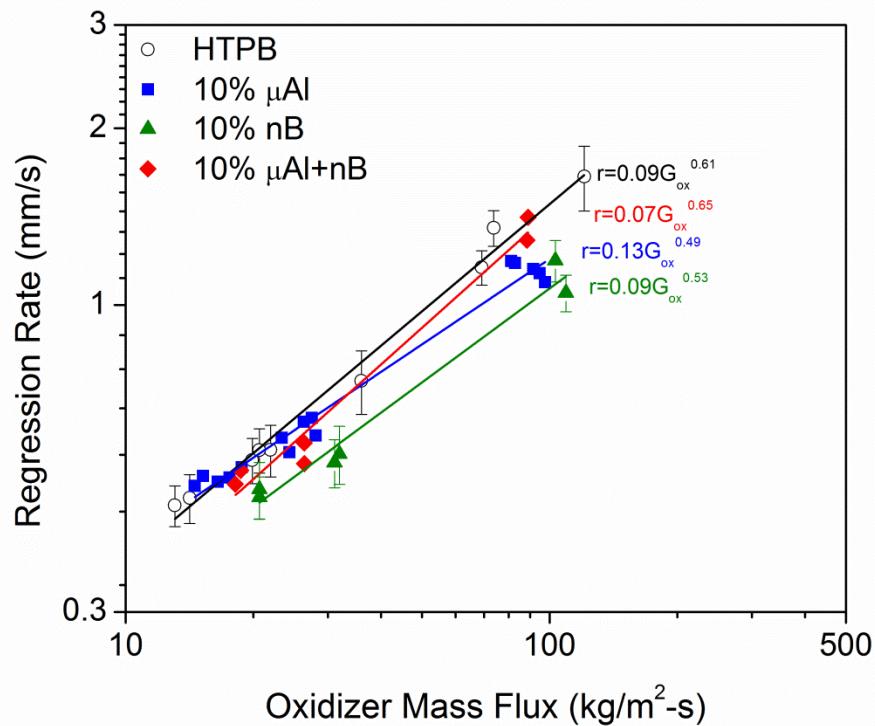


Figure 93. Regression rates of plain HTPB and fuel samples loaded with 10% micro-aluminum, nano-boron, and a 35:65 mixture of each.

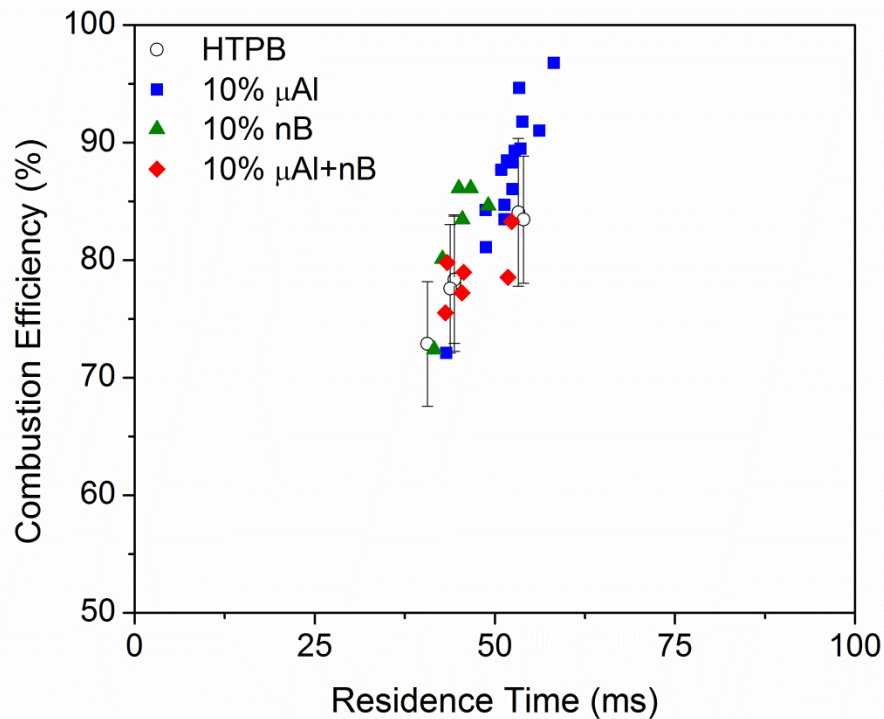


Figure 94. Combustion efficiencies of plain HTPB and fuel samples loaded with 10% micro-aluminum, nano-boron, and a 35:65 mixture of each.

The regression rates and combustion efficiencies of plain HTPB, HTPB loaded with 10% micro-magnesium, 10% nano-boron, and a 10% 35/65 blend of micro-magnesium and nano-boron, and 10% magnesium-coated nano-boron burning in GOX are shown in Figures 95 and 96, respectively. Motor firings of plain HTPB, HTPB loaded with micro-magnesium, HTPB loaded with nano-boron, HTPB loaded with a 10% blend of the two additives, and HTPB loaded with 10% magnesium-coated nano-boron are represented by open black circles, solid blue squares, solid green triangles, solid red diamonds, and solid magenta triangles respectively. The fuel containing magnesium-coated nano-boron performed similarly to the fuel contained plain nano-boron, and both

slightly outperformed the fuel containing a blend of micro-magnesium and nano-boron, suggesting no synergistic effects. The combustion efficiency data appear to collapse onto a single trend line within the experimental uncertainty.

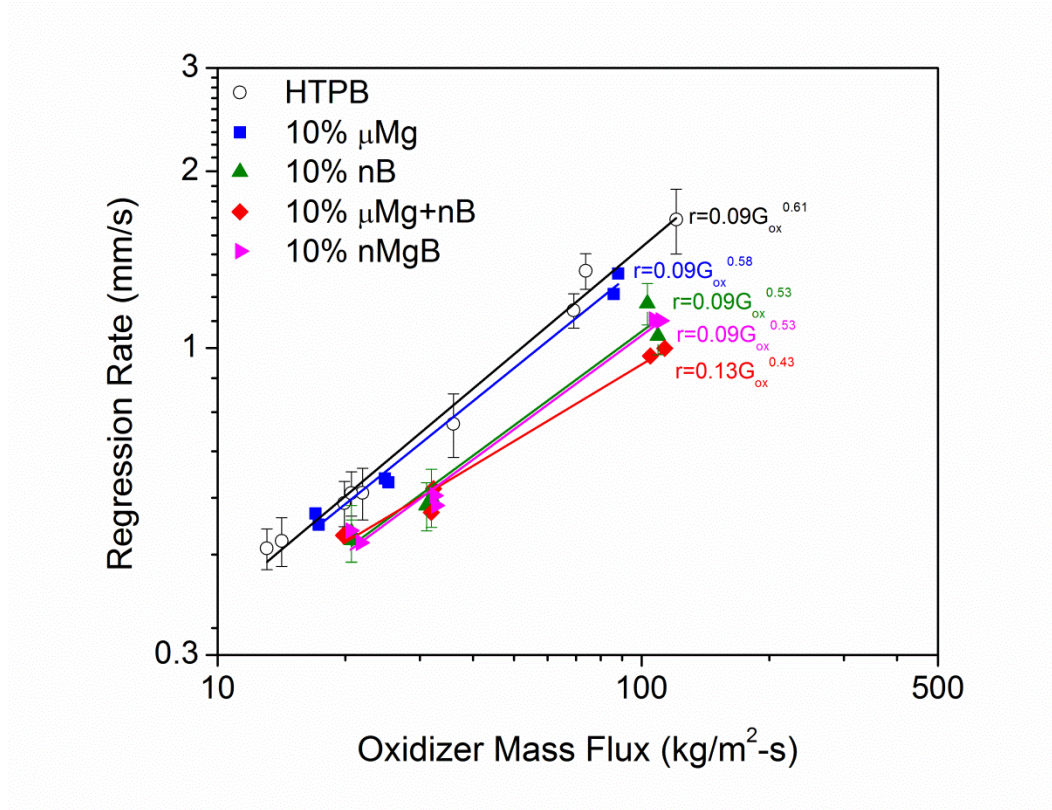


Figure 95. Regression rates of plain HTPB and fuel samples loaded with 10% micro-magnesium, nano-boron, a 35:65 mixture of each, and magnesium-coated nano-boron.

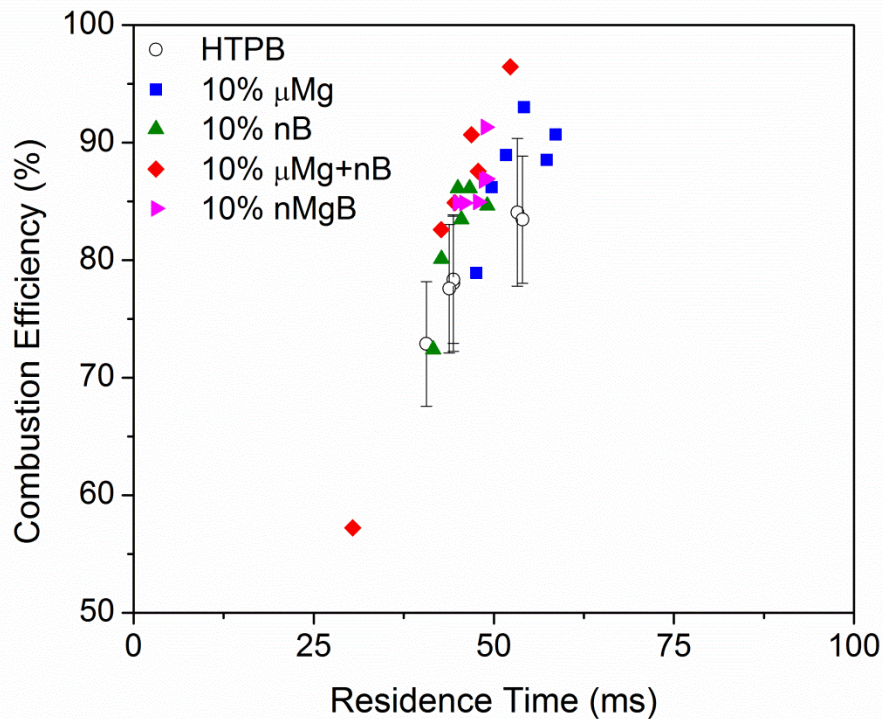


Figure 96. Combustion efficiencies of plain HTPB and fuel samples loaded with 10% micro-magnesium, nano-boron, a 35:65 mixture of each, and magnesium-coated nano-boron.

The regression rates and combustion efficiencies of plain HTPB, HTPB loaded with 10% micro-titanium, 10% nano-boron, and a 10% 35/65 blend of micro-titanium and nano-boron burning in GOX are shown in Figures 97 and 98, respectively. Motor firings of plain HTPB, HTPB loaded with micro-titanium, HTPB loaded with nano-boron, and HTPB loaded with a 10% blend of the two additives are represented by open black circles, solid blue squares, solid green triangles, and solid red diamonds, respectively. The fuel containing a bimetallic blend of micro-titanium and nano-boron performed similarly to the formulation containing plain nano-boron, suggesting no synergistic effects. The

combustion efficiency data appear to collapse onto a single trend line within the experimental uncertainty.

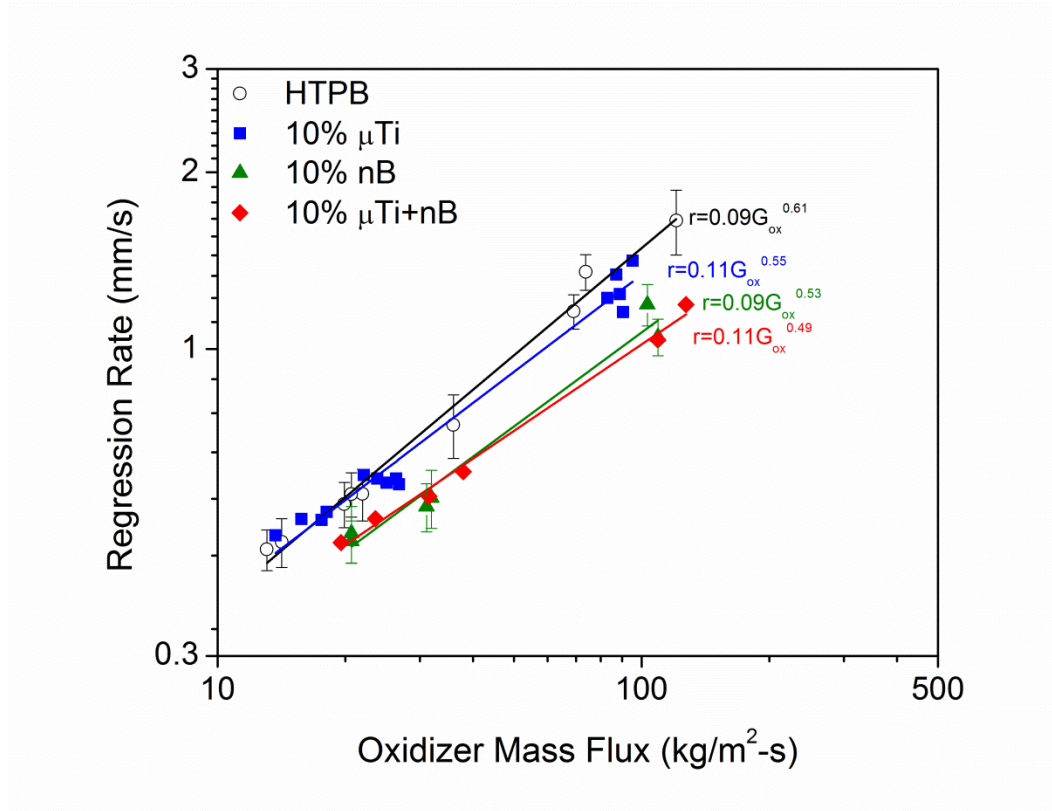


Figure 97. Regression rates of plain HTPB and fuel samples loaded with 10% micro-titanium, nano-boron, and a 35:65 mixture of each.

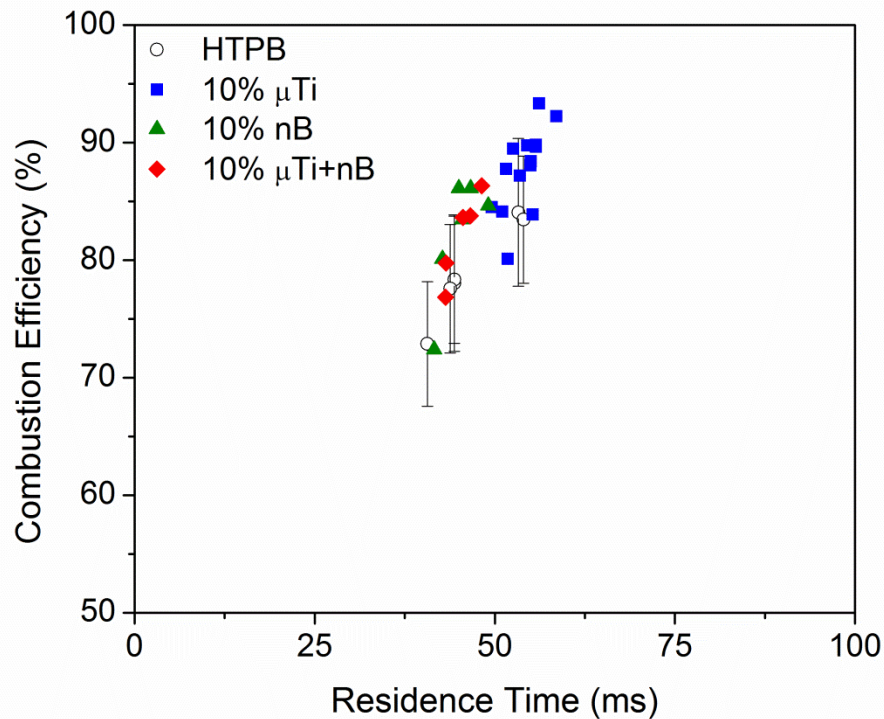


Figure 98. Combustion efficiencies of plain HTPB and fuel samples loaded with 10% micro-titanium, nano-boron, and a 35:65 mixture of each.

The regression rates and combustion efficiencies of plain HTPB, HTPB loaded with 10% micro-zirconium, 10% nano-boron, and a 10% 35/65 blend of micro-zirconium and nano-boron burning in GOX are shown in Figures 99 and 100, respectively. Motor firings of plain HTPB, HTPB loaded with micro-zirconium, HTPB loaded with nano-boron, and HTPB loaded with a 10% blend of the two additives are represented by open black circles, solid blue squares, solid green triangles, and solid red diamonds, respectively. The fuel containing a bimetallic blend of micro-zirconium and nano-boron performed similarly to the formulation containing plain nano-boron, suggesting no synergistic effects. The combustion efficiency data appear to collapse onto a single trend

line within the experimental uncertainty, but appear to be slightly lower for the plain micro-zirconium formulation.

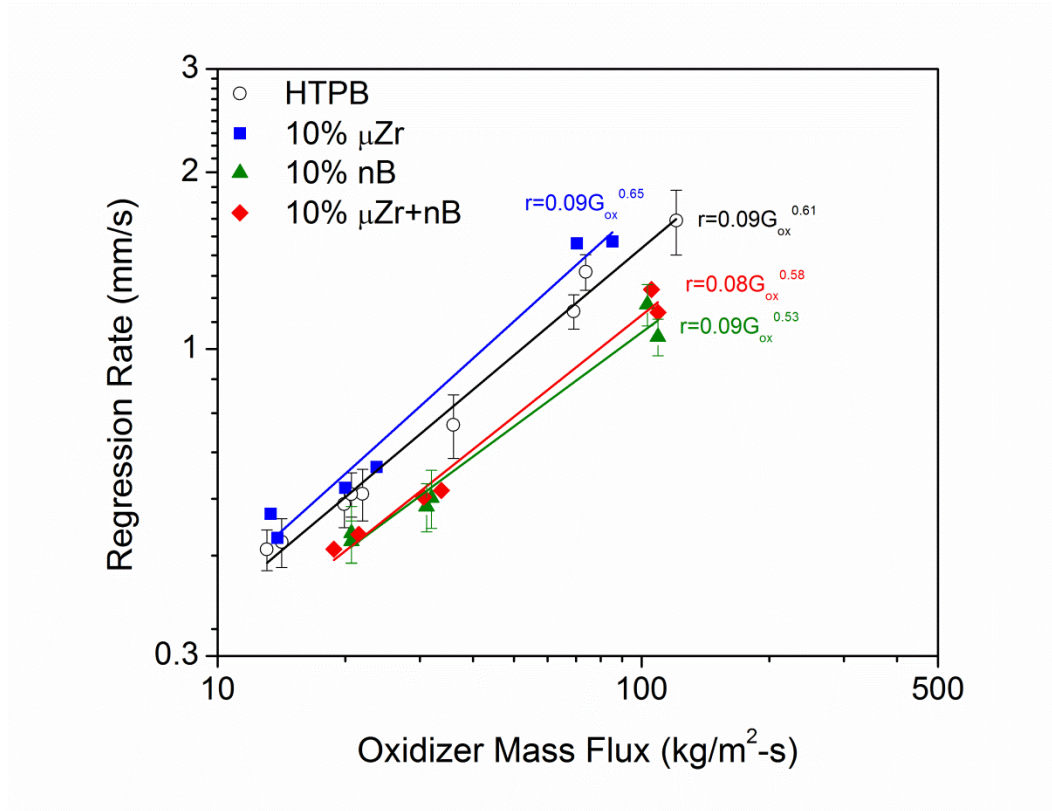


Figure 99. Regression rates of plain HTPB and fuel samples loaded with 10% micro-zirconium, nano-boron, and a 35:65 mixture of each.

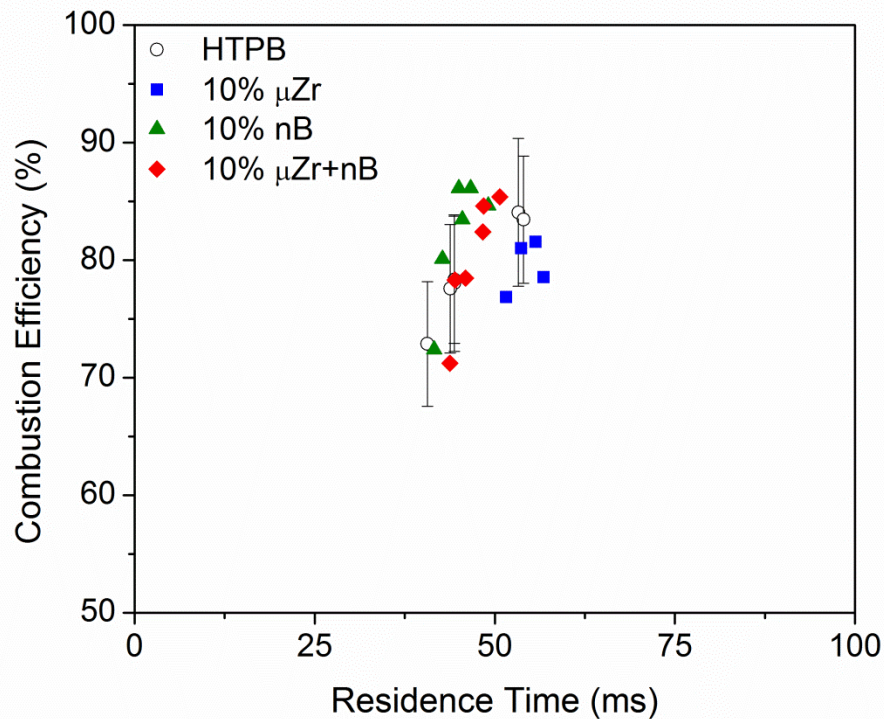


Figure 100. Combustion efficiencies of plain HTPB and fuel samples loaded with 10% micro-zirconium, nano-boron, and a 35:65 mixture of each.

The regression rates and combustion efficiencies of plain HTPB, HTPB loaded with 10% nano-aluminum, 10% nano-boron, and a 10% 35/65 blend of nano-aluminum and nano-boron burning in GOX are shown in Figures 101 and 102, respectively. Motor firings of plain HTPB, HTPB loaded with nano-aluminum, HTPB loaded with nano-boron, and HTPB loaded with a 10% blend of the two additives are represented by open black circles, solid blue squares, solid green triangles, and solid red diamonds, respectively. The fuel containing a bimetallic blend of nano-aluminum and nano-boron performed similarly to the formulation containing plain nano-boron, suggesting no synergistic effects. This result is in contrast to the formulation containing a bimetallic

blend of micro-aluminum and nano-boron, which warrants further investigation. The combustion efficiency data appear to collapse onto a single trend line within the experimental uncertainty, but appear to be slightly lower for the plain nano-aluminum formulation.

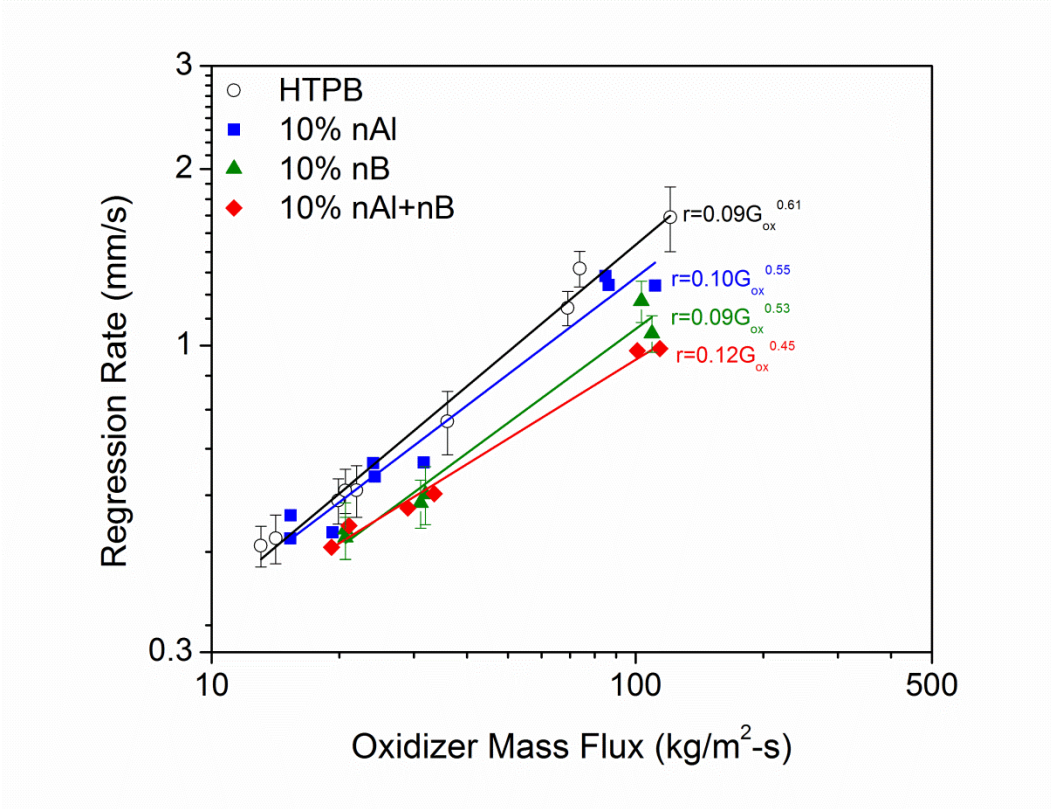


Figure 101. Regression rates of plain HTPB and fuel samples loaded with 10% nano-aluminum, nano-boron, and a 35:65 mixture of each.

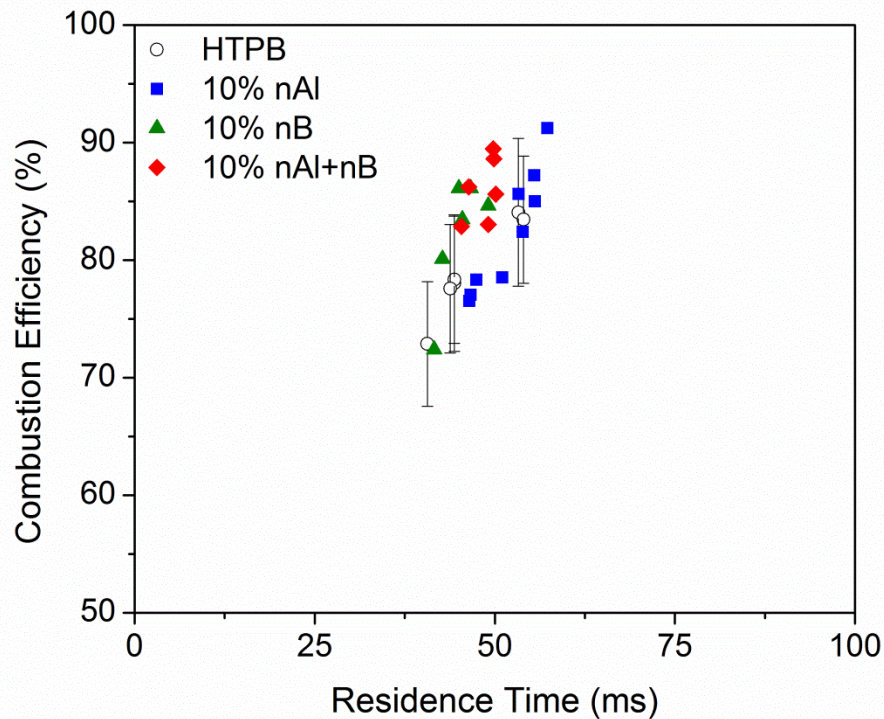


Figure 102. Combustion efficiencies of plain HTPB and fuel samples loaded with 10% nano-aluminum, nano-boron, and a 35:65 mixture of each.

9.9. Summary

In general, the inclusion of any of the selected additives (micro-aluminum, micro-magnesium, micro-titanium, micro-zirconium, nano-aluminum, nano-boron, and magnesium-coated nano-boron) into HTPB fuel burning in GOX led to a reduction in the regression rate and minor changes in the combustion efficiency behavior. The one exception to this trend was the formulation containing a 10% loading of micro-zirconium, which yielded a moderate (10-20%) increase in the fuel's regression rate.

The observed trends were generally more prevalent at higher oxidizer mass fluxes and higher additive loadings. The reduction in regression rate accompanying the inclusion

of nearly all the additives was attributed to a combination of slow metal reactions which may take place in the post-combustion chamber, rather than the combustion port, and heat transfer-blocking effects derived from accumulation of mass on the fuel surface layer. The enhanced regression rate and increase in the oxidizer mass flux exponent accompanied by the addition of 10% micro-zirconium led to the deduction that the blocking effect is the more dominant phenomenon of the two.

Fuel formulations containing high loadings (20% or 30%) of the nano-additives (nano-aluminum or nano-boron) exhibited poor combustion stability and large pressure excursions. Secondary motor firings exhibited significantly reduced regression rates. Post-combustion analysis showed thick molten layers accumulated on their fuel surfaces. The poor combustion performance was attributed to periodic shedding of the large accumulation of mass on the surface layer.

Bimetallic blends of each additive with nano-boron were evaluated at a loading of 10% to evaluate possible synergistic effects. In general, none of the fuels containing bimetallic blends outperformed the plain nano-boron fuel. The one exception to this trend was the fuel formulation containing a blend of micro-aluminum and nano-boron, which warrants further investigation.

To make direct comparisons between the metallic additives evaluated herein, the regression rate and combustion efficiency data for fuel formulations loaded with 10% additives are shown in Figures 103 and 104, respectively, and the regression rate and combustion efficiency data for fuel formulations loaded with 30% additives are shown in Figures 105 and 106, respectively. In Figures 103 and 104, plain HTPB and HTPB loaded

with 10% micro-aluminum, nano-aluminum, nano-boron, micro-magnesium, micro-titanium, and micro-zirconium are represented by open black circles, solid blue squares, solid green triangles, solid red diamonds, solid magenta triangles, solid brown pentagons, and solid purple stars, respectively. In Figures 105 and 106, plain HTPB and HTPB loaded with 30% micro-aluminum, nano-boron, micro-magnesium, micro-titanium, and micro-zirconium are represented by open black circles, solid blue squares, solid red diamonds, solid magenta triangles, solid brown pentagons, and solid purple stars, respectively.

Regarding the regression rates of HTPB loaded with 10% additives, the micro-zirconium outperformed all other formulations, and the nano-boron performed poorest. Regarding the regression rates of HTPB loaded with 30% additives, the micro-magnesium outperformed all other formulations, and the nano-boron performed poorest. Once again, the general trends observed within the regression rate data have been attributed to accumulation of mass on the combustion port surface. Post-combustion analysis of fuel grains (Figure 107) provided further evidence of this phenomenon. Qualitatively, the combustion ports shown in Figure 107 indicate mass accumulation is worse for higher metallic loadings, which is in agreement with the regression rate data.

The combustion efficiency data for the fuel formulations containing a 10% loading of additives appears to collapse onto a single trend line within the experimental uncertainty. This trend is well-represented by a linear approximation ($\eta_{c^*} = 0.98t_r + 32.5$) for the given range of data ($40 < t_r < 65$ ms). This linear approximation is system dependent and specific to the current experimental apparatus and testing conditions. Furthermore, this linear approximation would not hold true in a larger residence time

range, since the combustion efficiency should asymptote to 100% at long residence times and 0% at short residence times. The data do not collapse upon each other for the fuel formulations containing a 30% loading of additives. In this case, the micro-zirconium fuels exhibit the poorest combustion efficiency while the micro-aluminum and nano-boron fuels exhibit the highest combustion efficiencies.

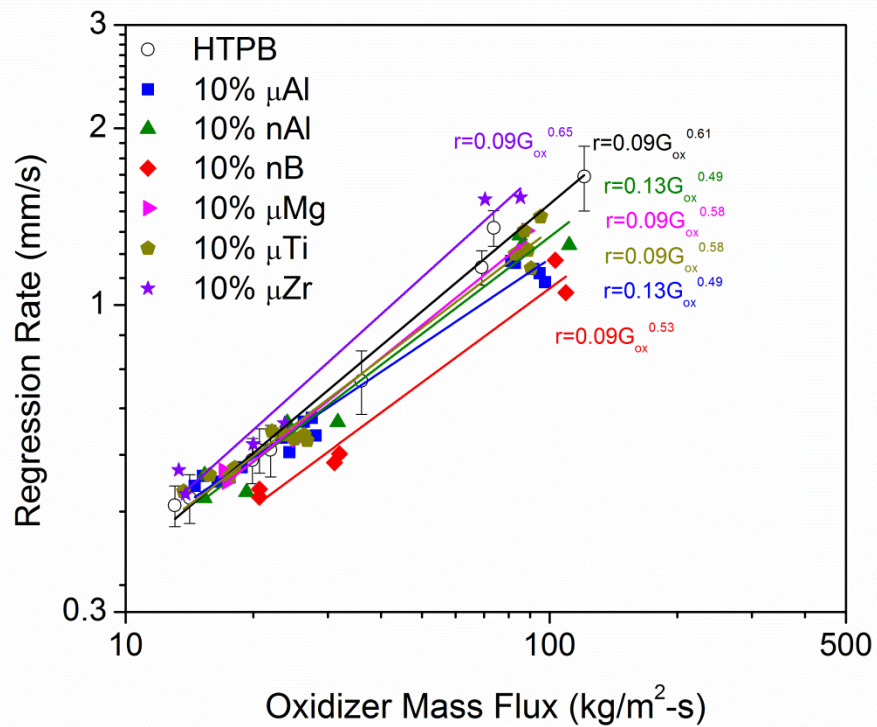


Figure 103. Relative effects of metallic additives at a loading of 10% on the regression rate of HTPB fuels burning in GOX.

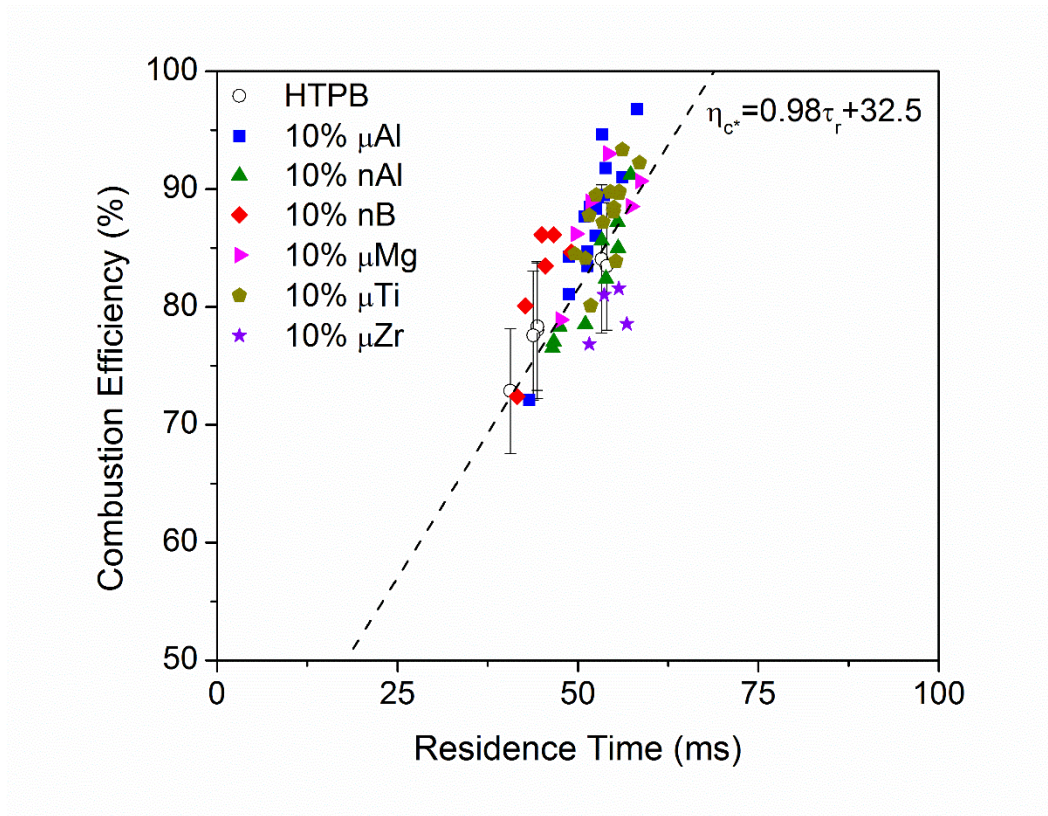


Figure 104. Relative effects of metallic additives at a loading of 10% on the combustion efficiency of HTPB fuels burning in GOX.

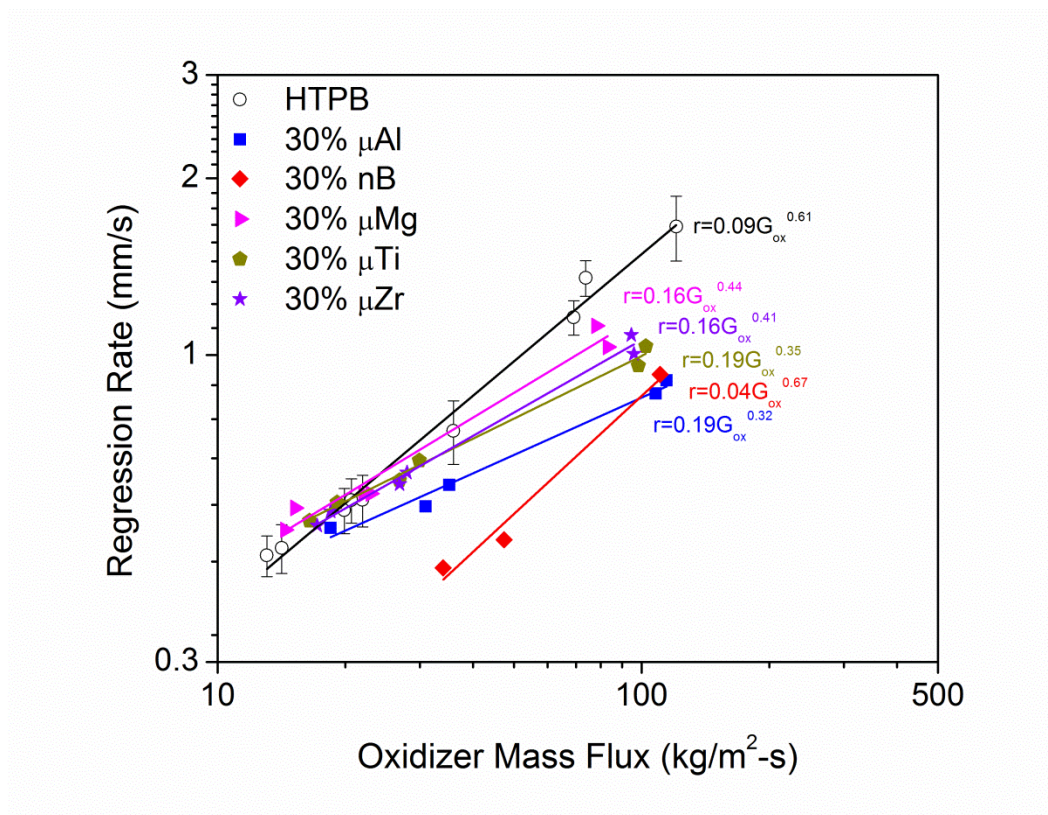


Figure 105. Relative effects of metallic additives at a loading of 30% on the regression rate of HTPB fuels burning in GOX.

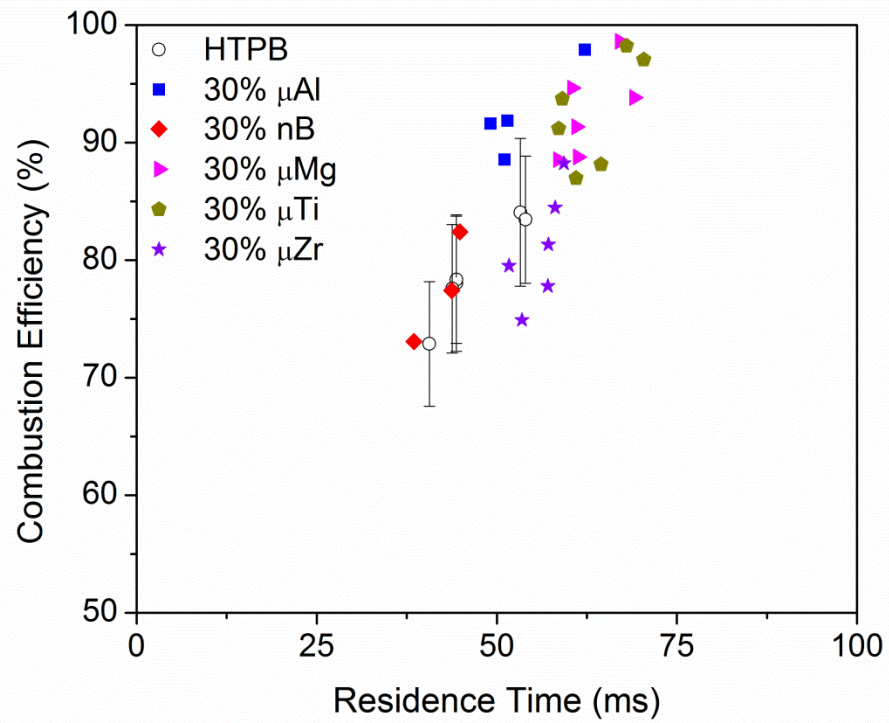


Figure 106. Relative effects of metallic additives at a loading of 30% on the combustion efficiency of HTPB fuels burning in GOX.

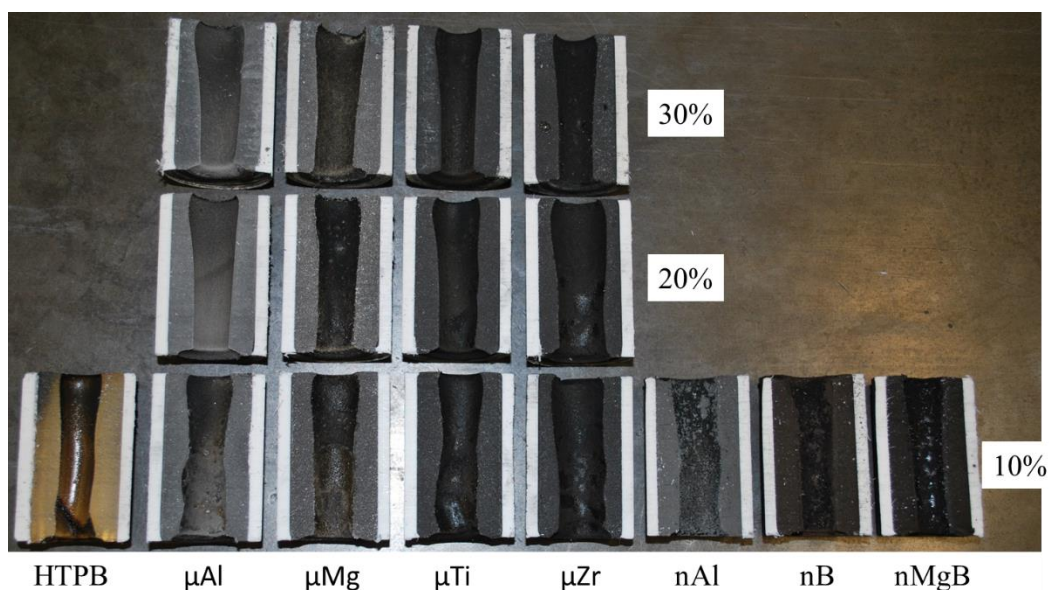


Figure 107. Post-combustion fuel ports surfaces for metallized fuels containing (top) 30%, (middle) 20%, and (bottom) 10% concentrations of metals. Motor formulations are shown left to right: baseline HTPB, micro-aluminum, micro-magnesium, micro-titanium, micro-zirconium, nano-aluminum, nano-boron, and magnesium-coated nano-boron.

The relative effects in terms of regression rate and fuel mass flux alteration in comparison to plain HTPB burning in GOX have been computed for each fuel formulation evaluated herein at an oxidizer mass flux of $100 \text{ kg/m}^2\text{-s}$ and are shown in Table 10 and depicted in Figure 108. Although all of these formulations yield increases in the density specific impulse of the HRE system, only two of the formulations led to an increase in the regression rate and only three of the formulations led to an increase in the fuel mass flux. Zirconium appears to be the best metallic additive available since it can yield the highest energy density at the lowest O/F ratio (Figure 32) without resulting in substantial decreases in the fuel regression rate and mass flux.

Table 10. Performance parameters of baseline and metal-loaded HTPB fuel formulations burning in GOX.

Formulation	Additives	ρ_f (kg/m ³)	a	n	R ²	\dot{r} (100) (mm/s)	$\rho_f \dot{r}$ (100) (kg/m ² -s)	$\Delta \dot{r}$ (%)	$\Delta \rho_f \dot{r}$ (%)
Baseline	-	930	0.09	0.61	0.99	1.49	1.38	-	-
μ Al-10	10% micro-Al	995	0.13	0.49	0.98	1.20	1.19	-19	-14
μ Al-20	20% micro-Al	1070	0.18	0.36	0.99	0.93	0.99	-38	-28
μ Al-30	30% micro-Al	1158	0.19	0.32	0.99	0.85	0.98	-43	-29
μ Al+nB-10	3.5% micro-Al, 6.5% nano-B	992	0.07	0.65	0.98	1.43	1.42	-4	3
nAl-10	10% nano-Al	995	0.10	0.55	0.97	1.31	1.30	-12	-6
nAl-20	20% nano-Al	1070	0.02	0.84	0.97	1.02	1.09	-31	-21
nAl+nB-10	3.5% nano-Al, 6.5% nano-B	992	0.12	0.45	0.99	0.95	0.94	-36	-32
nB-10	10% nano-B	990	0.09	0.53	0.97	1.07	1.06	-28	-23
nB-20	20% nano-B	1059	0.03	0.72	0.98	0.95	1.01	-36	-27
nB-30	30% nano-B	1137	0.04	0.67	0.98	0.85	0.97	-43	-30
μ Mg-10	10% micro-Mg	975	0.09	0.58	0.99	1.38	1.35	-7	-2
μ Mg-20	20% micro-Mg	1025	0.12	0.51	0.99	1.22	1.25	-18	-9
μ Mg-30	30% micro-Mg	1081	0.16	0.44	0.97	1.17	1.26	-21	-9
μ Mg+nB-10	3.5% micro-Mg, 6.5% nano-B	985	0.13	0.43	0.98	0.94	0.92	-37	-33
μ Ti-10	10% micro-Ti	1010	0.11	0.55	0.98	1.34	1.35	-10	-2
μ Ti-20	20% micro-Ti	1105	0.15	0.43	0.99	1.10	1.22	-26	-12
μ Ti-30	30% micro-Ti	1221	0.19	0.35	0.99	1.00	1.22	-33	-12
μ Ti+nB-10	3.5% micro-Ti, 6.5% nano-B	997	0.11	0.49	0.99	1.02	1.02	-31	-26
μ Zr-10	10% micro-Zr	1017	0.09	0.65	0.98	1.75	1.78	18	29
μ Zr-20	20% micro-Zr	1122	0.13	0.50	0.99	1.27	1.43	-14	3
μ Zr-30	30% micro-Zr	1252	0.16	0.41	0.99	1.06	1.33	-29	-4
μ Zr+nB-10	3.5% micro-Zr, 6.5% nano-B	999	0.08	0.58	0.99	1.14	1.14	-23	-17
nMgB-10	10% nano-MgB	986	0.09	0.53	0.98	1.05	1.04	-29	-25
nMgB-20	20% nano-MgB	1049	0.05	0.63	1.00	0.96	1.01	-35	-27

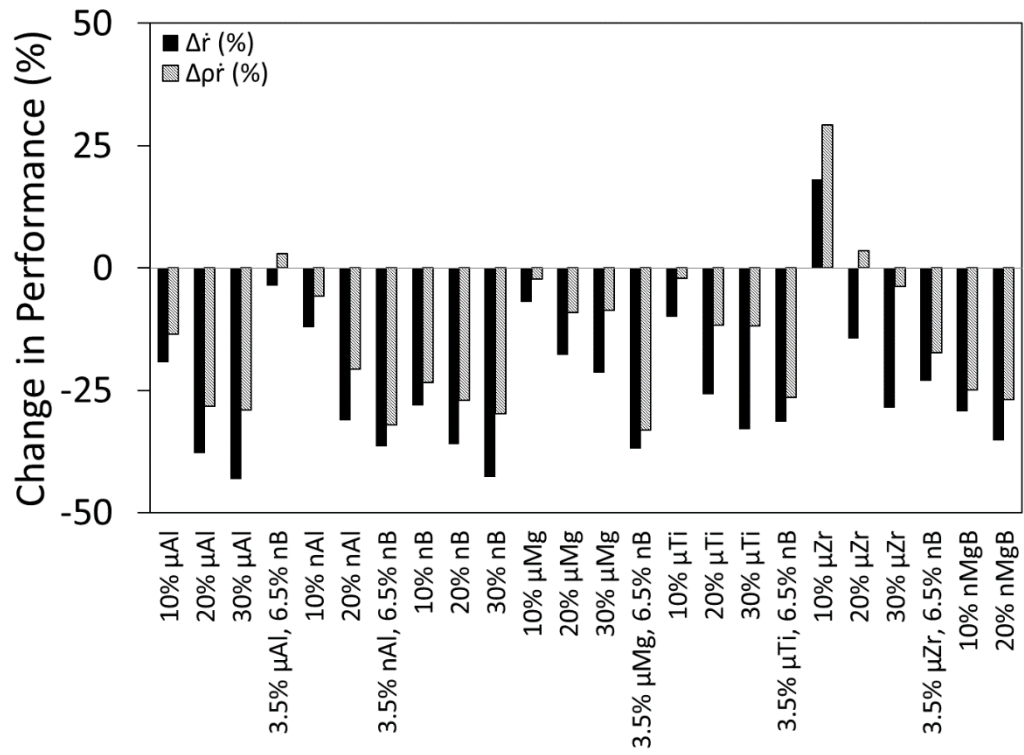


Figure 108. Relative effects of metallic additives on the regression rate (solid black) and fuel mass loss rate (dashed grey) of HTPB fuels burning in GOX at 100 kg/m²-s.

10. RESULTS AND DISCUSSION: MIXED-FUEL SYSTEMS

To evaluate the potential of mixed-fuel (HTPB/paraffin) systems for tailoring the regression rate of an HRE, fuel specimen composed of HTPB, paraffin, and HTPB loaded with paraffin at several concentrations (10, 25, 50, and 75%) were manufactured and burned in GOX. In contrast to the previously described metal-loaded fuel systems, fuel formulations described in this section were fired in the oxidizer blowdown configuration.

The average regression rate of all fuel grains burned in gaseous oxygen are plotted against the corresponding average oxidizer mass flux in Figure 109. The solid and dashed lines represent least-squares regression fits of the data to a power law approximation for plain HTPB and plain paraffin, respectively.

The paraffin fuel grains exhibited a regression rate increase of approximately 300% in comparison to plain HTPB over the evaluated testing conditions. In general, the mixed-fuel systems performed similar to the plain HTPB fuels and did not exhibit measureable enhancements in regression rates at any paraffin loading between 10 and 75%. Although all data points lie within the experimental scatter, at higher oxidizer mass fluxes ($>90 \text{ kg/m}^2\text{-s}$), the mixed-fuel systems appear to begin to outperform the plain HTPB fuel specimen. The observed lack of regression rate enhancement, even up to a paraffin loading of 75%, supports the hypothesis of a practical loading limit required prior to the realization of enhancement, but this explanation does not fully explain the observed results. These findings agree with those presented by Boronowsky [124], partially agree with the findings presented by Lee and Tsia [122-123], and are in conflict with the findings

presented by Sakote et al. [117] and Thomas et al. [128]. One explanation for the observed trends is that the paraffin and HTPB are homogeneously mixed, and the pyrolysis of HTPB dominates the regression process, so that no significant melt layer is formed during motor combustion. However, this explanation cannot fully account for the discrepancies between the current results and certain literature results.

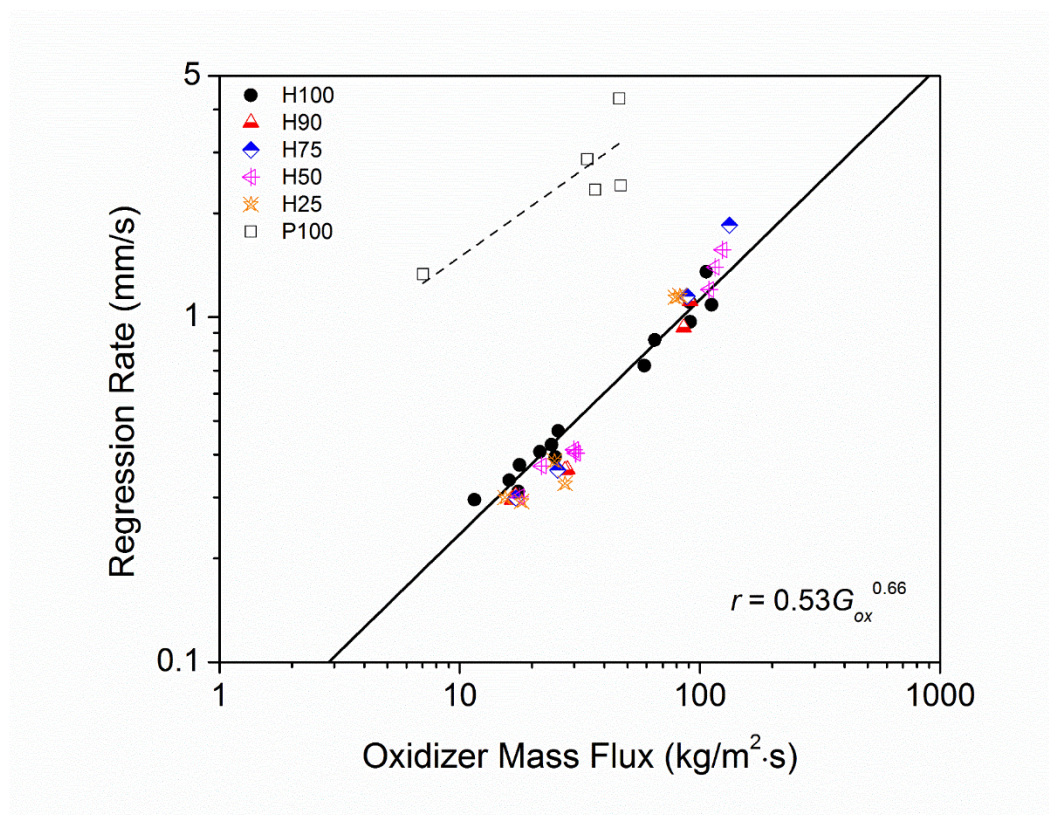


Figure 109. Measured regression rates for plain HTPB, plain paraffin, and mixed-fuel systems burning in GOX.

A summary of regression rate measurements of HTPB/paraffin fuel systems presented in the literature is shown in Table 11. Table 11 only includes studies where a direct comparison was made to a plain HTPB fuel specimen, so that the regression rate enhancement over the plain HTPB baseline could be evaluated. Furthermore, the hybrid

rocket studies shown in Table 11 only include experiments with axially flowing gaseous oxygen. The data in Table 11 from the experiment performed by Boronowsky [124] include fuel mixtures with paraffin included both as a molten liquid and as a solid particle; however, the subsequent discussion focuses entirely on fuel mixtures where the paraffin is incorporated as a molten liquid.

There is some disagreement between the studies, but there are also clear trends. The four presented hybrid rocket studies support the argument for a practical paraffin loading limit for realizable regression rate enhancement, because all loadings below 90% exhibit little to no enhancement, specifically for when the paraffin is included as molten liquid. One explanation for the discrepancies between the presented results of the selected experimental studies is that the operating conditions may play a significant role in regression rate enhancement of the mixed-fuel system. Within the dataset of the current study, the mixed-fuel systems' appear to begin to outperform the plain HTPB baseline at higher oxidizer mass fluxes ($>90 \text{ kg/m}^2\text{-s}$). The experiments of Boronowsky [124] showed no regression rate enhancement, and they were conducted at low oxidizer mass fluxes ($15\text{-}60 \text{ kg/m}^2\text{-s}$) and similar pressures. Lee and Tsai [122-123] observed a 10% regression rate enhancement for a paraffin loading of 50%, but their experiments were conducted at significantly larger oxidizer mass fluxes ($50\text{-}500 \text{ kg/m}^2\text{-s}$) and chamber pressures that were approximately 300% larger than the current study and that of Boronowsky [124]. Thomas et al. [128] observed a 20% increase in regression rate for a paraffin loading of 10%, but their experiments were conducted at chamber pressures that were also approximately 300% larger than the current study and that of Boronowsky [124]. This

comparison of experimental results suggests the operating conditions of motor firings, specifically the oxidizer mass flux and chamber pressure, may play a role in the effectiveness of mixed-fuel systems leading to regression rate enhancement. However, a comprehensive series of tests independently spanning a larger range of oxidizer mass fluxes and chamber pressures would be necessary to support this argument.

Table 11. Summary of relevant regression rate results for HTPB/paraffin binders.

Reference	Experiment	Paraffin Type/Loading	Enhancement
Sinha et al., 2015	DSC	Molten Liquid, 12.25%	5%
	3-43 K/min, 30-520 °C	Molten Liquid, 27.75%	33%
Lee and Tsia, 2008	Rocket (180x41 mm)	Molten Liquid, 50%	10%
	50-500 kg/m ² -s, 1.4-3.5 MPa	Molten Liquid, 90%	150%
Boronowsky, 2011	Rocket (40x20 mm) 15-60 kg/m ² -s, < 0.7 MPa	Molten Liquid, 15-30%	-
		Solid Particles (0.3-0.7 mm), 15%	25%
		Solid Particles (0.3-0.7 mm), 30%	40%
Thomas et al., 2017	Rocket (150x25 mm) 10-150 kg/m ² -s, < 1.5 MPa	Molten Liquid, 10%	20%
Current Study	Rocket (50x30 mm) 10-130 kg/m ² -s, < 0.9 MPa	Molten Liquid, 10-75%	-

11. SUMMARY AND CONCLUSIONS

Hybrid rockets have numerous advantages over their pure solid or liquid propellant counterparts, but their characteristically low regression rates and combustion efficiencies have hindered their widespread application. Following a brief introduction to their basic principles of operation and potential applications in Chapter 1, a thorough review of potential enhancement strategies for hybrid rockets was given in Chapter 2. These potential strategies included ideal selection of the oxidizer and fuel combination, manipulation of the oxidizer flow, augmentation of the combustion port geometry, inclusion of energetic additives, and implementation of unconventional geometries. Special emphasis was placed upon metal-based energetic additives and mixed-fuel systems.

Theoretical stoichiometric combustion and chemical equilibrium analyses were carried out in Chapter 3 for HTPB fuels loaded with various metal additives reacting with oxygen and nitrous oxide. These computations demonstrated the potential for metallic additives to yield significant improvement of hybrid rocket systems in terms of density specific impulse. Furthermore, relative performance rankings were given for metals incorporated in the HTPB/LOX system.

A state-of-the-art hybrid rocket model was developed in Chapter 4 and utilized to preliminary size components for a ballistic test stand. The design of the ballistic test stand was presented in detail in Chapter 5. The final configuration allows for economically feasible, time-efficient evaluation of multiple fuel formulations on a lab-scale

experimental apparatus. Furthermore, the modular design allows for manipulation of numerous experimental variables including oxidizer mass flow, oxidizer flow type, combustion chamber size, fuel grain length and initial diameter, and chamber pressure.

Several metallic additives (micro-aluminum, micro-magnesium, micro-titanium, micro-zirconium, nano-aluminum, nano-boron, and magnesium-coated nano-boron) were selected as potential candidates for hybrid rocket applications. Each additive was characterized by applicable microscopy techniques (SEM, TEM, and EDS) in Chapter 6 to determine relative particle size and composition, and assess their effects on combustion performance.

Fuel grain manufacturing techniques for plain HTPB, mixed-fuel (HTPB/paraffin), and metal-loaded HTPB fuel specimen were given in detail in Chapter 7. Ballistic testing procedures and data reduction methods were described in Chapter 8.

The regression rates and combustion efficiencies of plain HTPB and HTPB loaded with each additive at various loadings (10%, 20%, and 30%) burning in GOX were evaluated on the ballistic stand in Chapter 9. In general, the inclusion of any of the selected additives led to a reduction in the regression rate and minor changes in the combustion efficiency behavior. The one exception to this trend was the formulation containing a 10% loading of micro-zirconium, which yielded a moderate (10-20%) increase in the fuel's regression rate.

The observed trends were generally more prevalent at higher oxidizer mass fluxes and higher additive loadings. The reduction in regression rate accompanying the inclusion of nearly all the additives was attributed to a combination of slow metal reactions which

may take place in the post-combustion chamber, rather than the combustion port, and heat transfer-blocking effects derived from accumulation of mass on the fuel surface layer. The enhanced regression rate and increase in the oxidizer mass flux exponent accompanied by the addition of 10% micro-zirconium led to the deduction that the blocking effect is the more dominant phenomenon of the two.

Fuel formulations containing high loadings (20% or 30%) of the nano-additives (nano-aluminum or nano-boron) exhibited poor combustion stability and large pressure excursions. Secondary motor firings exhibited significantly reduced regression rates. Post-combustion analysis showed thick molten layers accumulated on their fuel surfaces. The poor combustion performance is attributed to periodic shedding of the large accumulation of mass on the surface layer.

Future work should focus on evaluation of the molten surface layer on a lab-scale apparatus with optical capabilities. In particular, evaluation of the effects of operating pressure on particle combustion in the diffusion flame and evaluation of particle geometry/size effects on their accumulation in the surface layer would prove useful.

Bimetallic blends of each additive with nano-boron were evaluated at a loading of 10% to evaluate possible synergistic effects. In general, none of the fuels containing bimetallic blends outperformed the plain nano-boron fuel. The one exception to this trend was the fuel formulation containing a blend of micro-aluminum and nano-boron, which warrants further investigation.

Combustion efficiency data of the plain HTPB and metal-loaded fuel formulations were not well correlated with the average O/F ratio, but they were well correlated to the

residence time. High combustion efficiencies (>95%) were achievable for all fuel formulations when a satisfactory residence time (~75 ms) was realized.

Although all of the metal-loaded HTPB fuel formulations yield increases in the theoretically calculated density specific impulse of the HRE system, only two of the formulations led to an increase in the regression rate, and only three of the formulations led to an increase in the fuel mass flux. Zirconium appears to be the best metallic additive available since it can yield the highest energy density at the lowest O/F ratio without resulting in substantial decreases in the fuel regression rate and mass flux.

In Chapter 10, the inclusion of paraffin in HTPB burning in GOX as a regression rate enhancement strategy was evaluated by inclusion of molten paraffin at mass loadings ranging from 10-75%. The plain paraffin fuel exhibited a 300% increase in regression rate in comparison to plain HTPB, but none of the mixed-fuel systems showed signs of regression rate enhancement at the tested operating conditions. Comparison of the current experimental results and the presented literature survey indicated that the manufacturing procedures of mixed HTPB/paraffin fuel systems and the operating conditions, such as the pressure and oxidizer mass flux, could play significant roles in any potential regression rate enhancement.

REFERENCES

- [1] M. J., "Regression Rate and Pyrolysis Behavior of HTPB-Based Solid Fuels in a Hybrid Rocket Motor," *Ph.D. Dissertation*, Pennsylvania State University, University Park, PA, 1997.
- [2] Chiaverini, M. J., "Review of Solid-Fuel Regression Rate Behavior in Classical and Nonclassical Hybrid Rocket Motors," *Fundamentals of Hybrid Rocket Combustion and Propulsion*, edited by M. J. Chiaverini and K. K. Kuo, Progress in Astronautics and Aeronautics, AIAA, Reston, VA, 2007, pp. 37-125.
- [3] Marxman, G. A., and Wooldridge, C. E., "Research on the Combustion Mechanism of Hybrid Rockets," *Advances in Tactical Rocket Propulsion*, edited by S. S. Penner, AGARD Conference Proceedings, Technivision Services, London, 1968, pp. 421-477.
- [4] Marxman, G. A., and Gilbert, M., "Turbulent Boundary Layer Combustion in the Hybrid Rocket," *Symposium (International) on Combustion*, Vol. 9, No. 1, 1963, pp. 371-383.
- [5] Marxman, G. A., "Boundary Layer Combustion in Propulsion," *Symposium (International) on Combustion*, Vol. 11, No. 1, 1967, pp. 269-289.
- [6] Smoot, L. D., and Price, C. F., "Regression Rates of Nonmetalized Hybrid Fuel Systems," *AIAA Journal*, Vol. 3, No. 8, 1965, pp. 1408-1413.
- [7] Smoot, L. D., and Price, C. F., "Regression Rates of Metalized Hybrid Fuel Systems," *AIAA Journal*, Vol. 4, No. 5, 1966, pp. 910-915.
- [8] Smoot, L. D., and Price, C. F., "Pressure Dependence of Hybrid Fuel Regression Rates," *AIAA Journal*, 1967, Vol. 5, No.1, pp. 102-106.
- [9] Muzzy, R. J., "Applied Hybrid Combustion Theory," *8th Joint Propulsion Specialist Conference*, AIAA, New Orleans, LA, 1972.
- [10] Ramohalli, K., and Stickler, D. B., "Polymer-Degradation Theory of Pressure-Sensitive Hybrid Combustion," *Symposium (International) on Combustion*, Vol. 13, No. 1, 1971, pp. 1059-1077.
- [11] G. P. Sutton, and O. Biblarz, *Rocket Propulsion Elements*, 8th ed., Wiley, NY, 2010.
- [12] Mead, Jr., F. B., "Early Developments in Hybrid Propulsion Technology at the Air Force Rocket Propulsion Laboratory," AIAA 1995-2946, *31st AIAA/ASME/SAE/ASEE Joint Propulsion Conference*, San Diego, CA, 1995.

- [13] Arves, J., Gnau, M., Joiner, K., Kearney, D., McNeal, C., and Murbach, M., "Overview of the Hybrid Sounding Rocket (HYSR) Project," AIAA 2003-5199, *39th AIAA/ASME/SAE/ASEE Joint Propulsion Conference*, Huntsville, AL, 2003.
- [14] Lavagna, M., Benvenuto, R., DeLuca, L. T., Maggi, F., and Graziano, M., "Contact-less Active Debris Removal: The Hybrid Propulsion Alternative," *5th European Conference for Aeronautics and Astronautics (EUCASS)*, Munich, Germany, 2013.
- [15] Tadini, P., Tancredi, U., Grassi, M., Anselmo, L., Pardini, C., Branz, F., Francesconi, A., Maggi, F., Lavagna, M., DeLuca, L. T., Viola, N., Chiesa, S., Trushlyakov, V., and Shimada, T., "Multi-Active Removal of Large Abandoned Rocket Bodies by Hybrid Propulsion Module," *10th International Conference on Flow Dynamics (ICFD)*, Sendai, Japan, 2013.
- [16] DeLuca, L. T., Lavagna, M., Maggi, F., Tadini, P., Pardini, C., Anselmo, L., Grassi, M., Pavarin, D., Francesconi, A., Branz, F., Chiesa, S., Viola, N., and Tancredi, U., "Large Debris Removal Mission in LEO Based on Hybrid Propulsion," *22nd Italian Association of Aeronautics and Astronautics Conference*, Napoli, Italy, 2013.
- [17] DeLuca, L. T., Bernelli, F., Maggi, F., Tadini, P., Pardini, C., Anselmo, L., Grassi, M., Pavarin, D., Francesconi, A., Branz, F., Chiesa, S., Viola, N., Bonnal, C., Trushlyakov, V., and Belokonov, I., "Active Space Debris Removal by Hybrid Propulsion Module," *Acta Astronautica*, Vol. 91, 2013, pp. 20-33.
- [18] Tadini, P., Tancredi, U., Grassi, M., Anselmo, L., Pardini, C., Francesconi, A., Branz, F., Maggi, F., Lavagna, M., DeLuca, L. T., Viola, N., Chiesa, S., Trushlyakov, V., and Shimada, T., "Active Debris Multi-Removal Mission Concept Based on Hybrid Propulsion," *Acta Astronautica*, Vol. 103, 2014, pp. 26-35.
- [19] Karabeyoglu, A., Stevens, J., Geyzel, D., and Cantwell, B., "High Performance Hybrid Upper Stage Motor," AIAA 2011-6025, *47th AIAA/ASME/SAE/ASEE Joint Propulsion Conference*, San Diego, CA, 2011.
- [20] Karabeyoglu, A., Falconer, T., Cantwell, B., and Stevens, J., "Design of an Orbital Hybrid Rocket Vehicle Launched from Canberra Air Platform," AIAA 2005-4096, *41st AIAA/ASME/SAE/ASEE Joint Propulsion Conference*, Tucson, AZ, 2005.
- [21] Smiley, M., Veno, M., and Bell, R., "Commercial Crew Development – Round One, Milestone 3: Overview of Sierra Nevada Corporation's Hybrid Motor Ground Test," AIAA 2011-5717, *47th AIAA/ASME/SAE/ASEE Joint Propulsion Conference*, San Diego, CA, 2011.

- [42] Chandler, A. A., Cantwell, B. J., Hubbard, G. S., and Karabeyoglu, A., "A Two-Stage, Single Port Hybrid Propulsion System for a Mars Ascent Vehicle," AIAA 2010-6635, *46th AIAA/ASME/SAE/ASEE Joint Propulsion Conference*, Nashville, TN, 2010.
- [23] Chandler, A., Cantwell, B. J., Hubbard, S., and Karabeyoglu, M. A., "Feasibility of Single Port Hybrid Propulsion System for a Mars Ascent Vehicle," *Acta Astronautica*, Vol. 69, 2011, pp. 1066-1072.
- [24] Shotwell, R., Benito, J., Karp, A., and Dankanich, J., "Drivers, Developments, and Options for a Mars Ascent Vehicle," *2016 IEEE Aerospace Conference*, Big Sky, MT, 2016.
- [25] Karp, A., Redmond, M., Nakazono, B., Vaughan, D., Shotwell, R., Story, G., and Jackson, D., "Technology Development and Design of a Hybrid Mars Ascent Vehicle Concept," *2016 IEEE Aerospace Conference*, Big Sky, MT, 2016.
- [26] Farias, E., Redmond, M., Karp, A., Shotwell, R., Mechentel, F., and Story, G., "Thermal Cycling for Development of Hybrid Fuel for a Notional Mars Ascent Vehicle," AIAA 2016-4563, *52nd AIAA/ASME/SAE/ASEE Joint Propulsion Conference*, Salt Lake City, UT, 2016.
- [27] Mechentel, F. S., Karp, A. C., Nakazono, B., Parker, M., and Vaughn, D., "Hybrid Propulsion In-situ Resource Utilization Test Facility Results for Performance Characterization," AIAA 2016-4566, *52nd AIAA/ASME/SAE/ASEE Joint Propulsion Conference*, Salt Lake City, UT, 2016.
- [28] Karp, A. C., Nakazono B., Benito, J., Shotwell, R., Vaughn, D., and Story, G., "A Hybrid Mars Ascent Vehicle Concept for Low Temperature Storage and Operation," AIAA 2016-4962, *52nd AIAA/ASME/SAE/ASEE Joint Propulsion Conference*, Salt Lake City, UT, 2016.
- [29] Shotwell, R., Benito, J., Karp, A., and Dankanich, J., "A Mars Ascent Vehicle for Potential Mars Sample Return," *2017 IEEE Aerospace Conference*, Big Sky, MT, 2017.
- [30] Karp, A., Nakazono, B., Shotwell, R., Benito, J., Kim, H., Brandeau, E., Vaughn, D., and Story, G., "A Hybrid Mars Ascent Vehicle Design and FY 2016 Technology Development," *2017 IEEE Aerospace Conference*, Big Sky, MT, 2017.
- [31] Benito, J., Noyes, C., Shotwell, R., Karp, A., Nakazono, B., Singh, G., Kim, H., Schoenenberger, M., Korzun, A., Lobbia, M., and Brandeau, E., "Hybrid Propulsion Mars Ascent Vehicle Concept Flight Performance Analysis," *2017 IEEE Aerospace Conference*, Big Sky, MT, 2017.

- [32] Karp, A. C., Nakazono, B., Shotwell, R., Benito, J., Vaughn, D., and Story, G., "Technology Development Plan and Preliminary Results for a Low Temperature Hybrid Mars Ascent Vehicle Concept," AIAA 2017-4900, *53rd AIAA/ASME/SAE/ASEE Joint Propulsion Conference*, Atlanta, GA, 2017.
- [33] Evans, B., and Karabeyoglu, A., "Development and Testing of SP7 Fuel for Mars Ascent Vehicle Application," AIAA 2017-4831, *53rd AIAA/ASME/SAE/ASEE Joint Propulsion Conference*, Atlanta, GA, 2017.
- [34] Karp, A. C., Nakazono, B., Vaughn, D., Story, G., Oglesby, B., and Prince, A., "Update on Technology Development Plan for a Low Temperature Hybrid Mars Ascent Vehicle Concept," AIAA 2018-4834, *54th AIAA/ASME/SAE/ASEE Joint Propulsion Conference*, Cincinnati, OH, 2018.
- [35] Story, G., Prince, A., Chaffin, J., Oglesby, B., Karp, A., and Kibbey, T., "Low Temperature Hybrid Mars Ascent Vehicle Concept Development and Planning at MSFC," AIAA 2018-4836, *54th AIAA/ASME/SAE/ASEE Joint Propulsion Conference*, Cincinnati, OH, 2018.
- [36] Estey, P. N., and Whittinghill, G. R., "Hybrid Rocket Motor Propellant Selection Alternatives," AIAA 1992-3592 *28th AIAA/ASME/SAE/ASEE Joint Propulsion Conference*, Nashville, TN, 1992.
- [37] Karabeyoglu, A., and Arkun, U., "Evaluation of Fuel Additives for Hybrid Rockets and SFRJ Systems," AIAA 2014-3647, *50th AIAA/ASME/SAE/ASEE Joint Propulsion Conference*, Cleveland, OH, 2014.
- [38] Heister, S., and Wernimont, E., "Hydrogen Peroxide, Hydroxyl Ammonium Nitrate, and Other Storable Oxidizers," *Fundamentals of Hybrid Rocket Combustion and Propulsion*, edited by M. J. Chiaverini and K. K. Kuo, Progress in Astronautics and Aeronautics, AIAA, Reston, VA, 2007, pp. 457-487.
- [39] Evans, B., Favorito, N. A., and Kuo, K. K., "Oxidizer-Type and Aluminum-Particle Addition Effects on Solid-Fuel Burning Behavior," AIAA 2006-4676, *42nd AIAA/ASME/SAE/ASEE Joint Propulsion Conference*, Sacramento, CA, 2006.
- [40] Lips, H. R., "Metal Combustion in High Performance Hybrid Rocket Propulsion Systems," AIAA 1976-640, *12th AIAA/ASME/SAE/ASEE Joint Propulsion Conference*, Palo Alto, CA, 1976.
- [41] Lips, H. R., "Heterogeneous Combustion of Highly Aluminized Hybrid Fuels," *AIAA Journal*, Vol. 15, No. 6, 1977, pp. 777-778.

- [42] Lips, H. R., "Experimental Investigation on Hybrid Rocket Engines Using Highly Aluminized Fuels," *Journal of Spacecraft and Rockets*, Vol. 14, No. 9, 1977, pp. 539–545.
- [43] Karabeyoglu, A., "Mixtures of Nitrous Oxide and Oxygen (Nytrox) as Oxidizers for Rocket Propulsion Applications," AIAA No. 2009-4966, *45th AIAA/ASME/SAE/ASEE Joint Propulsion Conference*, Denver, CO, 2009.
- [44] Karabeyoglu, A., "Mixtures of Nitrous Oxide, Carbon Dioxide, and Oxygen as Oxidizers for Mars Applications," AIAA 2010-6712, *46th AIAA/ASME/SAE/ASEE Joint Propulsion Conference*, Nashville, TN, 2010.
- [45] Karabeyoglu, A., "Nitrous Oxide and Oxygen Mixtures (Nytrox) as Oxidizers for Rocket Propulsion Applications," *Journal of Propulsion and Power*, Vol. 30, No. 3, 2014, pp. 696-706.
- [46] Ramohalli, K., and Dowler, W., "A Helping HAN for Hybrid Rockets," *Aerospace America*, 1955, pp. 20-21.
- [47] Biddle, R. A., and Sutton, E. S., U.S. Patent Application for a "Highly Soluble, Non-Hazardous Hydroxylammonium Salt Solutions for Use in Hybrid Rocket Motors," US Patent No. 4527389A, 1985.
- [48] Kang, S., and Kwon, S., "Difficulties of Catalytic Reactor for Hydroxylammonium Nitrate Hybrid Rocket," *Journal of Spacecraft and Rockets*, Vol. 52, No. 5, 2015, pp. 1508-1510.
- [49] Whitmore, S. A., Merkely, D. P., Walker, S. D., and Spurrier, Z. S., "Thermal Decomposition of Aqueous Hydroxyl-Ammonium Nitrate Solutions Using a Hybrid Propellant Gas Generator," AIAA 2015-4040, *51st AIAA/ASME/SAE/ASEE Joint Propulsion Conference*, Orlando, FL, 2015.
- [50] Belcher, T., Valenzuela, J. A., Vanhooose, J. H., Perea, N., and Love, N., "Hybrid Motor Regression Rate Using the Decomposition Products of a Green Monopropellant as the Oxidizer," AIAA 2018-4528, *54th AIAA/SAE/ASEE Joint Propulsion Conference*, Cincinnati, OH, 2018.
- [51] Schultz, R. D., and Dekker, A. O., "The Absolute Thermal Decomposition Rates of Solids—Part 1. The Hot-Plate Pyrolysis of Ammonium Chloride and the Hot-Wire Pyrolysis of Polymethylmethacrylate (Plexiglas 1A)," *Symposium (International) on Combustion*, Vol. 5, No. 1, 1955, pp. 260–267.

- [52] Chaiken, R. F., Andersen, W. H., Barsh, M. K., Mishuk, G. M., and Schultz, R. D., "Kinetics of the Surface Degradation of Polymethylmethacrylate," *Journal of Chemical Physics*, Vol. 32, No. 1, 1960, pp. 141–146.
- [53] McAlevy, R. F., III, and Hansel, J. G., "Linear Pyrolysis of Thermoplastics in Chemically Reactive Environments," *AIAA Journal*, Vol. 3:2, 1965, pp. 244–249.
- [54] Risha, G. A., Evans, B. J., Boyer, E., and Kuo, K. K., "Metals, Energetic Additives, and Special Binders Used in Solid Fuels for Hybrid Rockets," *Fundamentals of Hybrid Rocket Combustion and Propulsion*, edited by M. J. Chiaverini and K. K. Kuo, Progress in Astronautics and Aeronautics, AIAA, Reston, VA, 2007, pp. 413-456.
- [55] Humble, R. W. "Fuel Performance Enhancements for Hybrid Rockets" AIAA 2000-3437, *36th AIAA/ASME/SAE/ASEE Joint Propulsion Conference*, Huntsville, Alabama, May 2000.
- [56] Carrick, P. G. and Larson, C. W., "Lab Scale Test and Evaluation of Cryogenic Solid Hybrid Rocket Fuels," AIAA 1995-2948, *31st AIAA/ASME/SAE/ASEE Joint Propulsion Conference*, San Diego, CA, 1995.
- [57] Larson, C. W., Pfeil, K. L., DeRose, M.E., and Carrick, P. G., "High Pressure Combustion of Cryogenic Solid Fuels for Hybrid Rockets," AIAA 1996-2594, *32nd AIAA/ASME/SAE/ASEE Joint Propulsion Conference*, Lake Buena Vista, FL, 1996.
- [58] DeRose, M. E., Pfeil, K. L., Carrick, P. G., and Larson, C. W., "Tube Burner Studies of Cryogenic Solid Combustion," AIAA 1997-3076, *33rd AIAA/ASME/SAE/ASEE Joint Propulsion Conference*, Seattle, WA, 1997.
- [59] St. Clair, C. P., Rice, E. E., Knuth, W. H., and Gramer, D. J., "Advanced Cryogenic Solid Hybrid Rocket Engine Developments: Concept and Test Results," AIAA 1998-3508, *34th AIAA/ASME/SAE/ASEE Joint Propulsion Conference*, Cleveland, OH, 1998.
- [60] Gramer, D. J., Rice, E. E., Knuth, W. H., and St. Clair, C. P., "Experimental Investigation of a Metallized Cryogenic Hybrid Rocket Engine," AIAA 1998-3509, *34th AIAA/ASME/SAE/ASEE Joint Propulsion Conference*, Cleveland, OH, 1998.
- [61] Rice, E. E., Chiaverini, M. J., St. Clair, C. P., Knuth, W. H., and Gustafson, R. J., "Mars ISRU CO/O₂ Hybrid Engine Development Status," AIAA 2000-1066, *38th Aerospace Sciences Meeting*, Reno, NV, 2000.
- [62] Rice, E. E., and Gramer, D. J., "Methane and Methane/Aluminum Cryogenic Hybrid Rocket Engine for Mars ISRU Propulsion," AIAA 2000-1064, *38th Aerospace Sciences Meeting*, Reno, NV, 2000.

- [63] Karabeyoglu, M. A., Altman, D., and Cantwell, B. J., "Combustion of Liquefying Hybrid Propellants: Part 1. General Theory," *Journal of Propulsion and Power*, Vol. 18, No. 3, 2002, pp. 610-620.
- [64] Karabeyoglu, M. A., and Cantwell, B. J., "Combustion of Liquefying Hybrid Propellants: Part 2. Stability of Liquid Films," *Journal of Propulsion and Power*, Vol. 18, No. 3, 2002, pp. 621-630.
- [65] Karabeyoglu, M. A., Cantwell, B. J., and Stevens, J. "Evaluation of Homologous Series of Normal-Alkanes as Hybrid Rocket Fuels," AIAA 2005-3908, *41st AIAA/ASME/SAE/ASEE Joint Propulsion Conference*, Tucson, AZ, 2005.
- [66] Karabeyoglu, M. A., Cantwell, B. J., and Stevens, J. "Scale-Up Tests of High Regression Rate Paraffin-Based Hybrid Rocket Fuels," *Journal of Propulsion and Power*, Vol 20, No. 6, 2004, pp. 1037-1045.
- [67] Karabeyoglu, M. A., Cantwell, B. J., and Altman, D., "Development and Testing of Paraffin-Based Hybrid Rocket Fuels," AIAA 2001-4503, *37th AIAA/ASME/SAE/ASEE Joint Propulsion Conference*, Salt Lake City, UT, 2001.
- [68] Weinstein, A., and Gany, A., "Investigation of Paraffin Based Fuels in Hybrid Combustors," *International Journal of Energetic Materials and Chemical Propulsion*, Vol. 10, 2011, pp. 277-296.
- [69] Weinstein, A., and Gany, A., "Testing and Modeling Liquefying Fuel Combustion in Hybrid Propulsion," *Progress in Propulsion Physics*, Vol. 4, 2012, pp. 63-76.
- [70] Sisi, S. B., and Gany, A., "Heat and Mass Transfer Analysis for Paraffin/Nitrous Oxide Burning Rate in Hybrid Propulsion," *Acta Astronautica*, Vol. 120, 2016, pp. 121-128.
- [71] Karabeyoglu, M. A., Ziliac, G., Castellucci, P., Urbanczyk, P., Stevens, J., Inalhan, G., and Cantwell, B. J., "Development of High-Burning-Rate Hybrid-Rocket-Fuel Flight Demonstrators," AIAA 2003-5196, *39th AIAA/ASME/SAE/ASEE Joint Propulsion Conference*, Huntsville, Al, 2003.
- [72] Pelt, D. V., Hopkins, J., Skinner, M., Buchanan, A., Gulman, R., Chan, H., Karabeyoglu, and Cantwell, B. J., "Overview of a 4-inch OD Paraffin-Based Hybrid Sounding Rocket Program," AIAA 2004-3822, *40th AIAA/ASME/SAE/ASEE Joint Propulsion Conference*, Ft Lauderdale, DL, 2004.

[73] Dyer, J., Doran, E., Dunn, Z., Lohner, K., Bayart, C., Sadhwani, A., Zilliac, G., Cantwell, B., and Karabeyoglu, A., "Design and Development of a 100km Nitrous Oxide/Paraffin Hybrid Rocket Vehicle," AIAA 2007-5362, *43rd AIAA/ASME/SAE/ASEE Joint Propulsion Conference*, Cincinnati, OH, 2007.

[74] Dunn, Z., Dyer, J., Lohner, Doran, E., K., Bayart, C., Sadhwani, A., Zilliac, G., Karabeyoglu, A., and Cantwell, B., "Test Facility Development for 15,000 lb Thrust Peregrine Hybrid Sounding Rocket," AIAA 2007-5358, *43rd AIAA/ASME/SAE/ASEE Joint Propulsion Conference*, Cincinnati, OH, 2007.

[75] Dyer, J., Doran, E., Zilliac, G., Lohner, K., Cantwell, B., Karabeyoglu, A., Marzona, M., and Karlik, E., "Status Update for the Peregrine 100km Sounding Rocket Project," AIAA 2008-4829, *44th AIAA/ASME/SAE/ASEE Joint Propulsion Conference*, Hartford, CT, 2008.

[76] Zilliac, G., Waxman, B., Doran, E., Dyer, J., Karabeyoglu, A., and Cantwell, B., "Peregrine Hybrid Rocket Motor Ground Test Results," AIAA 2012-4017, *48th AIAA/ASME/SAE/ASEE Joint Propulsion Conference*, Atlanta, GA, 2012.

[77] Zilliac, G., Waxman, B., Karabeyoglu, A., Cantwell, B., and Evans, B. J., "Peregrine Hybrid Rocket Motor Development," AIAA 2014-3870, *50th AIAA/ASME/SAE/ASEE Joint Propulsion Conference*, Cleveland, OH, 2014.

[78] Kobald, M., Schmierer, C., Ciezki, H., Schlechtriem, S., Toson, E., and DeLuca, L. T., "Evaluation of Paraffin-Based Fuels for Hybrid Rocket Engines," AIAA 2014-3646, *50th AIAA Joint Propulsion Conference*, Cleveland, OH, July 28-30, 2014.

[79] Kobald, M., Verri, I., and Schlechtriem, S., "Theoretical and Experimental Analysis of Liquid Layer Instability in Hybrid Rocket Engines," *Space Propulsion Conference*, Cologne, Germany, 2014.

[80] Evans, B., Favorito, N. A., Boyer, E., Risha, G. A., Wehrman, R. B., and Kuo, K. K., "Characterization of Nano-Sized Energetic Particle Enhancement of Solid-Fuel Burning Rates in an X-Ray Transparent Hybrid Rocket Engine," AIAA 2004-3821, *40th AIAA/ASME/SAE/ASEE Joint Propulsion Conference*, Fort Lauderdale, FL, July 2004.

[81] Kobald, M., Petrarolo, A., and Schlechtriem, S., "Combustion Visualization of Liquefying Hybrid Rocket Fuels," AIAA 2015-4137, *51st AIAA/SAE/ASEE Joint Propulsion Conference*, Orlando, FL, 2015.

[82] Kobald, M., and Petrarolo, A., "Evaluation Techniques for Optical Analysis of Hybrid Rocket Propulsion," *12th International Conference on Flow Dynamics*, Sendai, Japan, 2015.

- [83] Petrarolo, A., Kobald, M., and Schleichtrien, S., "Optical Analysis of Hybrid Rocket Combustion with Decomposition Method," *2016 Space Propulsion Conference*, Rome, Italy, 2016.
- [84] Petrarolo, A., and Kobald, M., "Evaluation Techniques for Optical Analysis of Hybrid Rocket Propulsion," *Journal of Fluid Science and Technology*, Vol. 11, No. 4, 2016.
- [85] Petrarolo, A., Kobald, M., and Schleichtrien, S., "Optical Analysis of the Liquid Layer Combustion of Paraffin-Based Hybrid Rocket Fuels," *7th European Conference for Aeronautics and Space Sciences (EUCASS)*, Milan, Italy, 2017.
- [86] Petrarolo, A., Kobald, M., and Schleichtrien, S., "Liquid Layer Combustion Visualization of Paraffin-based Hybrid Rocket Fuels," AIAA 2017-4828, *53rd AIAA/SAE/ASEE Joint Propulsion Conference*, Atlanta, GA, 2017.
- [87] Petrarolo, A., Kobald, M., Ciezki, H. K., and Schleichtrien, S., "Optical Analysis of Liquid Film Instabilities in Paraffin-Based Hybrid Rocket Fuels," *68th International Astronautical Congress (IAC)*, Adelaide, Australia, 2017.
- [88] Petrarolo, A., Kobald, M., and Schleichtrien, S., "Understanding Kelvin-Helmholtz Instability in Paraffin-Based Hybrid Rocket Fuels," *Experiments in Fluids*, Vol. 59, No. 62, 2018.
- [89] Petrarolo, A., Kobald, M., and Schleichtrien, S., "Investigation of the Kelvin-Helmholtz Instability Process in Liquefying Hybrid Rocket Fuels," *2018 Space Propulsion Conference*, Sevilla, Spain, 2018.
- [90] Petrarolo, A., Kobald, M., and Schleichtrien, S., "Optical Analysis of the Liquid Layer Combustion of Paraffin-Based Hybrid Rocket Fuels," *Acta Astronautica*, Vol. 151, No. 1, 2018.
- [91] Petrarolo, A., Kobald, M., and Schleichtrien, S., "Visualization of Combustion Phenomena in Paraffin-Based Hybrid Rocket Fuels at Super-Critical Pressures," AIAA 2018-4927, *54th AIAA/SAE/ASEE Joint Propulsion Conference*, Cincinnati, OH, 2018.
- [92] Hikone, S., Maruyama, S., Isiguro, T., and Nakagawa, I., "Regression Rate Characteristics and Burning Mechanism of Some Hybrid Rocket Fuels," AIAA 2010-7030, *46th AIAA/ASME/SAE/ASEE Joint Propulsion Conference*, Nashville, TN, 2010.
- [93] Chandler, A., Jens, E., Cantwell, B. J., and Hubbard, G. S., "Visualization of the Liquid Layer Combustion of Paraffin Fuel for Hybrid Rocket Applications," AIAA 2012-3961, *48th AIAA/ASME/SAE/ASEE Joint Propulsion Conference*, Nashville, TN, 2012.

- [94] Jens, E. T., Mechentel, F. S., Cantwell, B. J., and Hubbard, G. S., “Combustion Visualization of Paraffin-Based Hybrid Rocket Fuel at Elevated Pressures,” AIAA 2014-3848, *50th AIAA/ASME/SAE/ASEE Joint Propulsion Conference*, Cleveland, OH, 2014.
- [95] Jens, E. T., Mechentel, F. s., Cantwell, B. J., and Hubbard, G. S., “Combustion Visualization of Paraffin-Based Hybrid Rocket Fuel at Elevated Pressures,” AIAA 2014-3848, *50th AIAA/ASME/SAE/ASEE Joint Propulsion Conference*, Cleveland, OH, 2014.
- [96] Jens, E. T., Narsai, P. B., Cantwell, B. J., and Hubbard, G. S., “Scglieren Imaging of the Combustion of Classical and High Regression Rate Hybrid Rocket Fuels,” AIAA 2014-3849, *50th AIAA/ASME/SAE/ASEE Joint Propulsion Conference*, Cleveland, OH, 2014.
- [97] Paravan, C., Bisin, R., Carlotti, S., Maggi, G., and Galfetti, L., “Diagnostics for Entrainment Characterization in Liquefying Fuel Formulations,” AIAA 2018-4663, *54th AIAA/SAE/ASEE Joint Propulsion Conference*, Cincinnati, OH, 2018.
- [98] Kobald, M., Schmierer, C., Ciezki, H. K., Schlectriem, S., Toson, E., and DeLuca, L. T., “Viscosity and Regression Rate of Liquefying Hybrid Rocket Fuels,” *Journal of Propulsion and Power*, Vol. 33, No. 5, 2017, pp. 1245-1251.
- [99] Paravan, C., Galfetti, L., and Maggi, F., “A Critical Analysis of Paraffin-Based Fuel Formulations for Hybrid Rocket Applications,” AIAA 2017-4830, *53rd AIAA/ASME/SAE/ASEE Joint Propulsion Conference*, Atlanta, GA, 2017.
- [100] Dermanci, O., and Karabeyoglu, A., “Effect of Nano Particle Addition on the Regression Rate of Liquefying Fuels,” AIAA No. 2015-4139, *51st AIAA/ASME/SAE/ASEE Joint Propulsion Conference*, Orlando, FL, 2015.
- [101] DeSain, J. D., Brady, B. B., Metzler, K. M., Curtiss, T. J., and Albright, T. V., “Tensile Tests of Paraffin Wax for Hybrid Rocket Fuel Grains,” AIAA No. 2009-5115, *45th AIAA/ASME/SAE/ASEE Joint Propulsion Conference*, Denver, CO, 2009.
- [102] Kim, S., Lee, J., Moon, H., Sung, H., Kim, J., and Cho, J., “Effect of Paraffin-LDPE Blended Fuel in Hybrid rocket Motor,” AIAA 2010-7031, *46th AIAA/ASME/SAE/ASEE Joint Propulsion Conference*, Nashville, TN, 2010.
- [103] Kim, S., Moon, H., Kim, J., Cho, J., “Evaluation of Paraffin–Polyethylene Blends as Novel Solid Fuel for Hybrid Rockets”, *Journal of Propulsion and Power*, Vol. 31, No. 6, 2015, pp. 1750-1760.
- [104] Pal, Y., and Kumar, V. R., “Physical and Ballistic Characterization of Aluminum-Loaded Paraffin Hybrid rocket Fuels,” *Energy and Fuels*, Vol. 31, no. 9, 2017, pp. 10133-10143.

- [105] Lyne, J. e., Naoumov, V. I., Scholes, J., Dodge, M., Elton, B., Wozniak, P., Austinand, D., and Combs, C., “First Steps in the Development and testing of Nontoxic, Bioderived Fuels for Hybrid Rocket Motors,” AIAA 2005-0741, *43rd AIAA Aerospace Sciences Meeting*, Reno, NV, 2005.
- [106] Naoumov, V., Haralambous, A., Goldreich, a., Boynton, T., and Koc, M., “Student-Faculty Research on the Combustion in Hybrid-Propellant Rocket Engine for Aerospace Specialization in Mechanical Engineering Curriculum,” AIAA 2012-0436, *50th AIAA Aerospace Sciences Meeting*, Nashville, TN, 2012.
- [107] Naoumov, V., Al-Masoud, N., Haralambous, A., Goldreich, A., and Monsy, E., “Senior Capstone Design Project for Aerospace Specialization and Student-Faculty Research on Propulsion,” AIAA 2013-0658, *51st AIAA Aerospace Sciences Meeting*, Grapevine, TX, 2013.
- [108] Naoumov, V., Haralambous, A., Goldreich, A., and Monsy, E., “Hybrid Propellant Rocket Engine Test Fixture and Research on the Combustion of Non-Conventional Fuels,” AIAA 2013-0450, *51st AIAA Aerospace Sciences Meeting*, Grapevine, TX, 2013.
- [109] Naoumov, V., Knochenhauer, N., Sansevero, P., Goldreich, A., Freeto, C., Kimiecik, T., and Frye, O., “Research on the Combustion of Bio-Derived Fuels in Hybrid Propellant Rocket Engine,” AIAA 2014-0309, *52nd AIAA Aerospace Sciences Meeting*, National Harbor, MD, 2014.
- [110] Naoumov, V., Al-Masoud, N., Sansevero, P., guadagnoli, L., Moni, A. M., and Loukides, D., “Design Project for Aerospace Specialization and student Research on the Combustion of Bio-Derived Rocket Fuels,” AIAA 2014-0060, *52nd AIAA Aerospace Sciences Meeting*, National Harbor, MD, 2014.
- [111] Naoumov, V., Al-Masoud, N., Skomin, P., and Deptula, P., “Undergraduate Research on Peculiarities of the combustion of ecologically Clean Paraffin Wax Fuels in Hybrid Propellant Rocket Engines,” AIAA 2015-1513, *53rd AIAA Aerospace Sciences Meeting*, Kissimmee, FL, 2015.
- [112] Naoumov, V., Skomin, P., and Deptula, P., “Combustion of Bio-Derived Fuels with Additives and Research on the Losses of Unburned Fuel in Hybrid Propellant Rocket Engines,” AIAA 2015-0923, *53rd AIAA Aerospace Sciences Meeting*, Kissimmee, FL, 2015.
- [113] Naoumov, V., Nguyen, H., and Alcalde, B., “Study of the Combustion of Beeswax and Beeswax with aluminum Powder in Hybrid Propellant Rocket Engine,” AIAA 2016-2145, *54th AIAA Aerospace Sciences Meeting*, San Diego, CA, 2016.

- [114] Naoumov, V., Al-Masoud, N., Nguyen, H., Patallo, E. C., and Mocarski, A., "Senior Capstone Design Project for Preparing Undergraduate Students for Work in a Research and Engineering Environment," AIAA 2016-1801, *54th AIAA Aerospace Sciences Meeting*, San Diego, CA, 2016.
- [115] Naoumov, V., Al-Masoud, N., Sherman, K., Doolittle, m., Ziegler, M., and Thorne, D., "Study of the Combustion of Pure Bio-Derived Fuels and Bio-Derived Fuels with additives in Hybrid Propellant rocket Engine," AIAA 2017-0833, *55th AIAA Aerospace Sciences Meeting*, Grapevine, TX, 2017.
- [116] Naoumov, V., and Al-Masoud, N., "Senior Capstone Design Research Project on Combustion of Bio-Derived Fuels in Hybrid Propellant Rocket Engine, *56th AIAA Aerospace Sciences Meeting*, Kissimmee, FL, 2018.
- [117] Sakote, R., Narendra, Y., Karmakar, S., Joshi, P. C., and Chatterjee, A. K., "Regression Rate Studies of Paraffin Wax-HTPB Hybrid Fuels Using Swirl Injectors," *Propellants, Explosives, and Pyrotechnics*, Vol. 39, No. 6, 2014, pp. 859-865.
- [118] Sinha, Y. K., Sridhar, B. T. N., Santhosh, M., "Thermal Decomposition Study of HTPB Solid Fuel in the Presence of Activated Charcoal and Paraffin," *Journal of Thermal Analysis and Calorimetry*, Vol. 119, No. 1, 2015, pp. 557–565.
- [119] Sinha, Y. K., Sridhar, B. T. N., and Kishnakumar, R., "Study of Thermo-Mechanical Properties of HTPB-Paraffin Solid Fuel," *Arabian Journal for Science and Engineering*, Vol. 41, No. 11, 2016, pp. 4683-4690.
- [120] Cardoso, K. P., Nagamachi, M. Y., Kawachi, E. Y., Araujo, T. B., and Nunes, R. F., "Thermogravimetric Analysis of the Decomposition of a Paraffin Particle/HTPB Fuel Grain for Hybrid Rocket Motors," AIAA 2015-0922, *53rd AIAA Aerospace Sciences Meeting*, Kissimmee, FL, 2015.
- [121] Hu, S., Wu, G., Hua, Y., Rashid, N. F., and Hu, H., "Study on Thermal Degradation Characteristics and Regression Rate Measurement of Paraffin-Based Fuel," *Energies*, Vol. 8, No. 9, 2015, pp. 10058-10081.
- [122] Lee, T. S., and Tsia, H. L., "Combustion Characteristics of a Paraffin-Based Fuel Hybrid Rocket," *9th Asia-Pacific International Symposium on Combustion and Energy Utilization*, Beijing, China, 2008.
- [123] Lee, T. S., and Tsia, H. L., "Fuel Regression Rate in a Paraffin-HTPB Nitrous Oxide Hybrid Rocket," *9th Asia-Pacific Conference on Combustion*, Taipei, Taiwan, 2009.

- [124] Boronowsky, K. M., "Non-Homogeneous Hybrid Rocket Fuel for Enhanced Regression Rates Utilizing Partial Entrainment," *Master's Thesis*, San Jose State University, San Jose, CA, 2011.
- [125] Sisi, S., and Gany, A., "Combustion of Plain and Reinforced Paraffin with Nitrous Oxide," *International Journal of Energetic Materials*, Vol. 14, No. 4, 2015, pp. 331-345.
- [126] Hansen, V. K., and Edwards, T. C., "Development of an O-Class Paraffin/HTPB-N₂O Hybrid Rocket Motor," *AIAA Region VI Student Conference*, Seattle, WA, 2012.
- [127] Edwards, T., Hansen, V., Slais, T., Chu, C., Hughes, M., Li, G., Finnegan, G., Ip, T., Hatt, A., Degang, B., Knowlen, C., Bruckner, A., Hermanson, and J., Mattick, T., "University of Washington DAQ Destroyer Hybrid Rocket," *7th Intercollegiate Rocket Engineering Competition*, Green River, UT, 2012.
- [128] Thomas, J. C., "Enhancement of Regression Rates in Hybrid Rockets with HTPB Fuel Grains by Metallic and Entrainment Additives," *Journal of Propulsion and Power*, In Preparation.
- [129] Rastogi, R. P., and Bajjal, S. K., "Boron Containing Polymers as Potential rocket Propellants," *AIAA Journal*, Vol. 6, No. 1, 1968.
- [130] Rastogi, R. P., and Bajjal, S. K., "Heterogenous Combustion of Boron-Containing Polymers," *AIAA Journal*, Vol. 9, No. 1, 1971.
- [131] Risha, G. A., Miller, A. g., Glass, R. A., Yeager, V. A., Chiaverini, M. J., and Tappan, B. C., "Regression Rates of Solid Fuels Containing High Nitrogen (HiN) Materials," *AIAA 2011-5912, 47th AIAA/ASME/SAE/ASEE Joint Propulsion Conference*, San Diego, CA, 2011.
- [132] Whitmore, S. A., Peterson, Z. W., and Eilers, S. D., "Comparing Hydroxyl Terminated Polybutadiene and Acrylonitrile Butadiene styrene as Hybrid Rocket Fuels," *Journal of Propulsion and Power*, Vol. 29, No. 3, 2013, pp. 582-592.
- [133] Whitmore, S. A., Wilson, J. R., Ritter, M. A., and Williams, L. T., "Estimating the Enthalpy of Gasification of Acrylonitrile-Butadiene-styrene Hybrid Rocket Fuels," *Journal of Propulsion and Power*, Vol. 31, No. 4, 2015, pp. 1033-1040.
- [134] Whitmore, S. A., Merkley, S. L., Tonc, L., and Mathias, S., "Survey of Selected Additively Manufactured Propellants for Arc-Ignition of Hybrid Rockets," *Journal of Propulsion and Power*, Vol. 32, No. 6, 2016, pp. 1494-1504.

- [135] Whitmore, S. A., “Three-Dimensional Printing of “Green” fuels for Low-Cost Small Spacecraft Propulsion Systems,” *Journal of Spacecraft and Rockets*, Vol. 55, No. 1, 2018, pp. 13-26.
- [136] Whitmore, S. A., and Bulcher, M. A., “Vacuum Test of a Novel Green-Propellant Thruster for Small Spacecraft,” AIAA 2017-5044, *53rd AIAA/ASME/SAE/ASEE Joint Propulsion Conference*, Atlanta, GA, 2017.
- [137] Whitmore, S. A., Merkely, D. P., Walker, S. D., and Spurrier, Z. S., “Thermal Decomposition of Aqueous Hydroxyl-Ammonium Nitrate Solutions Using a Hybrid Propellant Gas Generator,” AIAA 2015-4040, *51st AIAA/ASME/SAE/ASEE Joint Propulsion Conference and Exhibit*, Orlando, FL, 2015.
- [138] Whitmore, S. A., Inkley, N. R., Merkley, D. P., and Judson, M. I., “Development of a Power-Efficient, restart-Capable Arc Ignitor for Hybrid Rockets,” *Journal of Propulsion and Power*, Vol. 31, No. 6, 2015, pp. 1739-1749.
- [139] Whitmore, S. A., Marshall, J., Bulcher, M., Lui, L., Heiner, M., Chamberlain, B., Martinez, C., Armstrong, I., and Merkley, D. P., “Arc-Ignition of an 80% Hydrogen Peroxide/ABS Hybrid Rocket System,” AIAA 2017-5047, *53rd AIAA/ASME/SAE/ASEE Joint Propulsion Conference*, Atlanta, GA, 2017.
- [140] Whitmore, S. A., Merkley, S. L., Walker, S. D., Tonc, L., Spurrier, Z. S., and Mathias, S., “Survey of Selected Additively Manufactured Propellants for Arc-Ignition of Hybrid Rockets,” AIAA 2015-4034, *51st AIAA/ASME/SAE/ASEE Joint Propulsion Conference*, Orlando, FL, 2015.
- [141] Eilers, S. D., Whitmore, S. A., and Peterson, Z. W., “Development and Testing of the Regeneratively Cooled Multiple Use Plug Hybrid (for) Nanosats (MUPHyN) Motor,” AIAA 2012-4199, *48th AIAA/ASME/SAE/ASEE Joint Propulsion Conference and Exhibit*, Atlanta, GA, 2012.
- [142] Whitmore, S. A., and Merkley, S. L., “Throttled Launch-Assist hybrid rocket Motor for an Airborne NanoSat Launch Platform,” AIAA 2015-3940, *51st AIAA/ASME/SAE/ASEE Joint Propulsion Conference*, Orlando, FL, 2015.
- [143] Whitmore, S. A., Mathias, S., Kennedy, N., Bulcher, M., Cook, B., Montgomery, Z., Frandsen, R., Lewis, Z., and Teo, B., “Development and Testing of Three Alternative Designs for Additively Manufactured Hybrid Thrusters,” AIAA 2016-5068, *52nd AIAA/ASME/SAE/ASEE Joint Propulsion Conference*, Salt Lake City, UT, 2016.
- [144] Eilers, S. D., Whitmore, S. A., and Peterson, Z. W., “Regeneratively Cooled Multiple-Use Plug Hybrid for Nanosatellites,” *Journal of Propulsion and Power*, Vol. 29:6, 2013, pp. 1420-1434.

- [145] Whitmore, S. A., Walker, S. D., Merkley, D. P., and Sobbi, M., "High Regression Rate Hybrid Rocket Fuel Grains with Helical Port Structures," *Journal of Propulsion and Power*, Vol. 31:6, 2015, pp. 1727-1738.
- [146] Whitmore, S. A., and Walker, S. D., "Engineering Model for Hybrid Fuel Regression Rate Amplification Using Helical Ports," *Journal of Propulsion and Power*, Vol. 33:2, 2017, pp. 398-407.
- [147] Whitmore, S. A., Chamberlain, B. L., Armstrong, I. W., Mathais, S., and Fehlberg, S. A., "Consumable Spacecraft Structure with Integrated, 3-D Printed Acrylonitrile butadiene Styrene (ABS) Thrusters," AIAA 2017-4707, *53rd AIAA/ASME/SAE/ASEE Joint Propulsion Conference*, Atlanta, GA, 2017.
- [148] Whitmore, S. A., Wilson, J. R., Ritter, M. A., and Williams, L. T., "Pyrolysis of Acrylonitrile-Butadiene-styrene (ABS) Under High Heat Flux Conditions," AIAA 2014-3752, *50th AIAA/ASME/SAE/ASEE Joint Propulsion Conference*, Cleveland, OH, 2014.
- [149] Lengelle, G., "Solid-Fuel Pyrolysis Phenomena and Regression Rate, Part 1: Mechanisms," *Fundamentals of Hybrid Rocket Combustion and Propulsion*, edited by M. J. Chiaverini and K. K. Kuo, Progress in Astronautics and Aeronautics, AIAA, Reston, VA, 2007, pp. 127-166.
- [150] Lengelle, G., Fourest, B., Godon, J. C., and Guin, C., "Condensed Phase Behavior and Ablation Rate of Fuels for Hybrid Propulsion," AIAA 1993-2413, *29th AIAA/ASME/SAE/ASEE Joint Propulsion Conference*, Monterey, CA, 1993.
- [151] Lengelle, G., "Thermal Degradation Kinetics and Surface Pyrolysis of Polymers," *AIAA Journal*, Vol. 8, No. 11, 1970, pp. 1989-1996.
- [152] ASTM E1641-13, "Standard Test Method for Decomposition Kinetics by Thermogravimetry Using the Ozawa/Flynn/Wall Method," 2013.
- [153] George, P., Krishnan, S., Varkey, P. M., Ravindran, M., and Ramachandran, L., "Fuel Regression Rate in Hydroxyl-Terminated-Polybutadiene/Gaseous-Oxygen Hybrid Rocket Motors," *Journal of Propulsion and Power*, Vol. 17, No. 1, 2001, pp. 35-42.
- [154] DeLuca, L. T., Galfetti, L., Colombo, G., Maggi, F., Bandera, A., Boiocchi, M., Gariani, G., Merotto, L., Paravan, C., and Reina, A., "Time-Resolved Burning of Solid Fuels for Hybrid Rocket Propulsion," *Progress in Propulsion Physics*, Vol. 2, 2011, pp. 405-426.
- [155] Calabro, M., "Overview on Hybrid Propulsion," *Progress in Propulsion Physics*, Vol. 2, 2011, pp. 353-374.

- [156] Paccagnella, E., Barato, F., Pavarin, D., and Karabeyoglu, A., "Scaling of Hybrid Rocket Motors with Swirling Oxidizer Injection," AIAA 2015-3833, 51st AIAA/ASME/SAE/ASEE Joint Propulsion Conference, Orlando, FL, 2015.
- [157] Paccagnella, E., Barato, F., Pavarin, D., and Karabeyoglu, A., "Scaling of Hybrid Rocket Motors with Swirling Oxidizer Injection – Part 2," AIAA 2016-4750, 52nd AIAA/ASME/SAE/ASEE Joint Propulsion Conference, Salt Lake City, UT, 2016.
- [158] Summers, M. H., and Villarreal, J. K., "Small-Scale Hybrid Rocket Test Stand and Characterization of Swirl Injectors," AIAA 2013-3831, 49th AIAA/ASME/SAE/ASEE Joint Propulsion Conference, San Jose, CA, 2013.
- [159] Shin, K. H., Lee, C., Chang, S. Y., and Koo, J. Y., "The Enhancement of Regression Rate of Hybrid Rocket Fuel by Various Methods," AIAA 2005-0359, 43rd AIAA Aerospace Sciences Meeting, Reno, NV, 2005.
- [160] Tamura, T., Yuasa, S., and Yamamoto, K., "Effects of Swirling Oxidizer Flow on fuel Regression Rate of Hybrid Rockets," AIAA 1999-2323, 35th AIAA/ASME/SAE/ASEE Joint Propulsion Conference, Los Angeles, CA, 1999.
- [170] Yuasa, S., Yamamoto, K., Hachiya, H., Kitagawa, K., and Oowada, Y., "Development of a Small Sounding Hybrid Rocket with a Swirling-Oxidizer-type Engine," AIAA 2001-3537, 37th AIAA/ASME/SAE/ASEE Joint Propulsion Conference, Salt Lake City, UT, 2001.
- [171] Shiraishi, N., and Yuasa, S., "Prediction of Time Variation of Ballistic Parameters For a Swirling-Oxidizer-Flow-Type Hybrid Rocket Engine Using Burning Data," AIAA 2010-6874, 46th AIAA/ASME/SAE/ASEE Joint Propulsion Conference, Nashville, TN, 2010.
- [172] Chinatsu, S., Masafumi, S., Koshuke, H., Saburo, Y., Takashi, S., and Noriko, S., "Measurement of Axial-Direction Fuel Regression Rate of Swirling-Oxidizer-flow-Type Hybrid Rocket Engines," AIAA 2010-6547, 46th AIAA/ASME/SAE/ASEE Joint Propulsion Conference, Nashville, TN, 2010.
- [173] Miho, M., Tatsuya, I., Saburo, Y., Takashi, S., and Toru, S., "Visualization of Flames in Combustion Chamber of Swirling-Oxidizer-Flow-Type Hybrid Rocket Engines," AIAA 2010-6546, 46th AIAA/ASME/SAE/ASEE Joint Propulsion Conference, Nashville, TN, 2010.
- [174] Kousuke, H., Chinatsu, S., Saburo, Y., Moriko, S., and Takashi, S., "Fuel Regression Rate Behavior for Various Fuels in Swirling-Oxidizer-Flow-Type Hybrid Rocket Engines," AIAA 2011-5677, 47th AIAA/ASME/SAE/ASEE Joint Propulsion Conference, San Diego, CA, 2011.

- [175] Saburo, Y., Noriko, S., and Kousuke, H., "Controlling Parameters for Fuel Regression Rate of Swirling-Oxidizer-Flow-Type Hybrid Rocket Engine," AIAA 2012-4106, *48th AIAA/ASME/SAE/ASEE Joint Propulsion Conference*, Atlanta, GA, 2012.
- [176] Daisuke, S., Saburo, Y., Kousuke, H., Takashi, S., and Noriko, S., "Combustion Characteristics of Paraffin-fueled Swirling Oxidizer-Flow-Type Hybrid Rocket Engines," AIAA 2012-3904, *48th AIAA/ASME/SAE/ASEE Joint Propulsion Conference*, Atlanta, GA, 2012.
- [177] Hayashi, D., and Sakurai, T., "A Fundamental Study of an End-Burning Swirling-Flow Hybrid Rocket Engine Using Low Melting Temperature Fuels," AIAA 2015-4138, *51st AIAA/ASME/SAE/ASEE Joint Propulsion Conference*, Orlando, FL, 2015.
- [178] Tomizawa, T., and Sakurai, T., "Applicability of a Lox Vaporization Preburner for Swirling-Flow Hybrid Rocket Engines," AIAA 2015-4134, *51st AIAA/ASME/SAE/ASEE Joint Propulsion Conference*, Orlando, FL, 2015.
- [179] Oishige, Y., Hayashi, D., and Sakurai, T., "Fuel Regression Behavior of a Swirling-Injection End-burning Hybrid Rocket Engine using Paraffin-Based Fuels," AIAA 2016-4755, *52nd AIAA/ASME/SAE/ASEE Joint Propulsion Conference*, Salt Lake City, UT, 2016.
- [180] Sakurai, T., Yuasa, S., Ando, H., Kitagawa, K., and Shimada, T., "Performance and Regression Rate Characteristics of 5-kN Swirling-Oxidizer-Flow-Type Hybrid Rocket Engine," *Journal of Propulsion and Power*, Vol. 33, No. 4, 2017, pp. 891-901.
- [181] Hirata, Y., Aso, S., Hayashida, T., Nakawatase, R., Tani, Y., Morishita, K., and Shimada, T., "Improvement of Regression Rate and Combustion Efficiency of high Density Polyethylene Fuel and Paraffin Fuel of Hybrid Rockets with Multi-Section Swirl Injection Method," AIAA 2011-5907, *47th AIAA/ASME/SAE/ASEE Joint Propulsion Conference*, San Diego, CA, 2011.
- [182] Araki, K., Hirata, Y., Ohshima, S., Ohe, K., Aso, S., Tani, Y., and Shimada, T., "A Study on Performance Improvement of Paraffin Fueled Hybrid Rocket Engines with Multi-Section Swirl Injection Method," AIAA 2013-3634, *49th AIAA/ASME/SAE/ASEE Joint Propulsion Conference*, San Jose, CA, 2013.
- [183] Ohe, K., Mizuchi, M., Aso, S., Tani, Y., Ohshima, S., Araki, K., Tada, H., and Shimada, T., "Study on Hybrid Rocket with Multi-Section Swirl Injection Method toward Flight Experiments of Subscale Space Plane," AIAA 2014-3954, *50th AIAA/ASME/SAE/ASEE Joint Propulsion Conference*, Cleveland, OH, 2014.

- [184] Ozawa, K., Usuki, T., Mishima, G., Kitagawa, K., Yamashita, M., Mizuchi, M., Katakami, K., Maji, Y., Aso, S., Tani, Y., Wada, Y., and Shimada, T., “Static Burning Tests on a Bread Board Model of Altering-Intensity Swirling-Oxidizer-Flow-Type Hybrid Rocket Engine,” AIAA 2016-4964, *52nd AIAA/ASME/SAE/ASEE Joint Propulsion Conference*, Salt Lake City, UT, 2016.
- [185] Ohyama, S., Hirata, Y., Araki, K., Ohe, K., Aso, S., Tani, Y., and Shimada, T., “Effects of Multi-Section Swirl Injection Method on Fuel Regression Rate of High Density Polyethylene Fueled Hybrid Rocket Engine,” AIAA 2013-4040, *49th AIAA/ASME/SAE/ASEE Joint Propulsion Conference*, San Jose, CA, 2013.
- [186] Tadini, P., Paravan, C., and DeLuca, L. T., “Ballistic Characterization of Metallized HTPB-based Fuel with Swirling Oxidizer in Lab-Scale Hybrid Burner,” *9th High Energy Materials (HEM) Conference*, Sagamihara, Japan, 2013.
- [187] Pucci, J. M., “The Effects of Swirl Injector Design on Hybrid Flame-Holding Combustion Instability,” AIAA 2002-3578, *38th AIAA/ASME/SAE/ASEE Joint Propulsion Conference*, Indianapolis, IN, 2002.
- [188] Wilkinson, R., Hart, K., Day, R., and Coxhill, I., “Proof-of-concept Testing of a Sustained Vortex-Flow Configuration for Hybrid Rocket Motors,” AIAA 2010-6782, *46th AIAA/ASME/SAE/ASEE Joint Propulsion Conference*, Nashville, TN, 2010.
- [189] Bellomo, N., Barato, F., Faenza, M., Lazzarin, M., Bettella, A., and Pavarin, D., “Numerical and Experimental Investigation on Vortex Injection in Hybrid Rocket Motors,” AIAA 2011-5675, *47th AIAA/ASME/SAE/ASEE Joint Propulsion Conference*, San Diego, CA, 2011.
- [190] Shinohara, K., and Nakagawa, I., “Regression Rate Characteristics of Paraffin-Based Fuel under Swirled Oxidizer Flow,” AIAA 2012-4104, *48th AIAA/ASME/SAE/ASEE Joint Propulsion Conference*, Nashville, TN, 2012.
- [191] Bellomo, N., Faenza, M., Barato, F., Bettella, A., Pavarin, D., and Selmo, A., “The “Vortex Reloaded” Project: Experimental Investigation on fully Tangential Vortex Injection in N₂O – Paraffin Hybrid Motors,” AIAA 2012-4304, *48th AIAA/ASME/SAE/ASEE Joint Propulsion Conference*, Nashville, TN, 2012.
- [192] Bellomo, N., Faenza, M., Barato, F., Bettella, A., and Pavarin, D., “The “Vortex Reloaded” Project: Numerical Investigation on fully Tangential Vortex Injection in N₂O – Paraffin Hybrid Motors,” AIAA 2012-3903, *48th AIAA/ASME/SAE/ASEE Joint Propulsion Conference*, Nashville, TN, 2012.

- [193] Bellomo, N., Barato, F., Faenza, M., Lazzarin, M., Bettella, A., and Pavarin, D., “Numerical and Experimental Investigation of Unidirectional Vortex Injection in Hybrid Rocket Motors,” *Journal of Propulsion and Power*, Vol. 29, No. 5, 2013, pp. 1097-1113.
- [194] Komori, Y., Takahashi, K., and Nakagawa, I., “Combustion Characteristics of adding Micro-Sized Aluminum Powder to WAX-Based Hybrid Rocket Fuel by Using Axial and Swirl Flow,” AIAA 2017-4644, *53rd AIAA/ASME/SAE/ASEE Joint Propulsion Conference*, Atlanta, GA, 2017.
- [195] Boardman, T. A., Abel, T. M., Claffin, S. E., Shaeffer, C. W., “Design and Test Planning for a 250-klbf-Thrust Hybrid Rocket Motor Under the Hybrid Propulsion Demonstration Program,” AIAA 1997-2804, *33rd AIAA/ASME/SAE/ASEE Joint Propulsion Conference*, San Jose, CA, 1997.
- [196] Osmon, R. V., “An Experimental Investigation of a Lithium Aluminum Hydride–Hydrogen Peroxide Hybrid Rocket in *Aerospace Chemical Engineering*,” edited by D. J. Simkin, Chemical Engineering Progress Symposium Series, Vol. 62:21, American Institute of Chemical Engineers (AIChE), New York, NY, 1966, pp. 92–102.
- [197] Gany, A., and Timnat, Y. M., “Parametric Study of a Hybrid Rocket Motor,” *Israel Journal of Technology*, Vol. 10, No. 1, 1972, pp. 85–96.
- [198] Grosse, M., “Effect of a Diaphragm on Performance and Fuel Regression of a Laboratory Scale Hybrid Rocket Motor using Nitrous Oxide and Paraffin,” AIAA 2009-5113, *45th AIAA/ASME/SAE/ASEE Joint Propulsion Conference*, Denver, CO, 2009..
- [199] Kumar, R., and Ramakrishna, P. A., “Enhancement of Hybrid Fuel Regression Rate Using a Bluff Body”, *Journal of Propulsion and Power*, Vol. 30, No. 4, 2014, pp. 909-916.
- [200] Kumar, R., and Ramakrishna, P., “Effect of Protrusion on the Enhancement of Regression Rate in Hybrid Rocket, AIAA 2011-5913, *47th AIAA/ASME/SAE/ASEE Joint Propulsion Conference*, San Diego, CA, 2011.
- [201] Kumar, R., and Ramakrishna, P., “Effect of Protrusion on the Enhancement of Regression Rate, *Aerospace Science and Technology*, Vol. 39, 2014, pp. 169-178.
- [202] Kumar, P., and Kumar, A., “Effect of Diaphragms on Regression Rate in Hybrid Rocket Motors, *Journal of Propulsion and Power*, Vol. 29, No. 3, 2013, pp. 559–572.
- [203] Bellomo, N., Lazzarin, M., Barato, F., Grosse, M., “Numerical Investigation of the Effect of a Diaphragm on the Performance of a Hybrid Rocket Motor,” AIAA 2010-7033, *46th AIAA/ASME/SAE/ASEE Joint Propulsion Conference*, Nashville, TN, 2010.

- [204] Bettella, A., Lazzarin, M., Bellomo, N., Barato, F., Pavarin, D., and Grosse, M., "Testing and CFD Simulation of diaphragm Hybrid rocket Motors," AIAA 2011-6023, *47th AIAA/ASME/SAE/ASEE Joint Propulsion Conference*, San Diego, CA, 2011.
- [205] Bellomo, N., Lazzarin, M., Barato, F., Bettella, A., Pavarin, D., and Grosse, M., "Investigation of Effect of Diaphragms on the Efficiency of Hybrid Rockets," *Journal of Propulsion and Power*, Vol. 30, No. 1, 2014, pp. 175-185.
- [206] Grosse, M., "Effect of a Diaphragm on Performance and Regression of a Laboratory Scale Hybrid Rocket Motor Using Nitrous Oxide and Paraffin," AIAA 2009-5113, *45th AIAA/ASME/SAE/ASEE Joint Propulsion Conference*, Denver, CO, 2009.
- [207] Lorente, A. P., Yu, N., Zeng, P., and Zhao, B., "development and Three-Dimensional Numerical simulation of a Double-tube Hybrid Rocket Motor," AIAA 2014-3546, *50th AIAA/ASME/SAE/ASEE Joint Propulsion Conference*, Cleveland, OH, 2014.
- [208] Kim, J., Kim, S., Kim, J., and Moon, H., "Experimental Investigations of the Tapered Fuel Regression Rate of a Hybrid Rocket Motor," AIAA 2010-7119, *46th AIAA/ASME/SAE/ASEE Joint Propulsion Conference*, Nashville, TN, 2010.
- [209] Kim, J., So, J., Kim, S., Kim, J., and Moon, H., "Effect of a Midst Mixing Chamber on fuel Regression of a Laboratory Scale Hybrid Rocket Motor," AIAA 2011-5910, *47th AIAA/ASME/SAE/ASEE Joint Propulsion Conference*, San Diego, CA, 2011.
- [210] Ishiguro, T., Sinohara, K., Sakio, K., and Nakagawa, I., "A Study on Combustion Efficiency of Paraffin-Based Hybrid Rockets," AIAA 2011-5679, *47th AIAA/ASME/SAE/ASEE Joint Propulsion Conference*, San Diego, CA, 2011.
- [211] Sakashi, H., Saburo, Y., Kosuke, H., and Takashi, S., "Effectiveness of Concave-Convex Surface Grain for Hybrid Rocket Combustion," AIAA 2012-4107, *48th AIAA/ASME/SAE/ASEE Joint Propulsion Conference*, Atlanta, GA, 2012.
- [212] Yano, Y., "Combustion Characteristics of a Small-Scale, Tactical Hybrid Rocket Propulsion System," AIAA 2001-3538, *34th AIAA/ASME/SAE/ASEE Joint Propulsion Conference*, Salt Lake City, UT, July 2001.
- [213] George, P., Krishnan, S., Varkey, P. M., Ravindran, M., and Ramachandran, L., "Fuel Regression Rate Enhancement Studies in HTPB/GOX Hybrid Rocket Motors," AIAA 1998-3188, *38th AIAA/ASME/SAE/ASEE Joint Propulsion Conference*, Cleveland, OH, 1998.

- [214] Evans, B., Favorito, N. A., Boyer, E., and Kuo, K. K., "Characterization of Solid Fuel Mass-Burning Enhancement Utilizing an X-ray Translucent Hybrid Rocket Motor," *6th International Symposium on Special Topics in Chemical Propulsion*, Santiago, Chile, 2005.
- [215] Fuller, J. K., Ehrlich, D. A., Lu, P. C., Jansen, R. P., and Hoffman, J. D., "Advantages of Rapid Prototyping for Hybrid Rocket Motor Fuel Grain Fabrication," AIAA 2011-5821, *47th AIAA/ASME/SAE/ASEE Joint Propulsion Conference*, San Diego, CA, 2011.
- [216] Fuller, J. K., "Stereolithographic Rocket Motor Manufacturing Method," US Patent No. 20090217525A1.
- [217] Fuller, J. K., "Radial Flow Stereolithographic Rocket Motor," US Patent No. 20090217642A1.
- [218] Fuller, J. K., "Systems, Methods, and Apparatus for Providing a Multi-Fuel Hybrid Rocket Motor," US Patent No. 20130031888A1.
- [219] Arnold, D., Boyer, J. E., Kuo, K. K., DeSain, J. D., Curtiss, T. J., and Fuller, J. K., "Test of Hybrid Rocket Fuel Grains with Swirl Patterns Fabricated Using Rapid Prototyping Technology," AIAA 2013-4141, *49th AIAA/ASME/SAE/ASEE Joint Propulsion Conference*, San Jose, CA, 2013.
- [220] McKnight, B. R., Arnold, D., Boyer, J. E., Kuo, K. K., DeSain, J. S., Fuller, J. K., Brady, B. B., and Curtiss, T. J., "Testing of Hybrid Rocket Fuel grains at Elevated Temperatures with Swirl Patterns Fabricated Using Rapid Prototyping Technology," AIAA 2014-3754, *50th AIAA/ASME/SAE/ASEE Joint Propulsion Conference*, Cleveland, OH, 2014.
- [221] Creech, M., Crandell, a., Eisenhauer, N., Marx, S., Busari, T., Link, A., Gabl, J., and Pourpoint, T., "3D Printer for Paraffin Based Hybrid Rocket Fuel Grains," AIAA 2015-0924, *53rd AIAA/Aerospace Sciences Meeting*, Kissimmee, FL, 2015.
- [222] Catina, J., Nellis, B., Grigsby, D., and Castonguay, K., "Use of Additive Manufacturing to Develop Advanced Hybrid Rocket Designs," AIAA 2016-4506, *52nd AIAA/ASME/SAE/ASEE Joint Propulsion Conference*, Salt Lake City, UT, 2016.
- [223] McCulley, J., Bath, A. R., Eilers, S., and Whitmore, S. A., "Design and Testing of FDM Manufactured Paraffin-ABS Hybrid Rocket Motors," AIAA 2012-3962, *48th AIAA/ASME/SAE/ASEE Joint Propulsion Conference*, Atlanta, GA, 2012.

- [224] Remson, A. E., Crossley, W. A., Heister, S. D., and McMillin, J. E., "Consumable Satellite Structures for Apogee Insertion Applications, AIAA 2002-3574, 38th AIAA/ASME/SAE/ASEE Joint Propulsion Conference, Indianapolis, IN, 2002.
- [225] Elliott, T. S., Jenkins, B., Zeineldin, R., Johnson, J., Simons, M., Godfrey, J., and Mabry, T., "Additive Manufacturing of Small Scale Cartridges with Uniformly Distributed Aluminum Particles," AIAA 2016-4507, 52nd AIAA/ASME/SAE/ASEE Joint Propulsion Conference, Salt Lake City, UT, 2016.
- [226] Jones, R. D., "Additive Manufactured Thermoplastic-Aluminum Nanocomposite Hybrid Rocket Fuel Grain and Method of Manufacturing Same," US Patent No. 20170073281A1.
- [227] Johnson, S., Baier, M., Gunduz, I., and Son, S., "Additive Manufacturing of High Solids Loading Hybrid Rocket Fuel Grains," *The Summer Undergraduate Research Fellowship (SURF) Symposium*, Wes Lafayette, Indiana, 2017.
- [228] Raghunandan, B. N., Ravichandran, E. R., and Marathe, A. G., "Combustion Related to Solid-Fuel Ramjets," *Journal of Propulsion and Power*, Vol. 1, No. 6, 1985, pp. 502-504.
- [229] Frederick, R. A., Moser, M. D., Knox, L. R., and Whitehead, J. J., "Regression Rate Study of Mixed Hybrids Propellants," *Journal of Propulsion and Power*, Vol. 23, No. 1, 2007, pp. 175-180.
- [230] Marothiya, G., Kumar, R., and Ramakrishna, P. A., "Enhancement of Regression Rate in Hybrid Rockets," AIAA 2011-5911, 47th AIAA/ASME/SAE/ASEE Joint Propulsion Conference, San Diego, CA, 2011.
- [231] Wernimont, E. J., Meyer, S. E., and Ventura, M. C., "Hybrid Motor System with a Consumable Catalytic Bed, a Composition of the Catalytic Bed, and a Method of Using," U.S. Patent No. 5727368.
- [232] Takashita, Y., and Teramoto, Y., "Study of Gas-Hybrid Rocket (I)-Nitric Acid/AP Composite- Gas-Generator," *Journal of the Japan Explosives Society*, Vol. 57, No. 4, 1996, pp. 135-141.
- [233] Lund, G. K., Starrett, W. D., and Jensen, K. C., "Development and Lab-Scale Testing of a Gas Generator Hybrid Fuel in Support of the Hydrogen Peroxide Hybrid Upper Stage Program," AIAA 2001-3244, 34th AIAA/ASME/SAE/ASEE Joint Propulsion Conference, Salt Lake City, UT, July 2001.

- [234] Radinsky, S., Hermann, J., Maltbie, L., Vaherweg, J., and DeTurris, D., “Laboratory Scale Hybrid Rocket HTPB Fuel Grain Performance Enhancement and Manufacturing Techniques,” AIAA 2013-4139, *49th AIAA/ASME/SAE/ASEE Joint Propulsion Conference*, San Jose, CA, 2013.
- [235] Lee, D., and Lee, C., “The Effect of AP and Boron Additions on the Combustion Characteristics in a Staged Hybrid Rocket Engine,” AIAA 2016-4865, *52nd AIAA/ASME/SAE/ASEE Joint Propulsion Conference*, Salt Lake City, UT, 2016.
- [236] Matthews, J. D., Gabl, J. R., Pourpoint, T. L., “Reactive Colloidal Dispersions for High Performance Hybrid Propulsion,” AIAA 2017-5049, *53rd AIAA/ASME/SAE/ASEE Joint Propulsion Conference*, Atlanta, GA, 2017.
- [237] Matthews, J. D., Pourpoint, T. L., and Gabl, J., “High Performance Hybrid Rocket Colloidal Dispersion Propellants,” AIAA 2018-4662, *54th AIAA/SAE/ASEE Joint Propulsion Conference*, Cincinnati, OH, 2018.
- [238] DeLuca, L. T., “Overview of Al-Based Nanoenergetic Ingredients for Solid Rocket Propulsion,” *Defence Technology*, 2018, *In Press*.
- [239] Mead, F.B., and Bornhorst, B.R., “Certification Tests of a Hybrid Propulsion System for the Sandpiper Target Missile,” AFRPL-TR-69- 73, Air Force Rocket Propulsion Laboratory, Edwards AFB, CA, 1969.
- [240] Strand, L. D., Ray, R. L., Anderson, F. A., and Cohen, N. S., “Hybrid Rocket Fuel Combustion and Regression Rate Study,” AIAA 1992-3302, *28th AIAA/ASME/SAE/ASEE Joint Propulsion Conference*, Nashville, TN, 1992.
- [241] Strand, L. D., Ray, R. L., and Cohen, N. S., “Hybrid Rocket Combustion Study,” AIAA 1993-2412, *29th AIAA/ASME/SAE/ASEE Joint Propulsion Conference*, Monterey, CA, 1993.
- [242] Strand, L. D., Jones, M. D., Ray, R. L., and Cohen, N. S., “Characterization of Hybrid Rocket Internal Heat Flux and HTPB Fuel Pyrolysis,” AIAA 1994-2876, *30th AIAA/ASME/SAE/ASEE Joint Propulsion Conference*, Indianapolis, IN, 1994.
- [243] Chiaverini, M. J., Serin, N., Johnson, D., Lu, Y. C., Kuo, K. K., and Risha, G. A., “Regression Rate Behavior of Hybrid Rocket Solid Fuels,” *Journal of Propulsion and Power*, Vol. 16, No. 1, 2000, pp. 125–132.
- [244] Chiaverini, M. J., Serin, N., Johnson, D. K., Lu, Y. C., and Kuo, K. K., “Instantaneous Regression Behavior of HTPB Solid Fuels Burning with GOX in a Simulated Hybrid Rocket Motor,” *Challenges in Propellants and Combustion 100 Years After Nobel*, edited by K. K. Kuo, Begell House, New York, 1997, pp. 719–733.

- [245] Chiaverini, M. J., Harting, G. C., Lu, Y. C., Jones, S., Wygle, B., and Arves, J. P., "Pyrolysis Behavior of Hybrid Rocket Solid Fuels under Rapid Heating Conditions," AIAA 1997-3078, 33rd AIAA/ASME/SAE/ASEE Joint Propulsion Conference, Seattle, WA, 1997.
- [246] Chiaverini, M. J., Harting, G. C., Lu, Y. C., Kuo, K. K., Peretz, A., Jones, H. S., Wygle, B. S., and Arves, J. P., "Pyrolysis Behavior of Hybrid Rocket Solid Fuels Under Rapid Heating Conditions," *Journal of Propulsion and Power*, Vol. 15, No. 6, 1999, pp. 888-895.
- [247] Chiaverini, M. J., Kuo, K. K., Peretz, A., and Harting, G. C., "Regression-Rate and Heat Transfer Calculations for Hybrid Rocket Combustion," *Journal of Propulsion and Power*, Vol. 17, No. 1, 2001, pp. 99–110.
- [248] Evans, B., Risha, G.A., Favorito, N., Boyer, E., Wehrman, R. B., Libis, N., Kuo, K. K., "Instantaneous Regression Rate Determination of a Cylindrical X-Ray Transparent Hybrid Rocket Motor," AIAA 2003-4592, 39th AIAA/ASME/SAE/ASEE Joint Propulsion Conference, Huntsville, AL, July 2003.
- [249] Risha, G. A. "Enhancement of Hybrid Rocket Combustion Performance Using Nano-Sized Energetic Particles," *Ph.D. Dissertation*, Pennsylvania State University, University PA, Park, 2003.
- [250] Risha, G. A., Ulas, A., Boyer, E., Kumar, S., and Kuo, K. K., "Combustion of HTPB Based Solid Fuels Containing Nano-Sized Energetic Powder in a Hybrid Rocket Motor," AIAA 2001-3535, 37th AIAA/ASME/SAE/ASEE Joint Propulsion Conference, Salt Lake City, UT, 2001.
- [251] Risha, G. A., Boyer, E., Wehrman, R. B., and Kuo, K. K., "Performance Comparison of HTPB-Based Solid Fuels Containing Nano-Sized Energetic Powder in a Cylindrical Hybrid Rocket Motor," AIAA 2002-3576, 38th AIAA/ASME/SAE/ASEE Joint Propulsion Conference, Indianapolis, IN, 2002.
- [252] Risha, G. A., Boyer, E., Evans, B., Kuo, K. K., and Malek, R., "Characterization of Nano-Sized Particles for Propulsion Applications," *Synthesis, Characterization and Properties of Energetic/Reactive Nanomaterials*, Materials Research Society Symposium – Proceedings, Vol. 800, Material Research Society, 2003, pp. 243–254.
- [253] Risha, G. A., Evans, B., Boyer, E., Wehrman, R. B., and Kuo, K. K., "Nano-Sized Aluminum, and Boron-Based Solid-Fuel Characterization in a Hybrid Rocket Engine," AIAA 2003-4593, 39th AIAA/ASME/SAE/ASEE Joint Propulsion Conference, Huntsville, AL, 2003.

- [254] Evans, B., Boyer, E., Kuo, K. K., Risha, G., and Chiaverini, M., "Hybrid Rocket Investigations at Penn State University's High Pressure Combustion Laboratory: Overview and Recent Results," AIAA 2009-5349, *45th AIAA/ASME/SAE/ASEE Joint Propulsion Conference*, Denver, CO, 2009.
- [255] Evans, B., Favorito, N. A., and Kuo, K. K., "Study of Solid Fuel Burning-Rate Enhancement Behavior in an X-ray Translucent Hybrid Rocket," AIAA 2005-3909, *41st AIAA/ASME/SAE/ASEE Joint Propulsion Conference*, Tucson, AZ, 2005.
- [266] Kuo, K. K., Litzinger, T. A., Yang, V., Thynell, S. T., and Hsieh, W. H., "Fundamental Combustion Processes of Particle-Laden Shear Flows in Solid Fuel Ramjets," AD-A241 503, 1991.
- [267] Jarymowycz, T. A., and Yang, V. "Analysis of Boron Particle Ignition above a Burning Solid Fuel in a High-Velocity Environment," *International Journal of Energetic Materials and Chemical Propulsion*, Vol. 2, No. 1, 1991, pp. 303-331.
- [268] Jarymowycz, T. A., Yang, V., and Kuo, K., "Numerical Study of Solid-Fuel Combustion under Supersonic Crossflows," *Journal of Propulsion and Power*, Vol. 8, No. 2, 1992, pp. 346-353.
- [269] Fetherolf, B. L., Snyder, T. S., Bates, M. D., Peretz, A., and Kuo, K. K., "Combustion Characteristics and CO₂ Laser Ignition Behavior of Boron/Magnesium/PTFE Pyrotechnics," *Proceedings of the 14th International Pyrotechnics Seminar*, UK, 1989, pp. 691-711.
- [270] Chem, D. M., Hsieh, W. H., Snyder, T. S., Yang, V., Litzinger, T. A., and Kuo, K. K., "Combustion Behavior and Thermophysical Properties of Metal-Based Solid Fuels," *Journal of Propulsion and Power*, Vol. 7, No. 2, 1991, pp. 250-257.
- [271] Fetherolf, L., Chen, D. M., Snyder, T. S., Litzinger, T. A., and Kuo, K. K., "Ignition and Combustion Behavior of MTV Igniter Materials for Base Bleed Applications," *The First International Symposium on Special Topics in Chemical Propulsion: Base Bleed*, Athens, Greece, 1988.
- [272] Hsieh, W. H., Peretz, A., Huang, T., and Kuo, K. K., "Combustion Behavior of Boron-Based BAMO/NMMO Fuel-Rich Solid Propellants," *Journal of Propulsion and Power*, Vol. 7, No. 4, 1991, pp. 388-395.
- [273] Hsieh, W. H., Cheng, J. J., and Kuo, K. K., "Strand-Burning Characteristics of Advanced Boron-Based BAMO/NMMO Fuel-Rich Solid Propellants," *Technical Meeting of the Eastern Section of the Combustion Institute*, Clearwater Beach, FL, 1988.

- [274] Yang, A. S., Huang, I. T., and Hsieh, W. H., "Burning-Rate Characteristics of Boron/[BAMO/NMMO] Fuel-rich Solid Propellant under Broad Ranges of Pressure and Temperature," *International Journal of Energetic Materials and Chemical Propulsion*, Vol. 2, No. 1, 1991, pp. 412-426.
- [275] Pace, K. K., Jarymowycz, T. A., and Yang, V., "Effect of Magnesium-Coated Boron Particles on Burning Characteristics of Solid Fuels in High-Speed Crossflows," *International Journal of Energetic Materials and Chemical Propulsion*, Vol. 20, No. 4, 1993, pp. 332-347.
- [276] Yeh, C. L., and Kuo, K. K., "Ignition and Combustion of Boron Particles," *Progress in Energy and Combustion Science*, Vol. 220, No. 6, 1996, pp. 511-541.
- [277] Galfetti, L., Nasuti, F., Pastrone, D., and Russo, A. M., "An Italian Network to Improve Hybrid Rocket Performance: Strategy and Results," *Acta Astroautica*, Vol. 96, 2014, pp. 246-260.
- [278] Galfetti, L., Merotto, L., Boiocchi, M., Maggi, F., and DeLuca, L. T., "Ballistic and Rheological Characterization of Paraffin-Based Fuels for Hybrid Rocket Propulsion," AIAA 2011-5680, *47th AIAA/ASME/SAE/ASEE Joint Propulsion Conference*, San Diego, CA, 2011.
- [279] DeLuca, L. T., Galfetti, L., Maggi, F., Colombo, G., Merotto, L., Boiocchi, M., Paravan, C., Reina, A., Tadini, P., and Fanton, L., "Characterization of HTPB-Based Solid Fuel Formulations: Performance, Mechanical Properties, and Pollution," *Acta Astronautica*, Vol. 92, No. 2, 2013, pp. 150-162.
- [280] Paravan, C., Reina, A., Sossi, A., Manzoni, M., Massini, G., Rambaldi, G., Duranti, E., Adami, A., Seletti, E., and DeLuca, L. T., "Time-Resolved Regression Rate of Innovative Hybrid Solid Fuel Formulations," *Progress in Propulsion Physics*, Vol. 4, 2013, pp. 75-98.
- [281] Calabro, M., DeLuca, L. T., Galfetti, L., and Perut, C., "Advanced Hybrid Solid Fuels", *Proceedings of the 58th International Astronautical Congress*, Hyderabad, India, 2007.
- [282] Galfetti, L., DeLuca, L. T., Grassi, P., Paravan, C., Luoni, V., Bandera, A., Colombo, G., DeCillia, L., Sempio, R., Raina, H., "Advances in Hybrid Propulsion", *7th International Symposium on Special Topics in Chemical Propulsion*, Kyoto, Japan, 2007.
- [283] Maggi, F., Cariani, G., Galfetti, L., and DeLuca, L. T., "Theoretical Analysis of Hydrides in Solid and Hybrid Rocket Propulsion," *International Journal of Hydrogen Energy*, Vol. 37, No. 2, 2012, pp.1760-1769.

- [284] Galfetti, L., Merotto, L., Boiocchi, M., Maggi, F., and DeLuca, L. T., “Experimental Investigation of Paraffin-Based Fuels for Hybrid Rocket Propulsion,” *4th European Conference for Aeronautics and Astronautics (EUCASS)*, St. Petersburg, Russia, 2011.
- [285] Galfetti, L., Merotto, L., Boiocchi, M., Maggi, F., and DeLuca, L. T., “Experimental Investigation of Paraffin-Based Fuels for Hybrid Rocket Propulsion,” *Progress in Propulsion Physics*, Vol. 4, 2013, pp. 59-74.
- [186] Merotto, L., Boiocchi, M., Mazzetti, A., Maggi, F., Galfetti, L., and DeLuca, L. T., “Characterization of a Family of Paraffin-Based Solid Fuels,” *4th European Conference for Aeronautics and Astronautics (EUCASS)*, St. Petersburg, Russia, 2011.
- [287] Fanton, L., Paravan, C., and DeLuca, L. T., “Testing and Modeling Fuel Regression Rate in a Miniature Hybrid Burner,” *International Journal of Aerospace Engineering*, Vol. 2012, 2012, pp. 1-15.
- [288] DeLuca, L. T., Rossetini, L., Kappenstein, C., and Weiser, V., “Ballistic Characterization of AlH₃-Based Propellants for Solid and Hybrid Rocket Propulsion,” AIAA 2009-4874, *45th AIAA/ASME/SAE/ASEE Joint Propulsion Conference*, Denver, CO, 2009.
- [289] Qin, Z., Tang, Y., Paravan, C., Colombo, G., Shen, R., and DeLuca, L. T., “Ignition of HTPB-Based Fuels Loaded with and without Micro-Sized Metals,” *AASRI International Conference on Industrial Electronics and Applications*, London, UK, 2015.
- [290] Qin, Z., Paravan, C., Colombo, G., Zhao, F. Q., Shen, R. Q., Yi, J. H., and DeLuca, L. T., “Ignition and Combustion of HTPB-based Solid Fuels Loaded with Innovative Micro-Sized Metals,” *International Journal of Energetic Materials and Chemical Propulsion*, Vol. 16:2, 2018, pp. 139-150.
- [291] Maggi, F., Dossi, S., Paravan, C., DeLuca, L. T., and Liljedahl, M., “Activated Aluminum Powders for Space Propulsion,” *Powder Technology*, Vol. 270, 2015, pp. 46-52.
- [292] Sossi, A., Duranti, E., Manzoni, M., Paravan, C., DeLuca, L. T., Vorozhtsov, A. B., Lerner, M. I., Rodkevich, N. G., Gromov, A. A., and Savin, N., “Combustion of HTPB-Based Solid Fuels Loaded with Coated Nanoaluminum,” *Combustion Science and Technology*, Vol. 185, 2013, pp. 17-36.
- [293] Vadala, G., Leoni, P., Paravan, C., DeLuca, L. T., Vorozhtsov, A. B., Rodkevich, N. G., and Lerner, M. I., “Nano-sized Bimetallic Aluminum-Copper Powders in HTPB-Based Fuels,” *5th European Conference for Aeronautics and Astronautics (EUCASS)*, Munich, Germany, 2013.

- [294] Dossi, S., Maggi, F., Facciolati, L., and DeLuca, L. T., "Activation of Micrometric Aluminum-Metal Oxides Mixtures by Mechanical Milling," *5th European Conference for Aeronautics and Astronautics (EUCASS)*, Munich Germany, 2013.
- [295] Paravan, C., Stocco, M., Penazzo, S., Myzyri, J., De Luca, L. T., and L. Galfetti, "Effects of Aluminum Composites on the Regression Rates of Solid Fuels," *6th European Conference for Aeronautics and Astronautics (EUCASS)*, Krakow, Poland, 2015.
- [296] Galfetti, L., Merotto, L., Boiocchi, M., Maggi, F., and DeLuca, L. T., "Ballistic and Rheological Characterization of Paraffin-Based Fuels for Hybrid Rocket Propulsion," AIAA 2011-5680, *47th AIAA/ASME/SAE/ASEE Joint Propulsion Conference*, San Diego, CA.
- [997] Gany, A., and Netzer, D.W., "Combustion Studies of Metallized Fuels for Solid Fuel Ramjets," *Journal of Propulsion and Power*, Vol. 2, No. 5, 1985, pp. 423–427.
- [298] Gany, A., "Combustion of Boron-Containing Fuels in Solid Fuel Ramjets," *Combustion of Boron-Based Solid Propellants and Solid Fuels*, edited by K. K. Kuo and R. Pein, Begell House, New York, 1993, pp. 91–112.
- [299] Natan, B., and Gany, A., "Effects of Bypass Air on Boron Combustion in Solid Fuel Ramjets," *Journal of Propulsion and Power*, Vol. 9, No. 1, 1993, pp. 155–160.
- [300] Natan, B., and Gany, A., "Combustion Characteristics of a Boron-Fueled Solid Fuel Ramjet with Aft-Burner," *Journal of Propulsion and Power*, Vol. 9, No. 5, 1993, pp. 694–701.
- [301] Natan, B., and Netzer, D.W., "Experimental Investigation of the Effect of Bypass Air on Boron Combustion in a Solid Fuel Ramjet," *Combustion of Boron-Based Solid Propellants and Solid Fuels*, edited by K. K. Kuo and R. Pein, Begell House, New York, 1993, pp. 427–437.
- [302] Nability, J. A., Lee, T., Natan, B., and Netzer, D.W., "Combustion Behavior of Boron Carbide Fuel in Solid Fuel Ramjets," *Combustion of Boron-Based Solid Propellants and Solid Fuels*, edited by K. K. Kuo and R. Pein, Begell House, New York, 1993, pp. 287–302.
- [303] Natan, B., and Netzer, D. W., "Experimental Investigation of the Effect of Bypass Air on Boron Combustion in a Solid fuel Ramjet," *International Journal of Energetic Materials and Chemical Propulsion*, Vol. 2, No. 1, 1993, pp. 427-437.
- [304] Kubota, N., and Serizawa, C. "Combustion of Magnesium=Polytetrafluoroethylene," *Journal of Propulsion and Power*, Vol. 3 No. 4, 1987, pp. 303–307.

- [305] Koch, E. C., *Metal-Fluorocarbon Based Energetic Materials*, Wiley, Weinheim, Germany, 2012.
- [306] Shidlovskii, A. A., and Gorbunov, V. V., “Combustion of PTFE Mixed with Boron, Titanium, or Magnesium,” *Fizika Goreneniya I Vrzyva*, Vol. 14, No. 1, 1978, pp. 157-159.
- [307] Connell, T. L., Risha, G. A., Yetter, R. A., Roberts, C. W., and Young, G., “Combustion of Boron and Fluorocarbon Solid Fuels in a Hybrid Rocket,” AIAA 2013-3970, *49th AIAA/ASME/SAE/ASEE Joint Propulsion Conference*, San Jose, CA, 2013.
- [308] Connell, T. L., Risha, G. A., Yetter, R. A., Roberts, C. W., and Young, G., “Combustion of Boron and Fluorocarbon Solid Fuels in a Hybrid Rocket,” *Journal of Propulsion and Power*, Vol. 31, No. 1, 2015.
- [309] Connell, T. L., Risha, G. A., Yetter, R. A., Roberts, C. W., and Young, G., “Combustion of Boron and Fluorocarbon Solid Fuels in a Hybrid Rocket,” AIAA 2013-3970, *49th AIAA/ASME/SAE/ASEE Joint Propulsion Conference*, San Jose, CA, 2013.
- [310] Connell, T. L., Risha, G. A., Yetter, R. A., Roberts, C. W., and Young, G., “Boron and Polytetrafluoroethylene as a Fuel Composition for Hybrid Rocket Applications,” *Journal of Propulsion and Power*, Vol. 31, No. 1, 2015, pp. 373-385.
- [322] Young, G., Stoltz, C. A., Mason, B. P., Joshi, V. S., Johansson, R. H., Connell, T. L., Risha, G. A., and Yetter, R. A., “Combustion of PTFE-Boron Compositions for Propulsion Applications,” *International Journal of Energetic Materials and Chemical Propulsion*, Vol. 11, No. 5, 2012, pp. 451-471.
- [323] Corpening, J. H., Palmer, R. K., Heister, S. D., and Rusek, J. J. “Combustion of Advanced Non-Toxic Hybrid Propellants” 2003-4596, *39th AIAA/ASME/SAE/ASEE Joint Propulsion Conference*, Huntsville, Alabama, 2003.
- [324] DeSain, J. D., Curtiss, T. J., Metzler, K. M., and Brady, B. B., “Testing Hypergolic Ignition of Paraffin Wax/LiAlH₄ Mixtures,” AIAA 2010-6636, *46th AIAA/ASME/SAE/ASEE Joint Propulsion Conference*, Nashville, TN, 2010.
- [325] Stober, K. J., Thomas, A., Evans, B., and Cantwell, B., “An Investigation of the Hypergolic Performance of Additives to Paraffin Wax for In-Space Propulsion,” *39th Propellant and Explosives Development and Characterization (PEDCS) JANNAF Meeting*, Salt Lake City, UT, 2015.
- [326] Stober, K. J., and Cantwell, B., “An Investigation of Nitric Acid Hypergolicity with Lithium Aluminum Hydride and Paraffin Wax Fuels,” *Space Propulsion Conference*, Rome, Italy, 2016.

- [327] Stober, K. J., Thomas, A., Evans, B., and Cantwell, B., "Investigation of Green Hypergolic Propellants for Hybrid Rockets," AIAA 2016-4991, 52nd AIAA/ASME/SAE/ASEE Joint Propulsion Conference, Salt Lake City, UT, 2016.
- [328] Larson, D. B., Boyer, E., Wachs, T., Kuo, K. K., DeSain, J. D., Curtiss, T. J., and Brady, B. B., "Characterization of the Performance of Paraffin/LiAlH₄ Solid Fuels in a Hybrid Rocket System," AIAA 2011-5822, 47th AIAA/ASME/SAE/ASEE Joint Propulsion Conference, San Diego, CA, 2011.
- [329] Boiocchi, M., Galfetti, L., and DiLandro, L., "Paraffin-Based Solid Fuels for Hybrid Propulsion Filled with Lithium Aluminum Hydride: Thermal, Mechanical, and Ballistic Characterization," *International Journal of Energetic Materials and Chemical Propulsion*, Vol. 15, No. 6, 2016, pp. 501-527.
- [330] Sippel, T. R., Shark, S. C., Hinkelman, M., C., Pourpoint, T. L., Son, S. F., and Heister, S. D., "Hypergolic Ignition of Metal Hydride-Based Fuels with Hydrogen Peroxide," 7th US National Combustion Meeting, Atlanta, GA, 2011.
- [331] Shark, S. C., Zaseck, C. R., Pourpoint, T. L., Son, S. F., and Heister, S. D., "Performance of Dicyclopentadiene (DCPD)/Gaseous Oxygen Based Hybrid Rocket Propellants with Pyrophoric Fuel Additives," AIAA 2013-3966, 49th AIAA/ASME/SAE/ASEE Joint Propulsion Conference, San Jose, CA, 2013.
- [332] Shark, S. C., Pourpoint, T. L., Son, S. F., and Heister, S. D., "Performance of Dicyclopentadiene (DCPD)/H₂O₂-Based Hybrid Rocket Motors with Metal Hydride Additives," *Journal of Propulsion and Power*, Vol. 29, No. 5, 2013, pp. 1122-1129.
- [333] Shark, S. C., Zaseck, C. R., Pourpoint, T. L., Son, S. F., and Heister, S. D., "Performance and Visualization of Dicyclopentadiene Rocket Propellants with Metal Hydride Additives," *Journal of Propulsion and Power*, Vol. 32, No. 4, 2016, pp. 869-881.
- [334] Zaseck, C. R., Shark, S. C., Son, S. F., and Pourpoint, T. L., "Paraffin Fuel and Additive Combustion in an Opposed Flow Burner Configuration," AIAA 2012-3963, 48th AIAA/ASME/SAE/ASEE Joint Propulsion Conference, Atlanta, GA, 2012.
- [335] Young, G., Piekiet, N., Chowdhury, S., and Zachariah, M. R., "Ignition Behavior of α -AlH₃," *Combustion Science and Technology*, Vol. 182, No. 9, 2010, pp. 1341-1359.
- [336] Young, G., Risha, G. A., Miller, A. G., Glass, R. A., Connell, T. L., and Yetter, R. A., "Combustion of Alane-Based Solid Fuels," *International Journal of Energetic Materials and Chemical Propulsion*, Vol. 9, No. 3, 2010, pp. 249-266.

- [337] Weismiller, M. R., Connell, T. L., Jr., Risha G. A., and Yetter, R.A., "Characterization of Ammonia Borane (NH₃BH₃) Enhancement to a Paraffin Fueled Hybrid Rocket System", AIAA 2010-6639, *46th AIAA/ASME/SAE/ASEE Joint Propulsion Conference*, Nashville, TN, 2010.
- [338] Pfeil, M. A., Dennis, J. D., Son, S. F., Heister, S. D., Pourpoint, T. L., and Ramachandran, P. V., "Characterization of Ethylenediamine Bisborane as a Hypergolic Hybrid Rocket Fuel Additive," *Journal of Propulsion and Power*, Vol. 31, No. 1, 2015, pp. 365-372.
- [339] Pfeil, M. A., Kulkarni, A. S., Ramachandran, P. V., Son, S. F., and Hesiter, S. D., "Solid Amine-Boranes as High-Performance and Hypergolic Hybrid Rocket Fuels," *Journal of Propulsion and Power*, Vol. 32, No. 1, 2016, pp. 23-31.
- [340] Ramachandran, P. V., Kulkarni, A. S., Pfeil, M. A., Dennis, J. D., Willits, J. D., Heister, S. D., Son, S. F. and Pourpoint, T. L., "Amine-Boranes: Green Hypergolic Fuels with Consistently Low Ignition Delays," *Chemistry: A European Journal*, Vol. 20, 2014, pp. 16869-16872.
- [341] Farbar, E., Louwers, J., and Kaya, T., "Investigation of Metallized and Nonmetallized Hydroxyl Terminated Polybutadiene/Hydrogen Peroxide Hybrid Rockets," *Journal of Propulsion and Power*, Vol. 23, No. 2, 2007, pp. 476-486.
- [342] Liu, J. Z., Xi, J. F., Yang, W. J., Hu, Y. R., Zhang, Y. W., Wang, Y., and Zhou, J. H., "Effect of Magnesium on the Burning Characteristics of Boron Particles," *Acta Astroautica*, Vol. 96, No. 1, 2014, pp. 89-96.
- [343] Obuchi, K., Tanabe, M., and Kuwahara, T., "Ignition Characteristics of Boron Particles in the Secondary Combustor of ducted Rockets, Effects of Magnesium Particle Addition," AIAA 2008-0943, *46th AIAA Aerospace Sciences Meeting*, Reno, NV, 2008.
- [344] Hara, H., Ushijima, M., Muramatsu, A., and Kuwahara, T., "Combustion Characteristics of Ducted Rocket Engine in the Mars," AIAA 2011-5866, *57th AIAA/ASME/SAE/ASEE Joint Propulsion Conference*, San Diego, CA, 2011.
- [345] Mitsuno, M., Kuwahara, T., Kosaka, K., and Kubota, N., "Combustion of Metallized Propellants for Ducted Rockets," AIAA 1987-1724, *23rd AIAA/ASME/SAE/ASEE Joint Propulsion Conference*, San Diego, CA, 1987.
- [346] Carmicino, C., Sorge, A. R., Orlandi, O., Blanchard, H., Yvart, P., and Gautier, P., "Advanced Solid Fuels for Hybrid Propulsion: the Research Activity in Europe," AIAA 2011-5820, *47th AIAA/ASME/SAE/ASEE Joint Propulsion Conference*, San Diego, CA, 2011.

- [347] Carmicino, C., and Sorge, A. R., "Experimental Investigation into the Effect of Solid-Fuel Additives on Hybrid Rocket Performance," *Journal of Propulsion and Power*, Vol. 31, No. 2, 2015, pp. 699-713.
- [348] Pein, R., and Vinnemeier, F., "The Influence of Swirl and Fuel Composition of Boron-Containing Fuels on Combustion in a Solid Fuel Ramjet Combustion Chamber," AIAA 1989-2885, *25th AIAA/ASME/SAE/ASEE Joint Propulsion Conference*, Monterey, CA, 1989.
- [349] Pein, R., and Vinnemeier, F., "Swirl and Fuel Composition Effects on Boron combustion in Solid-Fuel Ramjets," *Journal of Propulsion and Power*, Vol. 8, No. 3, 1992, pp. 609-614.
- [350] Nability, J. A., Lee, T. H., Natan, B., and Netzer, D. W., "Combustion Behavior of Boron carbide Fuel in Solid Fuel Ramjets," *International Journal of Energetic Materials and Chemical Propulsion*, Vol. 2, No. 1, 1993, pp. 287-302.
- [351] Korotkikh, A., Glotov, O., and Sorokin, I., "Effect of Metal Additives on the Combustion Characteristics of High-Energy Materials," MATEC Paper 2016-01048, *Materials Science, Engineering, and Chemistry (MATEC) Web of Conferences*, Vol. 72, Heat and Mass Transfer in the System of Thermal Modes of Energy – Technical and Technological Equipment (HMTTSC), 2016.
- [352] Korotkikh, A., Slyusarskiy, K., Monogarov, K., and Selikhova, E., "Laser Ignition of High-Energy Materials Containing AlB₂ and AlB₁₂ Powders," MATEC Paper 2017-01042, *Materials Science, Engineering, and Chemistry (MATEC) Web of Conferences*, Vol. 110, Heat and Mass Transfer in the System of Thermal Modes of Energy – Technical and Technological Equipment (HMTTSC), 2017.
- [353] Korotkikh, A., Arkhipov, V., Slyusarskiy, K., and Sorokin, I., "Ignition Study of High-Energy Materials Containing Al, B, AlB₂, and TiB₂ Powders," MATEC Paper 2017-03016, *Materials Science, Engineering, and Chemistry (MATEC) Web of Conferences*, Vol. 115, 33rd Siberian Thermophysical Seminar (STS-33), 2017.
- [354] Korotkikh, A., Arkhipov, V., Slyusarskiy, K., Sorokin, I., and Selikhova, E., "Ignition of High-Energy Materials Containing Boron and Aluminum Diboride," *7th European Conference for Aeronautics and Space Sciences (EUCASS)*, Milan, Italy, 2017.
- [355] Oleg, G., Vladimir, Z., Grigory, S., and Alexander, K., "Agglomeration and Combustion Completeness of Boron in Composite Propellant," *7th European Conference for Aeronautics and Space Sciences (EUCASS)*, Milan, Italy, 2017.

- [356] Bondarchuk, S. S., Matveev, A. E., Promakhov, V. V., Vorozhtsov, A. B., Zhukov, A. S., Zhukov, I. A., and Ziatdinov, M. H., "Synthesis and Properties of Energetics Metal Borides for Hybrid Solid-Propellant Rocket Engines," *Proceedings of the Scientific-Practical Conference 'Research and Development – 2016'*, 2018, pp. 511-519.
- [357] Vorozhtsov, A., Zhukov, A., Ziatdinov, M., Bondarchuk, S., Lerner, M., and Rodkevich, N., "Novel Micro- and Nanofuels: Production, Characterization, and Applications for High Energy Materials," *Chemical Rocket Propulsion*, Ed. DeLuca, L. T., Shimada, T., Sinditskii, V. P., and Calabro, M., Springer Aerospace Technology, Springer, Cham, 2017, pp. 235-251.
- [358] Zhukov, A., Zhukov, I., Ziatdinov, M., Promakhov, V., Vorozhtsov, A., Vorozhtsov, S., and Dubkova, Y., "Self-Propagating High-Temperature Synthesis of Energetic Borides," *American Institute of Physics (AIP) Conference Proceedings*, 2016.
- [359] Gromov, A. A., and Popenko, E. M., "Aluminum Nanoparticles Burning – Still a Puzzle?," *Progress in Propulsion Physics*, Vol. 1, 2009, pp. 17-30.
- [360] Kwon, Y. S., Gromov, A. A., Ilyin, A. P., and Rim, G. H., "Passivation Process for Superfine Aluminum Powders Obtained by Electrical Explosion of Wires," *Applied Surface Science*, Vol. 211, No. 1, 2003, pp. 57-67.
- [361] Kwon, Y. S., Gromov, A. A., and Ilyin, A. P., "Reactivity of Superfine Aluminum Powders Stabilized by Aluminum Diboride," *Combustion and Flame*, Vol. 131, No. 2, 2002, pp. 349-352.
- [362] Il'in, A. P., Gromov, A. A., Tikhonov, D. V., Yablunovskii, G. V., and Ilyin, M. A., "Properties of Ultrafine Aluminum Powder Stabilized by Aluminum Diboride," *Combustion Explosion and Shock Waves*, Vol. 38, No. 1, 2002, pp. 123-126.
- [363] Kwon, Y. S., Gromov, A. A., Ilyin, A. P., and Rim, G. H., "Passivation Process for Superfine Aluminum Powders Obtained by Electrical Explosion of Wires," *Applied Surface Science*, Vol. 211, No. 1, 2003, pp. 57-67.
- [364] Gromov, A. A., Forter-Barth, U., Teipel, U., "Aluminum Nanopowders Produced by Electrical Explosion of Wires and Passivated by Non-Inert Coatings: Characterization and Reactivity with Air and Water," *Powder Technology*, Vol 164, No. 2, 2006, pp. 111-115.
- [365] Liu, L. L., Liu, P. J., and He, G. Q., "Ignition and Combustion Characteristics of Compound of Magnesium and Boron," *Journal of Thermal Analysis and Calorimetry*, Vol. 121, No. 3, 2015, pp. 1205-1212.

- [366] Suryanarayana, C., "Mechanical Alloying and Milling," *Progress in Materials Science*, Vol. 46, No. 1, 2001, pp. 1-184.
- [367] Trunov, M. A., Hoffmann, V. K., Schoenitz, M., and Dreizin, E. L., "Combustion of Boron-Titanium Nanocomposite Powders in Different Environments," *Journal of Propulsion and Power*, Vol. 24, No. 2, 2008, pp. 184-191.
- [368] Aly, Y., Schoenitz, M., and Dreizin, E. L., "Aluminum-Metal Reactive Composites," *Combustion Science and Technology*, Vol. 183, No. 10, 2011, pp. 1107-1132.
- [369] Zhu, X., Schoenitz, M., and Dreizin, E. L., "Mechanically Alloyed Al-Li Powders," *Journal of Alloys and Compounds*, Vol. 432, 2007, pp. 111-117.
- [370] Shoshin, Y. L., Mudryy, R. S., and Dreizin, E. L., "Preparation and Characterization of Energetic Al-Mg Mechanical Alloy Powders" *Combustion and Flame*, Vol. 128, 2002, pp. 259-269.
- [371] Dreizin, E. L., Shoshin, Y. L., Mudryy, R. S., and Hoffmann, V. K., "Constant Pressure Flames of Aluminum and Aluminum-Magnesium Mechanical Alloy Aerosols in Microgravity," *Combustion and Flame*, Vol. 130, 2002, pp. 381-385.
- [372] Schoenitz, M., Dreizin, E. L., and Shtessel, E., "Constant Volume Explosion of Aerosols of Metallic Mechanical Alloys and Powder Blends," *Journal of Propulsion and Power*, Vol. 19, No. 3, 2003, pp. 405-412.
- [373] Schoenitz, M., and Dreizin, E. L., "Structure and Properties of Al-Mg Mechanical Alloys," *Journal of Materials Research*, Vol. 18, No. 88, 2003, pp. 1827-1836.
- [374] Schoenitz, M., and Dreizin, E. L., "Oxidation Processes and Phase Changes in Metastable Al-Mg Alloys," *Journal of Propulsion and Power*, Vol. 20, No. 6, 2004, pp. 1064-1068.
- [375] Umbrajkar, S. M., Schoenitz, M., Jones, S. R., and Dreizin, E.L., "Effect of Temperature on Synthesis and Properties of Aluminum-Magnesium Mechanical Alloys," *Journal of Alloys and Compounds*, Vol. 40, No 1, 2005, pp. 70-77.
- [376] Aly, Y., Schoenitz, M., and Dreizin, E. L., "Ignition and Combustion of Mechanically Alloyed Al-Mg Powders with Customized Particle Sizes," *Combustion and Flame*, Vol. 160, No. 4, 2013, pp. 835-842.

- [377] Machado, M. A., Rodriguez, D. A., Aly Y., Schoenitz, M., Dreizin, E. L., and Shafirovich, E., "Nanocomposite and Mechanically Alloyed Reactive Materials as Energetic Additives in Chemical Oxygen Generators," *Combustion and Flame*, Vol. 161, 2014, pp. 2708-2716.
- [378] Corcoran A. L., Wang, S., Aly, Y., and Dreizin E. L., "Combustion of Mechanically Alloyed Al-Mg Powders in Products of a Hydrocarbon Flame," *Combustion Science and Technology*, Vol. 187, 2015, pp. 807-825.
- [379] Aly, Y., and Dreizin, E.L., "Ignition and Combustion of Al-Mg Alloy Powders Prepared by Different Techniques," *Combustion and Flame*, Vol. 162, 2015, pp. 1440-1447.
- [380] Rodriguez, D. A., Dreizin, E. L., and Shafirovich, E., "Hydrogen Generation from Ammonia Borane and Water through Combustion Reactions with Mechanically Alloyed Al-Mg Powder," *Combustion and Flame*, Vol. 162, 2015, pp. 1498-1506.
- [381] Quijano, D., Corcoran, A. L., and Dreizin, E. L., "Combustion of Mechanically Alloyed Aluminum-Magnesium Powders in Steam," *Propellants, Explosives, and Pyrotechnics*, Vol. 40, 2015, pp. 749-754.
- [382] Nie, H., Schoenitz, M., Dreizin E. L., "Oxidation of Differently Prepared Al-Mg Alloy Powders in Oxygen," *Journal of Alloys and Compounds*, Vol. 685, 2016, pp. 402-410.
- [383] Zhu, X., Schoenitz, M., and Dreizin, E. L., "Oxidation Processes and Phase Changes in Metastable Al-Ti Mechanical Alloys," *Materials Research Society Proceedings*, Vol. 800, 2004, pp. AA3.4.1-AA3.4.6.
- [384] Schoenitz, M., Zhu, X., and Dreizin, E. L. "Mechanical Alloys in the Al-rich Part of the Al-Ti Binary System," *Journal of Metastable and Nanocrystalline Materials*, Vol. 20, 2004, pp. 455-461.
- [385] Schoenitz, M., Zhu, X., and Dreizin, E. L., "Carbide Formation in Al-Ti Mechanical Alloys" *Scripta Materialia*, Vol. 53, No. 9, 2005, pp. 1095-1099.
- [386] Shoshin, Y. L., Trunov, M. A., Zhu, X., Schoenitz, M., and Dreizin, E. L., "Ignition of Aluminum-Rich Al-Ti Mechanical Alloys in Air," *Combustion and Flame*, Vol. 144, No. 4, 2006, pp. 688-697.
- [387] Shoshin, Y. L., and Dreizin, E. L., "Particle Combustion Rates for Mechanically Alloyed Al-Ti and Aluminum Powders Burning in Air," *Combustion and Flame*, Vol. 145, No. 4, 2006, pp. 714-722.

- [388] Zhu, X., Schoenitz, M., and Dreizin, E. L., "Oxidation Behavior of Al-Rich Al-Ti Mechanical Alloys," *Oxidation of Metals*, Vol. 65, No. 5, 2006, pp. 357-376.
- [389] Zhang, S., Schoenitz, M., and Dreizin E. L., "Oxidation, Ignition and Combustion of Al-Hydrocarbon Composite Reactive Powders," *International Journal of Energetic Materials and Chemical Propulsion*, Vol. 11, No. 4, 2012, pp. 353-373.
- [390] Sippel, T. R., Son, S. F., Groven, L. J., Zhang, S., and Dreizin, E. L., "Exploring Mechanisms for Agglomerate Reduction in Composite Solid Propellants with Polyethylene Inclusion Modified Aluminum," *Combustion and Flame*, Vol. 162, No. 3, 2015, pp. 846-854.
- [391] Stamatis, D., Jiang, X., Beloni, E., and Dreizin E. L., "Aluminum Burn Rate Modifiers Based on Reactive Nanocomposite Powders," *Propellants, Explosives, and Pyrotechnics*, Vol. 35, 2010, pp. 260-267.
- [392] Abraham A., MacDonald, N. A., and Dreizin E. L., "Reactive Materials for Evaporating Samarium," *Propellants, Explosives, and Pyrotechnics*, Vol. 41, No. 5, 2016, pp. 926-935.
- [393] Hastings, D. L., Schoenitz, M., and Dreizin, E. L., "High Density Reactive Composite Powders," *Journal of Alloys and Compounds*, Vol. 735, 2018, pp. 1863-1870.
- [394] Zhang, S., Schoenitz, M., and Dreizin, E. L., "Nearly Pure Aluminum Powders with Modified Protective Surface," *Combustion Science and Technology*, Vol. 185, No. 9, 2013, pp. 1360-1377.
- [395] Dreizin, E. L. "Metal-Based Reactive Nanomaterials," *Progress in Energy and Combustion Science*, Vol. 35, 2009, pp. 141-167.
- [396] Dreizin, E. L., and Schoenitz, M., "Mechanochemically Prepared Reactive and Energetic Materials: A Review," *Journal of Materials Science*, Vol. 52, No. 20, 2017, pp. 11789-11809.
- [397] Aly, Y., Hoffman, V. K., Schoenitz, M., and Dreizin, E. L. "Reactive, Mechanically Alloyed Al-Mg Powders with Customized Particle Sizes and Compositions," *Journal of Propulsion and Power*, Vol. 30, No. 1, 2014, pp. 96-104.
- [398] White, D. E., Reeves, R. V., Son, S. F., Mukasyan, A. S., "Thermal Explosion in Al-Ni System: Influence of Mechanical Activation," *Journal of Physical Chemistry A*, Vol. 113, 2009, pp. 13541-13547.

- [399] Filimonova, V. Y., Korchagin, M. A., Evstigneev, V. V., and Lyakhov, N. Z., "Anomalous Decrease in the Activation Energy and Initiation Temperature of a Thermal Explosion in the Mechanically Activated Composition 3Ni + Al," *Doklady Physics*, Vol. 54, No. 6, 2009, pp. 277-280.
- [400] Mason, B. A., Sippel, T. R., Groven, L. J., Gunduz, I. E., and Son, S. F., "Combustion of Mechanically Activated Ni/Al Reactive Composites with Microstructural Refinement Tailored using Two-Step Milling," *Intermetallics*, Vol. 66, 2015, pp. 88-95.
- [401] Hahma, A., Gany, A., and Palovuori, K., "Combustion of Activated Aluminum," *Combustion and Flame*, Vol. 145, 2006, pp. 464-480.
- [402] Sippel, T. R., Son, S. F., and Groven, L. J., "Altering Reactivity of Aluminum with Selective Inclusion of Polytetrafluoroethylene through Mechanical Activation," *Propellants, Explosives, and Pyrotechnics*, Vol. 38, No. 2, 2013, pp. 286-295.
- [403] Sippel, T. R., Son, S. F., and Groven, L. J., "Nanostructured Aluminum-Fluorocarbon Particles for Energetic Applications," *2012 American Institute of Chemical Engineers (AIChE) Annual Meeting*, Pittsburgh, PA, 2012.
- [404] Sippel, T. R., and Feng, L. Y., "Reaction Mechanism of Mechanically Activated Al-PTFE Composite Particles," *2014 American Institute of Chemical Engineers (AIChE) Annual Meeting*, Atlanta, GA, 2014.
- [405] Sippel, T. R., Son, S. F., and Groven, L. J., "Modifying Aluminum Reactivity with Poly (Carbon Monofluoride) via Mechanical Activation," *Propellants, Explosives, and Pyrotechnics*, Vol. 38, No. 3, 2013, pp. 321-326.
- [406] Koch, E. C., *Metal-Halocarbon Pyrolant Combustion in: Handbook of Combustion: New Technologies* (Eds.: M. Lackner; F. Winter; A. K. Agarwal), Wiley-VCH: Weinheim, 2010, pp. 355-365.
- [407] Beighley, C. M., Fish, W. R., Anderson, R. E., *Advanced Fuels and Oxidizers in: Propellants Manufacture, Hazards, and Testing* (Eds.: C. Boyars; K. Klager), American Chemical Society: Washington DC, 1969, pp. 319-320.
- [408] Watson, K. W., Pantoya, M. L., Levitas, V. I., "Fast Reactions with Nano- and Micrometer Aluminum: A Study on Oxidation vs. Fluorination," *Combustion and Flame*, Vol. 155, 2008, pp. 619-634.
- [409] Dolgoborodov, A. Y., Makhov, M. N., Kolbanev, I. V., Streletskii, A. N., Fortov, V. E., "Detonation in an Aluminum-Teflon Mixture," *Journal of Experimental and Theoretical Physics Letters*, Vol. 81, 2005, pp. 311-314.

- [410] Osborne, D. T., and Pantoya, M. L., “Effect of Al Particle Size on the Thermal Degradation of Al/Teflon Mixtures,” *Combustion Science and Technology*, Vol. 179, 2007, pp. 1467–1480.
- [411] Streletskii, A. N., Dolgoborodov, A. Y., Kolbanev, I. V., Makhov, M. N., Lomaeva, S. F., Borunova, A. B., Fortov, V. E., “Structure of Mechanically Activated High-Energy Al Plus Polytetrafluoroethylene Nanocomposites,” *Colloid Journal*, Vol. 71, 2009, pp. 852–860.
- [412] Dolgoborodov, A. Y., Streletskii, A. N., Makhov, M. N., Kolbanev, I. V., Fortov, V. E., “Explosive Compositions Based on the Mechanoactivated Metal-Oxidizer Mixtures,” *Russian Journal of Physical Chemistry B*, Vol. 1, 2007, pp. 606–611.
- [413] Pantoya, M. L., and Dean, S. W., “The Influence of Alumina Passivation on Nano-Al/Teflon Reactions,” *Thermochimica Acta*, Vol. 493, 2009, pp. 109–110.
- [414] Dossi, S., Paravan, C., Maggi, F., and Galfetti, L., “Enhancing Micrometric Aluminum Reactivity by Mechanical Activation,” AIAA 2015-4221, *51st AIAA/ASME/SAE/ASEE Joint Propulsion Conference*, Orlando, FL, 2015.
- [415] Dossi, S., Paravan, C., Maggi, F., Di Lorenzo, M., Ardalic, J., and Galfetti, L., “Novel Activated Metal Powders for Improved Hybrid Fuels and Green Solid Propellants,” AIAA 2016-4596, *52nd AIAA/ASME/SAE/ASEE Joint Propulsion Conference*, Salt Lake City, UT, 2016.
- [416] Boiocchi, M., Paravan, C., Dossi, S., Maggi, F., Colombo, G., and Galfetti, L., “Paraffin-Based Fuels and Energetic additives for Hybrid Rocket Propulsion,” 2015-4042, *51st AIAA/ASME/SAE/ASEE Joint Propulsion Conference*, Orlando, FL, 2015.
- [417] Rosenband, V., and Gany, A., “Agglomeration and Ignition of Aluminum Particles Coated by Nickel,” *International Journal of Energetic Materials*, Vol. 6, No. 2, 2007, pp. 143-151.
- [418] Rosenband, V. R., and Gany, A., “High-Reactivity Aluminum Powders,” *International Journal of Energetic Materials and Chemical Propulsion*, Vol. 10, No. 1, 2011, pp.19-32.
- [419] Liu, T. K., Luh, S. P., and Perng, H. C., “Effect of Boron Particle Surface Coating on Combustion of Solid Propellants for Ducted Rockets,” *Propellants, Explosives, and Pyrotechnics*, Vol. 16, No. 4, 1991, pp. 156-166.
- [420] Jin, R., and Li, S., “Improvement of Combustion Characteristics of Solid Propellant with Coated Boron,” AIAA 1999-2633, *35th AIAA/ASME/SAE/ASEE Joint Propulsion Conference*, Los Angeles, CA, 1999.

- [421] Liu, T. K., Shyu, I. M., and Hsia, Y. S., "Effect of Flourinated Graphite on Combustion of Boron and Boron-Based Fuel-Rich Propellants," *Journal of Propulsion and Power*, Vol. 12, No. 1, 1996, pp. 26-33.
- [422] Vummidi, S. L., Aly, Y. Schoenitz, M., and Dreizin, E. L., "Characterization of Fine Aluminum Powder Coated with Nickel as a Potential Fuel Additive," *Journal of Propulsion and Power*, Vol. 26, No. 3, 2010 pp. 454-460.
- [423] Chintersingh K., Schoenitz, M., and Dreizin, E. L., "Oxidation Kinetics and Combustion of Boron Particles with Modified Surface," *Combustion and Flame*, Vol. 173, 2016, pp. 288-295.
- [424] Liu, X., Gonzales, J., Schoenitz, M., and Dreizin E. L., "Effect of Purity and Surface Modification on Stability and Oxidation Kinetics of Boron Powders," *Thermochimica Acta*, Vol. 652, 2017, pp. 17-23.
- [425] Criner, C. B., "Production and Coating of Pure Boron Powders," *AFOSR/ONR Contractors Meeting - Combustion, Rocket Propulsion, Diagnostics of Reacting Flow*, AD-A225444, 1990.
- [426] "Mach I: Pioneer in Nano-Structure, Advanced Materials and Aerospace," Chemical Propulsion Information Agency (CPIA), *CPIA Bulletin*, Vol. 31, No. 2, 2005.
- [427] Gromov, A., Ilyin, A., Forter-Barth, U., and Teipel, U., "Characterization of Aluminum Powders: II. Aluminum Nanopowders Passivated by Non-Inert Coatings," *Propellants, Explosives, and Pyrotechnics*, Vol. 31, No. 5, 2006, pp. 401-409.
- [428] Lorente, A. P., Yu, N., and Zhao, B., "Testing and Evaluation of a Double-Tube Hybrid Rocket Motor," 2015-4035, *51st AIAA/ASME/SAE/ASEE Joint Propulsion Conference*, Orlando, FL, 2015.
- [429] Knuth, W. H., Chiaverini, M. J., Gramer, D. J., and Sauer, J. A., "Solid-Fuel Regression Rate and Combustion Behavior of Vortex Hybrid Rocket Engines," AIAA 1999-2318, *35th AIAA/ASME/SAE/ASEE Joint Propulsion Conference*, Los Angeles, CA, 1999.
- [430] Knuth, W. H., Chiaverini, M. J., Gramer, D. J., and Sauer, J. A., "Experimental Investigation of a Vortex-Driven High-Regression Rate Hybrid Rocket Engine," AIAA 1998-3348, *34th AIAA/ASME/SAE/ASEE Joint Propulsion Conference*, Cleveland, OH, 1998.
- [431] Knuth, W. H., Chiaverini, M. J., Sauer, J. A., and Gramer, D. J., "Solid-Fuel Regression Rate Behavior of Vortex Hybrid Rocket Engines," *Journal of Propulsion and Power*, Vol. 18, No. 3, 2002, pp. 600-609.

- [432] Paravan, C., Glowacki, J., Carlotti, S., Maggi, F., and Galfetti, L., "Vortex Combustion in a Hybrid Rocket Motor," AIAA 2016-4562, *52nd AIAA/ASME/SAE/ASEE Joint Propulsion Conference*, Salt Lake City, UT, 2016.
- [433] Paravan, C., Carlotti, S., Maggi, F., and Galfetti, L., "Quasi-Steady and Forced Transient Burning of a Vortex Flow Hybrid Motor," *7th European Conference for Aeronautics and Space Sciences (EUCASS)*, Milan, Italy, 2017.
- [434] Chen, Y. S., Lai, A., Lin, J. W., Chou, T. H., and Wu, J. S., "HTPB Hybrid Propulsion with Multiple Vortical-Flow Chamber Designs," AIAA 2014-3544, *50th AIAA/ASME/SAE/ASEE Joint Propulsion Conference*, Cleveland, OH, 2014.
- [435] Chen, Y. S., Lai, A., Lin, J. W., Wei, S. S., Chou, T. H., and Wu, J. S., "Investigation on Tri-Propellant Hybrid Rocket Performance," AIAA 2016-4659, *52nd AIAA/ASME/SAE/ASEE Joint Propulsion Conference*, Salt Lake City, UT, 2016.
- [436] Lai, G. R., Wei, S. S., Chou, T. h., Lin, J. W., and Wu, J. S., "Numerical and Experimental Investigations of HDPE Hybrid Propulsion with Dual Cortical-flow Chamber Designs," AIAA 2015-4135, *51st AIAA/ASME/SAE/ASEE Joint Propulsion Conference*, Orlando, FL, 2015.
- [437] Chen, Y. S., Cheng, R., Chang, H. C., Lai, A., Lin, J. W., Wei, S. S., Chou, T. H., Chen, T. L., Ho, M. T., Wu, J. S. Yang, L., and Wu, B., "Multifunction Sounding Rocket system Development with Advanced Hybrid Propulsion, AIAA 2015-4043, *51st AIAA/ASME/SAE/ASEE Joint Propulsion Conference*, Orlando, FL, 2015.
- [438] Chen, Y. S., Cheng, R., Chang, H. C., Yang, L., Wu, B., Lai, A., Lin, J. W., Wei, s. S., Chou, T. H., Chen, T. L., and Wu, J. S., "Multifunction Rocket System Development Based on Advanced Hybrid Propulsion," AIAA 2016-2586, *AIAA SpaceOps Conference*, Daejeon, Korea, 2016.
- [439] Chen, Y. S., Chou, T. H., and Wu, J. S., "Numerical Modeling of Hybrid N₂O-HTPB Combustion with Mixing Enhancers," AIAA 2013-0714, *49th AIAA/ASME/SAE/ASEE Joint Propulsion Conference*, San Jose, CA, 2013.
- [440] Chen, Y. S., Chou, T. H., and Wu, J. S., "N₂O-HTPB Hybrid Rocket Combustion Modeling with Mixing Enhancement Designs," AIAA 2013-3645, *49th AIAA/ASME/SAE/ASEE Joint Propulsion Conference*, San Jose, CA, 2013.
- [441] Li, X., Tian, H., Yu, N., and Cai, G., "Experimental Investigation of Combustion in Axial-Injection End-Burning Hybrid Rocket Motor," *Journal of Propulsion and Power*, Vol. 31, No. 3, 2015, pp. 930-936.

- [442] Matsuoka, T., and Nagata, H., "Combustion Characteristics of the End Burning Hybrid Rockets in Laminar Flow," *Acta Astronautica*, Vol. 68, No. 1, 2011, pp. 197-203.
- [443] Hasimoto, N., Nagata, H., Totani, T., and Kudo, I., "Determining Factor for the Blowoff Limit of a Flame Spreading in an Opposed Turbulent Flow, in a Narrow Solid-Fuel Duct" *Combustion and Flame*, Vol. 147, No. 3, 2006, pp. 222-232.
- [444] Nagata, H., Teraki, H., Saito, Y., Kanai, R., Yasukochi, H., Wakite, M., and Totani, T., "Verification Firings of End-Burning Type Hybrid Rockets," AIAA 2015-4199, 51st AIAA/ASME/SAE/ASEE Joint Propulsion Conference, Orlando, FL, 2015.
- [445] Saito, Y., Yokoi, T., Nagata, H., Yasukochi, H., Soeda, K., Totani, T., and Wakita, M., "Experimental and Analytical Investigation of Effect of Pressure on Regression rate of Axial Injection End-burning Hybrid Rockets," AIAA 2016-4752, 52nd AIAA/ASME/SAE/ASEE Joint Propulsion Conference, Salt Lake City, UT, 2016.
- [446] Saito, Y., Kimino, M., Ayumu, T., Okutani, Y., Yasukochi, H., Soeda, K., and Nagata, H., "Investigation of regression Characteristics under Relatively High-Pressure in Axial-Injection End-Burning Hybrid Rockets," AIAA 2017-4985, 53rd AIAA/ASME/SAE/ASEE Joint Propulsion Conference, Atlanta, GA, 2017.
- [447] Nagata, H., Teraki, H., Saito, Y., Kanai, R., Yasukochi, H., Wakita, M., and Totani, T., "Verification Firings of End-Burning Type Hybrid Rockets," *Journal of Propulsion and Power*, Vol. 33, No. 6, 2017, pp. 1473-1477.
- [448] Saito, Y., Yokoi, T., Yasukochi, H., Soeda, K., Totani, T., Wakita, M., and Nagata, H., "Fuel Regression Characteristics of a Novel Axial-Injection End-Burning Hybrid Rocket," *Journal of Propulsion and Power*, Vol. 34, No. 1, 2018, pp. 247-259.
- [449] Hitt, M. A., and Frederick, R. A., "Testing and Modeling of a Porous Polyethylene Axial-Injection, End-Burning Hybrid Rocket Motor," AIAA 2015-4038, 51st AIAA/ASME/SAE/ASEE Joint Propulsion Conference, Orlando, FL, 2015.
- [450] Hitt, M. A., and Frederick, R. A., "Testing and Modeling of a Porous Polyethylene Axial-Injection, End-Burning Hybrid Rocket Motor," *Journal of Propulsion and Power*, Vol. 32, No. 4, 2016, pp. 834-843.
- [451] Hitt, M. A., and Frederick, R. A., "Experimental Evaluation of a Polyethylene/Nitrous Oxide Axial-Injection, End-Burning Hybrid," AIAA 2016-4657, 52nd AIAA/ASME/SAE/ASEE Joint Propulsion Conference, Salt Lake City, UT, 2016.
- [452] Hitt, M. A., and Frederick, R. A., "Regression Rate Model Predictions of an Axial-Injection, End-Burning Hybrid Motor," AIAA 2017-4986, 53rd AIAA/ASME/SAE/ASEE Joint Propulsion Conference, Atlanta, GA, 2017.

- [453] Hitt, M. A., and Frederick, R. A., "Experimental Evaluation of a Nitrous-Oxide Axial-Injection, End-Burning Hybrid Rocket," *Journal of Propulsion and Power*, Vol. 33, No. 6, 2017, pp. 1555-1560.
- [454] McBride, B. J., and Gordon, S., "Computer Program for Calculation of Complex Chemical Equilibrium Compositions and Applications, Volume I. Analysis," NASA Reference Publication 1311, 1994.
- [455] McBride, B. J., and Gordon, S., "Computer Program for Calculation of Complex Chemical Equilibrium Compositions and Applications, Volume II. User's Manual and Program Description," NASA Reference Publication 1311, 1994.
- [456] Budynas, R. G., Nisbett, J. K., and Shigley, J. E., *Shigley's Mechanical Engineering Design*, 10th ed., McGraw-Hill, New York, 2011.
- [457] Kothandaraman, H., Venkatarao, K., Thanoo, B. C., "Crosslinking Studies of Polyether-Ester-Based Polyurethane Systems," *Journal of Applied Polymeric Science*, Vol. 39, 1990, pp. 943-954.
- [458] Haska, S. B., Bayramli, E., Pekel, K., Ozkar, S., "Mechanical Properties of HTPB-IPDI-Based Elastomers," *Journal of Applied Polymeric Science*, Vol. 64, 1997, pp. 2347-2354.
- [459] Manjari, R., Joseph, V. C., Pandureng, L. P., Sriram, T., "Structure-Property Relationship of HTPB-Based Propellants. I. Effect of Hydroxyl Value of HTPB Resin," *Journal of Applied Polymeric Science*, Vol. 48, 1993, pp. 271-278.
- [460] Manjari, R., Somasundaran, U. I., Joseph, V. C., Sriram, T., "Structure-Property Relationship of HTPB-Based Propellants. II. Formulation Tailoring for Better Mechanical Properties," *Journal of Applied Polymeric Science*, Vol. 48, 1993, pp. 279-289.
- [461] Manjari, R., Pandureng, L. P., Somasundaran, U. I., Sriram, T., "Structure-Property Relationship of HTPB-Based Propellants. III. Optimization Trials with Varying Levels of Diol-Triol Contents," *Journal of Applied Polymeric Science*, Vol. 51, 1994, pp. 435-442.
- [462] Hocaoglu, O., Ozbelge, T., Pekel, F., Ozkar, S., "Fine-Tuning the Mechanical Properties of Hydroxyl-Terminate Polybutadiene/Ammonium Perchlorate-Based Composite Solid Propellants by Varying the NCO/OH and Trio/Diol Ratios," *Journal of Applied Polymeric Science*, Vol. 84, 2002, pp. 2072-2079.
- [463] Wingborg, N., "Increasing the Tensile Strength of HTPB with Different Isocyanates and Chain Extenders," *Polymer Testing*, Vol. 21, 2002, pp. 283-287.

[464] Karabeyoglu, A., Cantwell, B., and Ziliac, G., "Development of Scalable Space-Time Averaged Regression Rate Expressions for Hybrid Rockets," AIAA 2005-3544, *41st AIAA/ASME/SAE/ASEE Joint Propulsion Conference*, Tucson, AZ, 2005.

[465] Karabeyoglu, A., Cantwell, B., and Ziliac, G., "Development of Scalable Space-Time Averaged Regression Rate Expressions for Hybrid Rockets," *Journal of Propulsion and Power*, Vol. 23, 2007, pp. 737-747.

[466] Bazyn, T., Krier, H., and Glumac, N., "Combustion of Nanoaluminum at Elevated Pressure and Temperature Behind Reflected Shock Waves," *Combustion and Flame*, Vol. 145, No. 4, 2006, pp. 703-713.

[467] Beckwith, T. G., Marangoni, R. D., and Lienhard V, J. H., *Mechanical Measurements*, 6th ed., Pearson, IN, 2007.

APPENDIX A

BURN SIMULATION PROGRAM

This appendix contains the matlab code used to produce burn simulations of the alternate hybrid rocket formulations for comparison. It is separated into three sections: the main simulation program, a regression and heat transfer function, and a rocket performance function.

A.1 Burn Simulation Program

```
%% Burn Simulation Program
% This program is designed to simulate the burning of hybrid motor fuel
% grains in a gaseous oxygen environment with prescribed rocket motor
% dimensions, oxidizer mass flow rate, and chamber pressure

% Clearing all past data
clc;
clear all;
close all;

%% System Parameters - USER SPECIFIED

% Oxidizer Mass Flow Rate
mdot_ox=4.46; %[g/s]

% Chamber Pressure
P_Chamber=75; %[psi]

% System Dimensions
% Motor Port Diameter and Length
D0=0.2; %[cm]
L=5; %[cm]
% Throat Diameter
D_t=0.2; %[cm]
% Nozzle Expansion Ratio
exp=6.275;

% Parameter Calcs for Standard Input
mdot_ox=mdot_ox/1000; %[kg/s]
L=L/100; %[m]
```

```

D_t=D_t/100; %[m]
A_t=(pi/4)*(D_t^2); %[m2]
D0=D0/100; %[m]
P_Chamber=P_Chamber*6894.75729; %[Pa]

%% Setting Simulation Time
dt=0.01; %[s]
t_final=10; %[s]
N=(t_final/dt);
t=0:dt:t_final;

%% Running Simulation

%Note: Run 1 is plain HTPB; Run 2 is HTPB + 30.6% Al
for k=1:2

    % Setting Fuel Formulation Parameters
    if k==1,

        % Plain HTPB {run:k=1}
        % Fuel Density;
        rho_f=930; %[kg/m3]
        % Fuel Effective Heat of Decomposition
        dhv_f=1.8; %[MJ/kg]
        % Regression Rate Correlation Parameters - For use with Gox [g/cm2-s] and dr/dt
        [mm/s]
        a=0.240;
        n=0.647;
        % Combustion Efficiency
        n_c=1;

    elseif k==2

        % HTPB + 30.6% Al {run:k=2}
        % Fuel Density;
        rho_f=1480; %[kg/m3]
        % Fuel Effective Heat of Decomposition
        dhv_f=4.61; %[MJ/kg]
        % Regression Rate Correlation Parameters - For use with Gox [g/cm2-s] and dr/dt
        [mm/s]
        a=0.343;
        n=0.596;
        % Combustion Efficiency
        n_c=1;
    end
end

```



```

end

% Implementing Burn Simulation

% Initial Value
D=D0; %Setting Initial Port Diameter
M_Exit_Old=3; %Required Guess for Initial Mach Number

for i=1:N+1

    % Implementing Regression Tracking Model
    [rdot, G_ox, mdot_f, OF, D_New, mdot_sys, Q, QFlux]=RegressionModel(L, D,
mdot_ox, a, n, rho_f, dhv_f, dt);

    % Calculating Combustion Gas Properties
    if k==1 %HTPB Properties @ Pc=75psi
        OFinterp=[0.2, 0.5, 1, 1.5, 2, 2.5, 3, 4, 5, 6.5, 8];
        cstarinterp=[3051.59, 3767.006, 4556.017, 5531.12, 5801.537, 5686.52,
5541.346, 5285.716, 5088.379, 4850.413, 4651.418]; % [ft/s]
        gammainterp=[1.148152, 1.221816, 1.298322, 1.260501, 1.236525, 1.228132,
1.223879, 1.21971, 1.218176, 1.218282, 1.220076];
        cstar=interp1(OFinterp,cstarinterp,OF); % [ft/s]
        cstar=cstar*0.3048; % [m/s]
        gamma=interp1(OFinterp,gammainterp,OF);
    elseif k==2 %HTPB + 30.6% Al Properties @ Pc=75psi
        OFinterp=[0.95, 1, 1.5, 2, 3, 4, 5, 6.5, 8];
        cstarinterp=[5203.839, 5515.905, 5700.264, 5450.113, 5221.048, 5010.354,
4844.958, 4642.178, 4461.289]; % [ft/s]
        gammainterp=[1.240191, 1.224845, 1.200629, 1.196873, 1.195724, 1.19697,
1.199074, 1.203058, 1.2077];
        cstar=interp1(OFinterp,cstarinterp,OF); % [ft/s]
        cstar=cstar*0.3048; % [m/s]
        gamma=interp1(OFinterp,gammainterp,OF);
    end

    % Implimenting Performance Model
    [P_Exit, M_Exit, CF, F, Isp]=NozzleModel(P_Chamber, gamma, mdot_sys, cstar,
exp, M_Exit_Old, n_c);

    % Choked Condition Check @ Nozzle
    P_ratio_c=((gamma+1)/2)^(gamma/(gamma-1));
    P_ratio=P_Chamber/P_Exit;
    if P_ratio<P_ratio_c

```

```

    display('Nozzle Not Operating Under Choked Conditions');
end

% Setting Stored Values in Comparable Units
ChamberPressure(i,k)=P_Chamber/6894.75729; %[psi]
ExitPressure(i,k)=P_Exit/6894.75729; %[psi]
ExitMach(i,k)=M_Exit;
RegressionRate(i,k)=rdot*1000; %[mm/s]
Radius(i,k)=D*100/2; %[cm]
OxidizerMassFlow(i,k)=mdot_ox*1000; %[g/s]
OxidizerMassFlux(i,k)=G_ox*1000/100/100; %[g/cm2-s]
FuelMassFlow(i,k)=mdot_f*1000; %[g/s]
OxidizerToFuelRatio(i,k)=OF;
TotalMassFlow(i,k)=mdot_sys*1000; %[g/s]
ThrustCoefficient(i,k)=CF;
ThrustForce(i,k)=F/4.44822; %[lbf]
SpecificImpulse(i,k)=Isp; %[s-1]
TotalImpulse(i,k)=dt*sum(ThrustForce(:,k)); %[lbf-s]
SpecificHeatRatio(i,k)=gamma;
CharacteristicVelocity(i,k)=cstar; %[m/s]
HeatFlow(i,k)=Q; %[kW]
HeatFlux(i,k)=QFlux; %[kW/m2]

%Setting Simulation New Values
D=D_New;
M_Exit_Old=M_Exit;

end

end

%% Plotting Results

% Pressure Plot
figure;
plot(t,ChamberPressure(:,1),'LineStyle','-','Color','r')
hold on
plot(t,ExitPressure(:,1),'LineStyle','-','Color','b')
plot(t,ExitPressure(:,2),'LineStyle','--','Color','b')
hold off
title('Pressure Plot');
xlabel('Testing Time [s]');
ylabel('Pressure [psi]');

```

```
legend('Chamber','Exit-HTPB','Exit-HTPB+Al');
```

% Mass Flow Plots

```
figure;  
plot(t,OxidizerMassFlow(:,1),'LineStyle','-','Color','b')  
hold on  
plot(t,FuelMassFlow(:,1),'LineStyle','-','Color','r')  
plot(t,FuelMassFlow(:,2),'LineStyle','--','Color','r')  
plot(t>TotalMassFlow(:,1),'LineStyle','-','Color','g')  
plot(t>TotalMassFlow(:,2),'LineStyle','--','Color','g')  
hold off  
title('Mass Flow Rate Plot');  
xlabel('Testing Time [s]');  
ylabel('Mass Flow Rate [g/s]');  
legend('Oxidizer','Fuel-HTPB','Fuel-HTPB+Al','Total-HTPB','Total-HTPB+Al');
```

```
figure;  
plot(t,OxidizerMassFlux(:,1),'LineStyle','-','Color','b')  
hold on  
plot(t,OxidizerMassFlux(:,2),'LineStyle','--','Color','r')  
hold off  
title('Mass Flux Plot');  
xlabel('Testing Time [s]');  
ylabel('Oxidizer Mass Flux [g/cm2-s]');  
legend('HTPB','HTPB+Al');
```

```
figure  
plot(t,OxidizerToFuelRatio(:,1),'LineStyle','-','Color','b')  
hold on  
plot(t,OxidizerToFuelRatio(:,2),'LineStyle','--','Color','r')  
hold off  
title('O/F Plot');  
xlabel('Testing Time [s]');  
ylabel('O/F');  
legend('HTPB','HTPB+Al');
```

% Regression Plots

```
figure  
plot(t,RegressionRate(:,1),'LineStyle','-','Color','b')  
hold on  
plot(t,RegressionRate(:,2),'LineStyle','--','Color','r')  
hold off  
title('Regression Rate Plot');  
xlabel('Testing Time [s]');
```

```
ylabel('Regression Rate [mm/s]');  
legend('HTPB','HTPB+Al');
```

```
figure  
plot(t,Radius(:,1),'LineStyle','-','Color','b')  
hold on  
plot(t,Radius(:,2),'LineStyle','--','Color','r')  
hold off  
title('Combustion Port Radius Plot');  
xlabel('Testing Time [s]');  
ylabel('Combustion Port Radius [cm]');  
legend('HTPB','HTPB+Al');
```

% Performance Plots

```
figure  
plot(t,ExitMach(:,1),'LineStyle','-','Color','b')  
hold on  
plot(t,ExitMach(:,2),'LineStyle','--','Color','r')  
hold off  
title('Mach Number Plot');  
xlabel('Time [s]');  
ylabel('Exit Mach Number');  
legend('HTPB','HTPB+Al');
```

```
figure  
plot(t,ThrustCoefficient(:,1),'LineStyle','-','Color','b')  
hold on  
plot(t,ThrustCoefficient(:,2),'LineStyle','--','Color','r')  
hold off  
title('CF Plot');  
xlabel('Testing Time [s]');  
ylabel('Thrust Coefficient');  
legend('HTPB','HTPB+Al');
```

```
figure  
plot(t,ThrustForce(:,1),'LineStyle','-','Color','b')  
hold on  
plot(t,ThrustForce(:,2),'LineStyle','--','Color','r')  
hold off  
title('Thrust Plot');  
xlabel('Testing Time [s]');  
ylabel('Thrust Force [lbf]');  
legend('HTPB','HTPB+Al');
```

```

figure
plot(t,SpecificHeatRatio(:,1),'LineStyle','-','Color','b')
hold on
plot(t,SpecificHeatRatio(:,2),'LineStyle','--','Color','r')
hold off
title('Specific Heat Ratio Plot');
xlabel('Testing Time [s]');
ylabel('Specific Heat Ratio');
legend('HTPB','HTPB+Al');

```

```

figure
plot(t,CharacteristicVelocity(:,1),'LineStyle','-','Color','b')
hold on
plot(t,CharacteristicVelocity(:,2),'LineStyle','--','Color','r')
hold off
title('Characteristic Velocity Plot');
xlabel('Testing Time [s]');
ylabel('Characteristic Velocity [m/s]');
legend('HTPB','HTPB+Al');

```

```

figure
plot(t,SpecificImpulse(:,1),'LineStyle','-','Color','b')
hold on
plot(t,SpecificImpulse(:,2),'LineStyle','--','Color','r')
hold off
title('Specific Impulse Plot');
xlabel('Testing Time [s]');
ylabel('Specific Impulse [s-1]');
legend('HTPB','HTPB+Al');

```

```

figure
plot(t>TotalImpulse(:,1),'LineStyle','-','Color','b')
hold on
plot(t>TotalImpulse(:,2),'LineStyle','--','Color','r')
hold off
title('Total Impulse Plot');
xlabel('Testing Time [s]');
ylabel('Total Impulse [lbf-s]');
legend('HTPB','HTPB+Al');

```

% Trend Checks

```

figure
loglog(OxidizerMassFlux(:,1),RegressionRate(:,1),'LineStyle','-','Color','b')

```

```

hold on
loglog(OxidizerMassFlux(:,2),RegressionRate(:,2),'LineStyle','--','Color','r')
hold off
title('Regression Rate Correlation');
xlabel('Oxidizer Mass Flux [g/cm2-s]');
ylabel('Regression Rate [mm/s]');
legend('HTPB','HTPB+Al')

```

```

figure
plot(OxidizerToFuelRatio(:,1),SpecificHeatRatio(:,1),'LineStyle','-','Color','b')
hold on
plot(OxidizerToFuelRatio(:,2),SpecificHeatRatio(:,2),'LineStyle','--','Color','r')
hold off
title('Specific Heat Ratio Trend');
xlabel('O/F Ratio');
ylabel('Specific Heat Ratio');
legend('HTPB','HTPB+Al')

```

```

figure
plot(OxidizerToFuelRatio(:,1),CharacteristicVelocity(:,1),'LineStyle','-','Color','b')
hold on
plot(OxidizerToFuelRatio(:,2),CharacteristicVelocity(:,2),'LineStyle','--','Color','r')
hold off
title('Characteristic Velocity Trend');
xlabel('O/F Ratio');
ylabel('Characteristic Velocity [m/s]');
legend('HTPB','HTPB+Al')

```

```

figure
plot(OxidizerToFuelRatio(:,1),SpecificImpulse(:,1),'LineStyle','-','Color','b')
hold on
plot(OxidizerToFuelRatio(:,2),SpecificImpulse(:,2),'LineStyle','--','Color','r')
hold off
title('Specific Impulse Trend');
xlabel('O/F Ratio');
ylabel('Specific Impulse [s-1]');
legend('HTPB','HTPB+Al')

```

% Heat Flow Plots

```

figure
plot(t,HeatFlow(:,1),'LineStyle','-','Color','b')
hold on
plot(t,HeatFlow(:,2),'LineStyle','--','Color','r')
hold off

```

```

title('Surface Heat Flow Plot');
xlabel('Testing Time [s]');
ylabel('Heat Transfer Rate [kW]');
legend('HTPB','HTPB+Al')

```

```

figure
plot(t,HeatFlux(:,1),'LineStyle','-','Color','b')
hold on
plot(t,HeatFlux(:,2),'LineStyle','--','Color','r')
hold off
title('Surface Heat Flux Plot');
xlabel('Testing Time [s]');
ylabel('Heat Transfer Flux [MW/cm2]');
legend('HTPB','HTPB+Al')

```

% Trend 1 - Radius

```

figure
loglog(Radius(:,1),HeatFlow(:,1),'LineStyle','-','Color','b')
hold on
loglog(Radius(:,2),HeatFlow(:,2),'LineStyle','--','Color','r')
hold off
title('Surface Heat Flow Trend');
xlabel('Radius [cm]');
ylabel('Heat Transfer Rate [kW]');
legend('HTPB','HTPB+Al')

```

```

figure
loglog(Radius(:,1),HeatFlux(:,1),'LineStyle','-','Color','b')
hold on
loglog(Radius(:,2),HeatFlux(:,2),'LineStyle','--','Color','r')
hold off
title('Surface Heat Flux Trend');
xlabel('Radius [cm]');
ylabel('Heat Transfer Flux [MW/cm2]');
legend('HTPB','HTPB+Al')

```

% Trend 2 - Oxidizer Mass Flux

```

figure
loglog(OxidizerMassFlux(:,1),HeatFlow(:,1),'LineStyle','-','Color','b')
hold on
loglog(OxidizerMassFlux(:,2),HeatFlow(:,2),'LineStyle','--','Color','r')
hold off
title('Surface Heat Flow Trend');

```

```

xlabel('Oxidizer Mass Flux [g/cm2-s]');
ylabel('Heat Transfer Rate [kW]');
legend('HTPB','HTPB+Al')

```

```

figure
loglog(OxidizerMassFlux(:,1),HeatFlux(:,1),'LineStyle','-','Color','b')
hold on
loglog(OxidizerMassFlux(:,2),HeatFlux(:,2),'LineStyle','--','Color','r')
hold off
title('Surface Heat Flux Trend');
xlabel('Oxidizer Mass Flux [g/cm2-s]');
ylabel('Heat Transfer Flux [MW/cm2]');
legend('HTPB','HTPB+Al')

```

% Trend 2 - Oxidizer to Fuel Ratio

```

figure
loglog(OxidizerToFuelRatio(:,1),HeatFlow(:,1),'LineStyle','-','Color','b')
hold on
loglog(OxidizerToFuelRatio(:,2),HeatFlow(:,2),'LineStyle','--','Color','r')
hold off
title('Surface Heat Flow Trend');
xlabel('O/F Ratio');
ylabel('Heat Transfer Rate [kW]');
legend('HTPB','HTPB+Al')

```

```

figure
loglog(OxidizerToFuelRatio(:,1),HeatFlux(:,1),'LineStyle','-','Color','b')
hold on
loglog(OxidizerToFuelRatio(:,2),HeatFlux(:,2),'LineStyle','--','Color','r')
hold off
title('Surface Heat Flux Trend');
xlabel('O/F Ratio');
ylabel('Heat Transfer Flux [MW/cm2]');
legend('HTPB','HTPB+Al')

```

%% Creating Results Table

% Calculating Relevant Values

```
for k=1:2
```

% Burn Time

```
t_b(k)=t_final; % [s]
```



```

% Initial and Final Diameters
D_i(k)=2*Radius(1,k); %[cm]
D_f(k)=2*Radius(N+1,k); %[cm]

% Average Conditions
mdot_ox_avg(k)=mean(OxidizerMassFlow(:,k)); %[g/s]
mdot_f_avg(k)=mean(FuelMassFlow(:,k)); %[g/s]
mdot_sys_avg(k)=mean(TotalMassFlow(:,k)); %[g/s]
G_ox_avg(k)=mean(OxidizerMassFlux(:,k)); %[g/cm2-s]
OF_avg(k)=mean(OxidizerToFuelRatio(:,k));
r_avg(k)=mean(RegressionRate(:,k)); %[mm/s]

```

```

% Average Performance
F_avg(k)=mean(ThrustForce(:,k)); %[lbf]
F_max(k)=max(ThrustForce(:,k)); %[lbf]
Isp_avg(k)=mean(SpecificImpulse(:,k)); %[s-1]
It(k)=max(TotalImpulse(:,k)); %[lbf-s]
Q_max(k)=max(HeatFlow(:,k)); %[kW]
Q_avg(k)=mean(HeatFlow(:,k)); %[kW]
QFlux_max(k)=max(HeatFlow(:,k)); %[MW/cm2]
QFlux_avg(k)=mean(HeatFlow(:,k)); %[MW/cm2]

```

end

```

% Making Table

```

```

figure;
Rows={'tb (s)', 'Di (cm)', 'Df (cm)', 'mdotox,avg (g/s)', 'mdotf,avg (g/s)', 'mdotsys,avg (g/s)', 'OFavg', 'Gox,avg (g/cm2-s)', 'rb,avg (mm/s)', 'Fmax (lbf)', 'Favg (lbf)', 'Isp (s-1)', 'It (lbf-s)', 'Qmax (kW)', 'Qavg (kW)', 'Q"max (MW/cm2)', 'Q"avg (MW/cm2)'};
Columns={'HTPB', 'HTPB+Al'};
for k=1:2
    Data(1,k)=t_b(k);
    Data(2,k)=D_i(k);
    Data(3,k)=D_f(k);
    Data(4,k)=mdot_ox_avg(k);
    Data(5,k)=mdot_f_avg(k);
    Data(6,k)=mdot_sys_avg(k);
    Data(7,k)=OF_avg(k);
    Data(8,k)=G_ox_avg(k);
    Data(9,k)=r_avg(k);
    Data(10,k)=F_max(k);
    Data(11,k)=F_avg(k);
    Data(12,k)=Isp_avg(k);
    Data(13,k)=It(k);

```

```

    Data(14,k)=Q_max(k);
    Data(15,k)=Q_avg(k);
    Data(16,k)=QFlux_max(k);
    Data(17,k)=QFlux_avg(k);
end
u = uitable('Data',Data,'RowName',Rows,'ColumnName',Columns,'Position',[0 0 350
350]);

%% End Program

```

A.2 Regression and Heat Transfer Function

```

function [rdot, G_ox, mdot_f, OF, D_New, mdot_sys, Q, QFlux] = RegressionModel(L,
D, mdot_ox, a, n, rho_f, dhv_f, dt)
%% Regression Model
%Inputs:  L - Motor Grain Length [m]
%         D - Combustion Port Diameter [cm]
%         mdot_ox - Oxidizer Mass Flow Rate [kg/s]
%         a - Empirical Burning Rate Constant [mm/s]
%         n - Empirical Burning Rate Constant
%         rho_f - Fuel Density [kg/m3]
%         dhv_f - Fuel Effective Heat of Decomposition [MJ/kg]
%         dt - Time Step [s]
%Outputs: rdot - Regression Rate [m/s]
%         G_ox - Oxidizer Mass Flux [kg/m2-s]
%         mdot_f - Fuel Mass Loss Rate [kg/s]
%         OF - Oxidizer to Fuel Ratio
%         D_New - New Combustion Port Diameter [m]
%         mdot_sys - Nozzel Mass Flow Rate [kg/s]
%         Q - Effective Surface Heat Flow [kW]
%         QFlux - Effective Surface Heat Fluw [MW/cm2]

%% Calculating Useful Burning Areas
A_c=(pi/4)*(D^2); %[m2]
A_b=pi*D*L; %[m2]

%% Calculating Regression Rate
G_ox=mdot_ox/A_c; %[kg/m2-s]
G_ox=G_ox*1000/100/100; %[g/cm2-s]
rdot=a*(G_ox^n); %[mm/s]
rdot=rdot/1000; %[m/s]

%% Calculating New Combustion Port Diameter

```

```

D_New=D+(2*rdot*dt); %[m]

%% Calculating Fuel Mass Loss Rate
mdot_f=rho_f*A_b*rdot; %[kg/s]

%% Calculating Oxidizer to Fuel Ratio
OF=mdot_ox/mdot_f;

%% Calculating Nozzle Mass Flow Rate
mdot_sys=mdot_ox+mdot_f; %[kg/s]

%% Calculating Surface Heat Flow
Q=mdot_f*dhv_f; %[MW]
QFlux=Q/A_b; %[MW/m2]

%% Output Redundancy and Standard Unit Corrections
rdot=rdot; %[m/s]
G_ox=G_ox*100*100/1000; %[kg/m2-s]
mdot_f=mdot_f; %[kg/s]
OF=OF;
D_New=D_New; %[m]
mdot_sys=mdot_sys; %[kg/s]
Q=Q*1000; %[kW]
QFlux=Q/A_b/100/100; %[MW/cm2]

%% Program Complete
end

```

A.3 Rocket Performance Function

```

function [P_Exit, M_Exit, CF, F, Isp] = NozzleModel(P_Chamber, gamma, mdot_sys,
cstar, exp, M_Exit_Old, n_c)
%% Nozzle Model
%Inputs:  P_Chamber - Chamber Pressure [Pa]
%         gamma - Products Specific Heat Ratio
%         mdot_sys - Nozzle Mass Flow Rate [kg/s]
%         cstar - Effective Exhaust Velocity [m/s]
%         exp - Nozzle Expansion Ratio
%         M_Exit_Old - Previous Exit Mach Number
%         n_c - Combustion Efficiency
%Outputs: P_Exit - Exit Pressure [psi]
%         M_Exit - Current Mach Number
%         CF - Thrust Coefficient

```

```

%      F - Thrust Force [N]
%      Isp - Specific Impulse [s-1]

%% Calculating Exit Mach Number
zero=@(x)(((1/x)*((2/(gamma+1))*(1+(((gamma-1)/2)*(x^2))))^((gamma+1)/(2*(gamma-1))))-exp);
M_Exit=fzero(zero,M_Exit_Old);

%% Calculating Exit Pressure
P_ratio=(1+(((gamma-1)/2)*(M_Exit^2)))*(gamma/(gamma-1));
P_Exit=P_Chamber/P_ratio; % [Pa]

%% Inputting Time Independent Atmospheric Pressure
P_atm=14.7; % [psi]
P_atm=P_atm*1000*1000/145.0377; % [Pa]

%% Calculating Thrust Coefficient
CFopt=(gamma^(1/2))*((2/(gamma+1))^((gamma+1)/(2*(gamma-1))))*((2*gamma/(gamma-1))*(1-((P_Exit/P_Chamber)^((gamma-1)/gamma))))^(1/2);
CF=CFopt+exp*((P_Exit-P_atm)/P_Chamber);

%% Calculating Thrust Force
F=mdot_sys*cstar*CF*n_c; % [N]

%% Calculating Specific Impulse
g0=9.81; % [m/s2]
Isp=F/(mdot_sys*g0); % [s-1]

%% Output Redundancy and Unit Corrections
P_Exit=P_Exit; % [Pa]
M_Exit=M_Exit;
CF=CF;
F=F; % [N]
Isp=Isp; % [s-1]

%% Program Complete
end

```

APPENDIX B

BURN SIMULATION PROGRAM OUTPUT

This appendix contains the output data for the burn simulation program as described in Chapter 4 of this thesis. Data are given for the simulation run with the parameters given in Table 3. Red and blue lines in Figures A.1-A.26 correspond to plain HTPB and HTPB loaded with 30.9% aluminum burning in GOX.

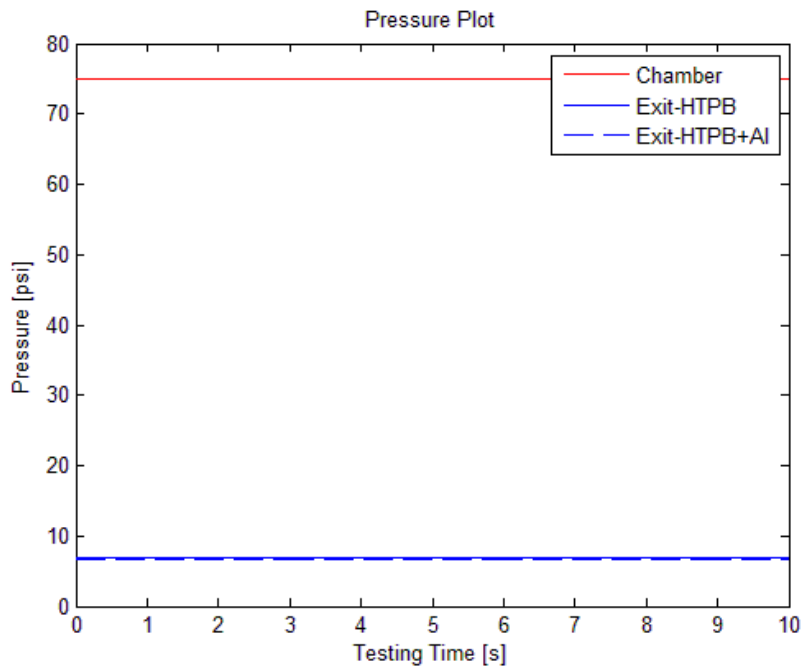


Figure B.1. Pressure of the combustion chamber and exit areas for HTPB and HTPB+Al vs time.

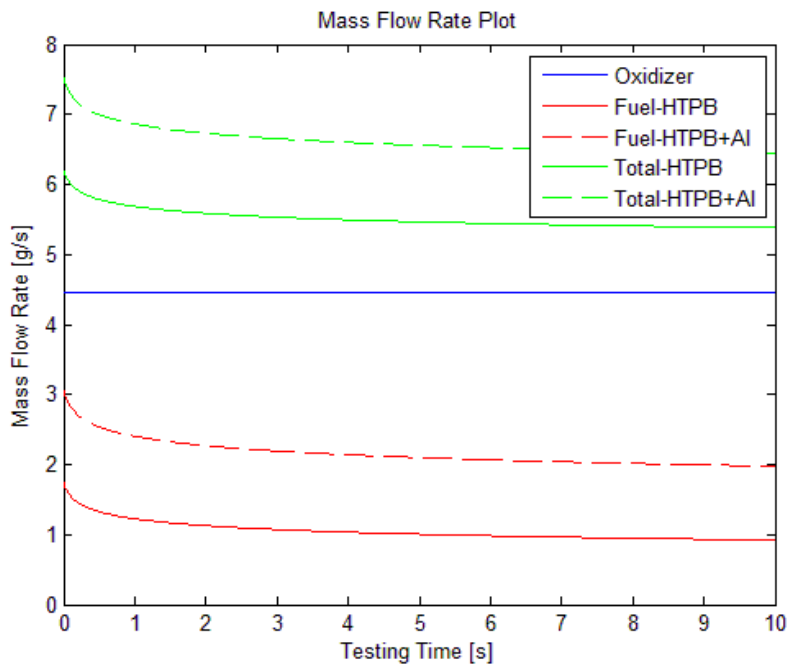


Figure B.2. Mass flow rates of different species vs time.

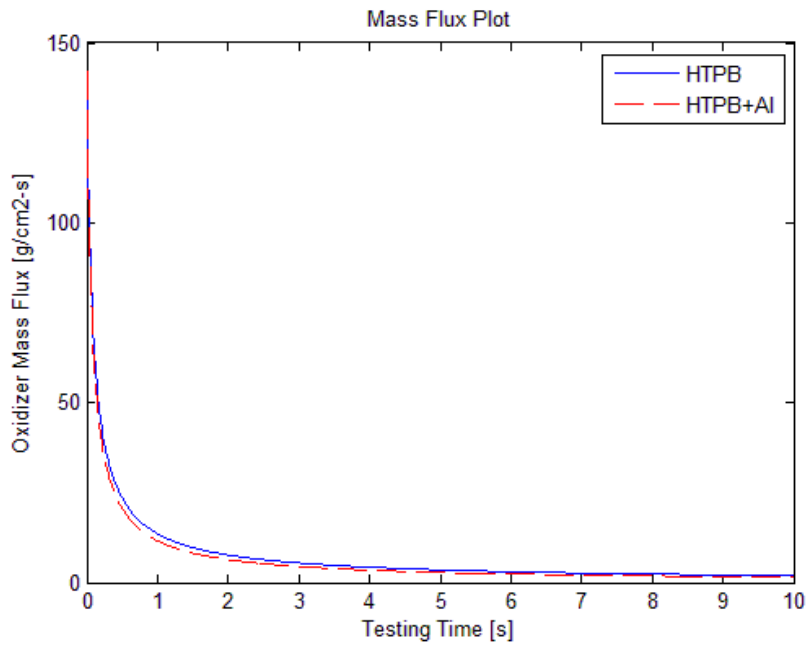


Figure B.3. Oxidizer mass flux for HTPB and HTPB+Al vs time.

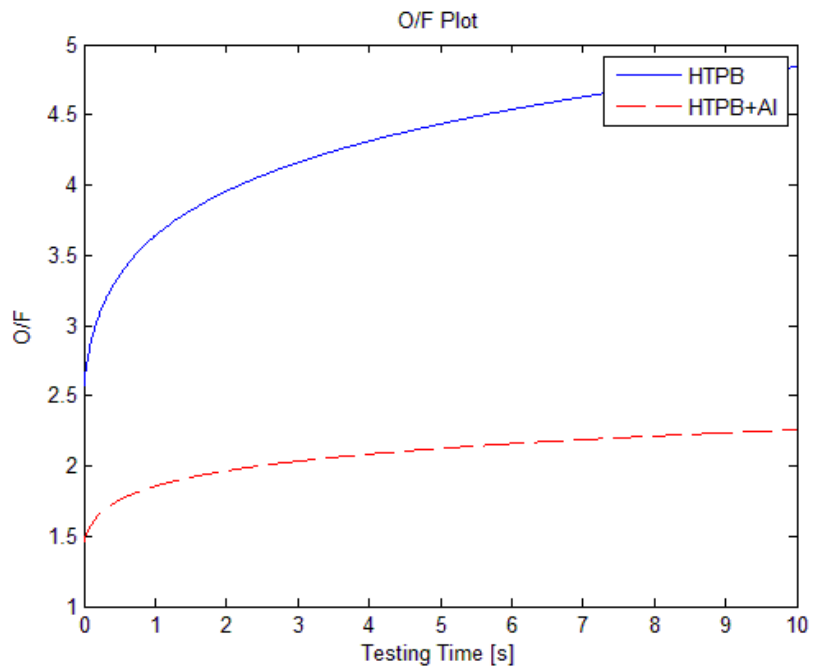


Figure B.4. Oxidizer fuel ratio for HTPB and HTPB+Al vs time.

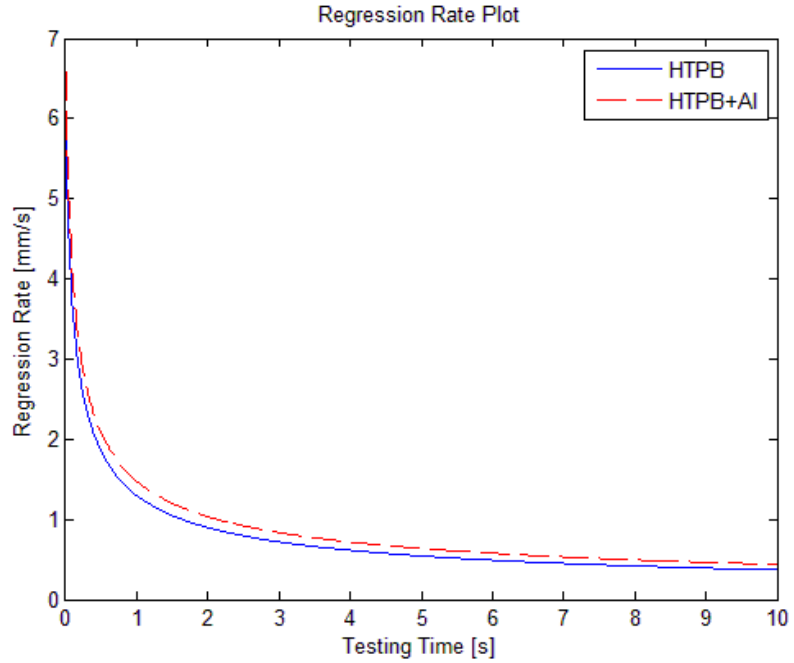


Figure B.5. Fuel radial regression rate for HTPB and HTPB+Al vs time.

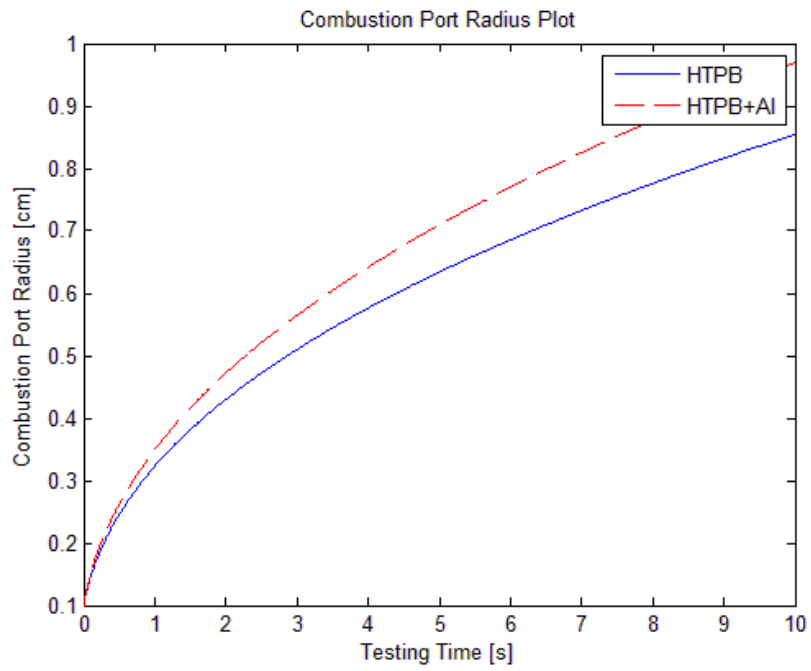


Figure B.7. Combustion port radius for HTPB and HTPB+Al vs time.

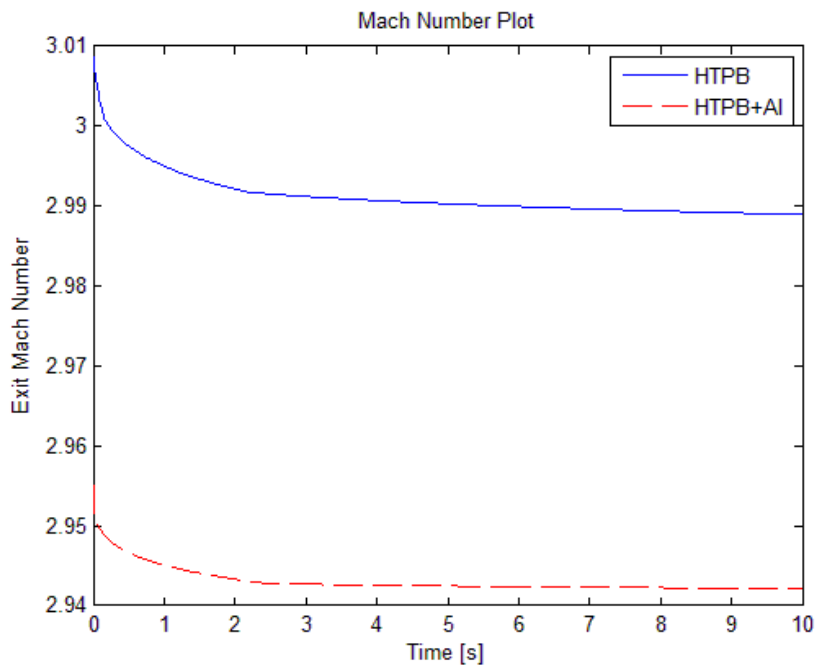


Figure B.8. Exit Mach number for HTPB and HTPB+Al vs time.

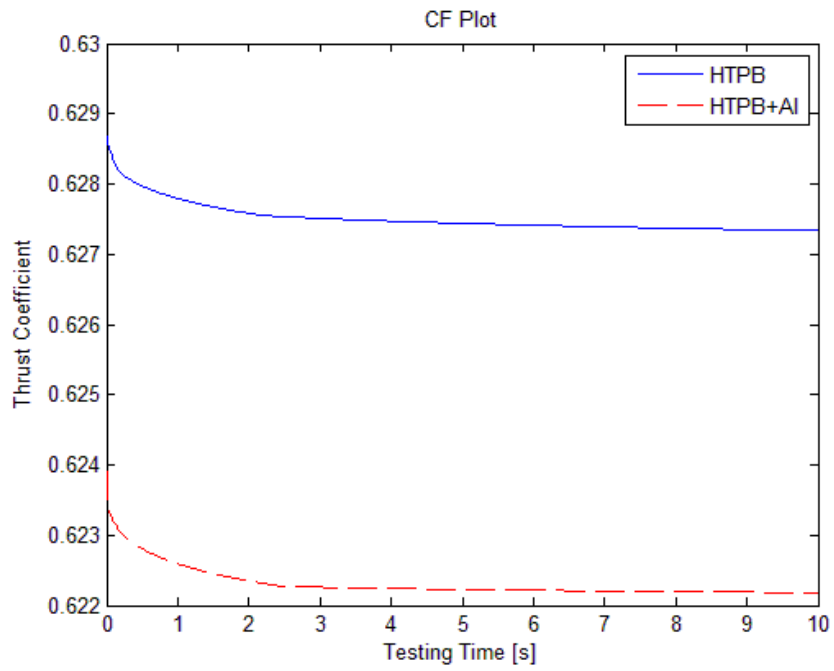


Figure B.9. Thrust coefficient for HTPB and HTPB+Al vs time.

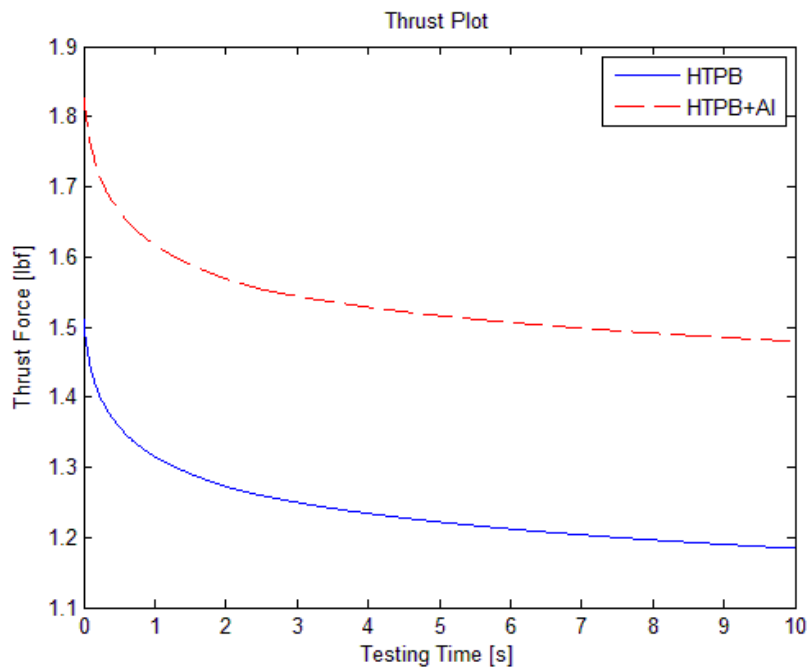


Figure B.10. Thrust force for HTPB and HTPB+Al vs time.

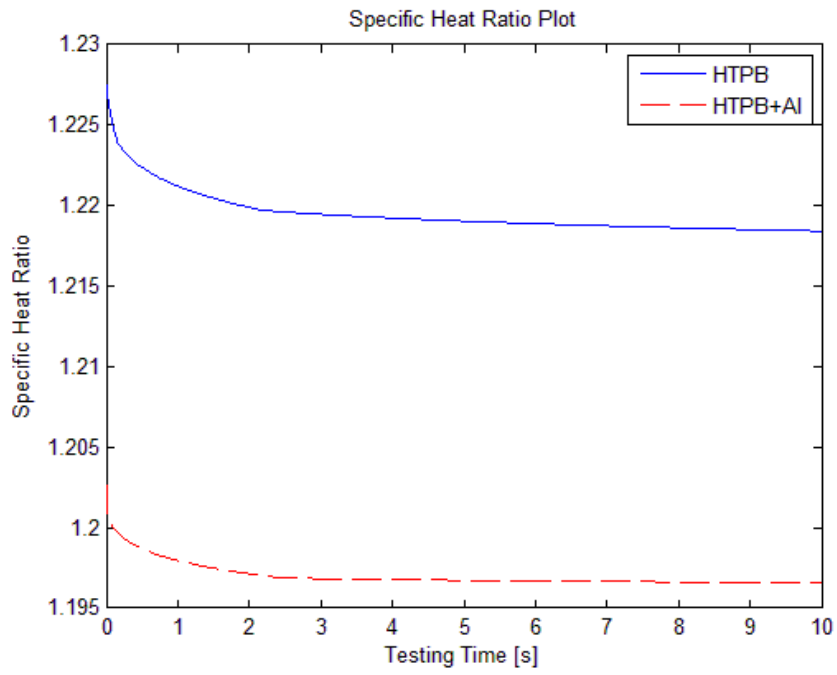


Figure B.11. Specific heat ratio for HTPB and HTPB+Al vs time.

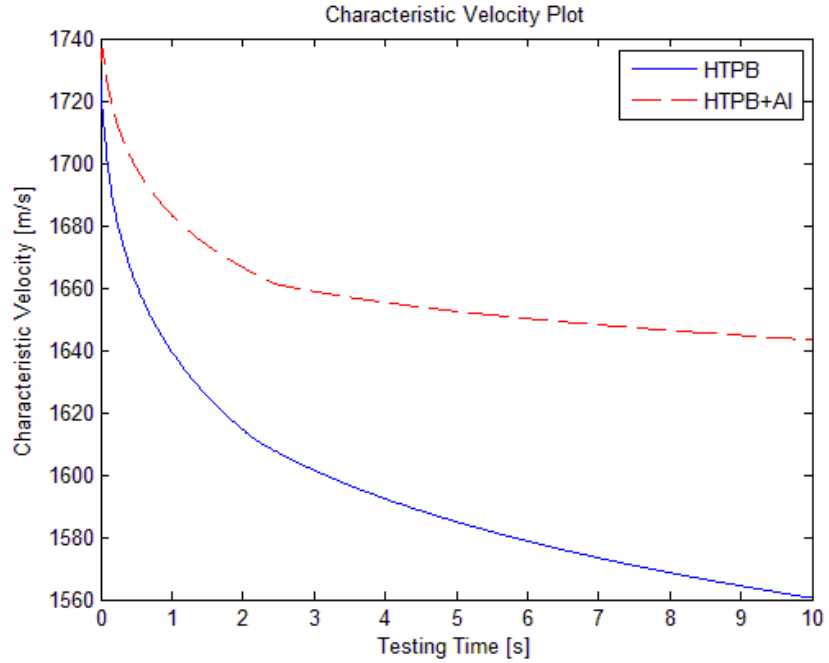


Figure B.12. Characteristic velocity for HTPB and HTPB+Al vs time.

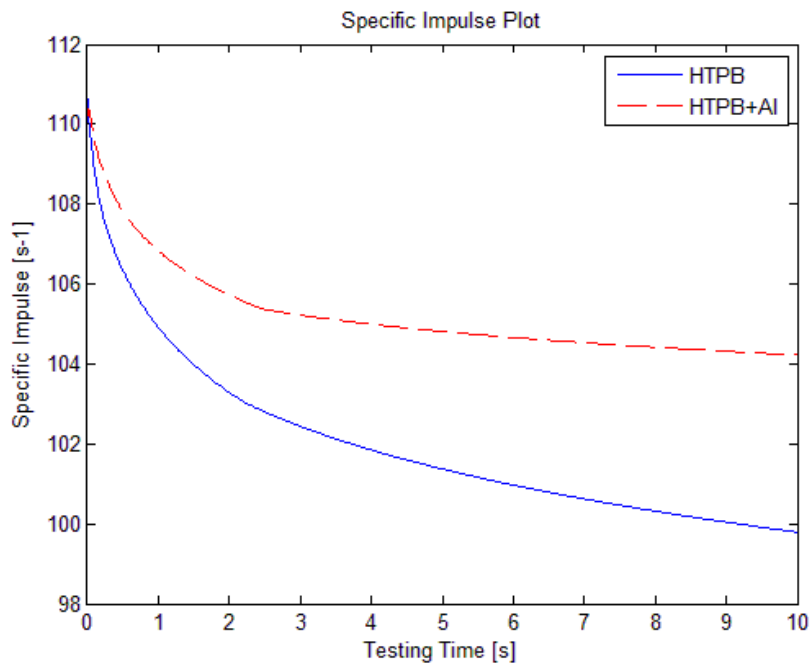


Figure B.13. Specific impulse for HTPB and HTPB+Al vs time.

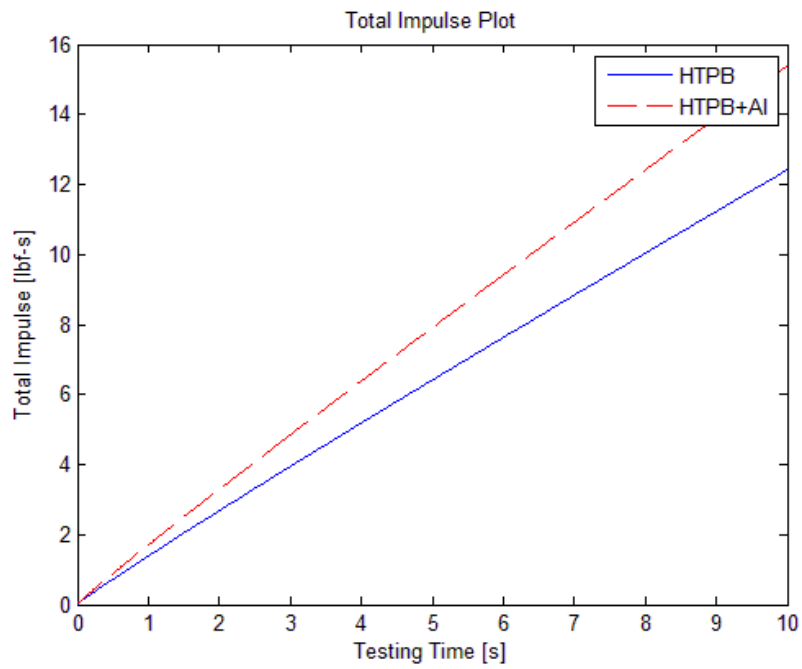


Figure B.14. Total impulse for HTPB and HTPB+Al vs time.

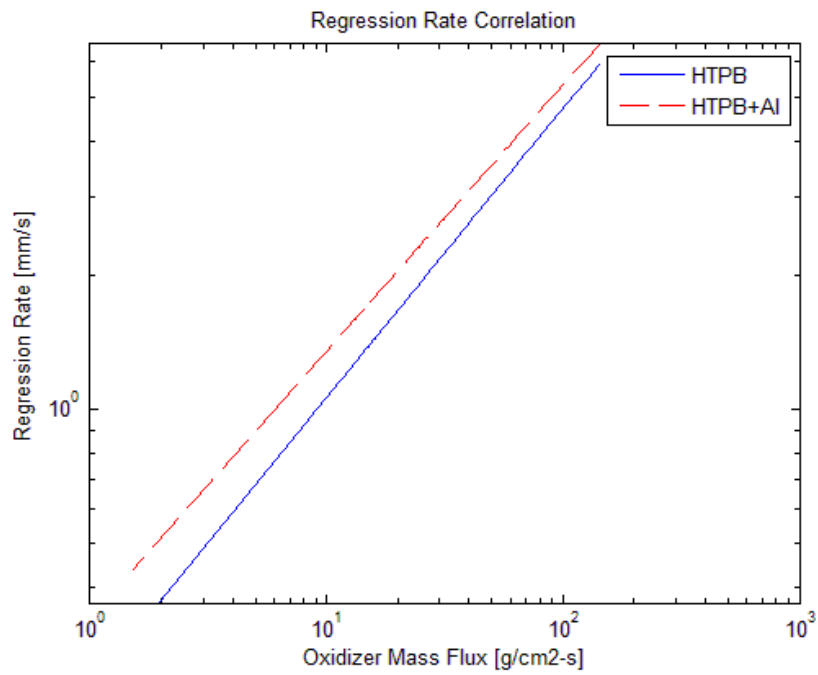


Figure B.15. Radial regression rate for HTPB and HTPB+Al vs oxidizer mass flux.

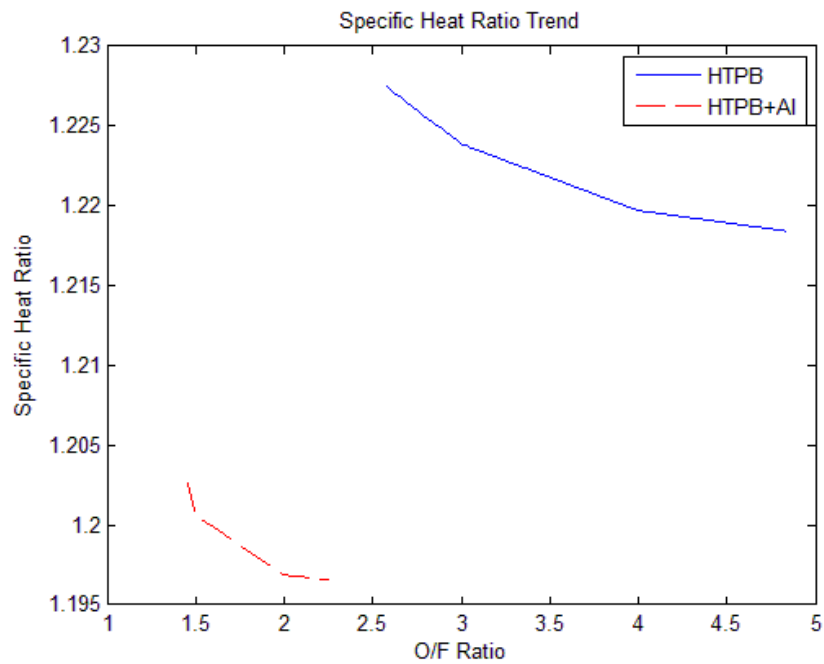


Figure B.16. Specific heat ratio for HTPB and HTPB+Al vs oxidizer fuel ratio.

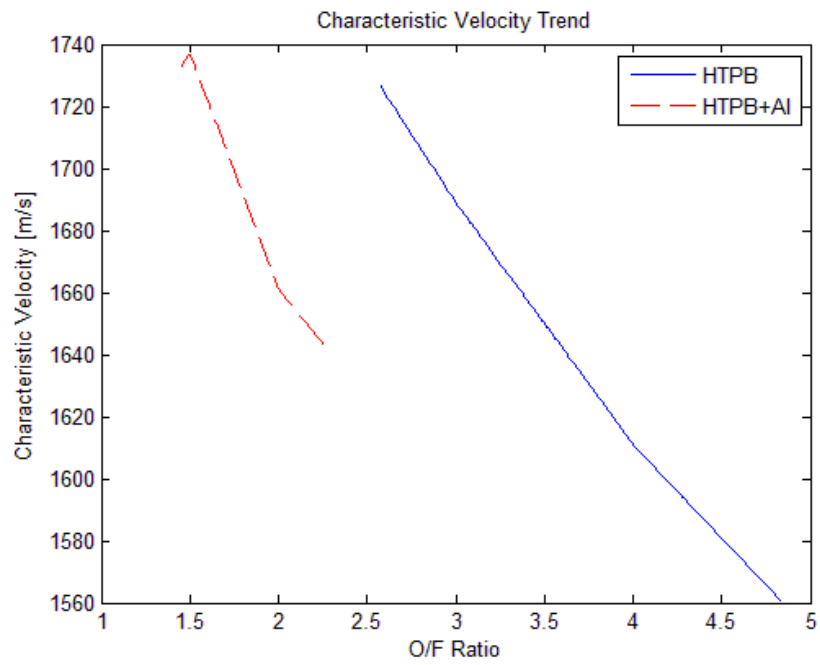


Figure B.17. Characteristic velocity for HTPB and HTPB+Al vs oxidizer fuel ratio.

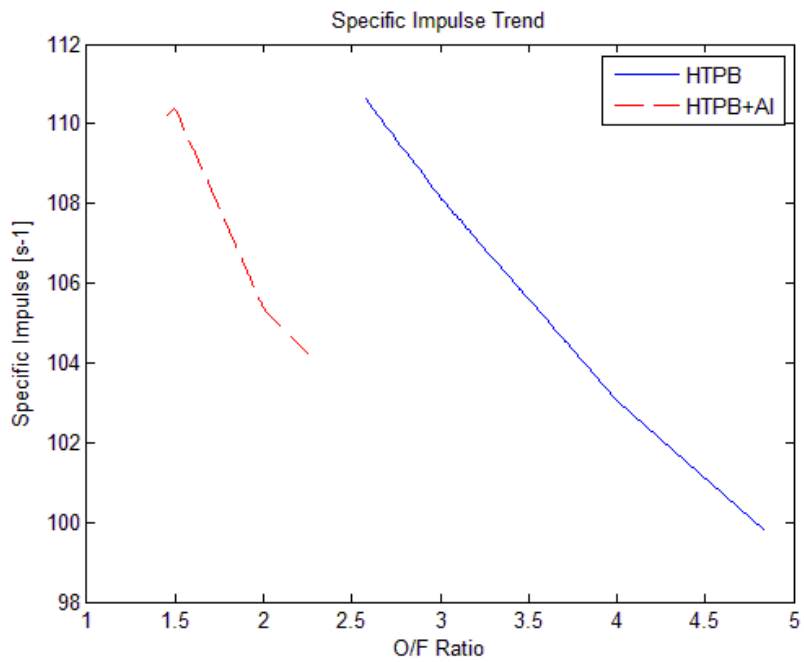


Figure B.18. Specific impulse for HTPB and HTPB+Al vs oxidizer fuel ratio

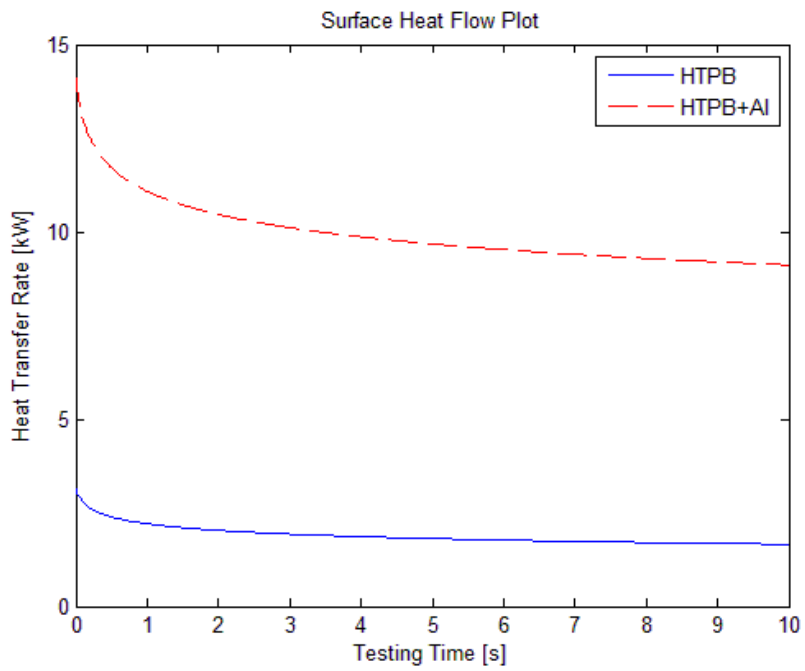


Figure B.19. Surface heat transfer rate for HTPB and HTPB+Al vs time.

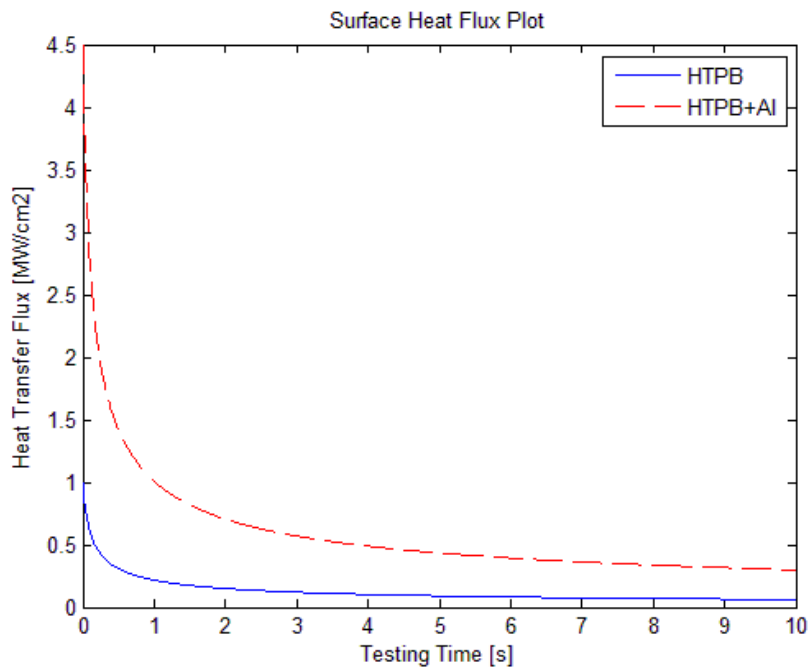


Figure B.20. Surface heat transfer flux for HTPB and HTPB+Al vs time.

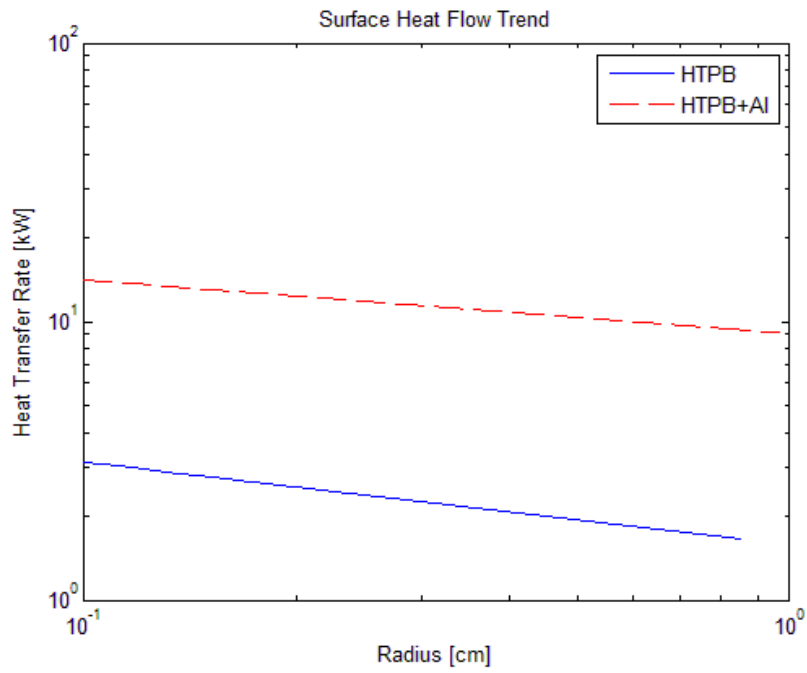


Figure B.21. Surface heat transfer rate for HTPB and HTPB+Al vs radius.

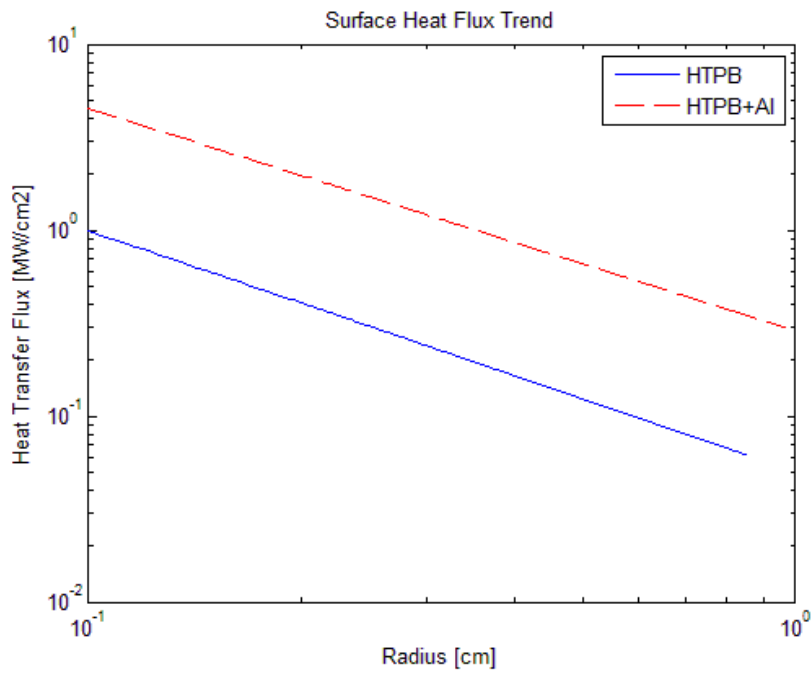


Figure B.22. Surface heat transfer flux for HTPB and HTPB+Al vs radius.

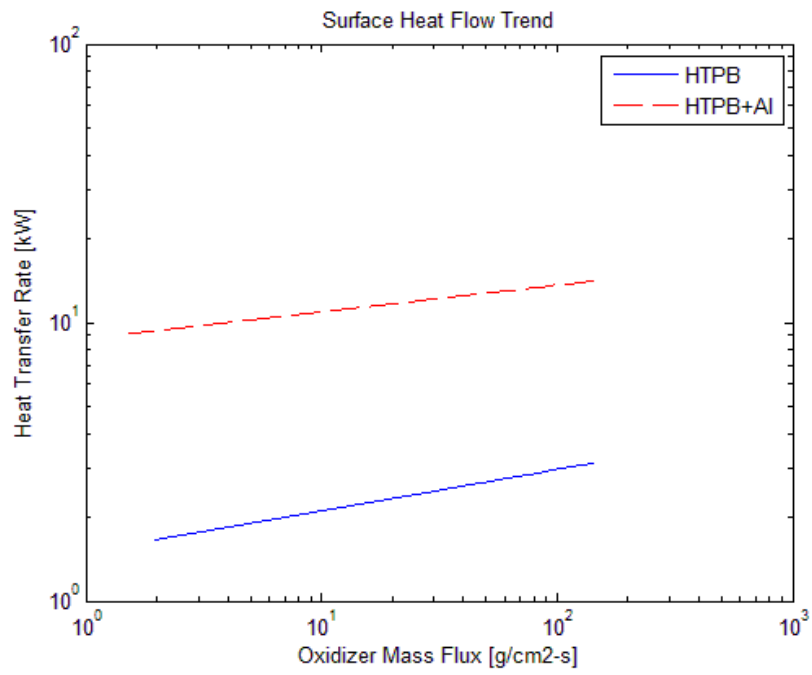


Figure B.23. Surface heat transfer rate for HTPB and HTPB+Al vs oxidizer mass flux.

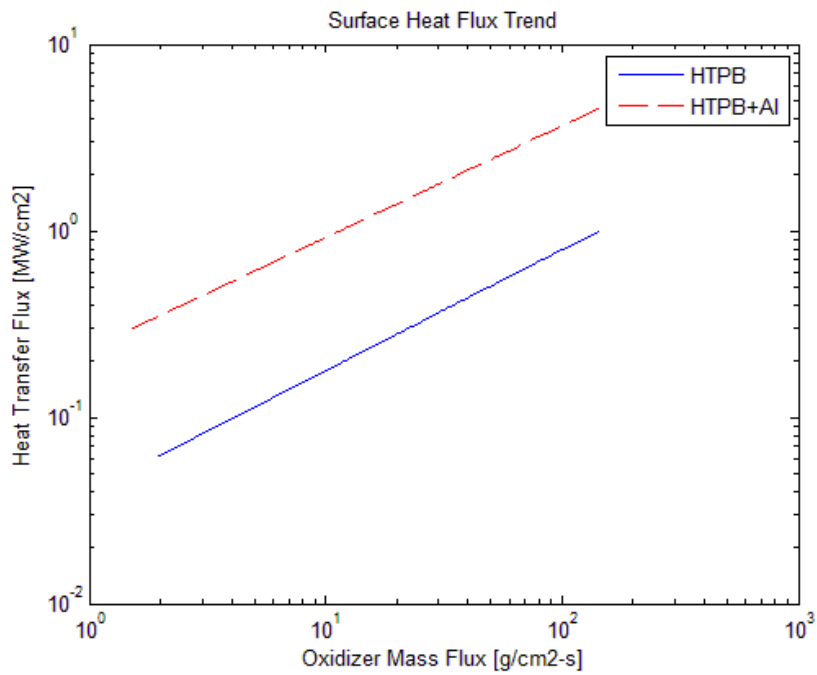


Figure B.24. Surface heat transfer flux for HTPB and HTPB+Al vs oxidizer mass flux.

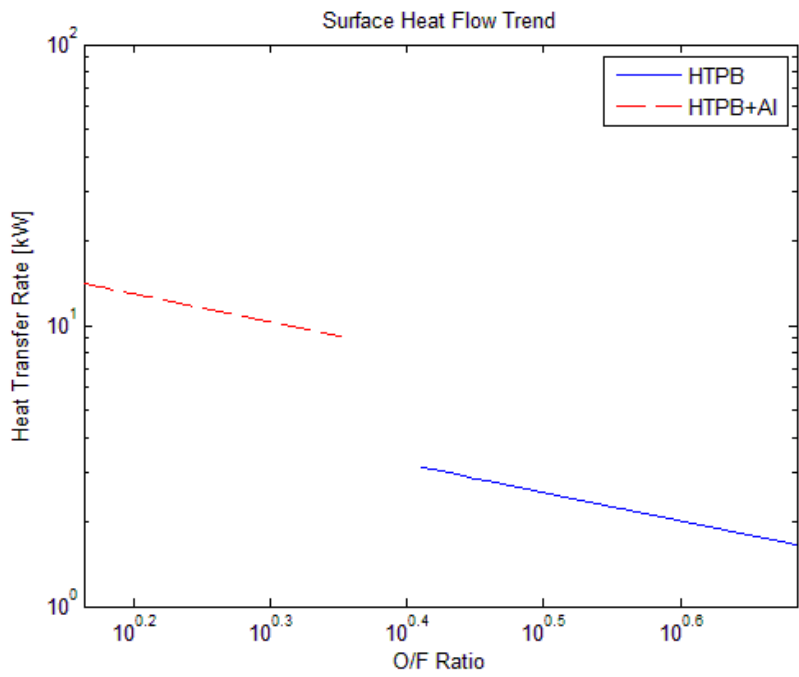


Figure B.25. Surface heat transfer rate for HTPB and HTPB+Al vs oxidizer fuel ratio.

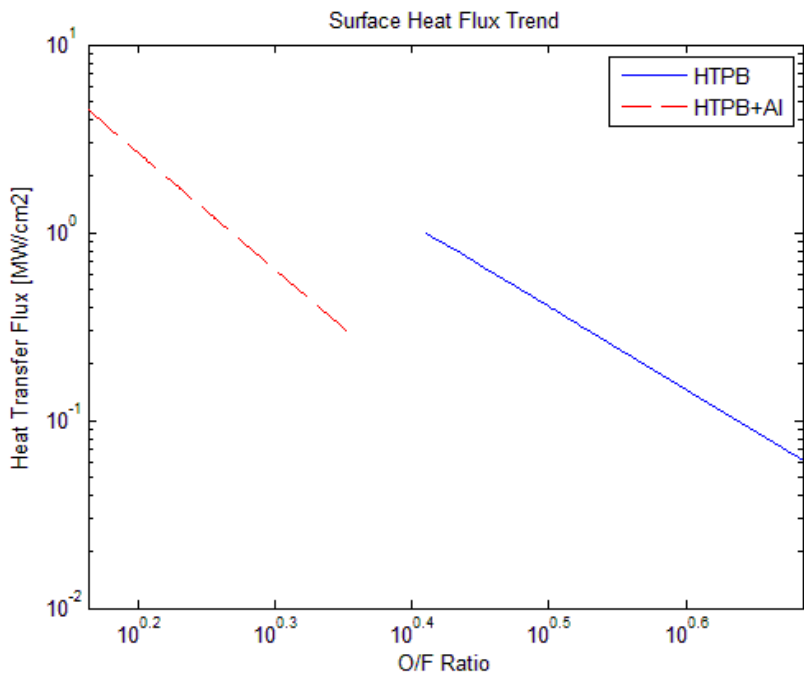


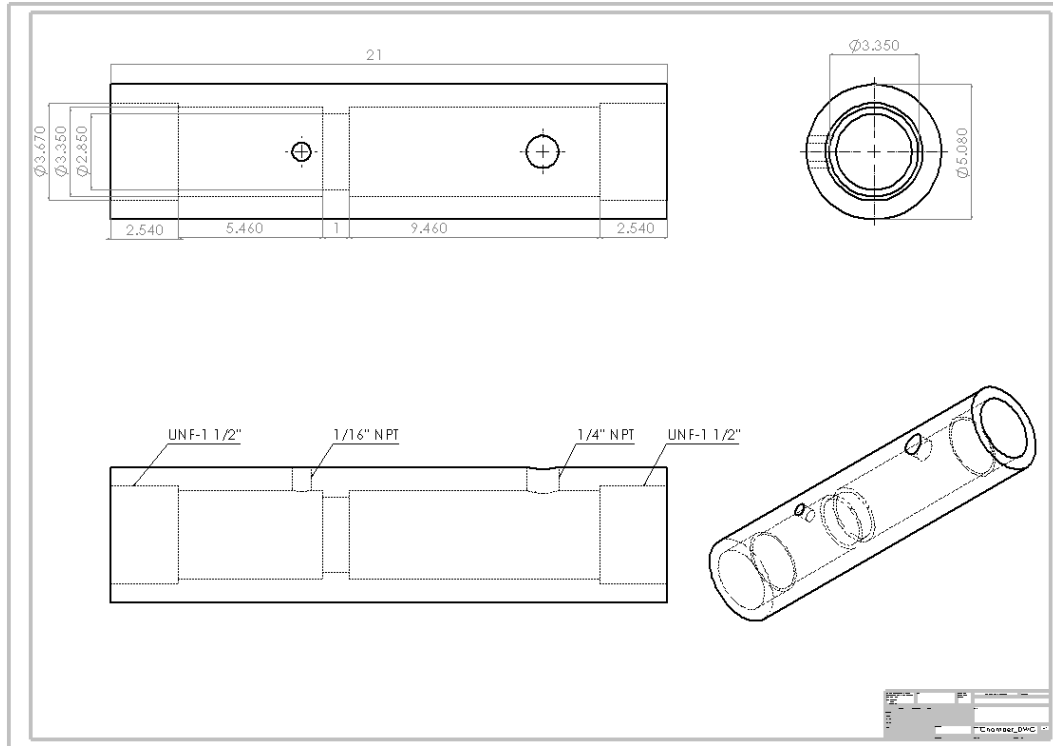
Figure B.26. Surface heat transfer flux for HTPB and HTPB+Al vs oxidizer fuel ratio.

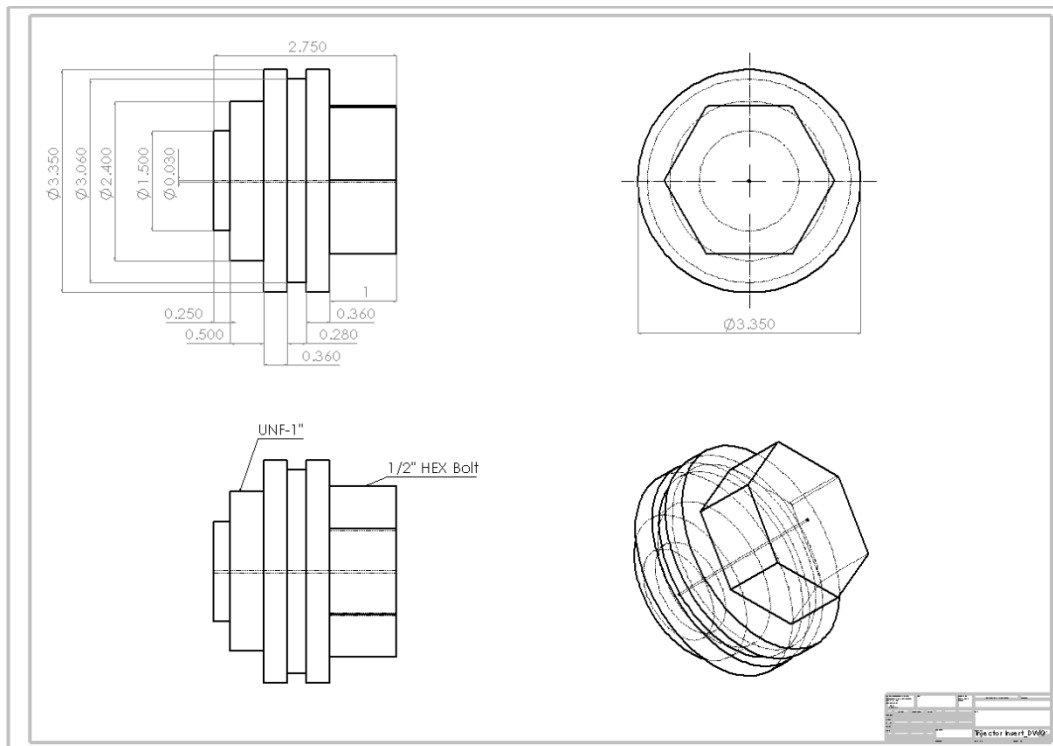
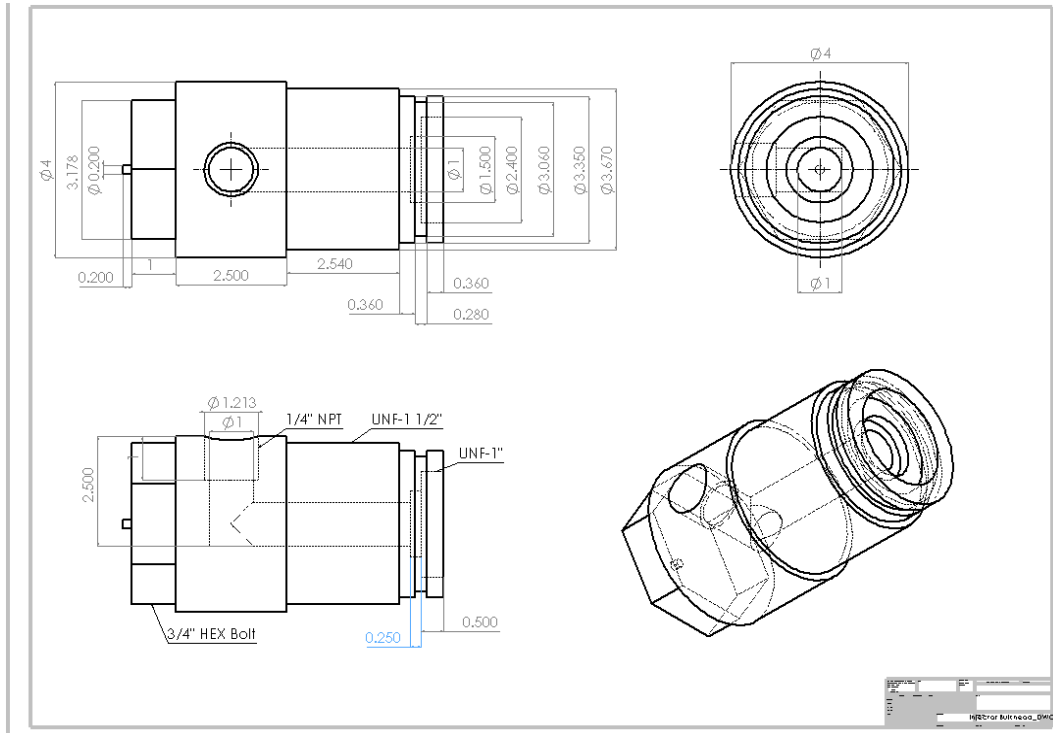
Table B.1. Summary of performance for HTPB and HTPB+Al.

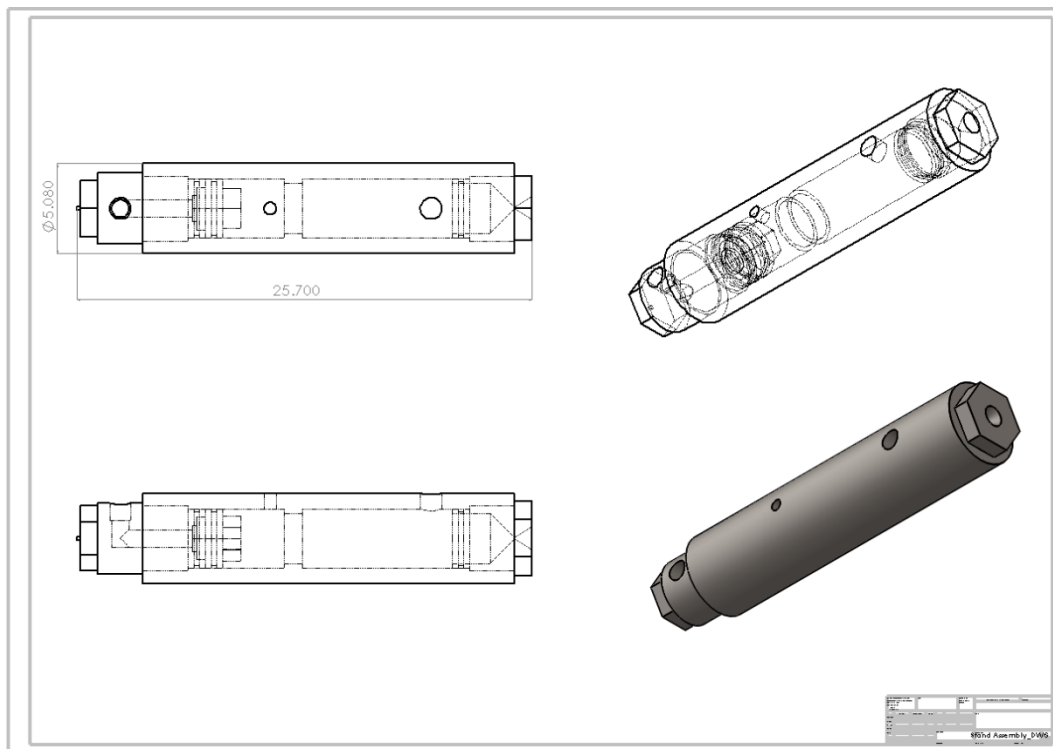
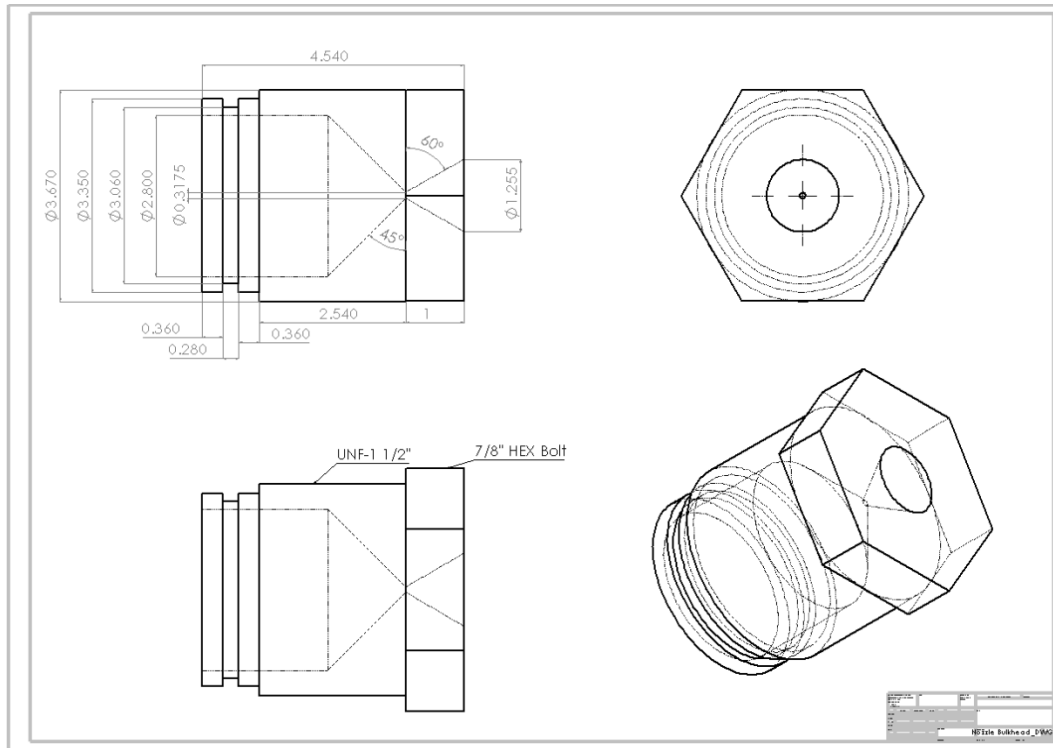
	HTPB	HTPB+Al
tb (s)	10	10
Di (cm)	0.2000	0.2000
Df (cm)	1.7085	1.9388
mdotox,avg (g/s)	4.4600	4.4600
mdotf,avg (g/s)	1.0499	2.1585
mdotsys,avg (g/s)	5.5099	6.6185
OFavg	4.3060	2.0795
Gox,avg (g/cm ² -s)	7.1826	6.1713
rb,avg (mm/s)	0.7539	0.8690
Fmax (lbf)	1.5106	1.8271
Favg (lbf)	1.2399	1.5363
Isp (s-1)	101.9839	105.2184
It (lbf-s)	12.4109	15.3779
Qmax (kW)	3.1159	14.0964
Qavg (kW)	1.8898	9.9505
Q"max (MW/cm ²)	3.1159	14.0964
Q"avg (MW/cm ²)	1.8898	9.9505

APPENDIX C

COMBUSTION CHAMBER DESIGN DRAWINGS







APPENDIX D

MEASUREMENT UNCERTAINTY ANALYSES

The measurement uncertainty of all computed parameters herein has been evaluated by the application of a Kline-McClintock (root-sum-of-squares) uncertainty analysis. [467] In general, a computed parameter, Y , is a function of N measured variables, X_i , and be written as:

$$Y = f(X_1, X_2, \dots, X_N)$$

The sensitivity of the computer parameter, δ_{Y,X_i} , to the absolute uncertainty of a single measured variable, δ_{X_i} , is given by:

$$\delta_{Y,X_i} = \frac{\partial Y}{\partial X_i} \delta_{X_i}$$

The total uncertainty in the computed parameter is the root sum of squares of all the sensitivity coefficients for each measured variable:

$$\delta_Y = \left[\sum_{i=1}^N (\delta_{Y,X_i})^2 \right]^{1/2} = \left[\sum_{i=1}^N \left(\frac{\partial Y}{\partial X_i} \delta_{X_i} \right)^2 \right]^{1/2}$$

The sensitivity coefficient and total uncertainty of all parameters computed herein are derived and given in the following sections.

D.1. Fuel Density

$$\rho_f = (D_i^2 - D_p^2)^{-1} \left[\frac{4m_T}{\pi L_f} - \rho_{PVC} (D_o^2 - D_i^2) \right]$$

$$\frac{\partial \rho_f}{\partial D_i} = -2D_i (D_i^2 - D_p^2)^{-2} \left[\frac{4m_T}{\pi L_f} - \rho_{PVC} (D_p^2 - D_o^2) \right]$$

$$\frac{\partial \rho_f}{\partial D_p} = -2D_p(D_i^2 - D_p^2)^{-2} \left[\frac{4m_T}{\pi L_f} - \rho_{PVC}(D_o^2 - D_i^2) \right]$$

$$\frac{\partial \rho_f}{\partial D_o} = -2(D_i^2 - D_p^2)^{-1} \rho_{PVC} D_o^2$$

$$\frac{\partial \rho_f}{\partial m_T} = \frac{4}{\pi L_f} (D_i^2 - D_p^2)^{-1}$$

$$\frac{\partial \rho_f}{\partial L_f} = -\frac{4m_T}{\pi L_f^2} (D_i^2 - D_p^2)^{-1}$$

$$\frac{\partial \rho_f}{\partial \rho_{PVC}} = -(D_i^2 - D_p^2)^{-1} (D_o^2 - D_i^2)$$

D.2. Final Combustion Port Diameter

$$D_f = \left[\frac{4(m_i - m_f)}{\pi \rho_f L_f} + D_i^2 \right]^{1/2}$$

$$\frac{\partial D_f}{\partial m_i} = -\frac{\partial D_f}{\partial m_f} = \frac{2}{\pi \rho_f L_f} \left[\frac{4(m_i - m_f)}{\pi \rho_f L_f} + D_i^2 \right]^{-1/2}$$

$$\frac{\partial D_f}{\partial \rho_f} = \frac{-2(m_i - m_f)}{\pi \rho_f^2 L_f} \left[\frac{4(m_i - m_f)}{\pi \rho_f L_f} + D_i^2 \right]^{-1/2}$$

$$\frac{\partial D_f}{\partial L_f} = \frac{-2(m_i - m_f)}{\pi \rho_f L_f^2} \left[\frac{4(m_i - m_f)}{\pi \rho_f L_f} + D_i^2 \right]^{-1/2}$$

$$\frac{\partial D_f}{\partial D_i} = D_i \left[\frac{4(m_i - m_f)}{\pi \rho_f L_f} + D_i^2 \right]^{-1/2}$$

$$\delta_{D_f} = D_f^{-1} \left\{ \left(\frac{2}{\pi \rho_f L_f} \right)^2 \left[\delta_{m_i}^2 + \delta_{m_f}^2 + (m_i - m_f)^2 \left[\left(\frac{\delta_{\rho_f}}{\rho_f} \right)^2 + \left(\frac{\delta_{L_f}}{L_f} \right)^2 \right] \right] + (D_i \delta_{D_i})^2 \right\}^{1/2}$$

D.3. Regression Rate

$$\bar{r} = \frac{D_f - D_i}{2t_b}$$

$$\frac{\partial \bar{r}}{\partial D_f} = \frac{1}{2t_b}$$

$$\frac{\partial \bar{r}}{\partial D_i} = -\frac{1}{2t_b}$$

$$\frac{\partial \bar{r}}{\partial t_b} = -\frac{D_f - D_i}{2t_b^2}$$

$$\delta_{\bar{r}} = \left(\frac{1}{2t_b}\right) \left\{ \delta_{D_f}^2 + \delta_{D_i}^2 + \left[\left(\frac{D_f - D_i}{t_b}\right) \delta_{t_b} \right]^2 \right\}^{1/2}$$

D.4. Oxidizer Mass Flux

$$\bar{G}_{ox} = \frac{16\bar{m}_{ox}}{\pi(D_i + D_f)^2}$$

$$\frac{\partial \bar{G}_{ox}}{\partial \bar{m}_{ox}} = \frac{16}{\pi(D_i + D_f)^2}$$

$$\frac{\partial \bar{G}_{ox}}{\partial D_i} = \frac{\partial \bar{G}_{ox}}{\partial D_f} = -\frac{32\bar{m}_{ox}}{\pi(D_i + D_f)^3}$$

$$\delta_{\bar{G}_{ox}} = \bar{G}_{ox} \left\{ \left(\frac{\delta_{\bar{m}_{ox}}}{\bar{m}_{ox}}\right)^2 + 2(\delta_{D_i}^2 + \delta_{D_f}^2) \right\}^{1/2}$$

D.5. Fuel Mass Loss Rate

$$\frac{\bar{m}_f}{L_f} = \frac{\pi\rho_f}{2}(D_i + D_f)\bar{r}$$

$$\frac{\partial(\bar{m}_f/L_f)}{\partial \rho_f} = \frac{\pi}{2}(D_i + D_f)\bar{r}$$

$$\frac{\partial(\bar{m}_f/L_f)}{\partial D_i} = \frac{\partial(\bar{m}_f/L_f)}{\partial D_f} = \frac{\pi\rho_f}{2}\bar{r}$$

$$\frac{\partial(\bar{m}_f/L_f)}{\partial \bar{r}} = \frac{\pi\rho_f}{2}(D_i + D_f)$$

$$\delta_{\bar{m}_f/L_f} = \left(\frac{\bar{m}_f}{L_f}\right) \left\{ \left(\frac{\delta_{\rho_f}}{\rho_f}\right)^2 + \left(\frac{\delta_{\bar{r}}}{\bar{r}}\right)^2 + \frac{\delta_{D_i}^2 + \delta_{D_f}^2}{(D_i + D_f)^2} \right\}^{1/2}$$

D.6. Fuel Mass Loss Rate (Alternative)

$$\frac{\bar{m}_f}{L_f} = \frac{(m_i - m_f)}{t_b L_f}$$

$$\frac{\partial(\bar{m}_f/L_f)}{\partial m_i} = -\frac{\partial(\bar{m}_f/L_f)}{\partial m_f} = \frac{1}{t_b L_f}$$

$$\frac{\partial(\bar{m}_f/L_f)}{\partial t_b} = -\frac{(m_i - m_f)}{t_b^2 L_f}$$

$$\frac{\partial(\bar{m}_f/L_f)}{\partial L_f} = \frac{(m_i - m_f)}{t_b L_f^2}$$

$$\delta_{\bar{m}_f/L_f} = \left(\frac{\bar{m}_f}{L_f}\right) \left[\frac{\delta_{m_i}^2 + \delta_{m_f}^2}{(m_i - m_f)^2} + \left(\frac{\delta_{t_b}}{t_b}\right)^2 + \left(\frac{\delta_{L_f}}{L_f}\right)^2 \right]^{1/2}$$

D.7. Oxidizer-to-Fuel Ratio

$$\frac{O}{F} = \frac{\bar{m}_{ox}}{\bar{m}_f} = \frac{\bar{m}_{ox}}{(\bar{m}_f/L_f)L_f}$$

$$\frac{\partial(O/F)}{\partial \bar{m}_{ox}} = \frac{1}{(\bar{m}_f/L_f)L_f}$$

$$\frac{\partial(O/F)}{\partial(\bar{m}_f/L_f)} = \frac{\bar{m}_{ox}}{(\bar{m}_f/L_f)^2 L_f}$$

$$\frac{\partial(O/F)}{\partial L_f} = \frac{\bar{m}_{ox}}{(\bar{m}_f/L_f)L_f^2}$$

$$\delta_{O/F} = \frac{o}{F} \left\{ \left(\frac{\delta \bar{m}_{ox}}{\bar{m}_{ox}} \right)^2 + \left[\frac{\delta(\bar{m}_f/L_f)}{(\bar{m}_f/L_f)} \right]^2 + \left(\frac{\delta L_f}{L_f} \right)^2 \right\}^{1/2}$$

D.8. Characteristic Velocity

$$\bar{c}^* = \frac{\bar{P}_c A_t}{\bar{m}_{ox} + (\bar{m}_f/L_f)L_f}$$

$$\frac{\partial \bar{c}^*}{\partial \bar{P}_c} = \frac{A_t}{\bar{m}_{ox} + (\bar{m}_f/L_f)L_f}$$

$$\frac{\partial \bar{c}^*}{\partial A_t} = \frac{\bar{P}_c}{\bar{m}_{ox} + (\bar{m}_f/L_f)L_f}$$

$$\frac{\partial \bar{c}^*}{\partial \bar{m}_{ox}} = \left[\frac{1}{\bar{m}_{ox} + (\bar{m}_f/L_f)L_f} \right] \frac{\bar{P}_c A_t}{\bar{m}_{ox} + (\bar{m}_f/L_f)L_f}$$

$$\frac{\partial \bar{c}^*}{\partial (\bar{m}_f/L_f)} = \left[\frac{L_f}{\bar{m}_{ox} + (\bar{m}_f/L_f)L_f} \right] \frac{\bar{P}_c A_t}{\bar{m}_{ox} + (\bar{m}_f/L_f)L_f}$$

$$\frac{\partial \bar{c}^*}{\partial L_f} = \left[\frac{(\bar{m}_f/L_f)}{\bar{m}_{ox} + (\bar{m}_f/L_f)L_f} \right] \frac{\bar{P}_c A_t}{\bar{m}_{ox} + (\bar{m}_f/L_f)L_f}$$

$$\delta_{\bar{c}^*} = \bar{c}^* \left\{ \left(\frac{\delta \bar{P}_c}{\bar{P}_c} \right)^2 + \left(\frac{\delta A_t}{A_t} \right)^2 + \left[\frac{1}{\bar{m}_{ox} + (\bar{m}_f/L_f)L_f} \right]^2 \left[\delta_{\bar{m}_{ox}}^2 + (L_f \delta_{(\bar{m}_f/L_f)})^2 + [(\bar{m}_f/L_f) \delta_{L_f}]^2 \right] \right\}^{1/2}$$

D.9. Combustion Efficiency

$$n_{c^*} = \frac{\bar{c}^*}{c_{th}^*}$$

$$\frac{\partial n_{c^*}}{\partial \bar{c}^*} = \frac{1}{c_{th}^*}$$

$$\frac{\partial n_{c^*}}{\partial c_{th}^*} = -\frac{\bar{c}^*}{(c_{th}^*)^2}$$

$$\delta_{n_{c^*}} = n_{c^*} \left[\left(\frac{\delta_{\bar{c}^*}}{\bar{c}^*} \right)^2 + \left(\frac{\delta_{c_{th}^*}}{c_{th}^*} \right)^2 \right]^{1/2}$$

APPENDIX E

THESIS PRESENTATION

**Mixed HTPB/Paraffin Fuels and Metallic Additives
for Hybrid Rocket Applications**

James Chris Thomas

Department of Mechanical Engineering
Texas A&M University



Ph.D. Defense

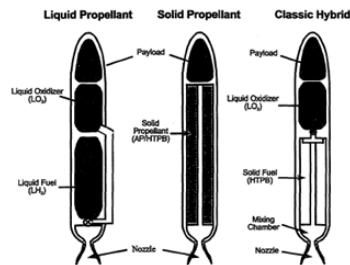
October 16, 2018

College Station, TX

Introduction



Hybrid rockets have advantages and disadvantages



Advantages

- Safer to fabricate, store, and transport
- High controllability
- Smooth thrust transition capability
- **High specific impulse and density specific impulse**
- Mechanically simpler than liquid propellant systems

Disadvantages

- Complicated internal motor ballistics
- Variation in O/F ratio
- Pressure instabilities
- Fuel residuals
- **Comparatively low combustion efficiencies**
- **Low solid fuel regression rates**

Introduction



Many methods have been explored for enhancement

- Non-Traditional Oxidizers and Fuels
 - Dense, High-Energy Oxidizers (HAN, H_2O_2)
 - **Paraffin Fuels**
- Energetic Additives
 - Oxidizers
 - **Metals**
 - Metal Hydrides
 - Metal Borides
 - Boron Carbide
 - Advanced Synthesis Additives
- Port Geometry Augmentation
 - High Burn Surface Areas
 - Additive Manufacturing
- Oxidizer Flow Manipulation
 - Swirl Flow
 - Bluff Bodies
 - Diaphragms
- Unconventional Geometries
 - End-Burning Hybrids
 - Pancake Hybrids

Introduction – Metal Fuels



Metal addition yields several potential benefits

Potential Benefits:

- Improved energy density
- Increased regression rate and fuel mass flow

Literature Summary:

- Achieved performance depends on additive:
 - Size
 - Geometry
 - Composition
 - Surface Chemistry
 - Concentration
 - Oxidizer/Fuel Combination
- Increased additive loadings yield diminished performance
 - Regression Rate
 - Combustion Efficiency
- Majority of studies completed on aluminum or boron
 - Increased radiation heat transfer and near-surface heat release

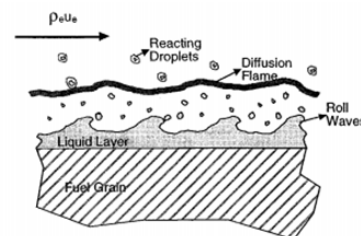
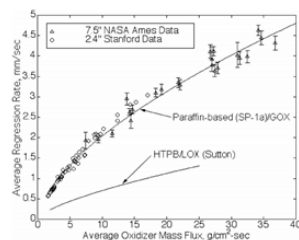
4

Introduction – Paraffin Wax Fuels



Paraffin waxes yield mass *entrainment* mechanism

- Carrick and Larson (AFRL) and Orbitec evaluated high-regression cryogenic fuels ($\Delta r=1000\%$ for ethylene)
- Karabeyoglu et al. (Stanford) evaluated paraffin waxes ($\Delta r=300\%$)
 - Enhancement Mechanisms:
 - Entrainment Mass Transfer
 - Reduced $(h_{fl} - h_w)$, $\Delta H_{v,eff}$
 - Increased \dot{Q} from reduced blocking and increased surface roughness



5

Images from Karabeyoglu et al., 2001 and Karabeyoglu et al., 2004

Project Objectives



- 1) Develop lab-scale hybrid rocket testing capabilities at Texas A&M University
- 2) Determine the relative effects of pure metal type and loading on the combustion of HTPB/GOX systems
- 3) Assess the synergistic performance benefits of bi-metallic fuel formulations in comparison plain boron
- 4) Evaluate mixed HTPB/paraffin fuel systems for hybrid rocket applications

6

Theoretical Performance Analyses

7

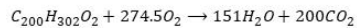
Stoichiometric Combustion



Metal addition can improve *volumetric energy density*

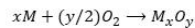
Stoichiometric Combustion

- HTPB

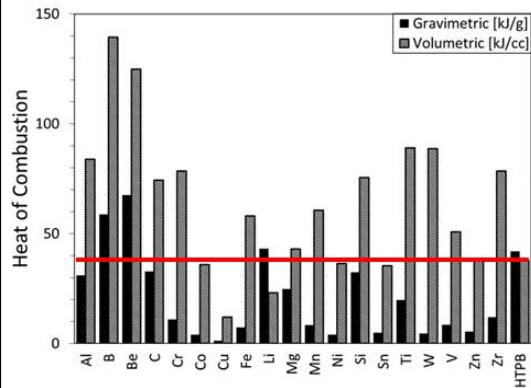


$$\Delta H_c^0 = (\bar{h}_{f,C_{200}H_{302}O_2}^0 + 274.5\bar{h}_{f,O_2}^0) - (151\bar{h}_{f,H_2O}^0 + 200\bar{h}_{f,CO_2}^0)$$

- Metals



$$\Delta H_c^0 = -(1/x)\bar{h}_{f,M_xO_y}^0$$

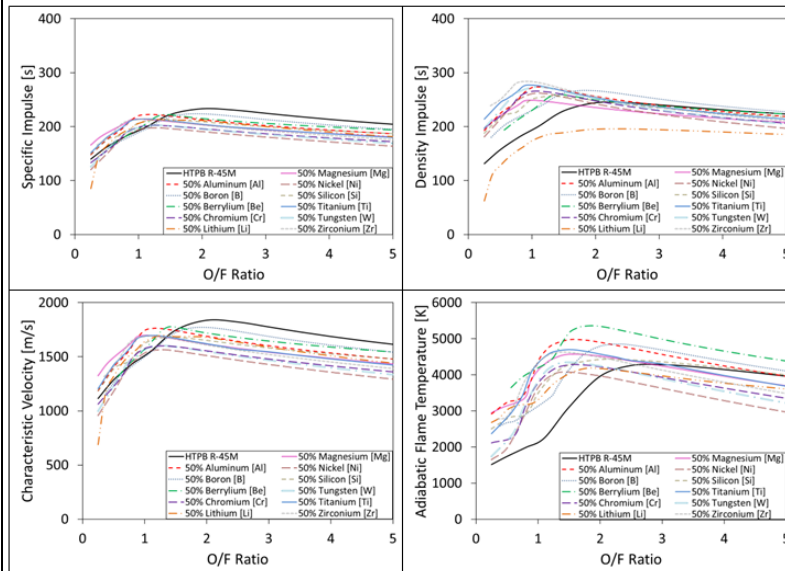


8

Chemical Equilibrium Analysis



Metal addition can *improve performance*



Metal Benefits:

- Density Impulse
- Flame Temperature
- O/F Shift

$I_{sp,v}$ Rankings:

- Zirconium [Zr]
- Titanium [Ti]
- Aluminum [Al]
- Tungsten [W]
- Boron [B]
- Chromium [Cr]
- Nickel [Ni]
- Beryllium [Be]
- Silicon [Si]
- Magnesium [Mg]

9

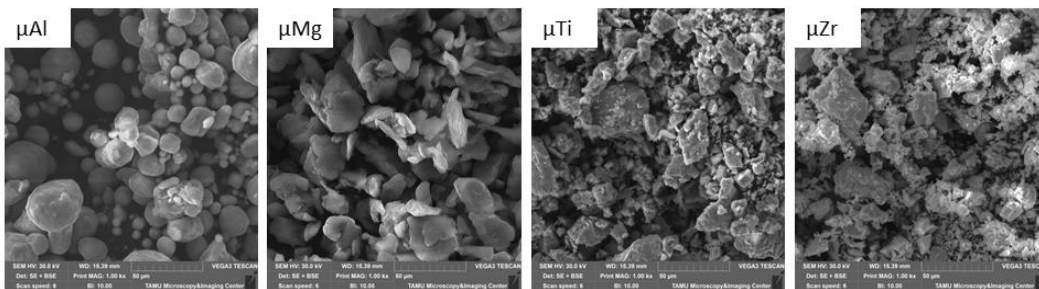
Additive Characterization

10

Additive Characterization – Micro-Metals



Micro-metals characterized with SEM



Additive	Manufacturer	ID	Size (μm)	Purity (%)	Geometry
micro-Al (μAl)	Valimet, Inc.	H-30	20-30	99.7	Spherical
nano-Al (nAl)	US Research Nanomaterials, Inc.	US-1043	0.1	99.9	Spherical
nano-B (nB)	SB Boron Corporation	SB-95	0.7	92.1-96.0	Irregular
micro-Mg (μMg)	US Research Nanomaterials, Inc.	US-1060	40	99.9	Flake
micro-Ti (μTi)	US Research Nanomaterials, Inc.	US-1038M	45	99	Irregular
micro-Zr (μZr)	US Research Nanomaterials, Inc.	US-1040M	75	99	Irregular
nano-MgB (nMgB)	Mach I Specialty Chemicals, Inc.	-	0.7	88	Irregular

11

Additive Characterization – Nano-Metals



Nano-aluminum characterized with TEM

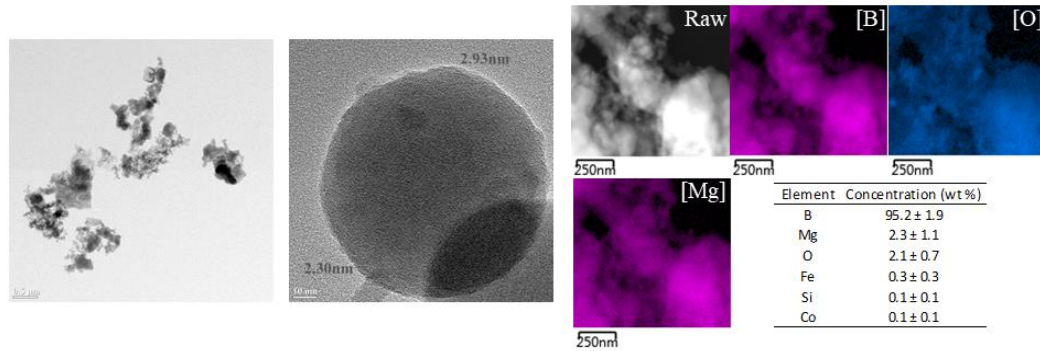


Additive	Manufacturer	ID	Size (μm)	Purity (%)	Geometry
micro-Al (μAl)	Valimet, Inc.	H-30	20-30	99.7	Spherical
nano-Al (nAl)	US Research Nanomaterials, Inc.	US-1043	0.1	99.9	Spherical
nano-B (nB)	SB Boron Corporation	SB-95	0.7	92.1-96.0	Irregular
micro-Mg (μMg)	US Research Nanomaterials, Inc.	US-1060	40	99.9	Flake
micro-Ti (μTi)	US Research Nanomaterials, Inc.	US-1038M	45	99	Irregular
micro-Zr (μZr)	US Research Nanomaterials, Inc.	US-1040M	75	99	Irregular
nano-MgB (nMgB)	Mach I Specialty Chemicals, Inc.	-	0.7	88	Irregular

Additive Characterization – Nano-Metals



Nano-boron characterized with TEM and EDS

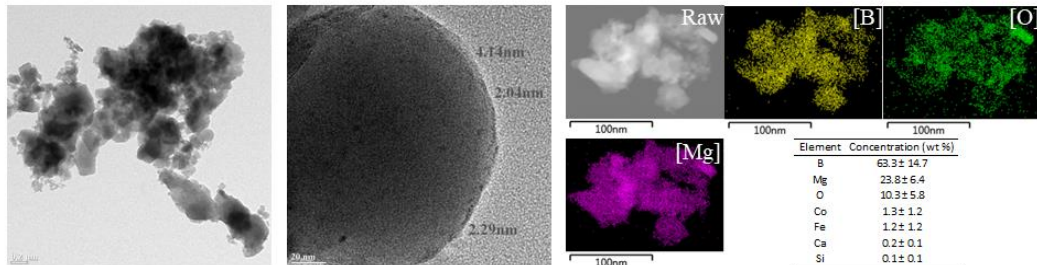


Additive	Manufacturer	ID	Size (μm)	Purity (%)	Geometry
micro-Al (μAl)	Valimet, Inc.	H-30	20-30	99.7	Spherical
nano-Al (nAl)	US Research Nanomaterials, Inc.	US-1043	0.1	99.9	Spherical
nano-B (nB)	SB Boron Corporation	SB-95	0.7	92.1-96.0	Irregular
micro-Mg (μMg)	US Research Nanomaterials, Inc.	US-1060	40	99.9	Flake
micro-Ti (μTi)	US Research Nanomaterials, Inc.	US-1038M	45	99	Irregular
micro-Zr (μZr)	US Research Nanomaterials, Inc.	US-1040M	75	99	Irregular
nano-MgB (nMgB)	Mach I Specialty Chemicals, Inc.	-	0.7	88	Irregular

Additive Characterization – Nano-Metals



Mg-coated nano-B characterized with *TEM* and *EDS*



Additive	Manufacturer	ID	Size (µm)	Purity (%)	Geometry
micro-Al (µAl)	Valimet, Inc.	H-30	20-30	99.7	Spherical
nano-Al (nAl)	US Research Nanomaterials, Inc.	US-1043	0.1	99.9	Spherical
nano-B (nB)	SB Boron Corporation	SB-95	0.7	92.1-96.0	Irregular
micro-Mg (µMg)	US Research Nanomaterials, Inc.	US-1060	40	99.9	Flake
micro-Ti (µTi)	US Research Nanomaterials, Inc.	US-1038M	45	99	Irregular
micro-Zr (µZr)	US Research Nanomaterials, Inc.	US-1040M	75	99	Irregular
nano-MgB (nMgB)	Mach I Specialty Chemicals, Inc.	-	0.7	88	Irregular

Experimental Methodology

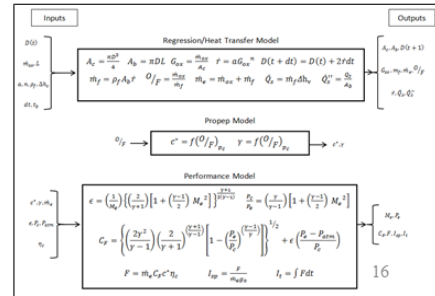
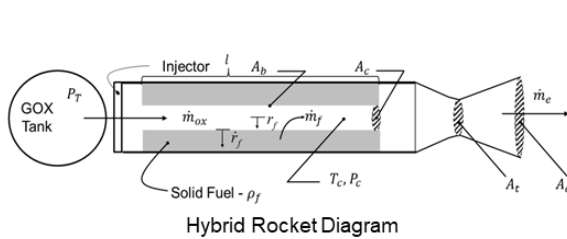
Experimental Methodology – HRE Modeling



First principles model developed to size ballistic stand

Engineering Principles:

- Oxidizer flow (ideal gas, 1D gas dynamics, choked flow)
- Fuel consumption (empirical regression, 1D geometry)
- Combustion gas properties (chemical equilibrium analysis)
- Chamber conditions (choked flow)
- Nozzle exit flow (isentropic flow)



Experimental Methodology – Ballistic Stand Sizing



Ballistic stand sized through iterative modeling

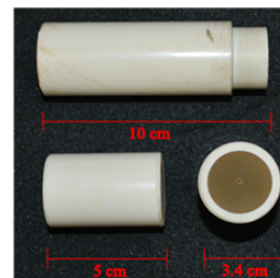
Design Goals:

- $G_{ox,max} \geq 150 \text{ kg/m}^2 - \text{s}$
- $P_c \sim 150 \text{ psia}$
- Neutral burn profiles
- Multiple burn capability
- Quick turn-around
- Small, cheap motors

Key Dimensions

Component	Size	Units
Injector Orifice Diameter	1, 2	mm
Fuel Grain Length	5-12	cm
Fuel Grain Outer Diameter	3.34	cm
Fuel Grain Inner Diameter	2-20	mm
Nozzle Diameter	2, 3.175	mm

Fuel Grains



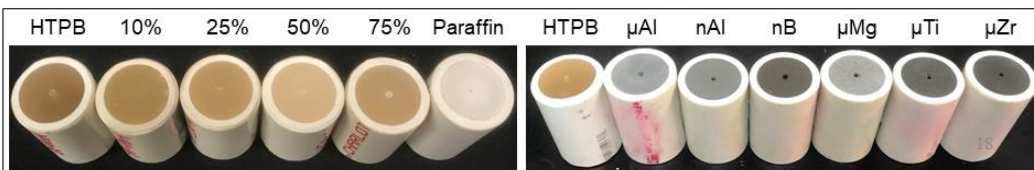
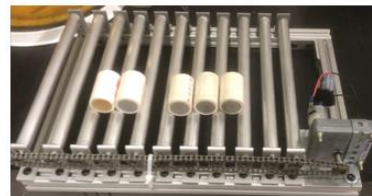
Experimental Methodology – Motor Manufacturing



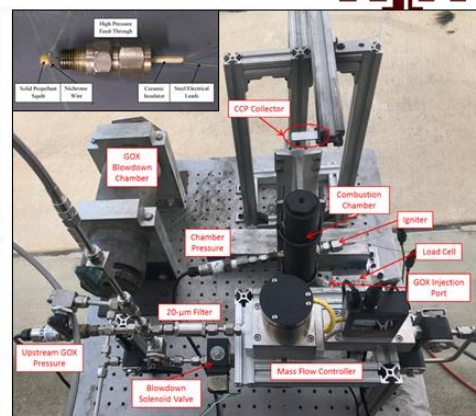
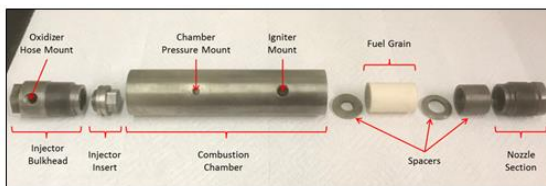
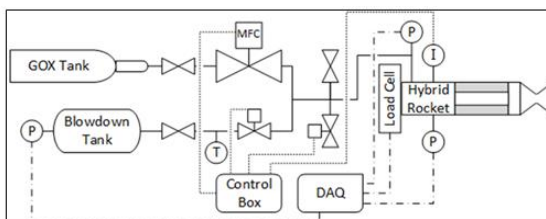
In-house fuel grain manufacturing procedures developed

Mixing/Manufacturing Procedures:

- 1) HTPB & metal additive mixed thoroughly
- 2) Fuel slurry is vacuumed
- 3) Curative (IPDI) added & mixed thoroughly
- 4) Fuel slurry is vacuumed
- 5) Fuel slurry is poured into motor mold & sealed
- 6) Mixture cures at 65 °C [1 wk]
- 7) Cut to length, port added



Experimental Methodology – Ballistic Stand



Key Diagnostics:

- Mass Flow Controller
- Pressure Transducers
- Thermocouple
- Load Cell
- CCP Collector

Controllable Parameters:

- Fuel Grain Length
- Combustion Port Diameter
- Oxidizer Mass Flowrate
- Injector Type/Size
- Nozzle Throat Size
- Post-Combustion Chamber

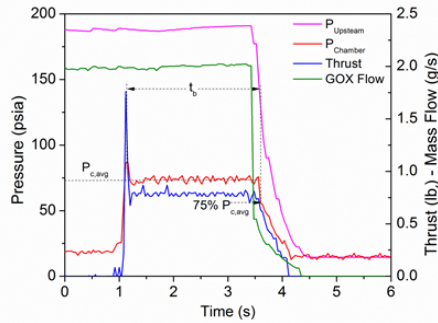
Dependent Parameters:

- Oxidizer Mass Flux
- Regression Rate
- Chamber Pressure
- O/F Ratio
- Residence Time
- Combustion Efficiency

Experimental Methodology – Data Analysis



TOT measurements are easy to implement on a lab-scale



Oxidizer Mass Flux

$$\bar{G}_{ox} = \frac{\bar{m}_{ox}}{A_c} = \frac{16\bar{m}_{ox}}{\pi(D_f + D_i)^2}$$

Characteristic Velocity

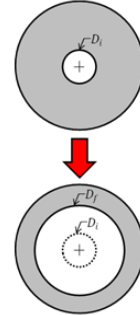
$$c^* \cong \frac{\bar{P}_c A_t}{(\bar{m}_{ox} + \bar{m}_f)}$$

Combustion Efficiency

$$n_{c^*} = \frac{c^*}{c_{th}^*}$$

Residence Time

$$t_r = \frac{V_c \rho_c}{\bar{m}_T}$$



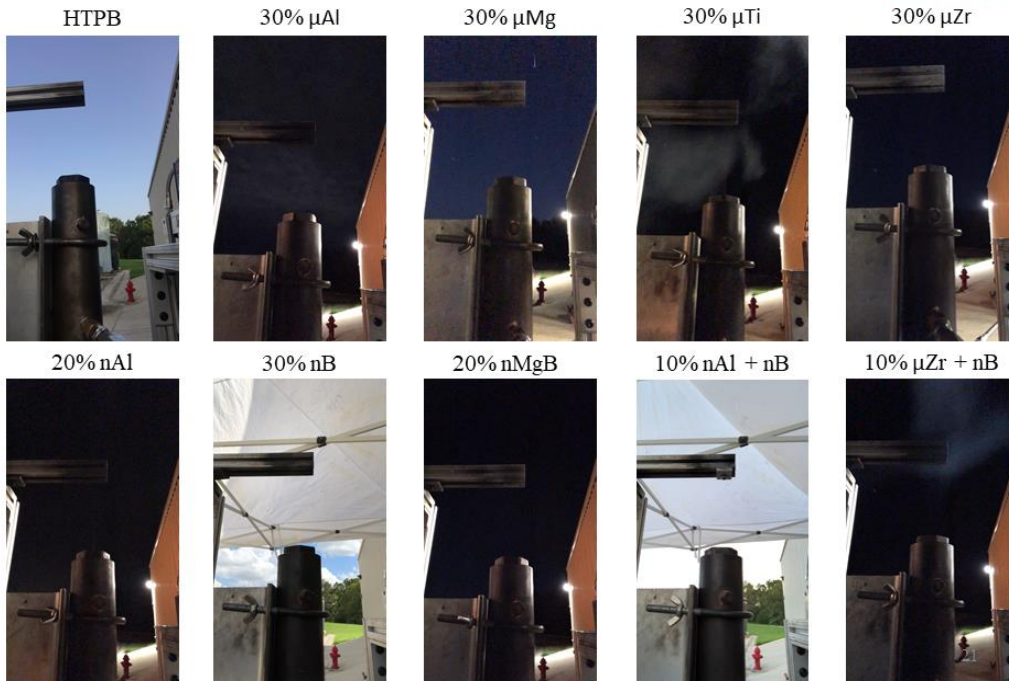
Regression Rate

$$D_f = \left[\frac{4(m_i - m_f)}{\pi \rho_f L} + D_i^2 \right]^{1/2}$$

$$r^i = \frac{D_f - D_i}{2t_b}$$

20

Experimental Methodology – Ballistic Testing Videos



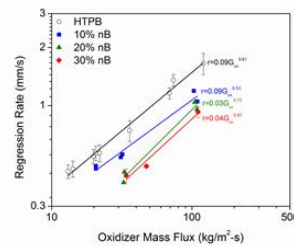
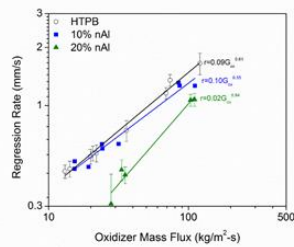
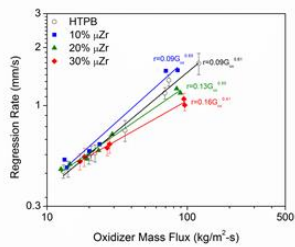
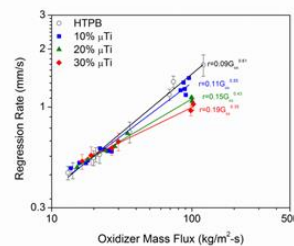
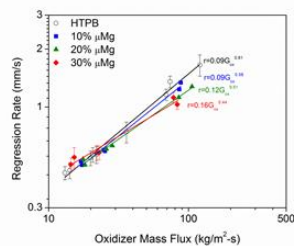
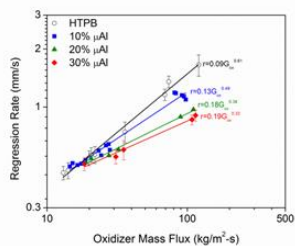
Results and Discussion: Metal Additives

22

Results – Pure Metals – Regression Rate



Metal additives *reduce regression rate* at high loadings

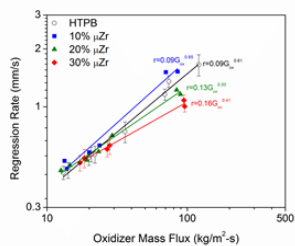
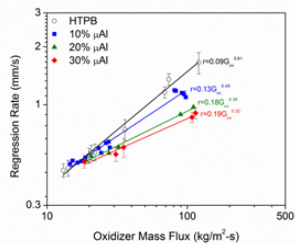


23

Results – Pure Metals – Regression Rate



Metal additives *reduce regression rate* at high loadings



Potential Mechanisms:

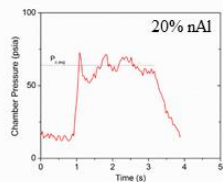
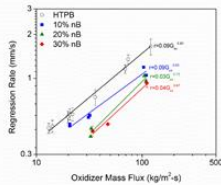
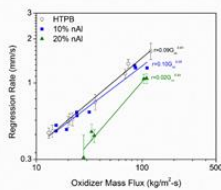
- Pressure-dependent ignition and reaction time of metal particles
- Metal reactions take place in the post-combustion chamber
- Mass accumulation yields significant heat transfer blocking

24

Results – Pure Metals – Surface Accumulation

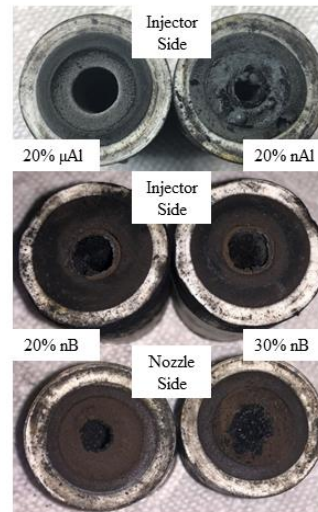


Mass accumulation was problematic for *nano-metals*



Nano-metals led to:

- Large surface accumulations
- Periodic surface-layer shedding
- Large pressure excursions
- Not an artifact of 're-burn' methodology

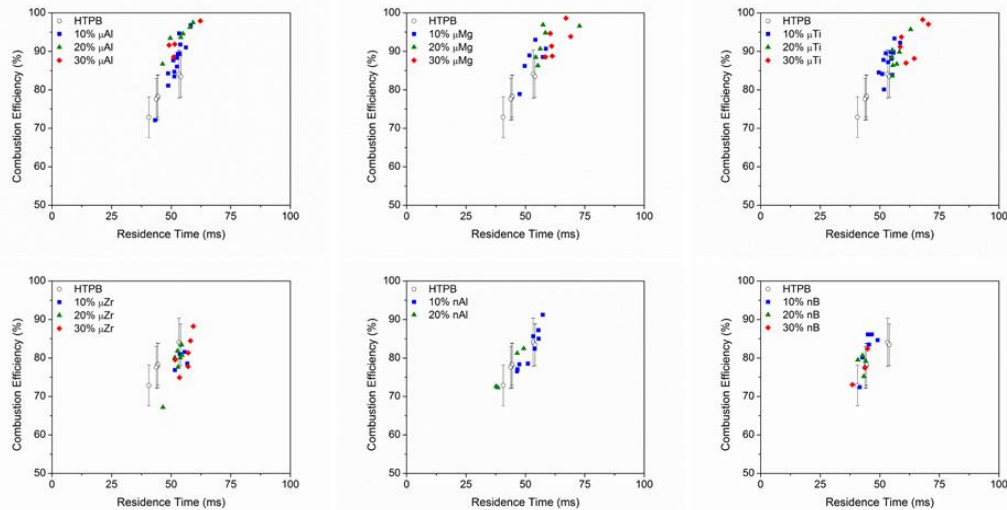


25

Results – Pure Metals – Combustion Efficiencies



Sufficient residence time is required



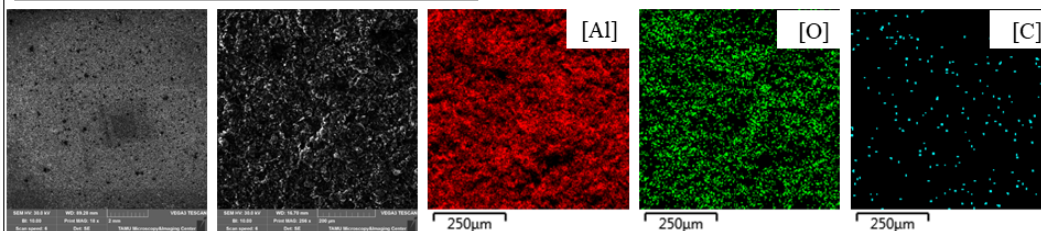
26

Results – Pure Metals – CCP Analyses



Oxygen absorption is high in CCP

Representative EDS Analysis (30% μAl)



EDS Analyses Summary

- Individual particles are not generally resolvable
- Oxygen absorption is generally high
- Carbon absorption is high, in some cases

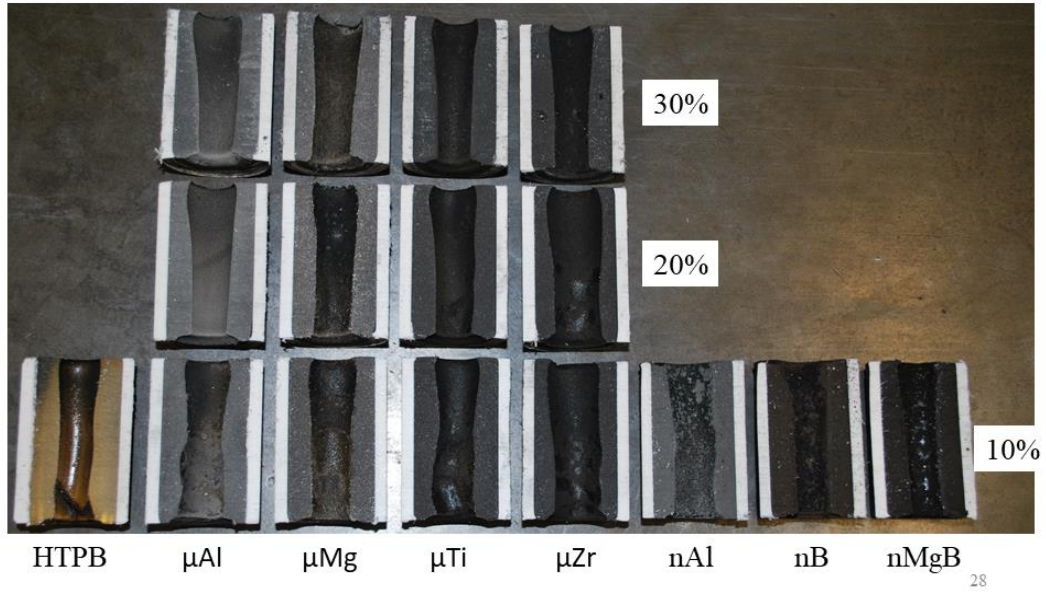
Metal	Oxide	O/F	η_{c^+} (%)	Composition (atomic %)			O/M Ratio	
				Metal	O	C	Theoretical	EDS
μAl	Al_2O_3	2.4	92	33	64	3	1.5	1.9
μMg	MgO	2.0	95	33	58	10	1.0	1.8
μTi	TiO_2	2.2	94	26	70	3	2.0	2.7
μZr	ZrO_2	2.0	88	13	59	28	2.0	4.5
nB	B_2O_3	3.2	73	25	43	31	1.5	1.7

27

Results – Pure Metals – Post-Combustion Analysis



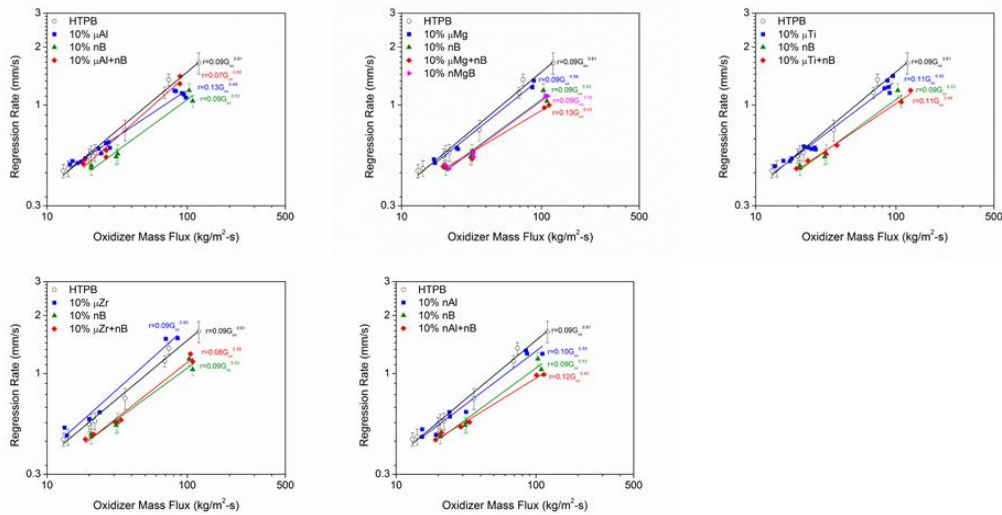
Particle accumulation observed in combustion ports



Results – Metal Blends – Regression Rate



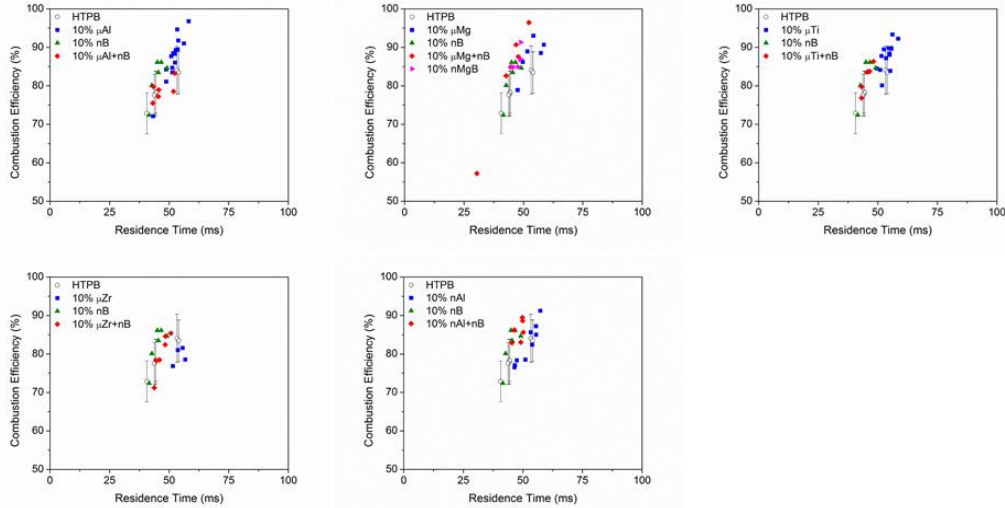
Metal additives reduce regression rate at high loadings



Results – Metal Blends – Combustion Efficiencies



Metal additives *reduce regression rate* at high loadings

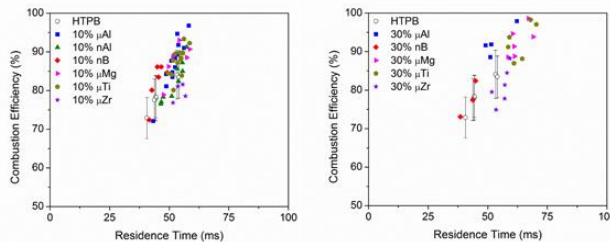
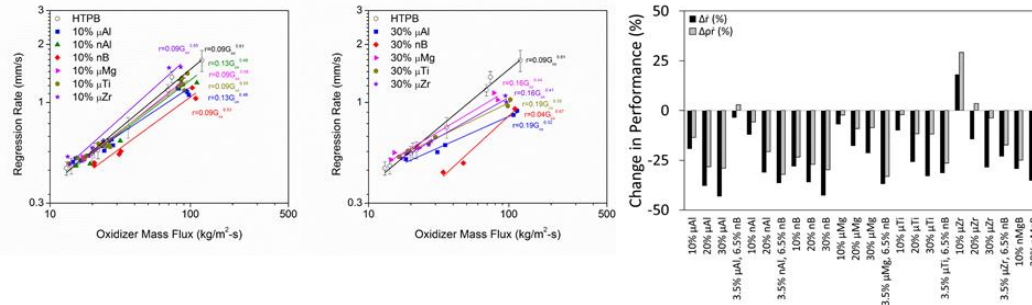


30

Results – Metal Fuels – General Comparisons



Zirconium *outperforms all other metals*



Key Findings:

- Regression rate generally decreases with metal addition or further loading
- High combustion efficiencies are achievable, but decrease with loading for some metals
- Zirconium yields highest performance benefits
 - \dot{r} , \dot{m}_f , $I_{sp,v}$

31

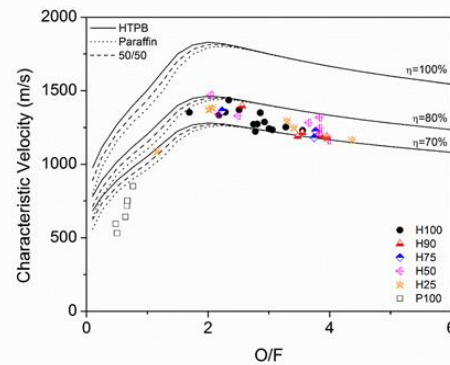
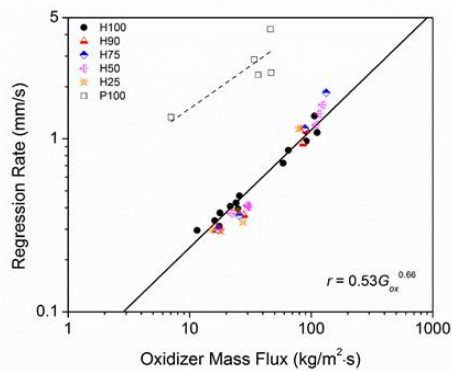
Results and Discussion: Mixed Fuel Systems

32

Results – Mixed Fuel Systems



Measureable *enhancement was not observed*



Potential Mechanism:

- HTPB pyrolysis behavior dominates regression behavior
- Substantial liquid surface layer is not formed

33

Summary



- Developed lab-scale hybrid rocket testing capabilities at Texas A&M University
- Evaluated relative effects of pure metal type and loading on the combustion of HTPB/GOX systems
 - Regression rate generally decreased due to mass blocking effect
 - High combustion efficiencies were obtained for sufficient t_r
 - Zirconium [Zr] outperformed all other additives
 - Nano-metals exhibited increased mass accumulation
- Assessed the synergistic performance benefits of bi-metallic fuels
 - No observed performance enhancement, except for $\mu\text{Al/B}$
- Evaluated mixed HTPB/paraffin fuel systems
 - No observed regression rate variation for reasonable paraffin loadings
- Suggested studies
 - Systematic and independent variation of: Pressure
Particle Geometry

34

Acknowledgements



- Advisor: Dr. Eric L. Petersen
- Committee: Dr. Waruna Kulatilaka
Dr. Timothy Jacobs
Dr. Adonios Karpetis
- Lab Colleagues: Felix Rodriguez
Catherine Dillier
Erica Petersen
Andrew Tykol
Jacob Stahl
Gordon Morrow
Andrew Demko³⁵

APPENDIX F – CURRICULUM VITAE

James Christopher Thomas

811 Mockingbird Street • Navasota, TX 77868 • (210) 859-8537 • ChrisThomas2009@live.com

Objective XX.

Education

- **Texas A&M University** – College Station, TX
 - Doctorate of Philosophy in Mechanical Engineering (GPA: 4.00) 01/2015 – 12/2018
 - Master of Science in Mechanical Engineering (GPA: 3.24) 05/2013 – 01/2015
 - Bachelor of Science in Mechanical Engineering (GPA: 3.29) 08/2009 – 05/2013

Work Experience

- **Texas A&M University Propulsion Laboratory** (Postdoctoral Research Associate) 2018 – Present
(Graduate Research Assistant) 2014 – 2018
(Undergraduate Research Assistant) 2011 – 2014
 - Supported strand bomb testing for measurement of burning rates, pressure responses, and combustion behavior of solid and liquid propellants containing numerous additives
 - Designed and constructed transient pressure control system for strand bomb testing
 - Supported redesign of strand bomb for propellant evaluation at extreme operation temperatures and pressures
 - Designed and implemented lab-scale mechanical, rheological, thermal, and safety property testing methods for solid and liquid propellants and solid fuels containing numerous additives
 - Designed and implemented manufacturing procedures for lab-scale, hybrid rocket fuel grains with various binders and additives
 - Designed lab-scale rocket stand for measurement of regression rates, combustion efficiencies, and thrust of hybrid motors
 - Managed summer research program for underprivileged or underrepresented undergraduate students
- **NASA Johnson Space Center** (Intern – Propulsion and Power Division) 2017
 - Aided in the design, construction, and testing of a Li-ion battery calorimeter for quantification of energy release during thermal runaway events
 - Supported design and testing of novel aluminum, active cooling, and vaporizing heat sink systems for mitigation of thermal runaway propagation in Li-ion battery packs
 - Evaluated and tested high-performance, novel chemistry battery systems for future spaceflight applications
- **The Aerospace Corporation** (Associate Technical Staff, Consultant – Propulsion Department) 2014 – Present
 - Supported rocket stand testing for measurement of regression rates and combustion efficiencies of hybrid motors with numerous additives
 - Supported redesign and upgrade construction of rocket stand for hybrid propellant evaluation at high chamber pressures and oxidizer mass fluxes
 - Assisted in upgrade and supported testing of particle-impact ignition shock tube at elevated temperature and pressure and high oxygen concentrations
- **Baker Engineering and Risk Consultants** (Intern – Blast Effects Section) 2009, 2010
 - Supported explosion testing in a large-scale vapor cloud explosion test rig
 - Supported design, construction, and testing of a larger full-scale vapor cloud explosion test rig
 - Assisted in construction and testing of lab-scale flammability limit evaluation apparatus
 - Prepared data input for petrochemical facility risk analyses
 - Supported various legal explosion cases through experimental design, testing, and analysis
- **PowerSwing** (Construction Engineer) 2008 – 2009
- **Wood and Water** (Carpenter’s Assistant) 2005 – 2008

Teaching Experience

- Instructor
 - MEEN 404 – Intermediate Design x2 Spring 2017
- Guest Lecturer
 - MEEN 344 – Fluid Mechanics x2 Spring 2016
- Teaching Assistant
 - MEEN 633 – Combustion Science Fall 2015
 - MEEN 472 – Gas Dynamics Fall 2014, Fall 2018

Relevant Coursework

- Advanced Engineering Thermodynamics, Intermediate Heat Transfer, Intermediate Fluid Mechanics
- Gas Dynamics, Combustion Science, Chemical Rocket Propulsion, Aerothermochemistry, Combustion Laser Diagnostics, Micro-Scale Thermodynamics, Process Safety Engineering
- Mechanical Behavior of Materials, Solid Mechanics
- Fundamentals of Space Life Sciences, Human Spaceflight Operations
- Intermediate Design, Bio-Inspired Engineering Design
- Advanced Calculus, Differential Equations, Methods of Applied Mathematics, Statistics in Research
- Future Faculty Preparation, Academy of Future Faculty

Organizations

- Association of Spaceflight Professionals (Astronauts for Hire) (Member) 2017 – Present
- Texas A&M University's Aggie Astronaut Corps (Member) 2017 – Present
- Sigma Xi Research Honor Society (Associate Member) 2016 – Present
- Students for the Exploration and Development of Space (SEDS) (Member) 2015 – Present
- The Combustion Institute (Member) 2013 – Present
- The American Institute of Aeronautics and Astronautics (AIAA) (Member) 2012 – Present
- Texas A&M's Energy and Propulsion Research Experience for Undergraduates (REU) (Manager) 2012 – Present
- Texas A&M University Intramural Sports (Student Athlete) 2009 – Present
- Texas A&M University Rugby Football Club (Varsity Athlete) 2009 – 2011
- Texas A&M University Residence Hall Association (Moses Hall President) 2009

Certifications

- Texas Board of Professional Engineers
 - Engineer in Training (EIT)
- Texas A&M University Center for Teaching Excellence
 - Academy of Future Faculty (AFF) Certificate
- United State Security Clearance
 - Confidential Level
- National Strength and Conditioning Association (NSCA)
 - Certified Personal Trainer (CPT)
- Professional Association of Diving Instructors (PADI)
 - Self-Contained Underwater Breathing Apparatus (SCUBA)
- American Heart Association (AHA)
 - Basic Life Support (BLS) Cardiopulmonary Resuscitation (CPR) and Automated External Defibrillator (AED)

Software Skills

- Microsoft Office: Word, Excel, PowerPoint, Visio, Paint	Expert
- Computer-Aided Drawing: AutoCAD, Solidworks, CREO Parametric, Inventor	Intermediate
- Mathworks MATLAB	Expert
- NASA Chemical Equilibrium with Applications (CEA)	Expert
- Propellant Performance and Evaluation Program (ProPEP)	Expert
- Lawrence Livermore National Laboratory's (LLNL) Cheetah 8.0	Intermediate
- Stanford JANNAF (STANJAN) Chemical Equilibrium Calculator	Expert
- Frozen Shockwave (FROSH) Calculator	Expert
- GRANTA CES EduPack Materials and Processes Database	Intermediate
- National Instrument Laboratory Virtual Instrument Engineering Workbench (LabVIEW)	Intermediate
- National Instrument Circuit Design Suite	Novice

Volunteering Activities

- American Institute of Aeronautics and Astronautics' Generation STEM Event (Volunteer)	2016 – Present
- Texas A&M University Junior Science Bowl (Moderator)	2015 – Present
- Texas A&M University Regional Science Bowl (Moderator)	2015 – Present
- Texas Junior Academy of Science (Technical Judge)	2015 – Present
- Texas Junior Science and Humanities Symposium (Technical Judge)	2015 – Present
- Texas Science Olympiad (Thermodynamics Supervisor)	2015 – Present
- Expanding Your Horizons Women's Engineering Outreach Event (Volunteer)	2015 – Present
- Aggie Big Event (Volunteer)	2010 – 2015
- Student Leaders of Tomorrow (Volunteer)	2010
- Aggie Shadows (Chaperone)	2009

Editorial Activities

- AIAA Journal of Propulsion and Power (Reviewer, 3/yr)	2016 – Present
- Polymer Composites (Reviewer, 1/yr)	2018 – Present
- Journal of Energetic Materials (Reviewer, 1/yr)	2018 – Present
- High Performance Polymers (Reviewer, 1/yr)	2018 – Present

Awards

- Mike J. Walker '66 Graduate Travel Fellowship	2018
- National Science Foundation (NSF) International Symposium on Combustion Travel Award	2018
- Combustion Institute International Symposium Travel Award	2018
- Central States Section of the Combustion Institute International Symposium Travel Award	2018
- Texas A&M University Mechanical Engineering Department Travel Grant	2016, 2017, 2018
- Central States Section of the Combustion Institute Regional Meeting Travel Award	2015, 2018
- 48 th JANNAF Combustion Meeting Best Student Paper Award	2017
- Texas Space Grant Consortium Fellowship	2017
- Sigma Xi Grants-in-Aid of Research Grant	2017
- Texas A&M University Graduate Teaching Fellowship	2017
- George Bush Presidential Library Foundation Travel Grant	2016
- American Institute of Aeronautics and Astronautics (AIAA) Spirit of Apollo Scholarship	2016
- United States Section of the Combustion Institute Travel Award	2015
- Texas A&M University Graduate and Professional Studies Travel Grant	2015
- Texas A&M University Graduate and Professional Studies Research Award	2014
- Texas A&M University Wesley and Anna Mae Neumann Scholarship	2009

Journal Publications

In Progress

- 1) D. P. Finegan, J. J. Darst, W. Walker, Q. Li, C. Yang, R. Jervis, T. M. M. Heenan, J. Hack, J. C. Thomas, A. Rack, P. R. Shearing, M. Keyser, and E. D. Darcy, "Comparison of Abuse Techniques to Instigate Thermal Runaway in Li-Ion Cells," *Journal of the Electrochemical Society*, 2019, *In Progress*.
- 2) J. C. Thomas and E. L. Petersen, "Thermal Cook-Off of Plain and Aged AF-M315E" *JANNAF Journal*, 2019, *In Progress*.
- 3) E. C. Darcy, J. J. Darst, J. C. Thomas, and S. Scharf, and S. Rickman, "Aluminum and Be-Al Alloy Interstitial Heat Sinks for Lightweight Thermal Runaway Prevention in Li-Ion Battery Systems," *Journal of the Electrochemical Society*, 2019, *In Progress*.
- 4) J. C. Thomas and E. L. Petersen, "Thermal Cook-Off of Liquid Monopropellants" *Journal of Propulsion and Power*, 2019, *In Progress*.
- 5) C. A. M. Dillier, A. R. Demko, J. C. Thomas, and E. L. Petersen, "Aluminum and Magnesium Coated Boron Particles for Solid Propellants," *Journal of Propulsion and Power*, 2019, *In Progress*.
- 6) J. C. Thomas, A. J. Tykol, F. A. Rodriguez, and E. L. Petersen, "Highly-Loaded Solid Fuel Formulations for Hybrid Rocket Applications," *Combustion Science and Technology*, 2019, *In Progress*.
- 7) D. P. Finegan, J. J. Darst, W. Walker, Q. Li, C. Yang, R. Jervis, T. M. M. Heenan, J. Hack, J. C. Thomas, A. Rack, P. R. Shearing, M. Keyser, and E. D. Darcy, "Design Features for Optimal Safety of 18650 Li-Ion Batteries," *Advanced Science*, 2018, *In Progress*.
- 8) C. A. M. Dillier, A. R. Demko, J. C. Thomas, T. Sammet, K. Grossman, S. Seal, and E. L. Petersen, "Experimental Investigation on the Effects of Graphene on the Properties of AP/HTPB-Based Solid Rocket Propellants," *Journal of Propulsion and Power*, 2018, *In Progress*.
- 9) J. C. Thomas, J. M. Stahl, A. J. Tykol, F. A. Rodriguez, E. L. Petersen, C. Paravan, L. Galfetti, "HTPB/Paraffin Fuel Blends for Hybrid Rocket Applications," *International Journal of Energetic Materials and Chemical Propulsion*, 2018, *In Progress*.
- 10) A. J. Tykol, J. C. Thomas, and E. L. Petersen, "Burning Rate Characterization of GN/BCN Propellants Containing Micro- and Nano-Sized Metal Oxides," *Propellants, Explosives, and Pyrotechnics*, 2018, *In Progress*.
- 11) J. M. Stahl, G. D. Homan-Cruz, J. C. Thomas, and E. L. Petersen, "Two-Phase Burning Behavior of Aqueous HAN Propellant," *Combustion and Flame*, 2018, *In Progress*.
- 12) J. C. Thomas, J. P. Anderson, E. L. Petersen, M. W. Crofton, and M. D. Worshum, "Particle-Impact Characterization Experiments at Liquid Rocket Engine Conditions Using a Miniature Shock Tube," *Journal of Thermophysics and Heat Transfer*, 2018, *In Progress*.

In Review

- 1) J. C. Thomas, G. R. Morrow, and E. L. Petersen, "Comprehensive Study of the Effects of AP Particle Size and Loading on the Burning Rate of Composite AP/HTPB Propellants," *Journal of Propulsion and Power*, 2018, *In Review*.
- 2) J. C. Thomas, A. R. Demko, J. M. Stahl, E. L. Petersen, B. B. Brady, J. D. DeSain, and J. H. Schilling, "Materials Compatibility and Corresponding Effects on the Combustion of AF-M315E," *JANNAF Journal of Propulsion and Energetics*, Vol. 10:1, 2019, *In Review*.

- 3) J. C. Thomas, A. R. Demko, J. M. Stahl, E. L. Petersen, B. B. Brady, J. D. DeSain, and J. H. Schilling, "Linear Burning Rates and Non-Catalytic Ignition Behavior of AF-M315E over a Wide Pressure Range," *JANNAF Journal of Propulsion and Energetics*, Vol. 10:1, 2019, *In Review*.
- 4) D. P. Finegan, J. Darst, W. Walker, Q. Li, C. Yang, R. Jervis, T. M. M. Heenan, J. Hack, J. C. Thomas, A. Rack, P. R. Shearing, M. Keyser, and E. Darcy, "Modelling and Experiments to Identify High-Risk Failure Scenarios for Testing the Safety of Lithium Ion Cells," *Journal of Power Sources*, 2018, *In Review*.

Accepted

- 1) J. C. Thomas, T. E. Sammet, C. A. M. Dillier, A. R. Demko, F. A. Rodriguez, and E. L. Petersen, "Aging Effects on the Burning Rate of Composite Solid Propellants with Nano-Additives," *Journal of Propulsion and Power*, 2018, *Accepted*.
- 2) J. C. Thomas, J. M. Stahl, G. D. Homan-Cruz, and E. L. Petersen, "The Effects of SiO₂ and TiO₂ on the Two-Phase Burning Behavior of Aqueous HAN," *Proceedings of the Combustion Institute*, Vol. 37:1, 2018, *Accepted*.

Published

- 1) A. R. Demko, T. W. Allen, J. C. Thomas, M. Johnson, G. R. Morrow, D. L. Reid, S. Seal, and E. L. Petersen, "Comparison of Commercially Available and Synthesized Titania Nano-Additives in Composite HTPB/AP Propellant," *Propellants, Pyrotechnics, and Explosives*, Vol. 42:2, 2017, pp. 158-166.
- 2) J. C. Thomas, A. R. Demko, T. Sammet, E. L. Petersen, D. L. Reid, and S. Seal, "Mechanical Properties of Composite AP/HTPB Propellants Containing Novel Titania Nanoparticles," *Propellants, Pyrotechnics, and Explosives*, Vol. 41:5, 2016, pp. 822-834.

Conference Proceedings

- 1) C. A. M. Dillier, A. R. Demko, J. C. Thomas, K. Grossman, S. Seal, and E. L. Petersen, "The Evaluation of Composite Propellants Utilizing Various Nano-Scale Aluminum and Boron Incorporation Methods," AIAA Paper 2019-XXXX, 55th AIAA Aerospace Sciences Meeting, San Diego, CA, January 7-11, 2019.
- 2) J. C. Thomas, J. M. Stahl, G. D. Homan-Cruz, and E. L. Petersen, "The Effects of SiO₂ and TiO₂ on the Two-Phase Burning Behavior of Aqueous HAN," 37th Symposium (International) on Combustion, Dublin, Ireland, July 29-August 3, 2018.
- 3) J. C. Thomas, T. E. Sammet, C. A. M. Dillier, A. R. Demko, F. A. Rodriguez, and E. L. Petersen, "Effects of Aging on the Burning Rates of Composite Solid Propellants with and without Nano-Sized Additives," AIAA Paper 2018-4960, 54th AIAA/ASME/SAE/ASEE Joint Propulsion Conference, Cincinnati, OH, July 9-11, 2018.
- 4) J. C. Thomas, G. R. Morrow, C. M. A. Dillier, and E. L. Petersen, "Comprehensive Study of AP Particle Size and Loading Effects on the Burning Rates of Composite AP/HTPB Propellants," AIAA Paper 2018-4874, 54th AIAA/ASME/SAE/ASEE Joint Propulsion Conference, Cincinnati, OH, July 9-11, 2018.
- 5) J. Darst, J. C. Thomas, D. P. Finegan, and E. Darcy, "Guidelines for Safe, High Performing Li-ion Battery Designs for Manned Vehicles," 48th Power Sources Conference, Denver, CO, June 11-14, 2018.
- 6) C. A. M. Dillier, A. R. Demko, J. C. Thomas, K. Grossman, S. Seal, and E. L. Petersen, "Performance of Aluminum-Coated Nano-Sized Boron Additives in AP/HTPB Propellants," Spring Technical Meeting of the Central States Section of the Combustion Institute, Minneapolis, MN, May 20-22, 2018.
- 7) J. C. Thomas, G. D. Homan-Cruz, J. M. Stahl, and E. L. Petersen, "The Effects of SiO₂ and TiO₂ on the Two-Phase Burning Behavior of Aqueous HAN," Spring Technical Meeting of the Central States Section of the Combustion Institute, Minneapolis, MN, May 20-22, 2018.

- 8) J. C. Thomas, G. D. Homan-Cruz, J. M. Stahl, and E. L. Petersen, "Catalytic Effects of Inert Particles on the Two-Phase Combustion Behavior of Aqueous HAN Monopropellant," 3rd Southwest Emerging Technology Symposium, El Paso, Texas, April 14, 2018.
- 9) J. C. Thomas, G. D. Homan-Cruz, J. M. Stahl, and E. L. Petersen "The Effects of SiO₂ and TiO₂ on the Two-Phase Burning Behavior of Aqueous HAN Propellant," Texas A&M University Student Research Week Symposium, College Station, TX, March 19-23, 2018.
- 10) J. C. Thomas, A. R. Demko, J. M. Stahl, E. L. Petersen, B. B. Brady, J. D. DeSain, and J. H. Schilling, "Materials Compatibility and Corresponding Effects on the Combustion of AF-M315E," JANNAF 2017-5445, 48th JANNAF Combustion Meeting, Newport News, VA, December 4-7, 2017.
- 11) J. C. Thomas, A. R. Demko, J. M. Stahl, E. L. Petersen, B. B. Brady, J. D. DeSain, and J. H. Schilling, "Linear Burning Rates and Non-Catalytic Ignition Behavior of AF-M315E over a Wide Pressure Range," JANNAF 2017-5435, 48th JANNAF Combustion Meeting, Newport News, VA, December 4-7, 2017.
- 12) J. C. Thomas, J. P. Anderson, E. L. Petersen, M. W. Crofton, and M. D. Worshum, "Particle-Impact Characterization Experiments at Liquid Rocket Engine Conditions Using a Miniature Shock Tube," AIAA Paper 2017-5072, 53rd AIAA/ASME/SAE/ASEE Joint Propulsion Conference, Atlanta, GA, July 10-12, 2017.
- 13) M. W. Crofton, J. H. Morehart, J. C. Thomas, and E. L. Petersen, "Particle-Impact Ignition Experiments at High Oxygen Pressure," AIAA Paper 2017-5073, 53rd AIAA/ASME/SAE/ASEE Joint Propulsion Conference, Atlanta, GA, July 10-12, 2017.
- 14) J. C. Thomas, J. M. Stahl, A. J. Tykol, F. A. Rodriguez, and E. L. Petersen, "Hybrid Rocket Studies Using HTPB/Paraffin Fuel Blends in Gaseous Oxygen Flow," 7th EUCASS, Milan, Italy, July 3-6, 2017.
- 15) J. C. Thomas, G. R. Morrow, A. R. Demko, and E. L. Petersen, "Correlation of the Effects of Particle Size and Loading on the Burning Rate of Composite AP/HTPB Propellants," 2nd Southwest Emerging Technology Symposium, El Paso, Texas, April 1, 2017.
- 16) J. C. Thomas, J. M. Stahl, G. M. Morrow, and E. L. Petersen, "Design of a Lab-Scale Hybrid Rocket Test Stand," AIAA Paper 2016-4695, 52nd AIAA/ASME/SAE/ASEE Joint Propulsion Conference, Salt Lake City, UT, July 25-27, 2016.
- 17) C. A. M. Dillier, A. R. Demko, T. Sammet, J. C. Thomas, and E. L. Petersen, "Burning Rate and Ignition Delay Times of AP/HTPB-Based Solid Rocket Propellants Containing Graphene," AIAA Paper 2016-4690, 52nd AIAA/ASME/SAE/ASEE Joint Propulsion Conference, Salt Lake City, UT, July 25-27, 2016.
- 18) J. C. Thomas, J. M. Stahl, and E. L. Petersen, "Development of a Micro-Burner for Hybrid Rocket Combustion Studies," 1st Southwest Emerging Technology Symposium, El Paso, Texas, April 9, 2016.
- 19) J. C. Thomas, E. L. Petersen, J. D. DeSain, and B. B. Brady, "Hybrid Rocket Enhancement by Micro- and Nano-scale Additives in HTPB Fuel Grains," AIAA Paper 2015-4041, 51st AIAA/ASME/SAE/ASEE Joint Propulsion Conference, Orlando, FL, July 27-29, 2015.
- 20) J. C. Thomas, E. L. Petersen, J. D. DeSain, B. B. Brady, "Regression Rate Enhancement in Hybrid Rockets with HTPB Fuel Grains by Nano-Aluminum Additives," 9th U.S. National Combustion Meeting, Cincinnati, Ohio, May 17-20, 2015.
- 21) C. A. M. Dillier, A. R. Demko, J. C. Thomas, T. Sammet, K. Grossman, S. Seal, and E. L. Petersen, "Determining the Effects of Graphene on the Burning Rate and Strength of AP/HTPB-Based Solid Rocket Propellants," 9th U.S. National Combustion Meeting, Cincinnati, Ohio, May 17-20, 2015.
- 22) J. C. Thomas, E. L. Petersen, J. D. DeSain, M. N. Riddlehuber, and B. B. Brady, "Hybrid Rocket Burning Rate Enhancement by Nano-scale Additives in HTPB Fuel Grains," AIAA Paper 2014-3955, 50th AIAA/ASME/SAE/ASEE Joint Propulsion Conference, Cleveland, OH, July 28-30, 2014.

- 23) A. R. Demko, J. C. Thomas, T. Sammet, E. L. Petersen, D. L. Reid, and S. Seal, "Temperature Sensitivity of Composite Propellants Containing Novel Nano-Additive Catalysts," AIAA Paper 2014-3691, 50th AIAA/ASME/SAE/ASEE Joint Propulsion Conference, Cleveland, OH, July 28-30, 2014.
- 24) J. C. Thomas, A. R. Demko, T. Sammet, E. L. Petersen, D. L. Reid, and S. Seal, "Mechanical Properties of Composite AP/HTPB Propellants with Titania Nanoparticles," Spring Technical Meeting of the Central States Section of the Combustion Institute, Tulsa, Oklahoma, March 16-18, 2014.
- 25) J. C. Thomas, J. D. DeSain, B. Brady, and E. L. Petersen, "Hybrid Rocket Burning Rate Enhancement by Nano-Scale Aluminum Additives in HTPB Fuel Grains," 3rd Southwest Energy Science and Engineering Symposium, El Paso, Texas, April 27, 2013.

Poster Presentations

- 1) J. C. Thomas, A. J. Tykol, F. A. Rodriguez, and E. L. Petersen, "Performance Enhancement of HTPB Fuels Burning in Gaseous Oxygen by Plain Metallic Additives," 37th International Symposium on Combustion, Dublin, Ireland, July 29-August 3, 2018.
- 2) J. C. Thomas, G. R. Morrow, C. A. M. Dillier, and E. L. Petersen, "Oxidizer Size and Concentration Effects on Composite AP/HTPB Propellant Burning Rates," 37th International Symposium on Combustion, Dublin, Ireland, July 29-August 3, 2018.
- 3) C. A. M. Dillier, A. R. Demko, J. C. Thomas, K. Grossman, S. Seal, and E. L. Petersen, "Performance of Aluminum-Coated Nano-Sized Boron Additives in AP/HTPB Propellants," 37th International Symposium on Combustion, Dublin, Ireland, July 29-August 3, 2018.
- 4) J. C. Thomas, B. B. Brady, J. D. DeSain, and E. L. Petersen, "Hybrid Rocket Burning Rate Enhancement by Nano-Scale Additives in HTPB Fuel Grains," 35th International Symposium on Combustion, San Francisco, CA, August 3-8, 2014.
- 5) A. R. Demko, J. C. Thomas, C. A. M. Dillier, T. Sammet, and E. L. Petersen, "Temperature Sensitivity of Composite Propellants Containing Novel Nano-Additive Catalysts," 35th International Symposium on Combustion, San Francisco, CA, August 3-8, 2014.
- 6) T. Sammet, J. C. Thomas, A. R. Demko, and E. L. Petersen, "Composite Propellant Mixture Viscosity," Texas A&M University Research Experience for Teachers, College Station, TX, August 2, 2013.
- 7) J. C. Thomas, and E. L. Petersen, "Burning Rate Enhancement of HTPB Fuel Grains in Hybrid Rocket Motors by the Addition of Nano-Scale Aluminum Particles," Texas A&M University Research Experience for Undergraduates, College Station, TX, August 3, 2012.

Invited Presentations

- 1) J. C. Thomas, E. L. Petersen, J. J. Darst, E. C. Darcy, and D. P. Finegan, "Consequence Analysis of Li-Ion Battery Thermal Runaway Events with Chemical Equilibrium Analysis," 2018 NASA Aerospace Battery Workshop, Huntsville, Alabama, November 27-29, 2018.
- 2) E. L. Petersen, J. C. Thomas, A. Tykol, and C. J. Aul, "REU Site: Undergraduate Research in Energy and Propulsion," 2nd Southwest Emerging Technology Symposium, El Paso, Texas, April 1, 2017.

Academic Publications

- 1) J. C. Thomas, "Mixed HTPB/Paraffin Fuels and Metallic Additives for Hybrid Rocket Applications," Ph. D. Dissertation, Department of Mechanical Engineering, Texas A&M University, College Station, TX, 2018.
- 2) J. C. Thomas, "Hybrid Rocket Burning Rate Enhancement by Nano-Scale Additives in HTPB Fuel Grains," M. S. Thesis, Department of Mechanical Engineering, Texas A&M University, College Station, TX, 2014.

Professional References

- 1) Eric L Petersen, Ph. D.
Nelson-Jackson Professor
Mechanical Engineering Department
Texas A&M University
EPetersen@tamu.edu
(407) 702-3694
Relationship: Academic Advisor
- 2) Brian B Brady, Ph. D.
Senior Research Scientist
Propulsion Science Department
The Aerospace Corporation
Brian.B.Brady@aero.org
(562) 301-6007
Relationship: Previous Manager
- 3) John D DeSain, Ph. D.
Research Scientist
Propulsion Scientist Department
The Aerospace Corporation
John.D.DeSain@aero.org
(310) 872-6747
Relationship: Previous Manager
- 4) Darren R Malik, M. S., P. E.
Senior Consultant
Blast Effects Section
Baker Risk and Engineering Consultants
DMalik@bakerrisk.com
(210) 363-6837
Relationship: Previous Manager
- 5) Partha P Mukherjee, Ph. D.
Associate Professor
Mechanical Engineering Department
Purdue University
PMukherjee@purdue.edu
(765) 494-2219
Relationship: Previous Professor
- 6) Eric C Darcy, Ph. D.
Battery Systems Technical Discipline Lead
Propulsion and Power Department
NASA Johnson Space Center
Eric.C.Darcy@nasa.gov
(713) 492-1753
Relationship: Previous Manager

Contact Information

James 'Chris' Thomas

Research Assistant
Propulsion Laboratory
TEES Turbomachinery Laboratory

Ph.D. Candidate, Instructor
Department of Mechanical Engineering
Texas A&M University

Cell Phone: (210) 859-8537
Work E-mail: James.Chris.Thomas@tamu.edu
Personal E-mail: ChrisThomas2009@live.com

LinkedIn: <https://www.linkedin.com/in/jameschristhomas/>
Research Gate: https://www.researchgate.net/profile/James_Thomas29
Google Scholar: <https://scholar.google.com/citations?user=PSgef4AAAAJ>
OrCID: 0000-0002-2555-6772